UC Berkeley
UC Berkeley Electronic Theses and Dissertations

Title
Large-eddy Simulation of the Nighttime Stable Atmospheric Boundary Layer

Permalink
https://escholarship.org/uc/item/4hj9h261

Author
Zhou, Bowen

Publication Date
2012

Peer reviewed|Thesis/dissertation

eScholarship.org Powered by the California Digital Library
University of California

Large-eddy Simulation of the Nighttime Stable Atmospheric Boundary Layer

by

Bowen Zhou

A dissertation submitted in partial satisfaction of the

requirements for the degree of

Doctor of Philosophy

in

Engineering – Civil and Environmental Engineering

in the

Graduate Division

of the

University of California, Berkeley

Committee in charge:

Professor Fotini K. Chow, Chair

Professor Mark T. Stacey

Professor David M. Romps

Fall 2012

Numerical Modeling of the Nighttime Stable Atmospheric Boundary Layer

Copyright © 2012

by

Bowen Zhou

Abstract

Numerical Modeling of the Stable Atmospheric Boundary Layer

by

Bowen Zhou

Doctor of Philosophy in Engineering – Civil and Environmental Engineering

University of California, Berkeley

Professor Fotini K. Chow, Chair

A stable atmospheric boundary layer (ABL) develops over land at night due to radiative surface cooling. The state of turbulence in the stable boundary layer (SBL) is determined by the competing forcings of shear production and buoyancy destruction. When both forcings are comparable in strength, the SBL falls into an intermittently turbulent state, where intense turbulent bursts emerge sporadically from an overall quiescent background. This usually occurs on clear nights with weak winds when the SBL is strongly stable. Although turbulent bursts are generally short-lived (half an hour or less), their impact on the SBL is significant since they are responsible for most of the turbulent mixing.

The nighttime SBL can be modeled with large-eddy simulation (LES). LES is a turbulence-resolving numerical approach which separates the large-scale energy-containing eddies from the smaller ones based on application of a spatial filter. While the large eddies are explicitly resolved, the small ones are represented by a subfilter-scale (SFS) stress model. Simulation of the SBL is more challenging than the daytime convective boundary layer (CBL) because nighttime turbulent motions are limited by buoyancy stratification, thus requiring fine grid resolution at the cost of immense computational resources. The intermittently turbulent SBL adds additional levels of complexity, requiring the model to not only sustain resolved turbulence during quiescent periods, but also to transition into a turbulent state under appropriate conditions. As a result, LES of the strongly stable SBL potentially requires even finer grid resolution, and has seldom been attempted.

This dissertation takes a different approach. By improving the SFS representation of turbulence with a more sophisticated model, intermittently turbulent SBL is simulated, to our knowledge, for the first time in the LES literature. The turbulence closure is the dynamic reconstruction model (DRM), applied under an explicit filtering and reconstruction LES framework. The DRM is a mixed model that consists of subgrid scale (SGS) and resolved subfilter scale (RSFS) components. The RSFS portion is represented by a scale-similarity model that allows for backscatter of energy from the SFS to the mean flow. Compared to conventional closures, the DRM is able to sustain resolved turbulence under moderate stability at coarser resolution (thus saving computational resources). The DRM performs equally well at fine resolution. Under strong stability, the

DRM simulates an intermittently turbulent SBL, whereas conventional closures predict false laminar flows. The improved simulation methodology of the SBL has many potential applications in the area of wind energy, numerical weather prediction, pollution modeling and so on.

The SBL is first simulated over idealized flat terrain with prescribed forcings and periodic lateral boundaries. A wide range of stability regimes, from weakly to strongly stable conditions, is tested to evaluate model performance. Under strongly stable conditions, intermittency due to mean shear and turbulence interactions is simulated and analyzed. Furthermore, results of the strongly stable SBL are used to improve wind farm siting and nighttime operations. Moving away from the idealized setting, the SBL is simulated over relatively flat terrain at a Kansas site over the Great Plains, where the Cooperative Atmospheric-Surface Exchange Study – 1999 (CASES-99) took place. The LES obtains realistic initial and lateral boundary conditions from a meso-scale model reanalysis through a grid nesting procedure. Shear-instability induced intermittency observed on the night of Oct 5th during CASES-99 is reproduced to good temporal and magnitude agreement. The LES locates the origin of the shear-instability waves in a shallow upwind valley, and uncovers the intermittency mechanism to be wave breaking over a standing wave (formed over a stagnant cold-air bubble) across the valley. Finally, flow over the highly complex terrain of the Owens Valley in California is modeled with a similar nesting procedure. The LES results are validated with observation data from the 2006 Terrain-Induced Rotor Experiment (T-REX). The nested LES reproduces a transient nighttime warming event observed on the valley floor on April 17 during T-REX. The intermittency mechanism is shown to be through slope-valley flow transitions. In addition, a cold-air intrusion from the eastern valley sidewall is simulated. This generates an easterly cross-valley flow, and the associated top-down mixing through breaking Kelvin-Helmholtz billows is analyzed. Finally, the nesting methodology tested and optimized in the CASES-99 and T-REX studies is transferrable to general ABL applications. For example, a nested LES is performed to model daytime methane plume dispersion over a landfill and good results are obtained.

To my grandparents

Contents

List of Figures

List of Tables

Acknowledgements

I would first and foremost like to thank my advisor at UC Berkeley, Prof. Tina Chow, for her great guidance, encouragement, friendship and mentorship in both academia and life. I am grateful for the summer of 2007, when she first took me in as an undergraduate student researcher, and guided me into the fantastic world of numerical modeling. I am grateful for the countless times when she carefully listened to and discussed with me on my immature and mostly failed ideas. She always shares my enthusiasm and challenges me to look further and deeper when things are going well; and provides great guidance and encourages me on when my research path seems bleak. I am in great debt to Tina for shaping me into who I am today. I could only hope to grow into someone like her someday, and pass on what I have learned from her.

I would also like to thank my committee members. To Prof. Mark Stacey, thank you for teaching me the basics of environmental fluids, and helping with my research from time to time. To Prof. Evan Variano, thank you for teaching me the essence of classical turbulence, I could only wish to be as knowledgeable as you someday. To Prof. David Romps, thank you for agreeing to be on my committee on the last minute, and all the helpful advises on my postdoc search. To Prof. Phil Marcus, thank you for your excellent courses in advanced fluid mechanics and spectral methods. I wished I had opportunities to interact with and learn more from you. To Prof. Robert Harley, thank you for teaching me all about air quality. It is good to learn about the applications of atmospheric science to environmental engineering.

I am most grateful to be part of the Environmental Fluid Mechanics (EFM) group. The EFM is likely a family to me. I appreciate all the lunch at the grass circle, coffee breaks, and beer hours spent with all of you. To Megan Daniels, thank you very much for helping me get started on ARPS and taking time to discuss many research topics with me even during your last year. To Audric Collignon and Rusty Holleman, you are the greatest and smartest neighbors that I could ever expect. I have complete faith in your future success in academia. To Jason Simon, thank you for bringing that Ping Pong Table into O'Brien Hall. It made my last year so much more tolerable. To Andreas Brand, thank you for taking me to coffee breaks, which I sincerely missed after you left. To Megan Williams, Audric and Wayne Wagner, thank you for taking me out the to the field, letting me drive the boat, teaching me how to tie knots, and saying smart things on the beach. Thanks to all my regular Ping Pong bubbies: Rusty, Jason, Ian Tse, Wayne, Gabriele Bellani and Cristina Poindexter. Thanks also to Maureen Downing-Kunz, Rudi Schuech, Kyle Pressel, Rebecca Leonardson, Lauren Goodfriend, Kevin Hsu, Nikola Marjanovic, David Wiersma, Mike Dvorak and many more for your help and friendship along the way.

My teachers and friends, I am so lucky to have met all of you who are so hard to say goodbye to.

I am grateful for support from National Science Foundation Grant ATM- 0645784 (Physical and Dynamic Meteorology Program). Acknowledgment is also made to the National Center for Atmospheric Research, which is sponsored by NSF, for the computing time used in this dissertation. The National Elevation Dataset and the National

Land Cover Database are available from U.S. Geological Survey. CASES-99 observation data is available through the National Center for Atmospheric Science/Atmospheric Technology Division. The observational data for the T-REX study are downloaded from the T-REX data Achieve, which is maintained by the National Center for Atmospheric Research's Earth Observation Laboratory (NCAR's EOL). I am also grateful to Prof. Dave Whiteman for the interesting discussions on intermittent turbulence, which led to T-REX study.

Chapter 1 Introduction

1. General Description and Motivation

The atmospheric boundary layer (ABL) is the region of the atmosphere adjacent to the earth's surface. It actively responds to changes in surface forcings and exhibit strong diurnal variations. After sunset, the ABL becomes stably stratified due to out-going long-wave surface radiation. Buoyancy stratification limits turbulent motions and permits gravity waves to form. The level of turbulence in the stable boundary layer (SBL) is determined by the competing forcings of shear and buoyancy. Depending on their relative strength, the SBL falls into the continuously turbulent regime dominated by shear production, the quiescent regime dominated by buoyancy destruction, or the intermittent regime where both forcings are important (Stull 1988).

In the classical description of the nighttime atmospheric boundary layer (Nieuwstadt 1984), turbulence is generated at the surface and transported upward. Turbulent quantities decrease in magnitude from the surface to the top of the SBL. Within the SBL, the production of turbulence by mean-shear dominates over the destruction by buoyancy, such that turbulence is temporally steady and continuous. The continuously turbulent SBL usually occurs under conditions of strong winds and/or large cloud cover which leads to reduced net radiative surface cooling (Van de Wiel et al. 2003).

Boundary layer processes have immediate effects on our daily lives. Improved understanding of the ABL dynamics is crucial for weather and climate prediction, air quality control, aviation safety, and so on (see Chow 2004, Chapter 1). In the area of air-quality control, the nighttime stable conditions are of particular concern because vertical mixing is reduced and limited to a shallow layer ~O(100 m) or less. For example, in the Bay Area of California, "Spare the Air Nights", on which wood burning is prohibited, are enforced on strongly stable nights due to health concerns. Another area that would benefit from improved predictability of the SBL is the wind energy industry. At nighttime, wind turbines extract more energy from the atmosphere due to increased wind speed at the turbine hub height ~80 m. However, turbines might also risk severe damage operating under nighttime conditions where elevated shear is strong across turbine blades, and turbulent events are highly intermittent.

Besides the needs for better understanding and prediction of the SBL, the current inadequacy of atmospheric models in representing SBL flows also motivated this dissertation work. Traditionally, ABL flows have been modeled at the regional-scale with limited area models (LAM). They rely on planetary boundary layer (PBL) schemes to represent turbulent mixing processes in the boundary layer. These PBL schemes were designed in the 1970s for use in low-resolution models (Baklanov et al. 2011). They are adequate steady-state flows over flat, horizontally homogeneous terrain under near neutral conditions. Numerically, they do not function well with increased-resolution models that aim to resolve more details of turbulent transport. Physically, they have poor representation of the dynamic processes under stable conditions, particularly on clear nights with weak winds.

2. Background

Past studies of the SBL comprised of both field observations and numerical simulations. In the last few decades, a number of field campaigns were, fully or in part, devoted to the SBL. Those include the Stable Boundary Layer Experiment in Spain (SABLES) (Cuxart et al. 2000), the Cooperative Atmospheric-Surface Exchange Study – 1999 (CASES-99) (Poulos et al. 2002), the Meteorological Experiment in Arizona's Meteor Crater (METCRAX) (Whiteman et al. 2008), and the Terrain-Induced Rotor Experiment (T-REX) (Vanda Grubisic et al. 2008). Turbulence-resolving numerical simulations have also been used extensively to study the characteristics of the SBL flows. Those include mostly direct numerical simulations (DNS) (Coleman et al. 1992; Shih et al. 2000; Chung and Matheou 2012), and large-eddy simulations (LES) (Saiki et al. 2000; Kosovic and Curry 2000; Jimenez and Cuxart 2005; Basu and Porté-Agel 2005; Beare et al. 2006; Zhou and Chow 2011). Although DNS resolves down to the Kolmogorov scale, requiring no turbulence closure, its usefulness is limited by computational resources to a tiny spatial fraction of the turbulent ABL. LES is more advantageous for ABL flows, because it separates the large-scale energy-containing eddies from the smaller ones based the definition of a spatial filter. While the large eddies are explicitly resolved, the small ones are represented by a subfilter-scale (SFS) stress model.

This dissertation uses LES to model the SBL, placing emphasis on both boundary layer dynamics and numerical methods. The findings for SBL dynamics help improve our understanding of the nighttime flows, which will be useful in engineering applications such as wind farm operations, numerical weather forecast and air quality control. The numerical methodologies developed are transferrable to other general applications requiring turbulence-resolving LES of the ABL. This is part of a grand effort to develop a universal framework for large-eddy simulation of atmospheric boundary layer flow over complex terrain. A universal framework for general LES applications over complex terrain is envisioned by my advisor Prof. Chow. This framework consists of a set of tools and methodologies, aiming to extend seamlessly the current meso-scale simulations down to the turbulence-resolving micro-scales with LES. The framework will be of helpful guidance to future high-resolution LES studies of real complex ABL flows. It will dramatically improve the current modeling capability of the ABL, and meet the demands for higher spatial and temporal accuracies for many science and engineering applications.

2.1 Boundary Layer Dynamics and Turbulence

In the realm of ABL dynamics, this dissertation explores "non-classical" turbulence behaviors in the SBL. The main focus is intermittent turbulence under strongly stable conditions. Three cases of the intermittently turbulent SBL with different underlying mechanisms are simulated with LES. They include turbulence and mean shear interactions, breaking gravity waves, and slope-valley flow transitions. In addition, a complete set of descriptions of the strongly stable boundary layer is provided with LES results. This includes vertical profiles of mean variables (wind speed, direction, and potential temperature), turbulent fluxes and variances (momentum and heat), as well as scaling laws and surface similarity relationships. Other "non-classical" SBL features explored include the backward transfer, known as backscatter, of turbulent kinetic energy

along the turbulence energy cascade, and elevated sources of turbulence and associated top-down mixing.

Intermittency, or *small-scale intermittency*, has been traditionally used in the classical fluid mechanics to describe the increasing non-Gaussian behavior in the probability density function (PDF) of dissipation quantities with decreasing scale (Sreenivasan and Antonia 1997). The flared out tails of the PDF at high Reynolds number indicate more frequent occurrences of extreme events at fine scales. In this dissertation intermittency, or *global intermittency*, refers of the case where eddies of all scales are missing or suppressed over a periodic of time (Mahrt 1999). Global intermittency, hereafter intermittency, usually happens on clear nights with weak winds when the SBL cools rapidly. Turbulent motions are strongly damped by buoyancy stratification and no longer continuous. When surface heat flux exceeds a certain threshold set by the geostrophic wind speed, the SBL decays into a quiescent state (Derbyshire 1990), where turbulence is suppressed over prolonged periods greater than the time scale of the dominant eddies (Nakamura and Mahrt 2005). During these times, energetic mixing events known as turbulent bursts occur intermittently over relatively short periods, and are usually responsible for the majority of upward/downward transport of heat and momentum (Coulter and Doran 2002).

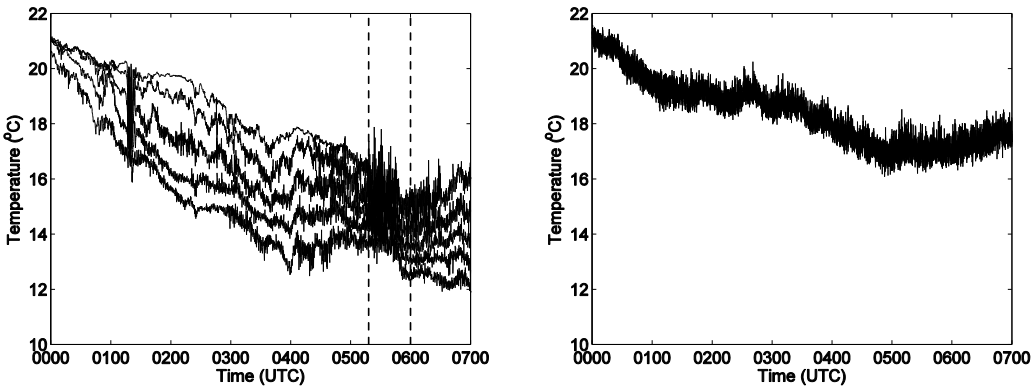

Figure 1-1 Time series of thermocouple temperature on (a) Oct 5-6 (IOP2) and (b) Oct 6-7, 1999 at the main tower during CASES-99. Data was measured at 11.3, 20.3, 29.3, 40.1, 50.9m AGL from bottom to top. On Oct. 6-7 the surface layer was well mixed so the lines overlap. Data are resampled at every 10s. The turbulent episode during IOP2 is enclosed by dashed lines.

A good example of an intermittently turbulent night is Oct 5-6 1996 at Kansas site during the CASES-99 field campaign. Figure 1-1 presents recordings of temperature at 5 different elevations on the main tower from 0000-0700 UTC (1900-0200 LST) for two consecutive nights. The night of Oct 5-6 is strongly stable. Temperature time series indicate the presence of an inversion layer, represented by increasing temperature with height. In comparison, the surface layer was well mixed on Oct 6-7, where temperature measurements at different heights are indistinguishable. Between 0000-0500 UTC on Oct

5-6, the amplitude of temperature fluctuations was small. This quiescent period was followed by a turbulent episode marked by rapid temperature fluctuations.

Besides short, intense turbulent fluctuations, another signature of bursting is warming below the elevation of such events (Whiteman et al. 2009). This is because intense vertical mixing tends to bring down potentially warm air from aloft, leading to a transient nighttime warming signal for a measurement at a fixed elevation. This should be differentiated from gravity wave signals when warming associated with wave troughs (downward-curving potential temperature isentropes) vanishes immediately after the wave passes. The latter usually occur on a much shorter time scale ~O(1 min).

Intermittent turbulence has been observed during several field experiments, yet its origin is not well understood. A few known mechanisms include passing density currents (J. L. Sun et al. 2002), breaking shear-instability waves (Newsom and Banta 2003), solitary waves and downward propagating gravity waves (J. L. Sun et al. 2004), turbulence and mean shear interactions (Nakamura and Mahrt 2005), and slope and valley flow transitions (Whiteman et al. 2009). Note that none of these disturbances are sufficient conditions for turbulence. Often times, under very stable conditions, referred to as the vSBL by Mahrt (1998), disturbances may pass through, barely affecting the SBL structure (Banta et al. 2007).

Turbulence and mean shear interactions are the most generic mechanism for intermittency, which can be described as the following cyclic process. High wind shear overcomes stratification and generates turbulence. Turbulent mixing reduces shear then decays due to the background stratification. The lack of turbulent momentum transfer leads to an increase in shear. Then the cycle repeats. Ohya et al. (2008) verified this mechanism with wind tunnel measurements. Bursts due to turbulence and mean shear interactions are usually observed below and sometimes above the low-level jet (LLJ) due to the elevated shear around the jet nose (Banta 2008). Since turbulence is generated aloft and transported downward, the structure of the SBL is considered “upside-down” in contrast to the traditional picture (Mahrt and Vickers 2002). Figure 2 presents a schematic of the traditional and the upside-down boundary layer structures following Banta et al. (2006). In the traditional picture, turbulence is generated at the surface and transported upwards. In the upside-down case, turbulence is generated aloft due to the elevated shear and transported downwards.

Overturning and breaking gravity waves due to shear-instability also lead to intermittent turbulence. During the Cooperative Atmospheric-Surface Exchange Study – 1999 (CASES-99) (Poulos et al. 2002), shear-instability waves were observed for a brief period of approximately 30 minutes on the night of Oct 5-6, 1999 (Blumen et al. 2001). The billows were at an elevation of ~40 m above ground level (AGL), had wavelength of ~350 m, and propagated with a phase speed of 5.25 ms^{-1} in the north-south direction. Newsom and Banta (2003) associated an inflection point in the mean wind profile with the onset of the billows. They pointed out that the increase in vertical shear was due to a slowing down of the flow from below. The cause of this flow retardation remained an open question due to the limited spatial coverage of field equipment.

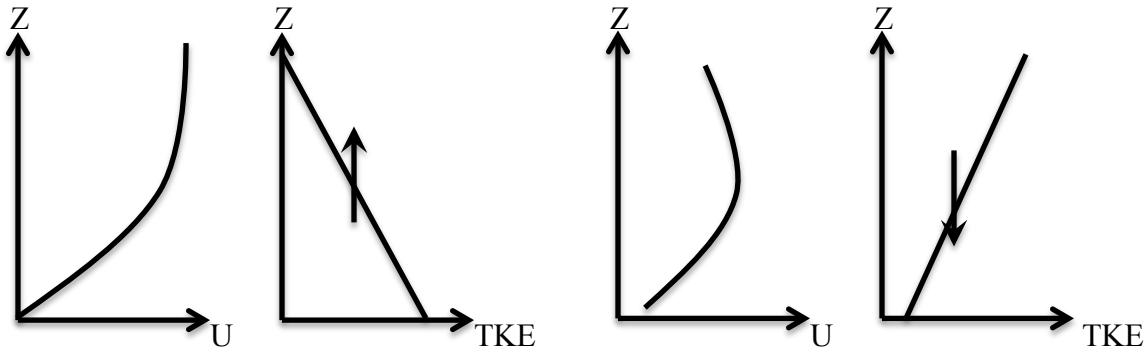

Traditional Boundary Layer Upside-Down Boundary Layer

Figure 1-2 Schematic of structure of traditional boundary layer (left) and upside-down boundary layer (right).

Most of the known intermittency mechanisms are derived from the CASES-99 field campaign over the nearly flat Great Plains. In other words, these mechanisms are generally non-terrain-induced, and quite generic. This is partly due to the lack of field observations of SBL over complex terrain. It is also because complexity in topography and heterogeneity in land-cover tend to enhance turbulent mixing (Derbyshire 1995b) leading to less strongly stratified conditions. One reported intermittent case over highly complex terrain is an observed nighttime warming episode in Owens Valley during the 2006 Terrain-Induced Rotor Experiment (T-REX) (Grubisic et al. 2008). On the night of Apr 17th, tower observations at the valley floor showed rapid drop in temperature after sunset at a rate of nearly 3 $^{o}Chr^{-1}$. A transient warming was recorded from 2040 LST when the temperature started to increase in the following half-hour period. Based on tower observations of wind speed and direction, Whiteman et al. (2009) associated the cause of the warming episode with the transition from slope to valley flows. However, the spatial and temporal extent of the event has not yet been verified, and requires numerical simulations.

2.2 Numerical Modeling

2.2.1 Turbulence Closures

In addition to SBL dynamics, this dissertation has a parallel focus on improving the LES methodology for SBL simulations. Most past LES studies of the ABL were performed under idealized conditions with flat terrain, prescribed forcings, and periodic lateral boundaries (Saiki et al. 2000; Kosovic and Curry 2000; Jimenez and Cuxart 2005; Basu and Porté-Agel 2005; Beare et al. 2006). LES of the SBL is further limited to weak or moderate stability under conditions of either high geostrophic pressure gradients or low surface cooling rates. This is because as stratification strengthens, turbulent motions are constrained by a reduced buoyancy length scale, requiring finer grid resolution. For moderate stability, Beare et al. (2006) suggested a grid resolution of 6.25 to 12.5m to sustain resolved turbulence. Therefore, LES of the vSBL soon becomes prohibitive due to overwhelming computational resource requirements.

Modeling the strongly stable regime is further complicated by physical mechanisms such as surface-decoupling (Derbyshire 1999) and intermittency-associated quiescent to turbulent flow transitions (Jimenez and Cuxart 2005). Beare et al. (2006) pointed out the conundrum of eddy viscosity formulations (corrected through an empirical Richardson number) that struggle to balance numerical stability (favoring long-tail functions) and physical reality (requiring short-tail functions). Furthermore, another inherent insufficiency in the formulation of eddy-viscosity closures are that they do not allow backscatter of turbulent kinetic energy (TKE) from the SFS to the mean flow. The backscatter process has been shown to be happening at the LES scale in the SBL (Carper and Porte-Agel 2004). Even the more advanced dynamic formulations usually do not allow backscatter, because they impose non-negative constraints on eddy-viscosity for numerical stability considerations (Wong and Lilly 1994).

A few studies have been performed in the strongly stable regime to model intermittent turbulence. Van de Wiel et al. (2002) simulated an intermittent SBL with a box model, utilizing a stability function that cuts off turbulent mixing beyond a critical Richardson number. Costa et al. (2011) used a single column model coupled to a land-surface model, to show periodic turbulent bursts in the decoupled surface layer. Chung and Matheou (2012) performed DNS of a stratified sheared turbulence in a 3D periodic domain, revealing turbulence collapses and formation of intermittent laminar and turbulent layers. Jimenez and Cuxart (2005) systematically explored the range of stable stratification that can be simulated with a TKE-based closure model. With a grid resolution of about 5 m, they were successful in simulating weakly and moderately stable conditions. Under strong stability, however, they reported model failure associated with runaway cooling, which is a result of the collapse of boundary layer turbulence.

Therefore, the challenging nature of buoyancy-suppressed-turbulence makes the SBL an ideal test bed for LES closures. Conventional LES closures developed and optimized for neutral and convective conditions are usually insufficient past moderate stability (Baklanov et al. 2011). An LES closure that can sustain resolved turbulence over a broad range of stability, and at the same time provide a good representation of the SFS mixing processes, is also expected to perform well under neutral and convective conditions when the SFS fraction is smaller.

2.2.2 Grid-nested Large-eddy Simulations for Atmospheric Boundary Layer Flows over Complex Terrain

Real ABL flows are affected by the topography and complex land-surface processes. Large-scale topographic features such as mountains and valleys have pronounced effects on ABL flows (Whiteman 2000). Small-scale terrain features over relatively flat terrain can also have significant effects; for example, drainage flows can be generated or modulated by very shallow slopes (Mahrt et al. 2001). Furthermore, heterogeneous land cover introduces additional variability into the flow (Derbyshire 1995). Therefore, to study real ABL flows, it is necessary to move away from the idealized flat terrain setting. Many studies have been stepping towards this direction. Some of them replace real topography with analytic terrain of similar dimensions. For example, Doyle and Durran (2007) replaced the Sierra-Nevada Range with a 3D analytic ridge to study the evolution

and vortex shedding of atmospheric rotors under mountain lee waves. Chemel et al. (2009) used an analytic valley and plain as a surrogate for the Riviera Valley to study gravity wave generation due to oscillatory motions of the down-slope flow (Fleagle 1950; McNider 1982).

Some studies have taken a step further and used real topography. Improved model predictions were reported, even though idealized lateral boundary conditions were still used. For example, Kumar et al. (2010) performed LES over real topography over the Great Plains with analytic boundary conditions. They showed improved model performance using a time-varying surface temperature bottom boundary, and time-height-varying geostrophic forcings obtained from observations. Chow and Street (2009) simulated flow over the Askervein Hill, and evaluated turbulence closures with observation data. To provide turbulent inflow as lateral boundary conditions, a separate neutral boundary layer simulation under was performed. Data extracted from a vertical slice were fed into the Askervein domain as inflow condition.

The next step for LES of ABL flows over complex terrain is to use realistic inflow and outflow conditions. This is achieved through grid nesting. Grid nesting takes information from the coarse grid and passes it to the fine grid as lateral boundary conditions. The outermost domain obtains its lateral boundary conditions from meso-scale model reanalysis (e.g. North American Regional Reanalysis, North American Mesoscale Analysis, and European Center for Medium-Range Weather Forecasts Analysis). This procedure can be repeated over several nests until the desired grid resolution, which resolves the motions of interest, is reached (Zhong and Chow 2012). Grid nesting has been used with LES to investigate fine flow features, such as effects of soil moisture and topographic shading on valley flows (Chow et al. 2006), katabatic winds on weak slopes (Zhong and Whiteman 2008), and scalar transport and dispersion over complex terrain (Michioka and Chow 2008).

Very few nested studies of ABL flows over complex terrain have been performed down to the turbulence resolving (LES) scale, i.e. grid spacing ~O(100 m) for the daytime convective boundary layer (CBL) and ~O(10 m) for the nighttime SBL. This is partly due to the limitations in computational resources, and partly to the many unresolved issues with nested LES. Since computing power has increasingly become available, this dissertation takes the next steps to explore nested LES at these scales. Problems associated with nested LES can be summarized into three questions.

- How should complex terrain be represented at different resolutions?
- How do resolvable turbulent motions evolve on nested LES grids?
- What turbulence model should be used at different resolutions?

The first question points to insufficiencies in terrain-following coordinates, used by most limited-area meso-scale models, in representing complex terrain on a fine LES grid. Lundquist et al. (2010) demonstrated the numerical errors associated with σ-coordinates, and proposed a novel immersed boundary method capable of representing highly complex terrain. The question is not touched in this dissertation, since the topography of the case study sites are within the function range of σ-coordinates.

The second and third questions are specific to the nesting configuration. In a periodic domain setup, the domain length can be considered infinite such that turbulence has sufficient time to spin-up and develop over time. With grid nesting, the lateral boundaries of the inner domain(s) with grid spacing Δ_f are derived from a coarse outer grid at a resolution of Δ_c. Δ_c is greater than (or equal to) Δ_f, the general rule of thumb being Δ_c/Δ_f = 3~5. Turbulent motions resolvable on the inner domain, but missing on the outer domain, i.e. with a wavenumber range of ($2\Delta_f$, $2\Delta_c$), have limited time and space to develop through nonlinear interactions before exiting the inner domain. If the required evolution time or space is longer than the advection time or the inner domain length, respectively, the flow will pass through barely generating any high wavenumber motions. In that case, the fine nest results are only as good as the coarser one, making the additional computation cost for the fine grid unnecessary. This type of effect is seen when finer nested grids give essentially the same quantitative results as the outer grid.

In the past few years, efforts have been made in several aspects of the nesting procedure to make nested LES worthwhile. Michioka and Chow (2008) demonstrated the importance of high frequency lateral boundary updates for the inner-domains. Belusic and Guttler (2010) showed that by turning down computational mixing, high frequency motions such as meso-scale meandering could be generated on a coarse LES grid. In this work, both high-frequency lateral boundary updates and low computational mixing are used. The focus of this dissertation is the role of turbulence closure in improving nest LES performance. By testing different closures in a nested LES configuration, an optimal one is suggested to not only realize but also maximize the benefits of nesting down to an LES grid.

2.2.3 Model Gray Zone – *Terra Incognita*

This dissertation also addresses an emerging issue for nested simulations, namely the *terra incognita*. The term was proposed in Wyngaard (2004), referring to the situation where the grid resolution Δ is comparable to the dominant length scale l of the flow. Taking convection for example, the size of the largest eddy in the daytime CBL spans roughly the boundary depth, l~O(1 km). When running in meso-scale mode with Δ~O(10 km), convection cells are entirely subgrid scale (SGS). This enables statistical treatments of the turbulent mixing processes in the CBL, i.e. the use of boundary layer parameterization schemes. On the other hand, in LES mode with Δ ~O(100 m) or less, convective motions are explicitly resolved for the most part. The LES turbulence closure takes care of the remaining SGS motions. However, when Δ and l are on the same order, a parameterization is no longer appropriate since the grid box is not large enough to contain a sufficient number of convection cells for statistical averaging. Meanwhile, l is too poorly resolved by Δ to be simulated with LES.

In nested simulations, the presence of a *terra incognita*, or gray zone, is inevitable due to the wide range in grid spacing across different nests. Some techniques have been proposed for modeling in this gray zone, such as scale-aware parameterizations, and quasi-3D multi-scale techniques (Arakawa et al. 2011), yet much remains to be developed and tested. This dissertation work proposes an empirical alternative to skip this gray zone in nested simulations through the following three steps:

1. *A priori* identification of the dominant length scale l of the flow field.
2. When nesting, skip the level of grid spacing ~ l. Two adjacent nests should be set up in a way that the following criterion $4\Delta_f < l < \Delta_c/3$ is approached.
3. The domain size of the inner grid should be enlarged by having more grid points to compensate for the wide jump in grid spacing, and keep a desired nesting ratio in terms of domain size.

In step 2, the multiplier 4 is proposed because minimal representation of l requires at least two grid cells (i.e. the Nyquist cutoff). l is better resolved with finer grid spacing. On the other hand, parameterization of l favors coarse grids. A multiplier of 1/3 means that a grid box of length and width Δ_c contains at least 9 such flow features. These multiplier values have not been rigorously tested, and are only empirical.

To demonstrate these steps, the CBL example is revisited. First, the dominant length scale is identified as the size of convective eddies, i.e. l ~1000 m. Next, nested simulations are performed starting from, for example the North American Mesoscale Analysis (NAM-ANL) fields at 12 km spacing. Following a 5 to 1 ratio, the first nest has horizontal grid spacing of 2400 m. On the 2400 m grid, a PBL parameterization is used. Based on the same nesting ratio, the second nest should have a spacing of 480 m, five times smaller than 2400 m. However, convective eddies are not expected to be well-resolved on the 480 m grid, since 480 m is only twice as small as l ~1000 m. Therefore, the 480 m grid is skipped, and a 240 m grid is used instead as the second nest to better resolve convection. Finally, the number of grid points is doubled in the horizontal direction on the 240 m grid so that a 5 to 1 ratio is preserved in terms of domain size. These steps have been followed and proved effective in all three nested studies presented in this dissertation. A schematic of the two alternative nesting configurations is presented in Figure **1-3**.

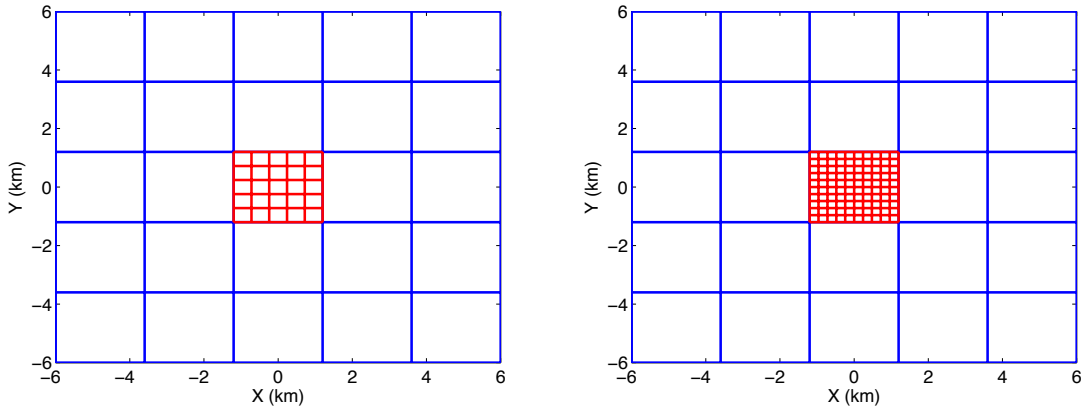

(a) (b)

Figure 1-3 A schematic two grid nesting configurations within a 2400 m outer grid (a) with a 480 m inner grid and (b) a 240 m inner grid.

Finally, while the *terra incognita* in the CBL is well recognized, the SBL counterpart has received little attention. This is because conventionally the dominant SBL length scale has been considered to be the buoyancy scale (e.g. the Ozmidov scale), which is ~O(10 m), and far beyond current high resolution NWP (Beare 2011). However, if gravity waves ~O(100 m) are considered, the SBL *terra incognita* is already a pressing issue for practical applications. As demonstrated in the case of Chapter 3, breaking gravity waves (wavelength λ~350 m) are not predicted on a 128 m grid. This results in a colder, more stable, and less mixed nighttime boundary layer. Thus if the *terra incognita* is unavoidable due to computational resource constraints, better parameterizations must be sought to represent SGS processes such as wave breaking events under certain circumstances.

3. Overview

This dissertation focuses on two broad areas: SBL dynamics and engineering applications. Chapters 2, 4 and 5 investigate the dynamics of the SBL over flat terrain, simple terrain at a Great Plains site, and a highly complex Owens Valley site, respectively. While the flat terrain case is driven with prescribed analytic forcings with periodic boundaries, the two real terrain cases are nested LES with realistic boundary conditions. The joint focus of these three cases is intermittency during strongly stable conditions, and three mechanisms are investigated in each chapter. Chapter 3 and Appendix 1 demonstrate the benefits of LES for ABL flows in engineering applications. Chapter 5 applies the simulation results in Chapter 2 in the area of wind energy and suggests implications for wind farm siting and operations. Appendix 1 applies the LES nesting methodology developed in Chapter 3 and 4 to quantify short-term methane gas emission over a landfill. A brief summary of each section is provided in the following.

In Chapter 2, LES of the stably stratified atmospheric boundary layer is performed using an explicit filtering and reconstruction approach over flat idealized terrain. The dynamic reconstruction model (DRM) can sustain resolved turbulence with less stringent resolution requirements than conventional closure models, even under strong atmospheric stability. This is achieved by proper representation of SFS backscatter of turbulent kinetic energy (TKE), which is absent in conventional eddy-viscosity formulations. The flow structure and turbulence statistics for the moderately stable boundary layer are analyzed with high-resolution simulations. The DRM simulations show good agreement with established empirical formulations such as flux and gradient based surface similarity, even at relatively coarse resolution. Similar results can be obtained with traditional closure models at the cost of higher resolution. SBL turbulence under strong stability is simulated, to our knowledge, for the first time in the LES literature. Simulations show an intermittent presence of elevated TKE below the low-level jet. Overall, the explicit filtering and reconstruction approach is advantageous for simulations of the SBL. At coarse resolution, it can extend the working range of LES to stronger stability, while maintaining agreement to similarity theory; at fine resolution, good agreement with theoretical formulations provides confidence in the results and allows for detailed investigation of the flow structure under moderate to strong stability conditions.

In Chapter 3, results from Chapter 2 are used to investigate SBL flow structures including mean profiles and turbulence statistics, which are relevant to wind energy applications. The applicability of power-law relations and empirical similarity formulations for predicting wind speed depend on the strength of stratification and are shown to be inadequate. Low-level jets form in the simulations. Under strong stability, vertical wind shear below the jet triggers intermittent turbulence. The associated sporadic "bursting" events are extremely energetic and last longer than the time scale of the largest eddies. Such phenomena can have adverse effects on turbine lifetime and performance.

In Chapter 4, the nighttime stable atmospheric boundary layer over complex terrain is modeled with nested high-resolution LES. The field site is located near Leon, Kansas, where the Cooperative Atmospheric-Surface Exchange Study – 1999 field program took place. The terrain is mostly flat with an average slope of 0.5^{o}. The main topographic feature is a shallow valley oriented in the east-west direction. The night of Oct 5-6 is selected to study intermittent turbulence on a strongly stable night with prevailing quiescent conditions, except for brief turbulent periods triggered by shear-instability waves. A major turbulent event is modeled with good magnitude and temporal precision with a sophisticated turbulence closure. In comparison, conventional closures fail to excite turbulent motions, and predict a false laminar flow. A new intermittency mechanism, previously illusive due to limited spatial instrument coverage, is uncovered with LES. Turbulent events are shown to occur through gravity wave breaking over a stagnant cold-air bubble in the valley upwind of the main tower. The bubble is preceded by the formation of a valley cold-air pool due to down-valley drainage flows during the evening transition. It grows in depth by entraining cold down-valley and down-slope flows from below, and is eroded by inflection point induced shear-instability waves on the top. The cyclic process of formation and erosion is repeated during the night leading to sporadic turbulent bursting.

Chapter 5 investigates the nighttime flow dynamics in Owens Valley, California during the Terrain-Induced Rotor Experiment. Nested high-resolution LES are performed to resolve the stable atmospheric boundary layer flows within the valley. On Apr. 17th 2006, a transient warming episode was observed at the valley floor. It is modeled with good magnitude and temporal precision with LES. Analysis of the LES flow field confirmed that the observed warming was a result of an intermittent turbulent event triggered by slope to valley flow transition, as suggested by Whiteman et al. (2009). On the same night, a northerly cold-air flow from the Great Basin was channeled through a pass on the eastern valley sidewall. The gravity current plunged down into the stable valley atmosphere, overshot the altitude at its neutral buoyancy, and returned to it in a large scale oscillatory motion. The resulting cross-valley flow created strong vertical shear against the down-valley flow in the lower layers of the atmosphere. LES resolved Kelvin-Helmholtz waves, ejection and sweep events at the two-layer interface, leading to vertical turbulent mixing from the top-down.

Chapter 6 gives an overall summary of the dissertation, including some recommendations for future work. In Appendix A, transport of the methane gas over the Sandtown landfill is simulated with nested LES to estimate of a travel time of gases emitted from the landfill to the downwind sampling location. The initial and lateral atmospheric boundary conditions are forced by analysis fields from the NAM-ANL,

while a canopy model (Shaw and Schumann 1992) is used to resolve canopy drag. The computational grid consists of three nested domains. The finest domain has 30 m horizontal and 5 m vertical resolution for the landfill. The travel time is estimated using the tracer technique of Deleersnijder et al. (2001). In Appendix B, some preliminary tests on the *terra incognita* for a convective boundary layer are discussed. In Appendix C, derivation for the critical Richardson number used in Chapter 2-5 is presented. In Appendix D, a Lagrangian averaged dynamic reconstruction model with explicit filtering is presented. The Lagrangian averaging approach is potentially more advantageous than volume averaging for flow over complex terrain. In Appendix E, USGS terrain and land cover data used in Chapter 4-5 are briefly described.

4. Summary of Contributions

In summary, the main contributions of this research are to:

1. Improve LES studies of the SBL over a wide stability range, including the strongly stable regime where turbulence is intermittent.

2. Demonstrate the importance of proper representation of SFS turbulence in SBL simulations, particularly the backscatter process of turbulent kinetic energy into the mean flow.

3. Investigate mean flow profiles and turbulent quantities for the strongly stable SBL flows with LES, and provide useful guidance for nighttime wind energy capture.

4. Validate intermittency mechanisms due to mean shear and turbulence interactions with idealized LES.

5. Investigate a new intermittency mechanism due to breaking gravity waves at a Kansas site during the CASES-99 field campaign with nested LES.

6. Validate an intermittency mechanism due to slope-valley flow transitions at Owens Valley during the T-REX field campaign with nested LES.

7. Investigate a cold-air intrusion event at Owens Valley, and related top-down mixing due to directional shear instability.

8. Demonstrate the feasibility and usefulness of nested LES of complex ABL flows over real terrain, and propose improvements on the nesting methodology and the choice of turbulence closures at different grids.

Chapter 2 Large-Eddy Simulation of the Stable Boundary Layer with Explicit Filtering and Reconstruction Turbulence Modeling[1]

Abstract

Large-eddy simulation (LES) of the stably stratified atmospheric boundary layer is performed using an explicit filtering and reconstruction approach with a finite difference method. Turbulent stresses are split into the resolvable subfilter-scale and subgrid-scale stresses. The former are recovered from a reconstruction approach, and the latter are represented by a dynamic eddy-viscosity model. The resulting dynamic reconstruction model (DRM) can sustain resolved turbulence with less stringent resolution requirements than conventional closure models, even under strong atmospheric stability. This is achieved by proper representation of subfilter-scale (SFS) backscatter of turbulent kinetic energy (TKE). The flow structure and turbulence statistics for the moderately stable boundary layer (SBL) are analyzed with high-resolution simulations. The DRM simulations show good agreement with established empirical formulations such as flux and gradient based surface similarity, even at relatively coarse resolution. Similar results can be obtained with traditional closure models at the cost of higher resolution. SBL turbulence under strong stability is also explored. Simulations show an intermittent presence of elevated TKE below the low-level jet. Overall, the explicit filtering and reconstruction approach is advantageous for simulations of the SBL. At coarse resolution, it can extend the working range of LES to stronger stability, while maintaining agreement to similarity theory; at fine resolution, good agreement with theoretical formulations provides confidence in the results and allows for detailed investigation of the flow structure under moderate to strong stability conditions.

2.1 Introduction

Turbulent motions in the stably stratified atmospheric boundary layer are limited by the buoyancy length scale, thus requiring much higher grid resolution in numerical simulations than for neutral or convective conditions. Large-eddy simulation (LES) can be used to resolve turbulent flows in the stable boundary layer (SBL) because it is based on the definition of a spatial filter that can be adjusted to resolve necessary flow features. The spatial filter separates the large resolved scales from the subfilter-scale (SFS) motions. The effect of subfiltered motions on the resolved scales must be represented with a turbulence model.

---

[1] This chapter is a reproduction of the paper "Large-Eddy Simulation of the Stable Boundary Layer with Explicit Filtering and Reconstruction Turbulence Modeling" by Bowen Zhou (the principle author), and Fotini Katopodes Chow, published in the Journal of the Atmospheric Science, September 2011, Volume 68, pages 2142-2155 [Zhou and Chow 2011], © Copyright 2011 American Meteorological Society.

LES of the SBL has been performed mostly under idealized conditions and is limited to weak or moderate stability with conditions of either high geostrophic forcing or a low surface cooling rate (Saiki et al. 2000; Kosovic and Curry 2000; Basu and Porté-Agel 2005). The need for high grid resolution is the primary constraint for extending the application of LES to strongly stable conditions. Over real complex terrain, performing LES of nighttime atmospheric flow is more challenging because the available spatial resolution for meso-scale simulations is even more limited. Given these constraints, the SFS representation of turbulence, that is, the LES turbulence closure model, becomes crucial for SBL simulations. Various turbulence models have emerged in the quest of accurately simulating SBL turbulence, for example, the nonlinear model (Kosovic and Curry 2000), the scale-dependent dynamic model (Sukanta Basu and Porté-Agel 2005), and the turbulent kinetic energy–based model (Jimenez and Cuxart 2005). The performance of many existing models with a moderate SBL can be found in the Global Energy and Water Cycle Experiment (GEWEX) Atmospheric Boundary Layer Study (GABLS) LES intercomparison study (Beare et al. 2006).

To perform LES of a turbulent SBL, the closure model must be able to sustain resolved turbulence, which is constantly consumed by both dissipation and buoyancy. The Smagorinsky model, for example, is generally too dissipative for SBL simulations (Mason and Derbyshire 1990). As stability increases, spatially and temporally intermittent turbulence can develop and eddy sizes are strongly damped. If the SFS model cannot sustain intermittency, resolved turbulence will diminish quickly. This results in a false laminar flow field. Jimenez and Cuxart (2005) systematically explored the range of stable stratification that can be simulated with a TKE based closure model. With a grid resolution of about 5 m, they were successful in simulating weakly and moderately stable conditions. Under strong stability, however, they reported runaway cooling, which is a result of the collapse of boundary layer turbulence.

Motivated by the difficulties in performing LES of the SBL, we attempt to relax the resolution requirement and, thus, extend the range of applicability of LES to strongly stable conditions, through better representation of SFS turbulence. The turbulence model used in this study is the dynamic reconstruction model (DRM) of Chow et al. (2005). The DRM has previously been shown to be advantageous in turbulent channel flow (Gullbrand and Chow 2003) and in neutral atmospheric boundary layer (ABL) simulations (Chow et al. 2005).

With a model setup similar to that for the GABLS case, we evaluate the performance of the DRM by first examining its ability to sustain resolved turbulence under moderate and strong atmospheric stability, with relatively coarse resolutions (section 4a). The quality of the coarse-resolution DRM simulations is checked by comparing mean turbulent statistics with flux-based surface similarity as well as high-resolution results. Simulations with other closures including the TKE-1.5 and the dynamic Wong–Lilly model are also performed to show the benefits of using the DRM closure. Furthermore, the SFS dissipation and backscatter of the turbulent kinetic energy is investigated (section 4b). The vertical structure of the SBL, including shear and turbulent Prandtl number, is examined using high-resolution simulations (sections 4c and 4d). The SFS representation with the DRM is analyzed through decomposition of heat flux and TKE (section 4e). Elevated TKE develops under the strongly stable setup in this LES study. Its intermittent

nature is examined in section 4f. Finally, we examine the resolved flow structure with respect to different atmospheric stability and SFS parameterizations (section 4g).

The Advanced Regional Prediction System (ARPS) (Xue et al. 2000; Xue et al. 2001) is used for the simulations. ARPS is a nonhydrostatic meso-scale and small-scale LES finite difference model. The code has been adapted to accommodate the new DRM SFS closure using the explicit filtering and reconstruction framework (Chow 2004).

2.2 Explicit filtering and reconstruction framework

The traditional approach toward LES has been to treat the discrete differentiation operation as an implicit filter to separate large from small scales in the governing equations. With finite volume and finite difference approaches, implicit filtering can lead to truncation and aliasing errors due to the nonlinear terms (Lund 1997). Explicit filtering can minimize the influence of truncation errors and has been shown to be beneficial in recent studies (Lund 1997; Gullbrand 2001; Carati et al. 2001; Winckelmans et al. 2001; Gullbrand and Chow 2003).

In this study, a 3D explicit filter (a top-hat filter of width Δ_f twice the grid spacing) is applied to the Navier–Stokes equations and is treated separately from the numerical differencing operators. The implicit discretization operator is denoted by a tilde and the explicit filtering operator by a bar. In our notation, the tilde operator is a loose representation of the implicit filter operation, as its nature depends on the discrete differentiation schemes. The LES governing equations for the resolved fields are the momentum, continuity, and scalar transport equations:

$$\frac{\partial \overline{\tilde{\rho}}\,\overline{\tilde{u}}_i}{\partial t} + \frac{\partial \overline{\tilde{\rho}}\,\overline{\tilde{u}}_i\,\overline{\tilde{u}}_j}{\partial x_j} = -\frac{\partial \overline{\tilde{p}}}{\partial x_i} - \overline{\tilde{\rho}}\,g\delta_{i3} + \overline{\tilde{\rho}}\epsilon_{imn}f_n\overline{\tilde{u}}_m - \frac{\partial \overline{\tilde{\rho}}\,\tilde{\tau}_{ij}}{\partial x_j}$$

$$\frac{\partial \overline{\tilde{\rho}}}{\partial t} + \frac{\partial \overline{\tilde{\rho}}\,\overline{\tilde{u}}_i}{\partial x_i} = 0$$

and

$$\frac{\partial \overline{\tilde{\theta}}}{\partial t} + \frac{\partial \overline{\tilde{\rho}}\,\overline{\tilde{u}}_i\overline{\tilde{\theta}}}{\partial x_i} = -\frac{\partial \overline{\tilde{\rho}}\,\tilde{\chi}_i}{\partial x_i}$$

where $\overline{\tilde{u}}_i$ are the velocity components, $\overline{\tilde{p}}$ the pressure, , $\overline{\tilde{\rho}}$ the density, f the Coriolis parameter, and $\overline{\tilde{\theta}}$ the potential temperature. Further details are given in (Chow 2004, appendixes C and D). The turbulent stresses and heat fluxes can be decomposed into resolvable subfilter-scale (RSFS) stresses and unresolvable subgrid-scale (SGS) stresses:

$$\tau_{ij} = \overline{u_i u_j} - \overline{\tilde{u}}_i\,\overline{\tilde{u}}_j = \underbrace{\overline{u_i u_j} - \overline{\tilde{u}_i \tilde{u}_j}}_{\tau_{\mathrm{SGS}}} + \underbrace{\overline{\tilde{u}_i \tilde{u}_j} - \overline{\tilde{u}}_i\,\overline{\tilde{u}}_j}_{\tau_{RSFS}}$$

$$\chi_i = \overline{u_i \theta} - \overline{\tilde{u}}_i\ \overline{\tilde{\theta}} = \underbrace{\overline{u_i \theta} - \overline{\tilde{u}_i\,\tilde{\theta}}}_{\chi_{\mathrm{SGS}}} + \underbrace{\overline{\tilde{u}_i\,\tilde{\theta}} - \overline{\tilde{u}}_i\ \overline{\tilde{\theta}}}_{\chi_{RSFS}}$$

The first set of parentheses on the rhs contains the SGS stresses τ_{SGS} and χ_{SGS}, which have scales finer than the grid resolution and, hence, must be modeled. The second set of parentheses contains the filtered-scale stresses τ_{RSFS} and χ_{RSFS}, which depend on the resolved and explicitly filtered velocity fields within the resolution domain. As the explicit filter function is well defined, it is theoretically possible to obtain $\tilde{u}_i$ from $\overline{\tilde{u}}_i$ and $\tilde{\theta}$from $\overline{\tilde{\theta}}$ by deconvolution (inverse filtering). In this work, reconstruction is performed through the approximate deconvolution method (ADM) of van Cittert (1931) and (Stolz et al. 2001):

$$\tilde{u}_i = \bar{\tilde{u}}_i + (I - G) \star \bar{\tilde{u}}_i + (I - G) \star [(I - G) \star \bar{\tilde{u}}_i] + \cdots$$

where I is the identity operator, G is the explicit filter, and asterisks denote the convolution operator. The RSFS term is computed by substituting the reconstructed velocity $\tilde{u}_i^*$ into the τ_{RSFS} term. Up to five levels of reconstruction are applied in this work to enhance the role of the RSFS stresses.

For subgrid-scale turbulence representation, we apply the Wong and Lilly (1994) dynamic eddy-viscosity model to represent SGS motions:

$$\tau_{\mathrm{SGS}} = -2\nu_{\mathrm{T}}\,\bar{\tilde{\mathrm{S}}}_{\mathrm{ij}}$$

where $\bar{\tilde{S}}_{ij} = (\partial\overline{\tilde{u}}_i/\partial x_j + \partial\overline{\tilde{u}}_j/\partial x_i)/2$ is the resolved strain rate tensor and the dynamic eddy viscosity is given by $\nu_T = C_\epsilon \Delta^{4/3}$. The coefficient C_ϵ is determined using the least squares method of Lilly (1992). More details on the RSFS–SGS model can be found on (Chow et al. 2005).

In the near-wall region, adjustments to the surface shear stress are necessary to improve LES performance near the surface (Brasseur and Wei 2010). We follow Chow et al. (2005), using a near-wall stress model to supplement the SGS stress based on the canopy stress model of Brown et al. (2001). Implementation of this near-wall model has proved successful in the work of Cederwall (2001), Chow et al. (2005), and Kirkpatrick et al. (2006).

The RSFS–SGS model framework can be viewed in terms of a mixed model (Bardina et al. 1983; Zang et al. 1993). The RSFS component is the so-called scale similarity term represented by reconstruction, and the SGS component is represented using an eddy-viscosity closure. The introduction of the RSFS terms decreases the required SGS contribution toward the total turbulent stresses. The original scale similarity model of Bardina et al. (1983) assumed that the smallest resolved scales possess a similar structure to the subfilter scales. The reconstruction model seeks a more accurate representation of the resolved scales by inverting the explicit filter operation. With higher levels of reconstruction, more details of high frequency motions approaching the grid cutoff are restored, thus improving the representation of the SFS stress. With zero-level reconstruction, the RSFS term reduces exactly to the scale similarity model of Bardina.

2.3 Model Configuration

Simulations are performed on a (640 m x 640 m x 640 m) domain over flat but rough terrain, similar to that used in previous work (Kosovic and Curry 2000; Saiki et al. 2000; (Basu and Porté-Agel 2005). Both anisotropic and isotropic grids for a range of spatial resolutions are used in this work (see Table 2-1). Vertical grid stretching is applied in the anisotropic runs to better resolve the surface layer. The finest spatial resolution used in this study is 3.125 m on a uniform grid. The GABLS intercomparison study suggested that LES results at this resolution are comparable to 2 m and 1 m resolution SBL simulations.

Table 2-1 List of simulations and parameters: HR (VHR) denote high (very high) resolution. All cases use a surface heat flux of -0.02 Kms^{-1} unless specified with CR. Run names with an asterisk represent simulations with isotropic grid resolution. DWL is the dynamic Wong–Lilly model, and DRM is the dynamic reconstruction model. The 05CR-VHR* cases are driven by a surface cooling rate of -2.0 K h^{-1}.

Run	Grid size	Δx (m)	Δz_{min} (m)	Heat flux (K m s^{-1})	Rec-level
Smagorinsky	(43, 43, 43)	16	5	-0.02	N/A
TKE-02CR	(43, 43, 43)	16	5	-0.02	N/A
TKE-03CR	(43, 43, 43)	16	5	-0.03	N/A
TKE-04CR	(43, 43, 43)	16	5	-0.04	N/A
TKE-05CR	(43, 43, 43)	16	5	-0.05	N/A
TKE-07CR	(43, 43, 43)	16	5	-0.07	N/A
TKE-02CR-VHR*	(195, 195, 195)	3.125	3.125	-0.02	N/A
TKE-05CR-VHR*	(195, 195, 195)	3.125	3.125	-0.05	N/A
DWL	(43, 43, 43)	16	5	-0.02	N/A
DRM-ADM0	(43, 43, 43)	16	5	-0.02	0
DMR-ADM1	(43, 43, 43)	16	5	-0.02	1
DRM-ADM2	(43, 43, 43)	16	5	-0.02	2
DRM-02CR(DRM-ADM5)	(43, 43, 43)	16	5	-0.02	5
DRM-03CR	(43, 43, 43)	16	5	-0.03	5
DRM-04CR	(43, 43, 43)	16	5	-0.04	5
DRM-05CR	(43, 43, 43)	16	5	-0.05	5
DRM-07CR	(43, 43, 43)	16	5	-0.07	5
DRM-02CR-HR	(83, 83, 83)	8	2.5	-0.02	5
DRM-02CR-VHR*	(195, 195, 195)	3.125	3.125	-0.02	5
DRM-05CR-VHR	(195, 195, 195)	3.125	3.125	-0.05	5

The lateral boundary conditions are periodic. Both the lower and upper boundary are set to be rigid walls. At the top boundary, Rayleigh damping is applied above 500 m. The boundary layer depth ranges from 100 to 200 m and therefore should not be affected by the Rayleigh damping. The surface momentum flux is prescribed by imposing Monin–Obukhov similarity at the first grid point above the ground:

$$U_s = \frac{u_*}{\kappa}\left[\ln\left(\frac{z+z_0}{z}\right) + \beta\frac{z}{L}\right], \quad L = -\frac{\theta_s}{g}\frac{u_*^3}{\kappa\overline{w\theta}_s}$$

where U is the wind speed, $u*$ is the surface friction velocity, κ the von Karman constant, and L the Obukhov length; surface quantities are subscripted s. In addition, β is a constant taken to be 4.7 from Businger et al. (1971), and z_0 is the surface roughness, set at 0.1 m. Both u and v have their surface values at $z = 0$. A displacement height equal to the roughness length has been added to the vertical coordinate.

The simulations are carried out at mid-latitude (43.29°N) where the Coriolis parameter f is 1.00 x 10^{-4} s^{-1}. The flow is driven by a geostrophic wind at (Ug, Vg) = (10 m s^{-1}, 0 m s^{-1}) and initialized using a uniform wind profile with horizontal velocity components equal to the geostrophic velocities to avoid inertial oscillations in the upper part of the domain. The initial potential temperature is uniform at 300 K (neutral conditions). A random perturbation of 0.1 K is applied to the bottom 150 m of the domain at initialization to trigger turbulence.

A constant surface heat flux is imposed on the bottom boundary to drive atmospheric cooling. In this study, five sets of surface heat flux (-0.02, -0.03, -0.04, -0.05, and -0.07 K m s^{-1}) are included. The strength of cooling is categorized based on the theoretical expression of Derbyshire (1990) for the minimum heat flux sustainable in a stable boundary layer:

$$\overline{w\theta}_{s,min} = -\frac{\theta_s R_f}{g\sqrt{3}} G^2 |f|$$

where G is the geostrophic wind speed and R_f is the flux Richardson number, a ratio of buoyancy destruction to shear production of TKE. The SBL is further categorized into regimes of continuous turbulence where R_f is below 0.25 (dynamically unstable); intermittent turbulence where R_f is between 0.25 and 1.0; and quiescent conditions where turbulence can no longer be sustained (dynamically stable). A derivation is given in Appendix C. The two strongest cooling cases of this study (-0.05, -0.07 K m s^{-1}) fall into the intermittent turbulence regime. All cases are shown on the SBL stability chart in Figure 2-1, where $B = -g/\theta_s\overline{w\theta}_s$ represents buoyancy destruction at the surface and two curves show R_f values of 1.0 and 0.25. Other LES studies of the SBL are also included in Figure 2-1 for reference. Note that the Derbyshire expression is only used here to qualitatively determine the state of the SBL. The recent work of Sorbjan (2010) presented a more accurate estimate of the minimum sustainable heat flux, based on the vertical velocity variance σ_w and a temperature scale $T_w = N\sigma_w\theta_0/g$.

A buoyancy length scale is computed a posteriori to confirm that the resolution used in this study is adequate. We choose the Ozmidov scale $L_o = \epsilon^{-1/2}N^{-3/2}$ to represent the characteristic length scale of buoyancy, where ϵ is the dissipation rate and N is the buoyancy frequency. Dissipation is estimated by the net loss of energy from the resolved field. For moderate cooling cases (-0.02, -0.03 K m s^{-1}), Ozmidov scales of 7 and 5 m are found around the center of the SBL (z/h = 0.5, where h is the boundary layer depth). Therefore, grid resolution in the vertical direction is sufficient even on the coarse grids (5

m near the surface) for these two cooling cases due to grid stretching. For the stronger cooling cases, the Ozmidov scale decreases to less than 2 m. Thus, the turbulence closure models are relied on more heavily.

A summary of the simulation cases is listed in Table 2-1. Since this LES study focuses on the quasi-steady-state SBL, the simulation results presented in the following sections are restricted to the later period of the simulations when a quasi-steady state is achieved.

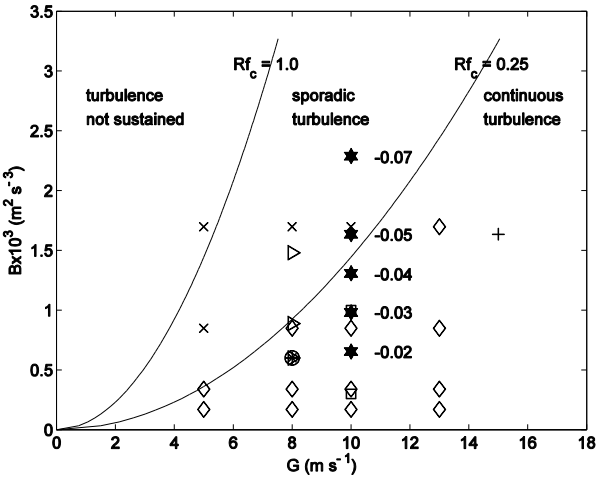

Figure 2-1 Stability region of simulation cases: the horizontal axis represents geostrophic winds G and the vertical axis represents buoyancy $B = -g/\theta_s \overline{w\theta}_s$. Stars represent five levels of stability in this study, with surface heat flux (K m s^{-1}) noted on the right; open squares represent simulations by Mason and Derbyshire (1990), plus sign by Saiki et al. (2000), right-pointing arrow by Kosovic and Curry (2000), asterisk by Beare et al. (2006), small open circle by Basu and Porté-Agel (2005), diamonds by Jimenez and Cuxart (2005), and the multiplication sign is used for attempted cases that suffer from runaway cooling by Jimenez and Cuxart (2005).

2.4 Simulation Results

2.4.1 Sustained Turbulence

All simulations are carried out for 50 000 s of physical time, with constant surface cooling. According to the GABLS study, a grid resolution of 6.25–12.5 m is required to sustain resolved turbulence under mild cooling for most turbulence models. In this study, the coarse-resolution simulations are performed on a grid with 16-m horizontal spacing and vertical stretching with 5-m spacing near the surface. The horizontal resolution used here is coarser than that of the GABLS study to test model performance. Note, however, that such resolution is still considered very high for current LES applications to real complex terrain (see, e.g., Michioka and Chow 2008).

First, we check if conventional closures can sustain resolved turbulence under the coarse resolutions used in this study. Simulations with the Smagorinsky model fail to generate resolved turbulence for moderate stability unless a spinup procedure is used to generate a convective atmospheric boundary layer as initial conditions. The TKE-1.5

simulations develop into a turbulent state with moderate cooling but produce laminar flow under strong stability, as do the Smagorinsky simulations. To confirm the role of proper SFS representation in preventing laminarization of the flow under strongly stable conditions, we also performed coarse-resolution simulations initialized from a turbulent field under strong stability. In Figure 2-2(a), time series of vertically integrated resolved TKE are presented as an indicator for resolved turbulence. Starting at 40 000 s from a DRM-generated flow field at strong stability, the Smagorinsky and TKE- 1.5 simulations show rapid decay of resolved TKE. A small amount of resolved TKE is maintained afterward. In comparison, it is well sustained at roughly the same levels throughout the simulation with the DRM. Figure 2-2(b) shows resolved TKE from DRM simulations with different surface heat fluxes between 30 000 and 50 000 s. Decreases in both the mean value and magnitude of fluctuations are observed with stronger stability. Note that some wavelike patterns are visible in the TKE time series. The peaks are associated with energetic mixing events, which will be discussed in section 2.4.6.

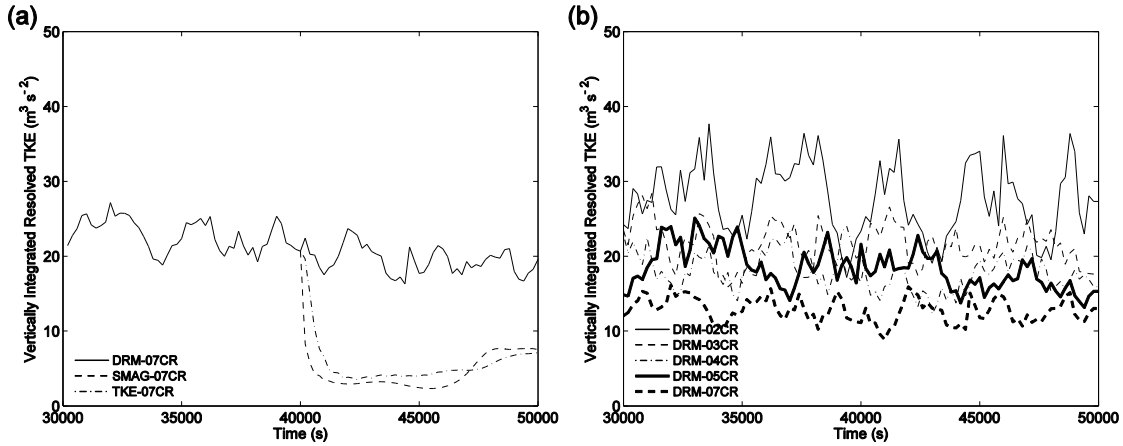

Figure 2-2 Vertically integrated resolved TKE from 30 000 to 50 000 s for the (a) Smagorinsky, TKE-1.5, and DRM simulations starting from a turbulent initial state at 40 000 s under a strong surface cooling rate ($\overline{w\theta}_s$= -0.07 K m s^{-1}) and (b) DRM simulations under five surface cooling rates. Coarse-resolution results are presented.

The quality of the simulations is also checked by computing the ratio of vertically integrated SFS TKE e to total TKE E as done in Jimenez and Cuxart (2005). For a fixed resolution, the e/E indicator must increase with stronger stability as the turbulent length scale decreases. The values are computed by averaging over the last 20 000 s of simulation and are presented in Table 2-2. The monotonic increase of the ratio with stability further supports that turbulence is properly maintained for DRM simulations, while the TKE closure displays the opposite effect, indicating runaway cooling (highlighted in boldface). Note that the absolute percentages of the SFS TKE are larger than those obtained by Jimenez and Cuxart (2005). This is due to the unique property of the DRM closure in which part of the SFS terms originates from the resolved field. Further discussion is presented in section 2.4.5.

In Table 2-2, the corresponding surface temperature drop with the TKE-1.5 simulations is much larger than with the DRM under the same surface heat flux for strong stability. This is because the TKE-1.5 closure is more dissipative than the DRM under stable conditions (see next subsection). Therefore, the TKE-1.5 simulations experience more limited turbulent mixing, resulting in shallower and colder boundary layers. Similar observations are also found in high-resolution simulations in which the TKE-1.5 and DRM simulations can end up in two very different states. For the purpose of comparing model performance under similar stability conditions for a strongly stable atmospheric boundary layer, the high-resolution TKE-1.5 (TKE-05CR-VHR*) and DRM (DRM-05CR-VHR*) simulations are driven by a constant surface temperature cooling rate of -2.0 K h^{-1} instead. This approach results in the same surface temperature and similar boundary layer depth—hence a similar vertical potential temperature gradient. The resulting surface heat flux at steady state is found to be around -0.05 K m s^{-1} for both cases.

Table 2-2 Surface cooling rates calculated by a linear fit: $\boldsymbol{e/E}$ presents the percentage of vertically integrated SFS TKE divided by total TKE. Statistics are obtained using horizontally averaged values from 30 000 to 50 000 s.

Run	Heat flux (K m s^{-1})	Cooling rate (K h^{-1})	e/E x (100%)
DRM-02CR	-0.02	-0.410	68.8
DRM-03CR	-0.03	-0.667	71.0
DRM-04CR	-0.04	-1.07	71.9
DRM-05CR	-0.05	-1.14	74.4
DRM-07CR	-0.07	-1.98	76.8
TKE-02CR	-0.02	-0.410	47.4
TKE-03CR	-0.03	-1.08	**40.4**
TKE-04CR	-0.04	-2.45	**24.8**
TKE-05CR	-0.05	-4.32	**17.8**
TKE-07CR	-0.07	-10.8	**10.3**

2.4.2 SFS Dissipation and Backscatter

In this section, we proceed to show that the reason for the less stringent resolution requirements with the DRM is because it allows backscatter of SFS energy. In the TKE equation, the term $\Pi = -\tau_{ij}S_{ij}$ represents energy transport between resolved and subfilter scales. It is called the SFS dissipation rate because it is mostly positive, indicating the transfer of energy from the resolved into the subfilter motions. But the reverse process, known as backscatter (negative Π values), also exists to feedback energy to the resolved scales, as confirmed in the field observations of Carper and Porte-Agel (2004).

Most canonical eddy-viscosity models are, however, purely dissipative by formulation. They tend to over-suppress turbulence development and cause flow to become laminar quickly under stable conditions (see section 2.4.1). In contrast, scale similarity models naturally allow for backscatter, which is desirable for sustaining resolved turbulence in

SBL simulations. In the DRM formulation, the RSFS stress is of the scale-similarity type. Therefore, the DRM includes backscatter, which is advantageous for simulations of the SBL.

Figure 2-3 compares the horizontally averaged SFS dissipation rate with that for the TKE-1.5, dynamic Wong–Lilly (DWL), and DRM models with four different levels of RSFS reconstruction. We observe that the reconstruction models are less dissipative than the TKE-1.5 model. Among the DRM results, Π increases with higher levels of reconstruction. This happens because eddies with higher wavenumbers toward the filter cutoff are restored under more reconstruction. Interactions between these relatively high wavenumber (small scale) motions are more likely to dissipate energy (Chow 2004). Note that the backscatter property is intrinsic to the reconstruction procedure and is different from the stochastic backscatter type of LES models (Mason and Thomson 1992), in which random perturbations are added to the model domain to obtain correct near-wall behavior in the boundary layer.

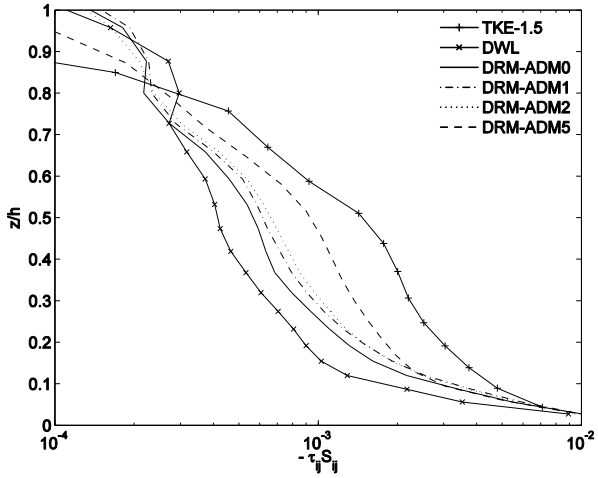

Figure 2-3 Horizontally and time-averaged (last 7200 s) vertical profile of SFS dissipation from six closure models for the moderate stability case ($\overline{w\theta}_s$ = -0.02 Kms^{-1}) The boundary layer depth h is 160 m.

In Figure 2-3, the SFS dissipation (Π) for the DRM–ADM5 closure decreases with height, which could be due to either less dissipation or more backscatter. To investigate the source of the decrease we examine the probability density distribution of Π at different vertical elevations. Figure 2-4 plots the probability density function (PDF) of Π obtained over 1000 s using 20 samples at 50-s intervals (different sampling intervals and averaging periods show similar results). A Gaussian kernel density estimation method is used in computing the PDF. Following Carper and Porte-Agel (2004), Π is normalized by its standard deviation, in which case $P(\Pi)$ on the y axis is a dimensionless number. The overall shape of the PDF "swings" to the backscatter side with increasing height, showing more frequent backscatter events. The percentage backscatter calculated by counting the

number of occurrences of negative of Π is about 5% near the surface to roughly 35% approaching the top of the SBL.

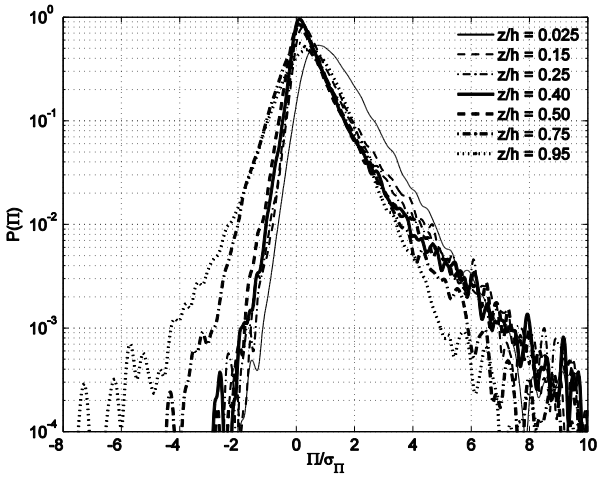

Figure 2-4 Normalized probability density function $p(\Pi)$ at different vertical levels: case DRM-02CR.

2.4.3 Vertical Shear

Vertical profiles of mean wind speed and potential temperature at quasi-steady state from the 3.125-mresolution simulations are plotted in Figure 2-5(a) and (b). A low-level jet (LLJ), located around the wind maximum, develops in all cases in Figure 2-5(a). The height of the wind maximum can be considered a measure for the SBL depth. The boundary layer depth is shallower under stronger stability, as expected due to more limited turbulent transport. For the same stability condition, the choice of turbulence models affects the depth of the boundary layer. The DRM produces a deeper SBL than for TKE-1.5 in both cases. The differences between the two closures are larger for strong stability (DRM 96 m, TKE 78 m) than for moderate stability (DRM 191 m, TKE 185 m). The dependence of SBL depth on the closure model is also documented in the GABLS study. It is interesting to note that the only two 1-m-resolution simulations of the GABLS study used a TKE-based model and a Smagorinsky model with stochastic backscatter. The latter produced a deeper (164 m) SBL than the former (149 m).

Monin–Obukhov (MO) similarity theory is used to test the performance of the simulations near the surface where the dimensionless height z/L is smaller than unity (Garratt 1992). Businger et al. (1971) experimentally obtained the following relationships for the SBL:

$$\phi_m = \frac{\kappa z}{u_*}\frac{\partial \overline{\widetilde{U}}}{\partial z} = 1 + \beta; \quad \phi_h = \frac{\kappa z}{\theta_*}\frac{\partial \overline{\widetilde{\theta}}}{\partial z} = 0.74 + \beta\zeta$$

where ϕ_m and ϕ_h are the dimensionless wind shear and potential temperature gradient, $\zeta = z/L$ is the dimensionless height, β is a constant equal to the inverse of the critical gradient Richardson number Ri, and θ_* is a generic turbulent temperature scale defined as the ratio of surface heat flux to friction velocity.

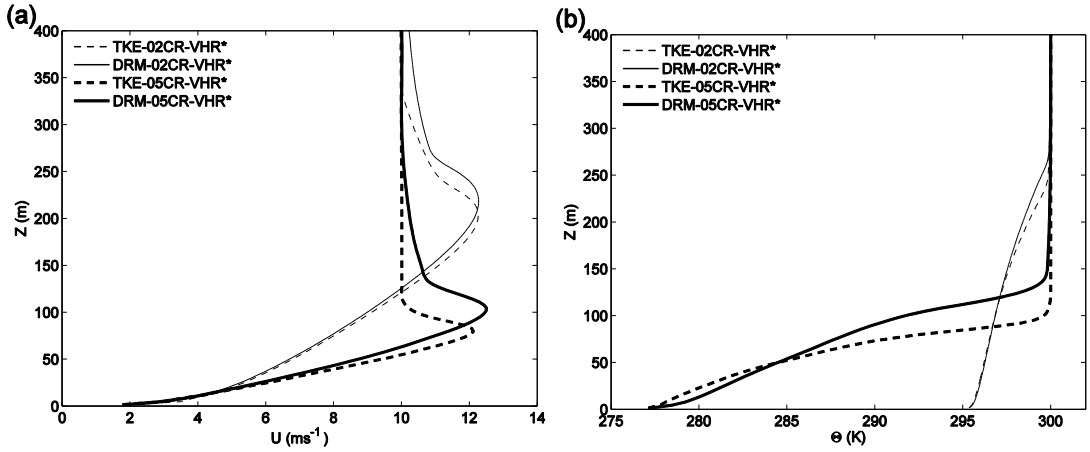

Figure 2-5 Horizontally and time-averaged (last 7200 s) vertical profiles for (a) wind speed and (b) potential temperature for the moderate and strong stability cases.

Horizontally and time averaged dimensionless quantities are presented as a function of Ri in Figure 2-6. Only the relevant ranges where MO similarity is valid (i.e., z/L < 1) are included in the plots. The dimensionless shear relationship is followed quite well for the DRM models in Fig. 6a, even at coarse resolution. In Figure 2-6(b), ϕ_h deviates from the Businger profile for small Richardson numbers. This could be due to the uncertainty in the surface Prandtl number, which is the intercept of Eq. 2-10 and is traditionally set at 0.74 (Grachev et al. 2007) Both the DRM and the TKE-1.5 runs are much better described by an intercept of 0.55 in Figure 2-6(b), which is the predicted surface Prandtl number in our simulations (see section 2.4.4 for further discussion).

The good agreement with MO similarity for level-5 reconstruction in DRM at coarse resolution is surprising since LES results at such resolutions are usually poor for conventional closures. The coarse-resolution simulations of DRM at four other reconstruction levels show improved agreement with surface similarity theory as levels of reconstruction increase. A similar finding is reported for LES of the neutral atmospheric boundary layer (Chow et al. 2005).

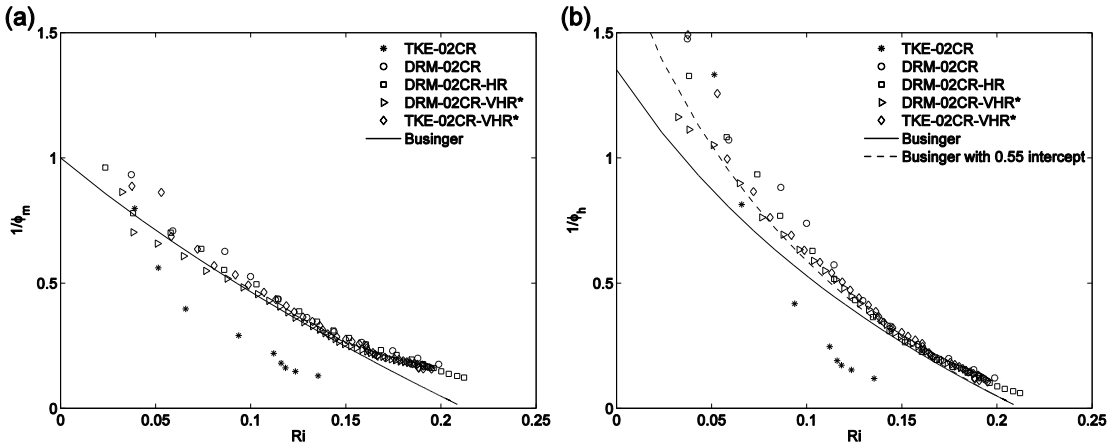

Figure 2-6 Horizontally and time-averaged (last 7200 s) inverse nondimensional (a) shear and (b) temperature gradient for the moderate stability case. Both dimensionless quantities are limited to z/L < 1. They are plotted as a function of gradient Richardson number and compared to MO similarity theory.

Although MO similarity theory provides a general guideline for surface flux scaling, it is much less certain that MO theory should apply under ‘‘universal’’ stable conditions, particularly under strong stability (Sorbjan 2006). Sorbjan and Grachev (2010), and Sorbjan (2010) introduced gradient-based scaling, which is applicable in a wider stability range. Therefore, the master scaling of Sorbjan (2010) is also used to examine the quality of the simulations:

$$\frac{\tau}{U_s^2} = \frac{1}{Ri(1+300Ri^2)^{3/2}}; \quad \frac{-\overline{w\theta}}{U_s T_s} = \frac{1}{0.9Ri^{\frac{1}{2}}(1+250Ri^2)^{3/2}}$$

where $U_s = \kappa z N$ and $T_s = \kappa z d\theta/dz$. The numerical coefficients were obtained using data from the Surface Heat Budget of the Arctic Ocean (SHEBA) field program in the Arctic (Sorbjan 2010). Figure 2-7(a) and (b) present statistics obtained from the 3.125-m simulations using the TKE-1.5 and DRM models. Results from both closures support the gradient-based formulation at moderate stability very well. For strong stability, the agreement is quite good. The TKE-1.5 results are slightly better for smaller Ri, while the DRM is better for larger Ri values. Even higher resolution simulations are likely needed for better comparison under strong stability.

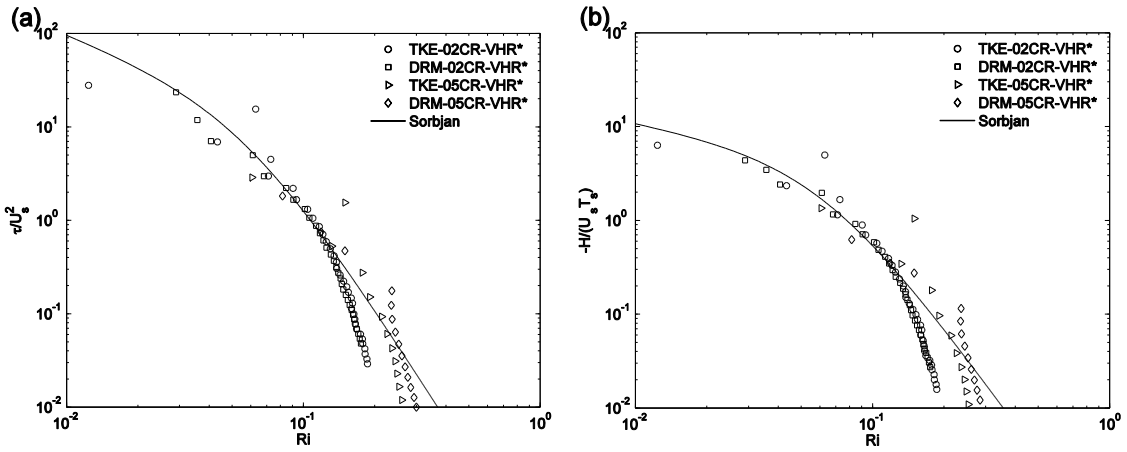

Figure 2-7 Horizontally and time-averaged (last 7200 s) nondimensional (a) shear and (b) temperature gradient for the moderate and strong stability cases. Both dimensionless quantities are limited to z/L < 1 and are plotted as a function of gradient Richardson number and compared to the gradient-based scaling.

2.4.4 Turbulent Prandtl Number

In the previous section, we noted that under moderate stability agreement with the dimensionless potential temperature gradient near the surface can be improved by choosing 0.55 as the turbulent Prandtl number Pr_T in the MO formulation. This conclusion is not limited to the DRM closures but is also true for TKE-1.5 closure at 3.125-m resolution (see Figure 2-6(b)). The Pr_T represents the relative efficiency of turbulent mixing for momentum versus heat. It is an important dimensionless number for flux parameterization in the SBL (Gerz et al. 1989) and is usually prescribed as a stability-dependent constant for LES with the Smagorinsky or TKE-1.5 closures. The variation of the Prandtl number in the SBL can be described using the formulation proposed by Schumann and Gerz (1995) for equilibrium flows:

$$Pr_T = Pr_{T0} \exp\left(-\frac{Ri}{Pr_{T0} Ri_\infty}\right) + \frac{Ri}{Ri_\infty}$$

where Pr_{T0} is a surface value and Ri_∞ is a constant gradient Richardson number limit in the SBL. Nieuwstadt (1984) hypothesized a constant value of 0.2 for Ri in the SBL as part of the ‘‘z-less’’ scaling hypothesis, which we adopt for the above formulation as Ri_∞.

Since LES with the DRM models independently predicts momentum and heat fluxes (Pr_T is not prescribed in advance) that agree well with similarity theory, the variation of Pr_T in the SBL can be quantified. As shown in Figure 2-8, Ri remains nearly constant at 0.2 from around z/h > 0.4 to the top of the SBL. A remarkably good fit with the Schumann and Gerz formulation is observed for Pr_T until 70% of the boundary layer depth. The Pr_T values for higher cooling cases show a similar pattern and agreement, with slightly different Pr_{T0}, and Ri_∞ values; for example, Pr_T = 0.4 and Ri_∞ = 0.25 gives the best fit for the case where $\overline{w\theta}_s$= -0.03 K m s^{-1} (not shown). The DRM results show that Pr_T exceeds unity approaching the top of the boundary layer, as the Richardson number

increases. While this is allowed by Eq. 2-12, it contradicts the gradient-based scaling in Eq. 2-11. Whether Pr_T can exceed 1 in the SBL is still a debated issue. Readers are referred to Grachev et al. (2007) for a more comprehensive discussion.

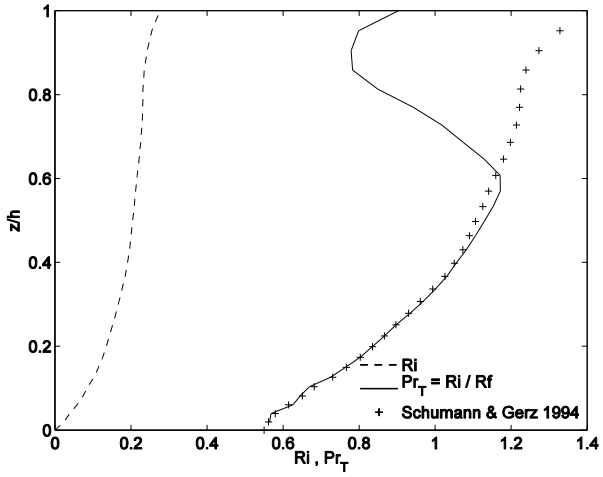

Figure 2-8 Horizontally and time-averaged (last 7200 s) vertical profiles of turbulent Prandtl number and gradient Richardson number for the moderate cooling case ($\overline{w\theta}_s$ = -0.02 Kms^{-1}) compared to the theory of Schumann and Gerz (1995).

2.4.5 Turbulent Flux Decomposition

The role of reconstruction in the DRM is investigated by comparing the resolved and subfilter-scale turbulent fluxes from the DRM with the standard TKE-1.5 closure. Figure 9 presents the horizontally averaged heat flux for the moderate cooling case. The total heat flux is nearly identical for both closures. The DRM has a larger SFS component and a smaller resolved component than does the TKE-1.5 model. This is due to the presence of the RSFS stress, which is extracted from the resolved field and is included in the SFS component of the model. The resolved stress is reduced accordingly.

The presence of the resolved subfilter-scale stresses allows us to directly compute SFS TKE. This is a unique property that many eddy-viscosity closures (such as the Smagorinsky model) do not have, since the sum of the trace of the stress tensor tkk is zero, and therefore a model must be used to estimate SFS TKE if needed. For the DRM, however, τ_{kk} is nonzero because of the RSFS part. Using Taylor series expansions, it can be shown that $\tau_{RSFS,kk}$ is a function of the sum of the squares of the velocity gradients multiplied by the filter width squared plus higher order terms. For example, the level-0 reconstructed stresses $\tau_{RSFS,kk}$ for an isotropically filtered field can be expressed as:

$$\tau_{RSFS,kk} = \overline{\bar{\tilde{u}}_k \bar{\tilde{u}}_k} - \bar{\tilde{u}}_k \bar{\tilde{u}}_k = \frac{\Delta^2}{12} \overline{\frac{\partial \bar{\tilde{u}}_k}{\partial x_j} \frac{\partial \bar{\tilde{u}}_k}{\partial x_j}} + O(\Delta^4)$$

where Δ is the explicit filter width (see Chow 2004, appendix A). Similar to heat flux, the vertical profiles of the total TKE from the DRM and the TKE-1.5 closure are similar,

with different partitioning of resolved/SFS components. This suggests that the DRM does offer a reliable direct measure of SFS TKE. In the present study of the SBL, it does so mostly by accounting for the vertical gradients in the filtered horizontal velocity field ($\tilde{\bar{u}}$, $\tilde{\bar{v}}$).

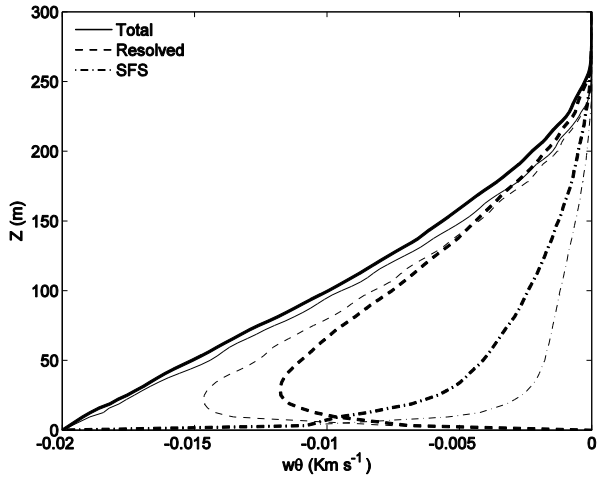

Figure 2-9 Comparison of horizontally and time-averaged (last 7200 s) heat flux components of the DRM-02CR-VHR* (thick lines) and TKE-02CR-VHR* (thin lines) for the moderate stability case ($\overline{w\theta}_s$= -0.02 Kms^{-1}).

2.4.6 Low-level Jet and Elevated TKE

In a classical SBL, turbulence is generated at the surface and transported upward. In a nonclassical SBL, turbulence can also be generated aloft due to strong shear above and below the low-level jet. This TKE generation mechanism is referred to as the turbulence and mean shear interactions by Nakamura and Mahrt (2005). In the numerical simulation literature, elevated TKE was previously simulated by Conangla and Cuxart (2006) and Cuxart and Jimenez (2007).

The mean vertical shear profile for moderate and strong stability is presented in Figure 2-10 for the DRM results at 3.125-m resolution. At the high cooling rate, mean shear increases significantly within the SBL. This increase of shear is due to the decrease in the boundary layer depth h. Furthermore, the shear strength also greatly increases above the jet nose. As the mean shear strengthens, greater amounts of mechanical production of TKE can be expected. The rate of TKE growth or decay, however, must be evaluated by also considering the buoyancy destruction process. In Figure 2-10, the vertical potential temperature gradient shows a local maximum above the top of the boundary layer, which presents a severe limit to turbulent mixing processes. Although shear increases both below and above the jet, turbulent bursting events are more likely to occur in the subjet region.

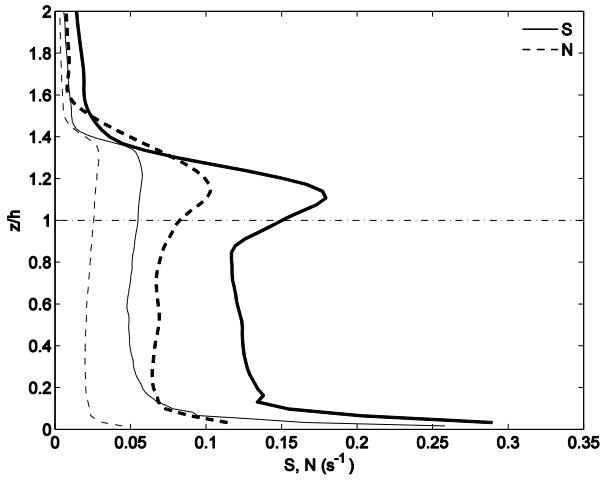

Figure 2-10 Horizontally and time-averaged (last 7200 s) vertical profiles of mean shear $S = \left(\frac{d^2u}{dz^2} + \frac{d^2v}{dz^2}\right)^{-1/2}$ and buoyancy frequency $N = \left(\frac{g}{\theta}\frac{d\theta}{dz}\right)^{-1/2}$ thin lines represent the moderate stability case ($\overline{w\theta}_s$= -0.02 K m s^{-1}), and thick lines represent the strong stability case ($\overline{w\theta}_s$= -0.05 K m s^{-1}). The dashed–dotted line shows the dimensionless SBL height z/h = 1.

The presence of TKE in the subjet region is identified by looking at time series of point measurements at different elevations in the SBL. The turbulent kinetic energy in Figure 2-11 is computed by $e = 1/2(u'^2 + v'^2 + w'^2)$, where u', v', and w' are the fluctuating components of time-detrended velocities, to represent what might be seen at a meteorological tower with sonic anemometers at different heights. We observe extended periods where e is suppressed under strong stability conditions. This is more significant at higher elevations toward the LLJ nose at 100 m (z/h = 1). In between the quiescent periods, large increases of e over a relatively short time scale are present. Therefore, the nature of the elevated TKE appears intermittent. Quantitatively, intermittency can be measured by sorting a turbulent quantity in descending order according to its absolute magnitude and then counting the fraction of time that makes up the first 50% of the total time-integrated quantity. This is adapted from the intermittency definition by Coulter and Doran (2002) using heat flux as the turbulence indicator. In the continuous limit, this fraction will be 0.5, meaning that 50% of the total quantity is achieved in 50% of the total time. Here, the fraction computed for e is found to be 25% at 80 m (z/h = 0.8), which confirms the intermittent nature of the elevated TKE.

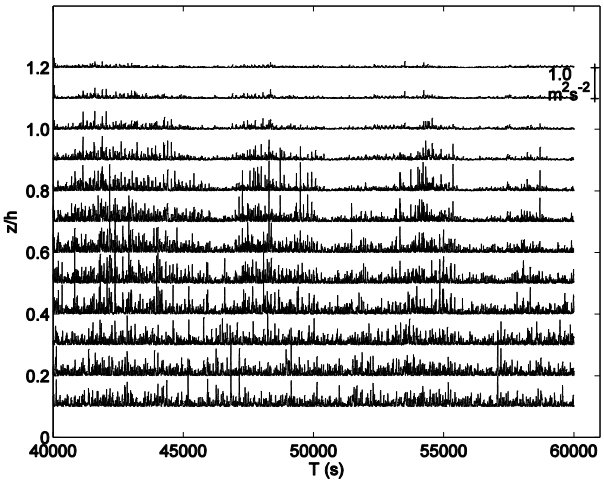

Figure 2-11 Time series $e = (u'^2 + v'^2 + w'^2)^{-1/2}$ of at different elevations for the strong stability case DRM-05CR-VHR* ($\overline{w\theta}_s$= -0.05 K m s^{-1}).

2.4.7 Spectra and Velocity Structure

Figure 2-12 shows the one-dimensional energy spectra of the streamwise velocity $\tilde{\bar{u}}$ at different heights within the SBL. Time-averaged data from each height are used to generate the spectra for the moderate and strong stability cases. The scaling procedure of Perry et al. 1986) and Porte-Agel et al. (2000) is adopted to collapse the data. A limited inertial subrange region is present in a small region of the energy spectra for the moderate case. For the stronger stability case, the presence of the inertial subrange is hard to identify. Considering the Ozmidov scale in the center depth of the boundary layer to be 2 m in this case, even higher resolution than 3.125 m may be needed to fully resolve the turbulence in the SBL, though finite difference errors will always tend to limit the extent of the inertial subrange.

The flow structure is of practical importance for studying scalar transport and dispersion processes in the atmospheric boundary layer. The structure of the resolved flow is sensitive to the SFS parameterization, and large differences are usually found in the near-surface layers Ludwig et al. 2009). The variability of flow with the TKE-1.5 and DRM closures is examined from contour plots of the instantaneous streamwise velocity in the horizontal plane at 20 m above the surface, as shown in Figure 2-13. Under moderate stability, velocity contours of the TKE-1.5 and DRM closures are similar. The size of the fluctuations qualitatively shows the limited eddy sizes in the SBL. Under strong stability, differences are observed between the two closures. The TKE-1.5 model reveals banded streak-like structures aligned with the mean wind vector near the surface. Such a pronounced linear extent of the TKE-1.5 closure has been observed in other studies (Ludwig et al. 2009); Mirocha et al. 2010) for the neutral atmospheric boundary layer. In comparison, the DRM predicts a more realistic flow structure without any banded patterns. The eddy sizes are much smaller in the DRM simulations corresponding to the more limited turbulent length scale.

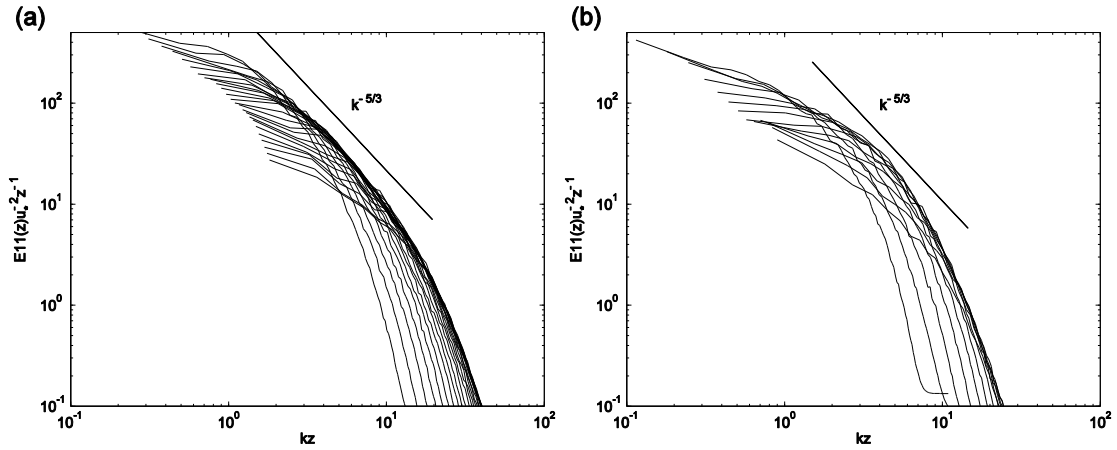

Figure 2-12 Normalized one-dimensional energy spectrum for (a) DRM-02CR-VHR* and (b) DRM-05CR-VHR*. Each curve is a different height above the wall, starting at the left at z/h = 0.1 up to z/h = 0.9. All spectra are time averaged from 40 000 to 50 000 s.

2.5 Summary

This study performed LES of the stably stratified atmospheric boundary layer using the explicit filtering framework and dynamic reconstruction turbulence model of Chow et al. (2005). With constant geostrophic forcing and prescribed surface cooling, a quasi-steady state SBL was simulated with sustained turbulence, at coarser resolutions than typically recommended for SBL simulations, even under strong cooling scenarios. The DRM is capable of capturing atmospheric dynamics, for example the proper representation of SFS backscatter, that do not conform to traditional assumptions of gradient diffusion turbulence models. The net energy drain from the resolved fields is therefore reduced to prevent the false laminarization problem experienced by other conventional eddy-viscosity closures. The probability distribution of dissipation reveals increased percentage backscatter with height, confirming the importance for choosing SFS models that have some backscatter component for SBL simulation purposes.

Compared with the TKE-1.5 closure, we found that the dynamic reconstruction model improves the representation of MO surface similarity under moderate stability even at coarse resolutions (e.g., 16-m horizontal spacing). The improvement was shown to be a result of higher levels of reconstruction, which increasingly restores turbulent scales near the filter cutoff. Overall, the DRM's ability to sustain turbulence and better represent mean shear and potential temperature gradient profiles at coarse resolution opens up possibilities for performing LES over real complex terrain under stable conditions, where spatial resolution is usually more limited than in idealized SBL studies.

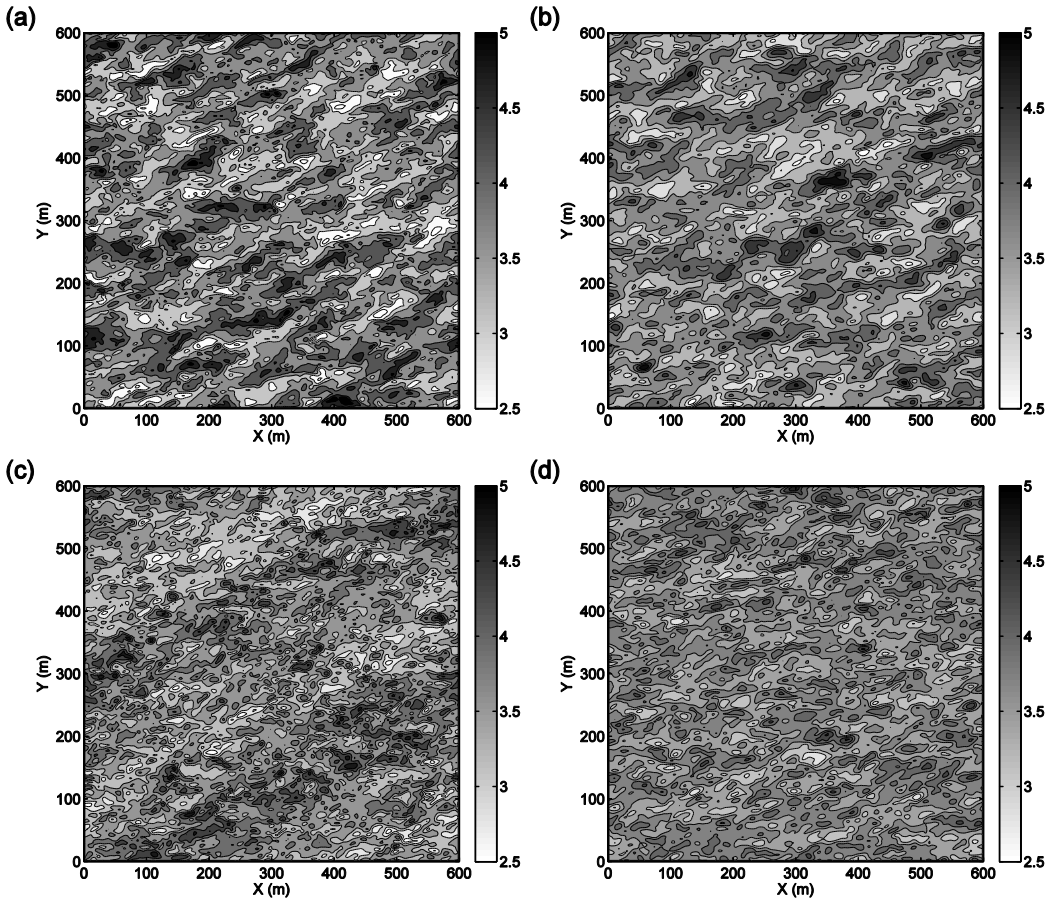

Figure 2-13 Contours of instantaneous u velocity in the horizontal plane at around 20 m above the surface for the (top) moderate and (bottom) strong stabilities simulated with the (left) TKE-1.5 and (right) DRM closures: (a) TKE-02CR-VHR*, (b) DRM-02CR-VHR*, (c) TKE-05CR-VHR*, and (d) DRM-05CR-VHR*.

High-resolution simulations were used to investigate the flow structure and turbulent statistics of the SBL. General agreement with the Businger–Dyer flux-based similarity is observed in the surface layer. The LES results also support the gradient-based similarity formulation of Sorbjan (2010), although results at strong stability likely require even higher resolution simulations. The turbulent Prandtl number calculated from DRM closures supports the formulation of Schumann and Gerz (1995). This suggests the use of a Richardson number–based turbulent Prandtl number formulation for SBL simulations.

Flux decomposition was used to show the unique feature of the DRM to include the RSFS component. The DRM allows direct prediction of the SFS TKE. Comparison with the TKE-1.5 model showed that this is a reliable measure. The presence of elevated TKE below the low-level jet was also described. This is a result of increased shear in the subjet region. This elevated TKE is shown to be intermittent in nature. Finally, spectra and near-surface velocity contours were presented. Under strong stability, the TKE-1.5 closure shows banded streak structures, which is likely unrealistic. The flow structures from the

DRM are more reliable, as they become finer as stability increases without developing any correlated structures in the flow direction.

We have demonstrated the ability of explicit filtering and dynamic reconstruction models to successfully simulate the boundary layer under stable conditions. LES with DRM is capable of covering a wide range of stability conditions, extending into the intermittent turbulence regime where traditional LES closures usually fail. The approach described has the advantage that almost any existing SGS model can be adapted to an explicit filtering and reconstruction framework. This is achieved most simply by adding a scale similarity component (RSFS) to existing SGS closures (see Chow and Street 2009; Chow et al. 2005). The present study provides a promising outlook for the success of future LES applied to real terrain under stable conditions.

Chapter 3 Turbulence Modeling for the Stable Atmospheric Boundary Layer and Implications for Wind Energy[2]

Abstract

The near-surface structure of atmospheric turbulence affects the design and operation of wind turbines and is especially difficult to predict under stably stratified conditions. This study uses large-eddy simulation (LES) to explore properties of the stable boundary layer (SBL) using an explicit filtering and reconstruction turbulence modeling approach. Simulations of the atmospheric boundary layer over flat terrain, under both moderately and strongly stable conditions are performed. Results from high-resolution simulations are used to investigate SBL flow structures including mean profiles and turbulence statistics, which are relevant to wind energy applications. The applicability of power-law relations and empirical similarity formulations for predicting wind speed depend on the strength of stratification and are shown to be inadequate. Low-level jets form in the simulations. Under strong stability, vertical wind shear below the jet triggers intermittent turbulence. The associated sporadic "bursting" events are extremely energetic and last longer than the time scale of the largest eddies. Such phenomena can have adverse effects on turbine lifetime and performance.

3.1 Introduction

Wind turbines sit in the atmospheric boundary layer, where winds are highly turbulent, shear events are intermittent, and land-surface interactions may be strong. Turbine hub heights have increased over the years to now be between 80 and 120 m above ground level (AGL), with blade diameters of 80–120 m (Archer and Jacobson 2004). Current operational practices for wind farm operation and siting rely on power-law estimates for the wind speed variation with height and assume neutral stratification. Similarly, practical guidelines for impacts of turbulence and shear on turbines are based on theoretical estimates for idealized flows (Storm et al. 2009). Thus, wind farm operators may risk severe damage to the rotors and blades by operating under conditions that lead to excess fatigue, depending on the prevailing atmospheric conditions.

High-resolution simulations of atmospheric flow are currently being developed to provide predictions for wind turbine micro-siting and operational wind power forecasting. For example, Palma et al. (2008) used numerical simulations to examine the vertical structure of turbulence and wind shear at a coastal wind farm and found that many

[2] This chapter is a reproduction of the paper "Turbulence Modeling for the Stable Atmospheric Boundary Layer and Implications for Wind Energy" by Bowen Zhou (the principle author), and Fotini Katopodes Chow, published in Flow, Turbulence and Combustion, 2012, Volume 88, pages 255-277 [Zhou and Chow 2012], © Copyright Springer Science + Business Media B.V. 2011

atmospheric conditions violated the design criteria for turbine operation (turbulence intensity too high or wind shear too high). Large-eddy simulation (LES), in particular, has shown promise for application to wind energy because it can adequately resolve turbulent flow in the lowest few hundred meters of the atmospheric boundary layer (ABL). LES is based on the definition of a spatial filter which can be adjusted to resolve necessary flow features. The spatial filter separates the large resolved scale from the subfilter-scale (SFS) motions. The effect of SFS scales on the resolved scales must be represented with a turbulence model. Basu et al. (2008) simulated a full diurnal cycle with LES, focusing on boundary layer transitions, showing the predictive capabilities of LES specifically with wind energy applications in mind. Several recent studies have used LES over isolated hills to examine turbulence structure, with applications to wind energy (Bechmann and Sorensen 2011; Calaf et al. 2010; Chow and Street 2009; Paiva et al. 2009).Porté-Agel et al. (2010) performed LES of wind-turbine wakes in neutrally stratified flows to evaluate different turbine parameterizations, and achieved good agreement with wind tunnel measurements.

One of the greatest current challenges in applying LES to wind energy lies in the representation of turbulence in the ABL, which is strongly affected by the stability of the atmosphere. The stable boundary layer (SBL) occurs nearly every night over land including features such as low-level jets (LLJ), inertial oscillations, and gravity waves. In the Southern Great Plains region of the United States, for example, LLJs occur regularly at night and represent a large untapped wind resource (due to higher wind speeds) but also a hazard for turbine operation due to strong vertical shear and turbulence (Sisterson and Frenzen 1978). Turbine failures and fatigue show strong correlation to high wind shear and turbulence intensity Kelley et al. (2006). Storm et al. (2009)used the Weather Research and Forecasting (WRF) mesoscale atmospheric model to study LLJs over the Southern Great Plains for wind forecasting purposes. They found that while WRF tended to overestimate the LLJ heights and underestimate the LLJ wind speeds, predictions were much improved over standard power-law relations.

In this work we focus on simulations of the stably stratified boundary layer which generates favorable winds for wind power extraction in some regions of the world. The main challenge in simulating stable conditions is that the length scale of turbulent eddies in the atmospheric boundary layer is much smaller than under convective or neutral conditions, thus requiring higher grid resolution. Previous numerical simulations of the SBL have been limited to mild stability, with conditions of either high geostrophic forcing or low surface cooling rate (Basu and Porté-Agel 2005; Saiki et al. 2000). Both conditions result in turbulence profiles within the continuous regime.

Although nighttime SBL turbulence is often continuous under strong winds and overcast conditions, it can become intermittent on clear nights with weak winds. Observational evidence from the Cooperative Atmosphere-Surface Exchange Study-99 (CASES-99) showed frequent occurrence of SBL intermittency at the field site in Kansas, in the Great Plains region (Poulos et al. 2002). Intermittency in the atmosphere is characterized by buoyancy-suppressed turbulence over prolonged periods greater than the time-scale of the dominant eddies (Nakamura and Mahrt 2005), with sporadic bursting when energetic turbulent mixing events occur over relatively short periods. While low

turbulence intensity under strongly stable conditions is ideal for wind power extraction, transient bursting events are a potential threat to wind turbines (Kelley et al. 2006).

There are several mechanisms that trigger SBL intermittency. These include turbulence and mean shear interactions, breaking gravity waves and Kelvin–Helmholtz (KH) billows, terrain-induced drainage flows, and propagating density currents(J. L. Sun et al. 2004). Some of those mechanisms, such as breaking gravity waves and KH billows are well understood, and have been reproduced with numerical simulations. Cederwall (2001) used LES to investigate enhanced turbulence episodes associated with the breakdown of large-scale wave-like structures in the SBL. The current LES study focuses on the first, and perhaps the most common, cause for intermittency. This mechanism is often thought of as a feedback loop between turbulence and vertical shear under strongly stable conditions. High wind shear overcomes stratification and generates turbulence. Turbulent mixing then smooth out the shear and decays due to the background stratification. The lack of turbulent momentum transfer leads to an increase in wind shear so that the cycle repeats. Ohya et al. (2008) verified this mechanism with experiments conducted in a stably stratified wind tunnel. Van de Wiel et al. (2002) simulated an intermittently turbulent SBL with a box model.

In this study, the applicability of LES to stable atmospheric flows is extended towards the strongly stable regime, allowing intermittency events to develop. This is accomplished by better representation of turbulence through a new closure model. The LES methodology adopted in this study uses explicit filtering and dynamic reconstruction (Chow et al. 2005). Zhou and Chow (2011) demonstrated the ability of the dynamic reconstruction model (DRM) to sustain resolved turbulence under strongly stable conditions. In comparison, LES with conventional eddy-viscosity closures is known to experience difficulties such as runaway cooling under strongly stable conditions (Jimenez and Cuxart 2005), and hence is unable to predict intermittency with the above mechanism. In addition, the (DRM) has previously been shown to be advantageous in turbulent channel flow (Gullbrand and Chow 2003) and in neutral atmospheric boundary layer flow (Chow et al. 2005). Almost any existing SGS model can be adapted to an explicit filtering and reconstruction framework.

The Advanced Regional Prediction System (ARPS) (Xue et al. 2000; Xue et al. 2001) is used for the simulations. ARPS is a non-hydrostatic meso-scale and small-scale LES finite difference model. The code has been adapted to accommodate the new DRM closure. We consider both moderate and strong surface cooling, which places the boundary layer turbulence in the continuous and intermittent regime respectively. We specifically focus on the vertical structure of mean winds and turbulence in the SBL, which is of interest in wind energy applications. To facilitate the discussion of our results, we will consider a generic wind turbine with hub height at 80 m AGL and a blade diameter of 80 m, which is typical of today's wind turbine configurations (Archer and Jacobson 2004).

3.2 Explicit Filtering and Reconstruction Turbulence Approach

3.2.1 Governing Equations

The traditional approach towards LES has been to treat discrete differentiation as an implicit filter to separate large from small scales in the governing equations. With finite volume and finite difference approaches, implicit filtering depends on the discrete differentiation schemes whose effects cannot usually be exactly characterized. High frequencies that arise from the nonlinear terms may not be properly removed by implicit filters, which can lead to aliasing errors (Lund 1997). In comparison, explicit filtering of the nonlinear terms can minimize the influence of truncation errors and has been shown to be beneficial in recent studies (e.g. Gullbrand and Chow (2003)). Here we adopt the explicit filtering approach of Gullbrand and Chow (2003) which was applied to the ABL by Chow et al. (2005). A 3D explicit filter (typically a tophat filter of width twice the grid spacing) is applied to the Navier-Stokes equations, and is treated separately from the numerical differencing operators. In our notation, the implicit discretization operator is denoted by a tilde and the explicit filtering operator by an overbar. The LES governing equations for the resolved fields are the momentum, continuity, and scalar transport equations:

$$\frac{\partial \overline{\tilde{\rho}}\,\overline{\tilde{u}}_i}{\partial t} + \frac{\partial \overline{\tilde{\rho}}\,\overline{\tilde{u}}_i\,\overline{\tilde{u}}_j}{\partial x_j} = -\frac{\partial \overline{\tilde{p}}}{\partial x_i} - \overline{\tilde{\rho}}\, g\delta_{i3} + \overline{\tilde{\rho}}\epsilon_{imn} f_n \overline{\tilde{u}}_m - \frac{\partial \overline{\tilde{\rho}}\,\tilde{\tau}_{ij}}{\partial x_j}$$

$$\frac{\partial \overline{\tilde{\rho}}}{\partial t} + \frac{\partial \overline{\tilde{\rho}}\,\overline{\tilde{u}}_i}{\partial x_i} = 0$$

and

$$\frac{\partial \overline{\tilde{\theta}}}{\partial t} + \frac{\partial \overline{\tilde{\rho}}\,\overline{\tilde{u}}_i\overline{\tilde{\theta}}}{\partial x_i} = -\frac{\partial \overline{\tilde{\rho}}\,\tilde{\chi}_i}{\partial x_i}$$

where $\overline{\tilde{u}}_i$ are the velocity components, $\overline{\tilde{p}}$ the pressure, , $\overline{\tilde{\rho}}$ the density, f the Coriolis parameter, and $\overline{\tilde{\theta}}$ the potential temperature. The turbulent stresses and heat fluxes are defined as follows:

$$\tau_{ij} = \overline{u_i u_j} - \overline{\tilde{u}}_i\,\overline{\tilde{u}}_j = \underbrace{\overline{u_i u_j} - \overline{\tilde{u}_i \tilde{u}_j}}_{\tau_{SGS}} + \underbrace{\overline{\tilde{u}_i \tilde{u}_j} - \overline{\tilde{u}}_i\,\overline{\tilde{u}}_j}_{\tau_{RSFS}}$$

$$\chi_i = \overline{u_i \theta} - \overline{\tilde{u}}_i\,\overline{\tilde{\theta}} = \underbrace{\overline{u_i \theta} - \overline{\tilde{u}_i\,\tilde{\theta}}}_{\chi_{SGS}} + \underbrace{\overline{\tilde{u}_i\,\tilde{\theta}} - \overline{\tilde{u}}_i\,\overline{\tilde{\theta}}}_{\chi_{RSFS}}$$

The first set of parentheses on the right-hand side contains the unresolvable subgrid-scale (SGS) stresses, τ_{SGS} and χ_{SGS}, which represent the difference between the total and resolved stress components and must be modeled. The second set of parentheses contains the resolvable subfilter-scale (RSFS) stresses, τ_{RSFS} and χ_{RSFS}, which depend on the resolved and explicitly filtered velocity fields within the resolution domain. As the

explicit filter function is well defined, it is theoretically possible to obtain $\tilde{u}_i$ from $\overline{\tilde{u}}_i$ and $\tilde{\theta}$ from $\overline{\tilde{\theta}}$ by deconvolution (inverse filtering).

The RSFS/SGS model framework can be viewed in terms of a mixed model (Bardina et al. 1983; Zang et al. 1993). The RSFS piece is the so-called "scale similarity" term represented by reconstruction, and the SGS piece is represented using an eddy-viscosity closure. With zero level reconstruction, the RSFS term reduces exactly to the scale similarity model of Bardina. With higher levels of reconstruction, more details of high frequency motions approaching the grid cutoff are restored, thus improving the representation of the SFS stress. Using the same approach, Chow et al. (2005) performed simulations of the neutral boundary layer which reproduced the expected logarithmic velocity profile and better represented turbulent stresses compared to standard eddy-viscosity models.

3.2.2 RSFS Reconstruction Model

Reconstruction of the RSFS stress is accomplished through the approximate deconvolution method (ADM) (Stolz et al. 2001). The unfiltered quantity can be reconstructed in an iterative fashion by successive filtering operations (G) applied to the filtered quantities:

$$\tilde{u}_i = \bar{\tilde{u}}_i + (I - G) \star \bar{\tilde{u}}_i + (I - G) \star [(I - G) \star \bar{\tilde{u}}_i] + \cdots$$

where I is the identity operator, G is the explicit filter, and asterisks denote the convolution operator. Higher orders of accuracy can be achieved by including more terms in the series expansion, simply by repeated application of the same filtering operation. The RSFS term is computed by substituting the reconstructed velocity $\tilde{u}_i^\star$ into the τ_{RSFS} term (i.e. $\tau_{RSFS} = \overline{\tilde{u}_i^\star \tilde{u}_j^\star} - \overline{\tilde{u}_i^\star}\,\overline{\tilde{u}_j^\star}$) In this work, up to five levels of reconstruction are applied to enhance the role of the RSFS stresses.

3.2.3 SGS Turbulence and Wall Models

Reconstruction of the RSFS stress is only able to capture motions up to the Nyquist grid cutoff, thus the SGS model must represent any motions smaller than the grid spacing. We apply the (Wong and Lilly 1994) dynamic eddy-viscosity model to represent SGS motions:

$$\tau_{SGS} = -2\nu_T \bar{\tilde{S}}_{ij}$$

where $\bar{\tilde{S}}_{ij} = (\partial\overline{\tilde{u}}_i/\partial x_j + \partial\overline{\tilde{u}}_j/\partial x_i)/2$ is the resolved strain rate tensor and the dynamic eddy viscosity is given by $\nu_T = C_\epsilon \Delta^{4/3}$. The coefficient C_ϵ is determined using the least squares method of Lilly (1992).

Because the near-wall stresses are usually under-predicted with dynamic SGS models applied in ABL flows, a near-wall stress model is often required to improve the near wall stress profile (Brasseur and Wei 2010). The canopy stress model of Brown et al. (2001) is

adopted. Implementation of this near-wall model has proved successful in the work of Cederwall (2001), Chow et al. (2005), and Kirkpatrick et al. (2006). The near-wall stress is given by:

$$\tau_{i,near-wall} = -\int C_c a(z) \left|\overline{\tilde{u}}\right| \overline{\tilde{u}}_i dz$$

where C_c is a strength factor, and the function $a(z)$ is a shape factor to set a smooth decay of $\tau_{i,near-wall}$ to zero at the specified cutoff height h_c.

The complete dynamic reconstruction model is a mixed model for the total SFS stress consisting of the RSFS and SGS components, which are respectively scale similarity and eddy-viscosity terms with near-wall enhancement:

$$\tau_{ij} = \underbrace{\overline{\tilde{u}_i^\star \tilde{u}_j^\star} - \overline{\tilde{u}_i^\star}\,\overline{\tilde{u}_j^\star}}_{\tau_{RSFS}} \underbrace{- 2C_\epsilon \Delta^{4/3} \overline{\tilde{S}}_{ij} + \tau_{i,near-wall}}_{\tau_{SGS}}$$

3.3 Model Configuration

Simulations are performed on a (640 m, 640 m, 640 m) domain over flat but rough terrain, similar to that used in previous work (Basu and Porte-Agel 2006; Kosovic and Curry 2000; Saiki et al. 2000). The spatial resolution used in this study is 3.125 m on isotropic grids. The resolution of 3.125 m is chosen based on the suggestions from the GEWEX Atmospheric Boundary Layer Study (GABLS) intercomparison LES study of the SBL (R. Beare et al. 2006). The study concluded that 3.125 m is sufficiently fine under the moderately stable atmospheric conditions, as the results were close to their extremely fine (2 or 1 m) resolution simulations.

The lateral boundary conditions are set to be periodic, and the lower boundary is a rigid wall. At the top boundary, Rayleigh damping is applied above 500 m. The boundary layer height ranges from 100–200 m and thus should not be affected by the Rayleigh damping. The initial potential temperature is uniform at 300 K (neutral conditions). A random perturbation of 0.1 K is applied to the bottom 150 m of the domain at initialization to trigger turbulence. ARPS adopts a mode-splitting time integration technique, the large integration time step used is 0.1 s, and small integration time step for only the acoustically active terms is 0.005 s.

Atmospheric stratification is usually quantified by the Richardson number, a ratio of buoyancy destruction to shear production of turbulent kinetic energy (TKE). Turbulence is continuous when the flux Richardson number (R_f) is below 0.25, intermittent when R_f is between 0.25 and 1.0, and strongly damped when R_f exceeds unity (Stull 1988). Derbyshire Derbyshire (1990) derived an expression to estimate the flux Richardson number based on the surface heat flux $\overline{w\theta}_s$, the geostrophic wind speed G, and the Coriolis parameter f :

$$R_f = \sqrt{3}\,\frac{-\frac{g}{\theta_s}\overline{w\theta}_s}{G^2|f|}$$

In this study, a constant geostrophic wind at (U_g, V_g) = (10 m s^{-1}, 0 m s^{-1}) is applied for all simulations. The threshold value of surface heat flux distinguishing continuous and intermittent turbulence is about −0.03 Km s^{-1} corresponding to R_f= 0.25. Therefore, a constant surface heat flux is imposed at −0.02 Km s^{-1} to simulate a continuously turbulent SBL under moderate atmospheric stability.

The intermittently turbulent SBL is simulated by imposing a constant surface cooling rate of −2.0 K hr^{-1} instead. The surface heat flux boundary condition above is not used, since it is no longer appropriate for strongly stable conditions. Malhi (1995) presented the existence of a dual solution for surface sensible heat flux, embedded in the log-linear formulation of the Monin–Obukhov (MO) similarity. According to the MO formulation (Businger et al. 1971), surface heat flux increases in magnitude until a certain maximum associated with the wind speed is reached. Beyond that point, turbulent transfer in the surface layer is strongly damped by stratification, such that further increase of heat flux from an increase in temperature gradient is no longer possible. Basu et al. (2008) further showed that strongly stable conditions, consistent with the MO formulation, can only be achieved in numerical simulations by specifying a surface temperature cooling rate. The surface heat flux for the strongly stable setup decreases with time and reaches a value around −0.05 Km s−1 at quasi-steady state, as presented in Figure 3-1. Therefore, the SBL does reach an intermittent state according to the qualitative expression of Derbyshire (1990).

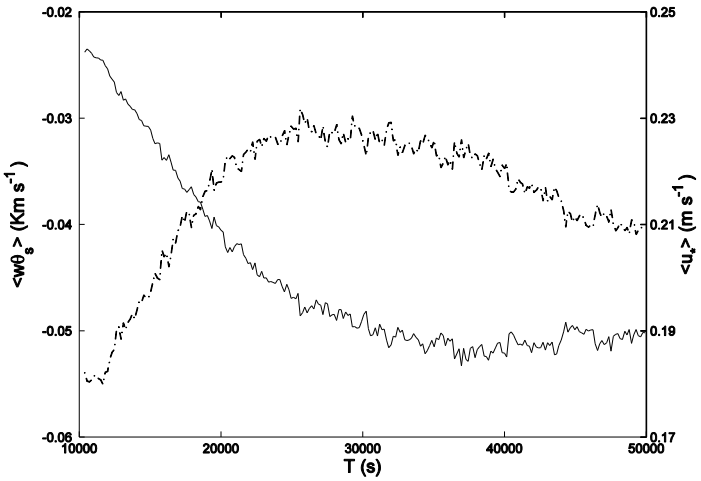

Figure 3-1 Horizontally averaged surface heatflux (*solid line*) and friction velocity (*dash-dotted line*) for the strongly stable cases

Simulations are carried out for a total of 50,000 s. Such extended periods of cooling create an idealized nighttime boundary layer reaching quasi-steady state. In real atmospheric flows, surface cooling is a combined result of non-turbulent processes such as surface radiation, and turbulent processes such as latent and sensible heat transport. The resulting boundary layer flow is highly non-stationary. This LES study isolates many of the boundary layer processes and only focuses on the flow structures and turbulence

under relatively stationary conditions. Although the conclusions do not directly apply to any particular wind farm under real flow conditions, results from this study can still provide some useful implications for the wind energy industry. Furthermore, being able to simulate strongly stable conditions, and reproducing the most common intermittency mechanism under idealized conditions, is considered a first step towards applying the LES technique to simulations of real SBL flows.

3.4 Simulation Results and Discussion

3.4.1 Mean Profiles

The daytime atmospheric boundary layer (ABL) depth is limited by a capping inversion usually at 1–2 km AGL. The nighttime ABL depth is much shallower. Generally, strong mesoscale forcings (geostrophic wind) and weak surface cooling result in a deep and turbulent SBL, while weak geostrophic wind and strong surface cooling produce a shallow and sporadically turbulent SBL. In Figure 3-2, horizontally and time averaged (between 42,800 and 50,000 s) wind speed for the moderate and strong cooling cases is presented. The vertical height of the low-level jet (LLJ), which is one of the measures of the SBL depth, indicates that the moderately stable boundary layer is about twice as deep as the strongly stable boundary layer. This is also evident from the depth of the capping temperature inversion, as well as wind direction shifts presented in Figure **3-3**.

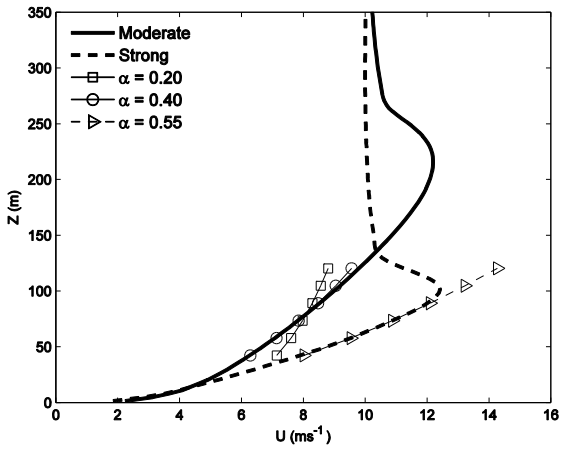

Figure 3-2 Horizontally and time averaged (between 42,800 and 50,000 s) vertical profiles of wind speed for the moderately and strongly stable cases, including power law fits in the 40–120 m region with different shear exponents.

A shallower SBL under strongly stable conditions means the maximum winds are closer to the ground, thus making a greater amount of wind power available at lower altitudes. For example, wind speed at 80 m increases from 8 m s^{-1} to around 11 m s^{-1} (see Figure **3-2**) under stronger surface cooling, which translates to a 160% power increase. At the same time, wind shear increases significantly as SBL depth decreases. The shear exponent α in the conventional power-law relation $V(z) = V_r(z/z_r)^{\alpha}$ provides a measure of the strength of wind shear, where z_r and V_r are the reference height and wind

speed taken usually at hub height. In Figure **3-2**, a power-law relation is fitted to the wind profile across the rotor sweep area of the generic wind turbine between 40 and 120 m. Shear exponent values of 0.40 and 0.55 are found for the two cases, both exceeding the International Electronic Commission (IEC) specification value of 0.2 for wind turbine design (IEC 2005). The power-law relation also fails for the strong stability case in which a wind shear reversal occurs due to the presence of the LLJ at 100 m. Based on a one-year study in the Southern Great Plains, Smith et al. (2002) showed that turbine fault time at local wind farms is highly correlated with the wind shear exponent from midnight to early morning where stable conditions prevail. The predicted deviations from standard profiles can be important for wind energy applications.

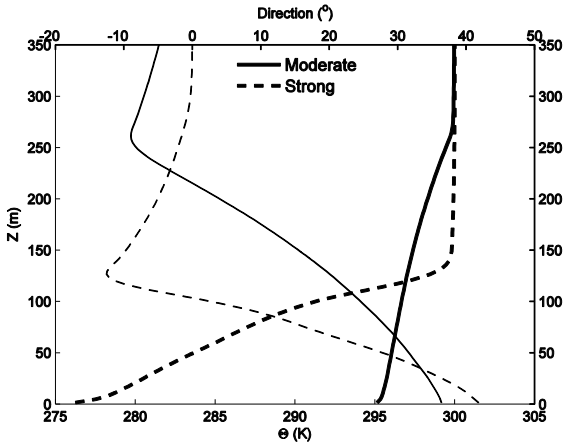

Figure 3-3 Horizontally and time averaged (between 42,800 and 50,000 s) vertical profiles of potential temperature and wind direction of the moderately and strongly stable cases. *Thick lines* represent potential temperature with the x-axis on the *bottom*; *thin lines* represent wind direction with the x-axis on the *top*

Wind direction also varies as SBL depth and stability change, as shown in Figure 3-3. As pointed out by Grisogono and Enger (2010), the angle between the near-surface and geostrophic wind vector can be an important parameter for meso-scale prediction models that do not resolve the atmospheric boundary layer. The simulated surface angle under moderate stability is around 35◦, which agrees well with previous numerical studies of Beare et al. (2006). In the strongly stable case, our simulation shows that the surface angle increases to 40◦. Both results agree well with the field observations of Van Ulden and Holtslag (1985) under their respective stability classes.

3.4.2 Vertical Shear Profiles

Besides power-law relations, empirical surface similarity formulations are also frequently used to predict wind speed and potential temperature under stable conditions. Monin–Obukhov (MO) surface similarity (Businger et al. 1971) is widely used to predict

dimensionless wind shear and temperature gradient as functions of the normalized height z/L, where L is the Obukhov length:

$$L = -\frac{\theta_s}{g}\frac{u_*^3}{\kappa \overline{w\theta}_s}$$

where $u*$ is the friction velocity, $w\theta$ is the heat flux, $\kappa = 0.41$ is the von Karman constant, $g = 9.81$ m s^{-2} is the gravitational constant and the subscript 's' denotes surface quantities. In Businger et al. (1971), κ was chosen to be 0.35 to fit observation data. This value has also been tested in the simulations. The change in κ shows little effect on the results and conclusions of this study. For wind energy applications, MO similarity must be used with caution under strong stability conditions for predicting wind at turbine heights. This is because MO similarity is valid only within a fraction of the surface layer. The Obukhov length L decreases as the surface heat flux becomes more negative. In our simulation, L is 86 m for the moderately stable case, and only 14 m for the strongly stable case, thus MO similarity theory should not be used to estimate wind speed above those heights.

A more general similarity formulation for the SBL is based on the dimensionless height z/Λ, where Λ is the local Obukhov length proposed by (Nieuwstadt 1984). Observational evidence (Hogstrom 1996) suggests a linear formulation of the stability functions ϕ_m and ϕ_h evaluated in terms of local fluxes:

$$\phi_m = \frac{\kappa z}{u_*}\frac{\partial \overline{\widetilde{U}}}{\partial z} = 1 + \alpha_m \frac{z}{\Lambda}, \quad \phi_h = \frac{z}{\theta_*}\frac{\partial \overline{\widetilde{U}}}{\partial z} = 1 + \alpha_h \frac{z}{\Lambda}$$

The analysis of Van de Wiel et al. (2008) demonstrated the physical relevance of z/Λ using an extended mixing-length argument that accounts for buoyancy effects.

Both ϕ_m and ϕ_h for the moderately and strongly stable conditions exhibit linear behavior near the surface (small z/Λ values) in Figure 3-4. The best linear fit to the near surface ϕ_m values gives an estimate of the slope α_m in Eq. 5-12, and is included in the figures. A slope of 4.5 for the moderate case in Figure 3-4(a) is consistent with the findings from the direct numerical simulations of Van de Wiel et al. (2008). For the strong case, a slope of 2.5 is found to best describe the simulation results. The surface layer depth represented by $z/L = 1$, as well as the 80 m hub height are marked for reference on the figures. Under moderate stability, ϕ_m and ϕ_h up to hub height can be very well described by a linear formulation. Under strong stability, the linear formulation also gives good approximations at heights even above the surface layer; however, the hub height extends beyond the scope of the figure, where the local similarity formulation is no longer applicable. Finally, notice that ϕ_h follows a milder slope than ϕ_m. The ratio of ϕ_h/ϕ_m is a turbulent Prandtl number, representing the relative efficiency of turbulent transfer of heat vs. momentum. In both the moderately and strongly stable cases, ϕ_h/ϕ_m is found to be around 0.7, consistent with the field measurements of Businger et al. (1971).

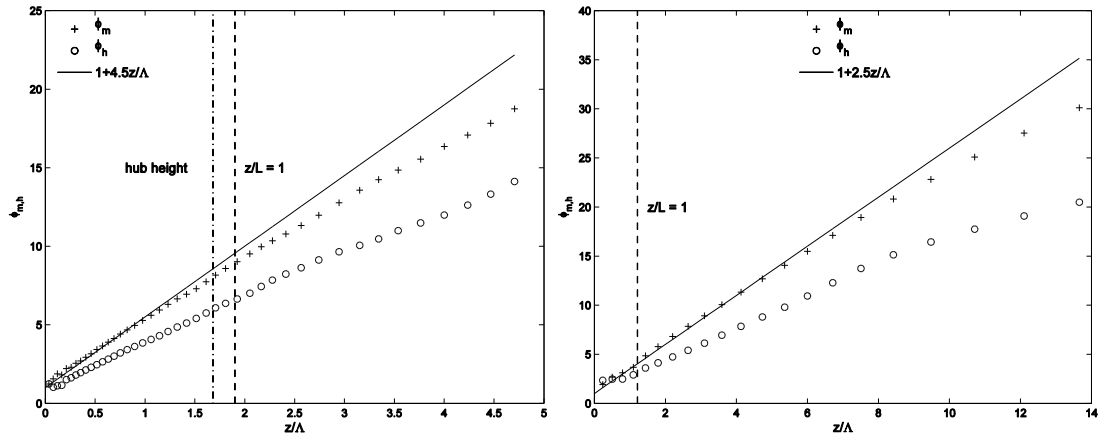

(a) (b)

Figure 3-4 Horizontally and time averaged (between 42,800 and 50,000 s) dimensionless shear and temperature gradient for the (a) moderately, (b) strongly stable conditions. *Dashed line* indicates the height where *z/L* = 1, *dash-dotted line* indicates hub height. Data points include the lower 70% of the SBL depth (the lower 130 m and 70 m)

3.4.3 Turbulence and Spectra

In the SBL, the turbulence length scale is primarily limited by buoyancy away from the near-surface region. To quantify the strength of stratification, we compute a characteristic length scale of buoyancy, the Ozmidov scale $L_o = \epsilon^{-1/2} N^{-3/2}$. In the LES setup, ϵ is the total dissipation of TKE, which is estimated by the net loss of energy from the resolved field, and *N* is the buoyancy frequency. Ozmidov scales of 7 and 3 m are found at half the boundary layer depth for the moderately and strongly stable cases. The difference in turbulence length scales is reflected in the slice plots of the resolved vertical velocity in Figure 3-5 (turbine blades would cover the region between 40 and 120 m). The structures of $\widetilde{w}$ are finer and exhibit more spatial variations for the strongly stable case. In contrast, larger structures, some of which occupy nearly 3/4 of the vertical length of the generic turbine blade zone are found in the moderately stable case. The magnitude of the vertical velocities decreases with stronger stratification as expected.

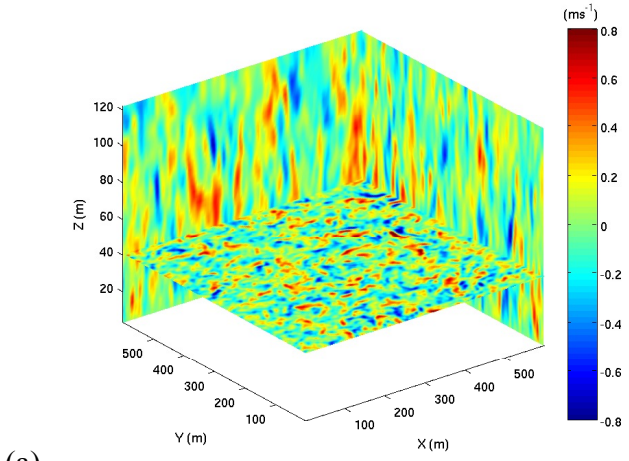

(a)

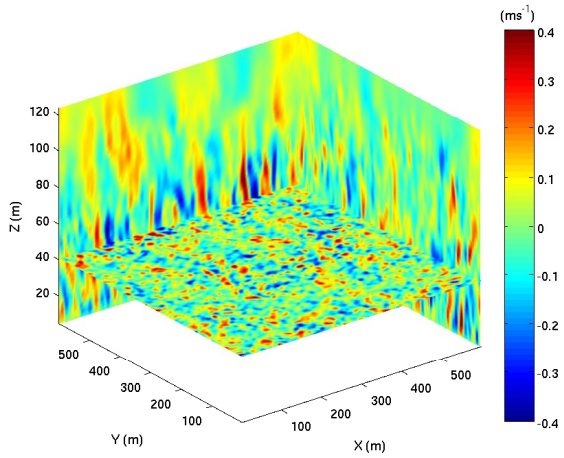

(b)

Figure 3-5 3D slices of the vertical velocity at 50,000 s under (a) moderately and, (b) strongly stable conditions

It is worth noting that part of the region of interest, between 80 and 120 m, extends beyond the SBL depth (~100 m) in the strongly stable case (recall Figure 3-2 and Figure 3-3). The shallow SBL depth explains the absence of significant vertical motions above 80 m in Figure 3-5(b). Another consequence of a shallow SBL is the reversal of the vertical shear, defined as $\partial\overline{\widetilde{U}}/\partial z$, where $\overline{\widetilde{U}}$ is the wind speed. In Figure 3-6(b), the vertical wind shear changes sign from positive below the LLJ to negative above. Vertical shear above the LLJ is relatively uniform due to the strong temperature inversion. The magnitude of vertical shear at 40 m for the strong case is also larger than in the moderate case presented in Figure 3-6(a).

At the generic turbine hub height of 80 m, vertical motions show more spatial variations in the moderate than the strong cooling case, as presented in Figure 3-7. This is contrary to the slice plots at 40 m on the x-y plane in Fig. 5, where the scale of vertical motions is finer due to a smaller buoyancy length for the strong case. The lack of variations in the strong case can again be explained by the shallow SBL depth h. When

normalized by the SBL depth, the 80 m hub height is at $z/h = 0.8$ for the strong case. As we approach the nose of the LLJ ($z/h = 1$), the vertical shear decreases significantly, resulting in relatively quiescent atmospheric conditions. Occasional turbulent bursting events, however, can completely alter the picture, as explained in the following subsection.

At the generic turbine hub height of 80 m, vertical motions show more spatial variations in the moderate than the strong cooling case, as presented in Figure 3-7. This is contrary to the slice plots at 40 m on the x-y plane in Figure 3-5, where the scale of vertical motions are finer due to a smaller buoyancy length for the strong case. The lack of variations in the strong case can again be explained by the shallow SBL depth h. When normalized by the SBL depth, the 80 m hub height is at $z/h = 0.8$ for the strong case. As we approach the nose of the LLJ ($z/h = 1$), the vertical shear decreases significantly, resulting in relatively quiescent atmospheric conditions. Occasional turbulent bursting events, however, can completely alter the picture, as explained in the following subsection.

The streamwise normalized 1D energy spectrum is presented in Fig. 8 at the hub height (80 m), as well as the top and bottom tip of the blades (40 and 120 m). An inertial subrange is resolved at all three heights for the moderate cooling case. For the strong case, we do not observe the $-5/3$ region at 80 and 120 m due to both the weak turbulence intensity, and the extremely small buoyancy length scale compared to the grid spacing, right below and above the LLJ. The spectrum shows more energetic motions at all scales for the moderate cooling case, which confirms the observations made from the magnitude of vertical motions discussed above.

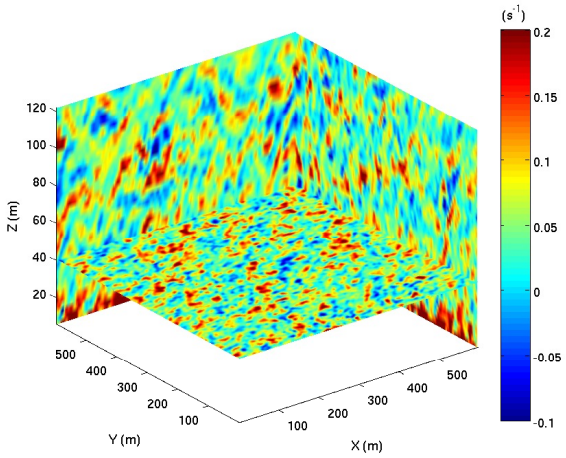

(a)

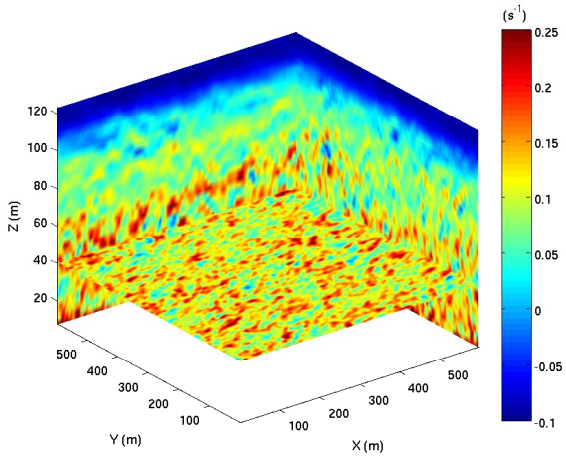

(b)

Figure 3-6 3D slices of the vertical shear at 50,000 s under (a) moderately and, (b) strongly stable conditions

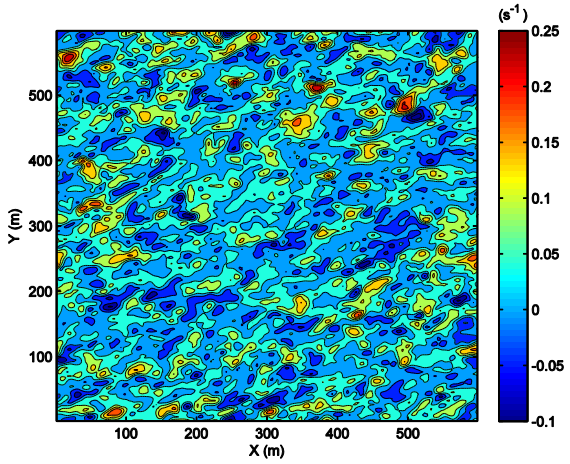

(a)

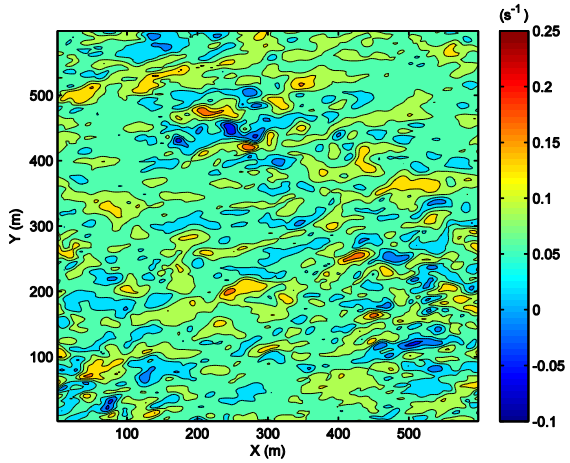

(b)

Figure 3-7 3D Contours of the vertical shear at 50,000 s in the horizontal x-y plane at 80 m AGL, under (a) moderately stable conditions, with maximum and minimum values of −0.10 and 0.25 s^{-1}, (b) strongly stable conditions, with maximum and minimum values of −0.05 and 0.2 s^{-1}. Contour levels are separated by 0.05 s^{-1}

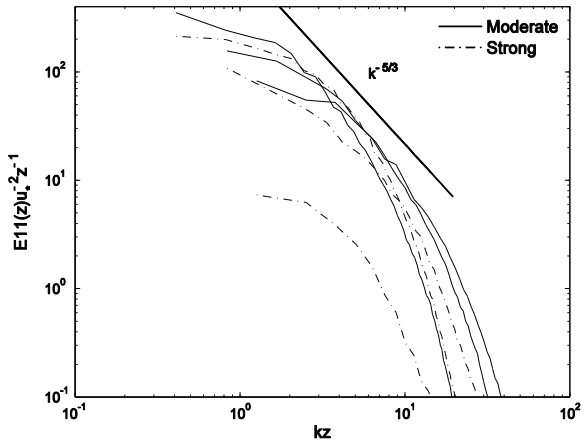

Figure 3-8 Streamwise normalized 1D energy spectrum for moderately and strongly stable conditions. *Curves* starting from *left* to *right*, *top* to *bottom* are plotted at 40 m, 80 m and 120 m, and time averaged from 40,000 to 50,000 s

3.4.4 Intermittent turbulence and bursting events

Strongly stable conditions together with weak mesoscale forcings often lead to intermittently turbulent flows. Intermittency can be identified qualitatively by looking at time series of turbulent quantities like turbulent kinetic energy, presented in Figure 3-9. Turbulent velocities are recorded at 12 points from 10 to 120 m at 10 m intervals in the model domain, to represent what might be seen by a meteorological tower with sonic anemometers at different heights. The turbulent kinetic energy is computed by $e = \frac{1}{2}(u'^2 + v'^2 + w'^2)$, where u', v', and w' are the fluctuating components of time-detrended velocities. This definition is adopted to be consistent with measurements from field experiments. In Fig. 9, we observe extended periods when *e* is suppressed. This is more significant at higher elevations approaching the LLJ nose at 100 m. These extended periods are much longer than the time scale of the largest eddies, which can be roughly estimated by $h/\sqrt{e}$, in this case about 300 s at 80 m, where h is the boundary layer depth. In between quiescent periods there are large increases of *e* over a relatively short time scale. For example, at the 80 m hub height, strongly turbulent episodes are observed between 48,000 to 50,000 s, 54,000–55,000 s, as well as 57,000–58,000 s. The magnitude and duration of these episodes decrease in time due to a shallower boundary layer as surface cooling continues. The magnitude of *e* also depends strongly on the elevation above the ground. More energetic motions are observed at lower elevations, while above the LLJ (100 m), *e* mostly decreases with time.

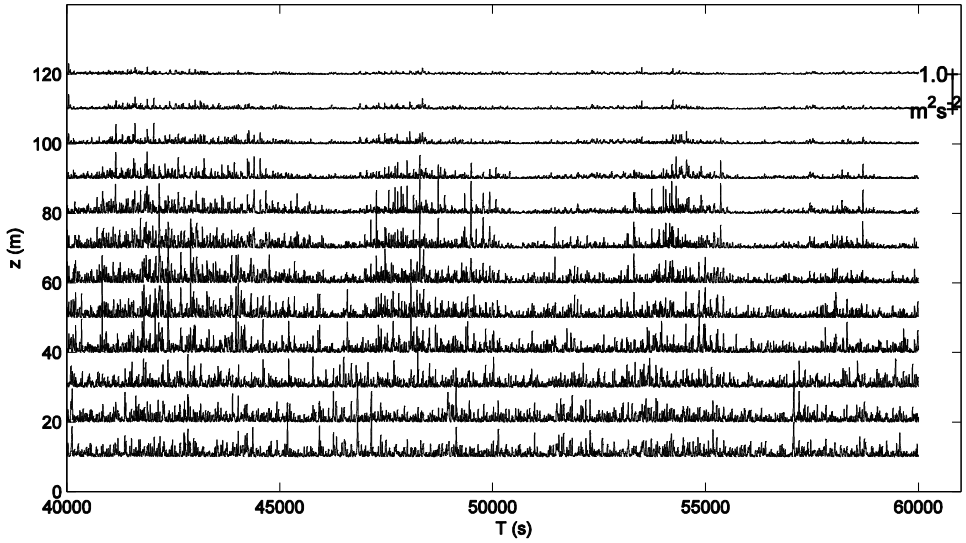

Figure 3-9 Time series of $\boldsymbol{e} = \frac{\mathbf{1}}{\mathbf{2}}(\boldsymbol{u'^2} + \boldsymbol{v'^2} + \boldsymbol{w'^2})$ between 40 m to 120 m sampled at 4 Hz, for the strongly stable conditions

To quantitatively describe intermittency, we adopt the approach used by Coulter and Doran (2002). They took measurements of 1-min averaged vertical heat fluxes $\overline{w'\theta'}$ obtained from sonic anemometer data during the CASES-99 field campaign, and sorted them in ascending order (from most negative to positive) within one night. They defined an "intermittency fraction" as the fraction of time which makes up the first 50% of the cumulative heat flux. Intermittency fractions as low as 17% were reported by Coulter and Doran (2002), meaning that 50% of the cooling was accomplished in short bursts of strong cooling that took only 17% of the time. The cumulative distribution curve for sorted heat flux for the strongly stable case is presented in Figure 3-10. A 5-min time averaged heat flux is used here to smooth out some positive heat flux values. Data at quasi-steady state from 40,000 to 60,000 s are used to generate the distribution curve at different elevations. The thick gray line represents a continuously turbulent theoretical scenario where 50% of the total cooling is achieved in 50% of the time. In the strong cooling case, the intermittency fraction decreases from around 30% at 40 and 60 m, to around 25% at 80 m, and further down to 20% at 100 and 120 m. The values agree well with observations from Coulter and Doran (2002). The decrease of intermittency fraction with increasing height suggests more intermittently turbulent flow at higher elevations, which is consistent with the qualitative observations made from Figure 3-9.

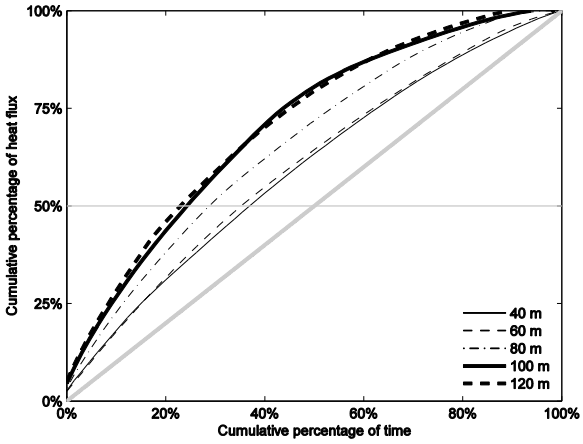

Figure 3-10 Cumulative distribution of 5-min averaged sensible heat flux between 40,000 and 60,000 s, for the strongly stable conditions

Contours of the horizontally averaged resolved TKE ($\frac{1}{2}(<\widetilde{\overline{u}}_i\widetilde{\overline{u}}_i> - <\widetilde{\overline{u}}_i><\widetilde{\overline{u}}_i>)$ are presented in Figure 3-11, where <> denotes horizontal averaging. The same intermittency pattern observed from point measurements is also present with the horizontally averaged quantities. This suggests that these turbulent bursting events occur over much of the horizontal extent of the domain (640 m). The same pattern is also present in the heat flux contour (not shown).

Intermittency observed in our simulations can be explained by the interaction between turbulence and mean shear. Such a mechanism is explained in Van de Wiel et al. (2002) with a zero-dimensional model, and confirmed in the CASES-99 field (Van de Wiel et al. 2002(b); Van de Wiel et al. 2003). The gradient Richardson number *Ri* is the key dimensionless quantity that the argument is based on.

$$Ri = \frac{\frac{g}{\overline{\widetilde{\theta}}}\frac{\partial\,\overline{\widetilde{\theta}}}{\partial\, z}}{\left[\left(\frac{\partial\,\overline{\widetilde{u}}}{\partial z}\right)^2 + \left(\frac{\partial\overline{\widetilde{v}}}{\partial \mathrm{z}}\right)^2\right]}$$

Large *Ri* values suggest weak turbulence, while small *Ri* values suggest continuous turbulence. The critical Richardson number when laminar flow becomes turbulent is 0.25 (Miles 1961). This theoretical threshold value is derived based on linear stability analysis and should be treated only as a reference value in real atmospheric flows. Ten-minute averaged *Ri* and the mean shear *S* presented in Figure 3-12 are used here to explain one of the bursting events around 53,000 s at the hub height (80 m).

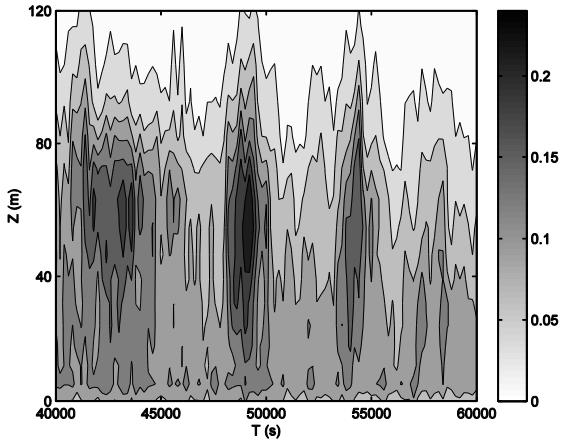

Figure 3-11 Horizontally averaged contours of resolved TKE for the strongly stable conditions. The TKE contour levels are separated by 0.03 $m^2 s^{-2}$

Starting from 50,000 s, Figure 3-12(b) shows that *Ri* is around 0.45, indicating rather weak turbulence. This is also reflected in the low TKE *e* values in Figure 3-9 at 80 m. Under such conditions, the vertical turbulent transport of momentum is strongly suppressed. As a result, flow in the upper portion of the SBL no longer "feels" the existence of the surface, and accelerates under the geostrophic forcing. In contrast, flow in the near surface region is retarded by surface friction, and balanced by the geostrophic wind. The net result is a continuous increase of vertical shear *S* from 50,000 s onwards, as shown in Figure 3-12(a). As vertical shear grows stronger, *Ri* decreases until eventually turbulence is triggered and upsets the previously quiescent conditions. Around 53,000 s, when *Ri* is around 0.3, a turbulent bursting event takes place (see Figure 3-9). The upper and lower portions of the SBL "reattach" through turbulent mixing. The mean shear is quickly smoothed by turbulent momentum exchange. Finally, *Ri* increases again as *S* decreases, suppressing turbulence, and the whole cycle repeats. It is encouraging to note that Nakamura and Mahrt (2005) also reported *Ri* values of 0.4 and 0.3 before and after turbulent bursting events from field observations, which agrees well with our simulation results. The exact threshold value *Ri* to characterize intermittency in the SBL remains an open question, requiring more detailed field measurements.

During a turbulent bursting event, the Reynolds stress field ($u'w', v'w', u'v'$) can develop coherent patches of turbulence containing a broad range of frequencies. Excitation of the inherent modal responses in the turbine rotor as well as the supporting structure could lead to large load excursions and subsequently fatigue damage (Kelley et al. 2000). Following the procedures outlined in Kelley et al. (2000), we perform continuous wavelet transform analysis (using the Morlet wavelet) of the Reynolds stress at 80mhub height to show the development of turbulent structures at the onset of the bursting event starting at 53200 s. Time series of the off-diagonal terms of the Reynolds stress are presented in Figure 3-13(a). Large variations in the stress components develop after about 80 s. In Figure 3-13(b), Reynolds stresses are quantitatively broken down into wave forms that are localized both in time and frequency. Red areas indicate frequency

bands that contain high values of stress energy, and blue areas indicate low values of stress energy. Figure 3-13(b) shows that cyclic wave frequencies between 0.25 to 1 Hz are excited from 80 s onwards. Taking the CWE300 Turbine used in Kelley et al. (2000) for example, the rotor's 1st bending modal response (between 0.234 to 0.469 Hz for symmetric flap bending, and 0.469–0.938 Hz for asymmetric lag bending) could be excited during this bursting event, leading to possible rotor fatigue. Kelley et al. (2000) also found Reynolds stresses containing excitations of this frequency range in the field data, under stable conditions.

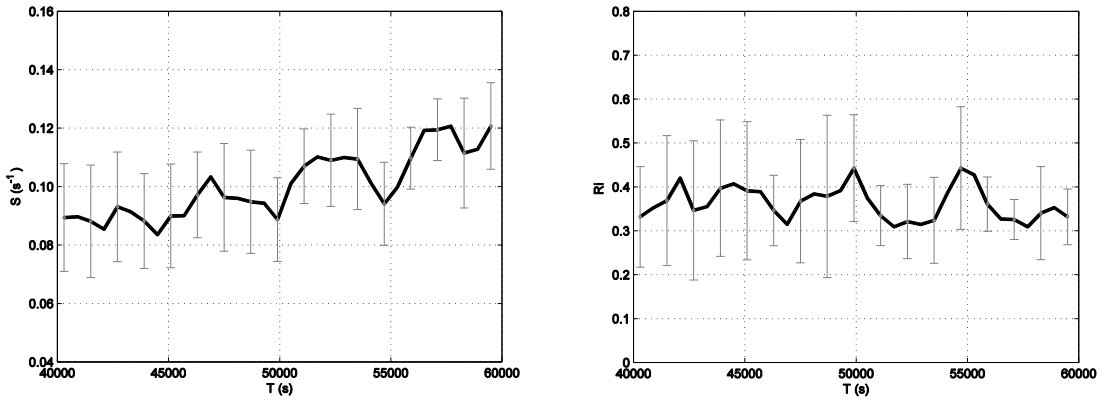

(a) (b)

Figure 3-12 10-min averaged time series of (a) strain rate *S*, (b) gradient Richardson number *Ri*, at 80 m hub height for the strongly stable conditions. Error bars are standard deviations for every 10-min interval, indicating that the range of the fluctuations in *Ri* and *S* varies with time

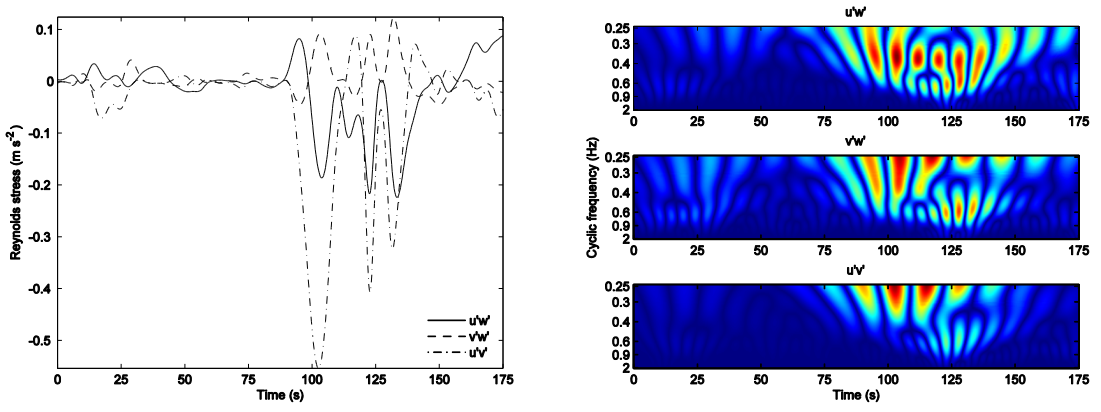

(a) (b)

Figure 3-13 Time series of (a) Reynolds stress components, (b) wavelet analysis of the Reynolds stress components at the onset of a bursting event from 53,200 s, at 80 m hub height

3.4.5 SFS Dissipation and Backscatter

The subfilter scale (SFS) dissipation is defined as $\Pi = -\tau_{ij}S_{ij}$, and represents the energy transport between resolved scales and subfilter scales. Closure models with eddy viscosity assumptions are absolutely dissipative in general, since $\Pi = \nu_T|S|^2$ unless negative eddy viscosity ν_T is allowed. In practice, negative eddy viscosity values cause numerical instability, so even dynamic eddy viscosity closures are almost entirely dissipative. In contrast, field experiments designed to mimic an LES setup (Carper and Porte-Agel 2004) found a non-Gaussian distribution of Π with significant portions of negative values, which is known as the backscatter process. SFS backscatter represents the merging of fine scale motions into large resolved scales.

In contrast to conventional eddy-viscosity models, the DRM closure is capable of predicting backscatter in the SBL simulations. In Figure 3-14, the normalized probability density function (PDF) of SFS dissipation rate Π is calculated at five different heights in the region of interest. PDFs are computed with a Gaussian kernel estimation technique. Negative values of Π normalized by the standard deviation σ_Π represent backscatter, while positive values represent dissipation. In the strong cooling case, PDFs of Π at all 5 vertical elevations show significant amounts (around 50%) of backscatter. The backscattering process in the DRM models is a result of including the RSFS stresses, which can be viewed as a scale similarity model that naturally allows backscatter.

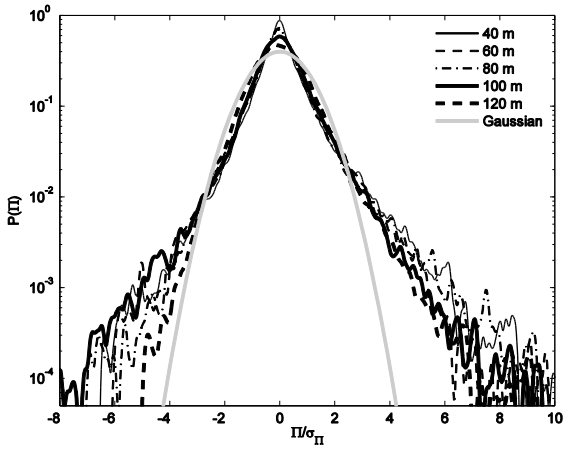

Figure 3-14 Normalized probability density function (PDF) of SFS dissipation rate $P(\Pi)$ between 40,000 and 60,000 s, at five vertical levels, for the strongly stable conditions

3.5 Summary

To achieve optimum turbine micro-siting, obtain reliable estimates of wind resources, and prevent rotor damage and fatigue, accurate predictions of wind speed and turbulence in the near-surface boundary layer are required. This study performed LES of the stably-stratified atmospheric boundary layer using the explicit filtering framework and dynamic reconstruction turbulence model of (Chow et al. 2005). A quasi-steady state SBL was simulated under both moderate and strong surface cooling, to mimic conditions of

overcast nights with strong winds, and clear nights with weak winds. A generic wind turbine with a hub height of 80 m was used here to illustrate flow features of interest in this region of the boundary layer.

Simulations show a decrease of boundary layer depth as stronger surface cooling is applied. As a result, the shear exponent in a power-law wind speed fit increased from 0.40 to 0.55, both of which are much larger than the existing IEC standard of 0.2 for wind turbine design. This supports the observed high positive correlation between turbine fault time and shear exponent at wind farms in the Midwest region of the US (Smith et al. 2002), suggesting that better guidelines are required for turbine design and operation under stable stratification. Wind speed predictions based on similarity formulations do account for the effects of stratification; however, the slope and the range of applicability of the "log-linear" type similarity formulations depend on the stratification strength, and should be applied with caution.

Turbulence statistics were examined for two stability cases with continuous and intermittent flows. The length scale of "large eddies", primarily limited by buoyancy stratification, decreases with increasing stability. The same is true for the magnitude of vertical motions. Since the strong cooling case develops a quite shallow boundary layer, part of the generic wind turbine considered extends beyond the SBL. Field data from CASES-99 even show cases where the entire wind turbine could be sitting above the SBL. While operating conditions might seem ideal near and above the top of the SBL because of the strong winds from the low-level jet and suppressed turbulence due to decreased shear, intermittent turbulence with sporadic bursting events in the sub-jet as well as above-jet regions can occur. Although bursting events typically exist for less than 20% of the nighttime period, these energetic motions account for more than 50% of the turbulent mixing in the SBL, and are potential hazards for wind turbines. The intermittency mechanism in this study is found to be due to turbulence and vertical shear interactions, a frequently observed mechanism in the field. The threshold Ri distinguishing intermittency and continuous turbulence is found to be between 0.3 and 0.4 in this LES study. The exact value is undetermined, and requires further field observations.

In conclusion, we have demonstrated the ability of the explicit filtering and dynamic reconstruction models to successfully simulate the boundary layer under stable conditions. LES with DRM is capable of covering a wide range of stability conditions, extending into the intermittent turbulence regime where traditional LES closures usually fail. The approach described has the advantage that almost any existing SGS model can be adapted to an explicit filtering and reconstruction framework. This is achieved most simply by adding a scale similarity component (RSFS) to existing SGS closures (see Chow et al. (2005); Chow and Street (2009)). Using LES with DRM closures as a tool for SBL simulations, we expect that wind power production could be maximized by providing accurate vertical wind speed profiles. Turbine fatigue and fault time could be minimized by predicting potentially high shear and turbulence events around turbines.

Chapter 4 Nested Large-Eddy Simulations of the Intermittently Turbulent Stable Atmospheric Boundary Layer over Real Terrain

Abstract

The nighttime stable atmospheric boundary layer over complex terrain is modeled with nested high-resolution large-eddy simulations (LES). The field site is located near Leon, Kansas, where the Cooperative Atmospheric-Surface Exchange Study – 1999 field program took place. The terrain is mostly flat with an average slope of 0.5o. The main topographic feature is a shallow valley oriented in the east-west direction. The night of Oct 5-6 is selected to study intermittent turbulence on a strongly stable night with prevailing quiescent conditions, except for brief turbulent periods triggered by shear-instability waves. A major turbulent event is modeled with good magnitude and temporal precision with a sophisticated turbulence closure. In comparison, conventional closures fail to excite turbulent motions, and predict a false laminar flow. A new intermittency mechanism, previous unknown due to limited spatial coverage of field instruments, is unveiled with LES. Intermittent turbulent events are shown to be through gravity wave breaking over a stagnant cold-air bubble in the valley upwind of the main tower. The bubble is preceded by the formation of a valley cold-air pool due to down-valley drainage flows during the evening transition. The cold-air bubble grows in depth by entraining cold down-valley and down-slope flows from below, and is eroded by inflection point induced shear-instability waves on the top. The cyclic process of formation and erosion is repeated during the night, leading to sporadic turbulent bursting.

4.1 Introduction

After sunset, the atmospheric boundary layer becomes stably stratified due to out-going long-wave surface radiation. Buoyancy stratification limits turbulent motions, and allows gravity waves to form. The level of turbulence in the stable boundary layer (SBL) is determined by the competing forcings of shear and buoyancy. Depending on their relative strength, the SBL falls into the continuously turbulent regime dominated by shear production, the quiescent regime dominated by buoyancy destruction, or the intermittent regime where both forcings are important (Stull 1988).

Intermittency in the atmosphere is characterized by buoyancy-suppressed turbulence over prolonged periods greater than the time scale of the dominant eddies (Nakamura and Mahrt 2005). It is characterized by energetic mixing events occurring over relatively short periods, known as turbulent bursts. Turbulence in the SBL is often intermittent, especially on clear nights with weak winds. Both factors contribute to a shallow layer of cold air confined to the surface, because strong stratification and low shear suppress upward mechanical mixing. This is referred to as boundary layer decoupling over cold surfaces (Derbyshire 1999). Under these circumstances, sporadic bursts of turbulence can

re-couple the surface layer with the atmosphere above; these bursts are responsible for the majority of the upward/downward transport of heat and momentum.

Several types of atmospheric disturbances are known to trigger intermittent turbulent mixing in the SBL. These include turbulence and mean shear interactions (Nakamura and Mahrt 2005), breaking gravity waves and KH billows (Blumen et al. 2001), terrain-induced drainage flows (Whiteman et al. 2009), and propagating density currents (Sun et al. 2004). Note that none of these disturbances are sufficient conditions for turbulence. Often times, under very stable conditions, referred to as vSBL by Mahrt (1998), disturbances may pass through, barely affecting the SBL structure (Banta et al. 2007).

During the Cooperative Atmospheric-Surface Exchange Study – 1999 (CASES-99) (Poulos et al. 2002), shear-instability waves were observed for a brief period of approximately 30 minutes on the night of Oct 5-6, 1999 (Blumen et al. 2001). The billows were at an elevation of ~40 m above ground level (AGL), had wavelength of ~350 m, and propagated with a phase speed of 5.25 ms^{-1} in the north-south direction. Newsom and Banta (2003) (hereafter NB03) associated an inflection point in the mean wind profile with the onset of the billows. They pointed out that the increase in vertical shear was due to a slowing down of the flow from below. The cause of this flow retardation remained an open question due to the limited spatial coverage of field equipment.

Motivated by the puzzle, this paper sets out to investigate this event, in the hope of advancing the understanding of intermittency from wave-generated turbulence. With a numerical modeling approach, we attempt to reconstruct a complete 3D history of the formation, evolution, and breaking of the shear-instability waves.

In the past decades, turbulence-resolving numerical simulations have been used extensively to study the characteristics of the SBL flows. Those include mostly direct numerical simulations (DNS) (Coleman et al. 1992; Shih et al. 2000; Chung and Matheou 2012), and large-eddy simulations (LES) (Saiki et al. 2000; Kosovic and Curry 2000; Jimenez and Cuxart 2005; Basu and Porté-Agel 2005; Beare et al. 2006; Zhou and Chow 2011). Although DNS resolves down to the Kolmogorov scale, requiring no turbulence closure, its usefulness is limited by computational resources to a tiny spatial fraction of the turbulent atmospheric boundary layer (ABL). In comparison, LES is more advantageous for ABL flows, because it separates the large-scale energy-containing eddies from the smaller ones based the definition of a spatial filter. While the former are explicitly resolved, the latter are represented by a subfilter-scale (SFS) model.

Most of the past LES studies of the ABL were performed under idealized conditions with flat terrain, prescribed forcings, and periodic lateral boundaries. LES of the SBL is further limited to weak or moderate stability under conditions of either high geostrophic pressure gradients or low surface cooling rates. This is because as stratification strengthens, turbulent motions are constrained by a reduced buoyancy length scale, requiring finer grid resolution. For moderate stability, Beare et al. (2006) suggested a grid resolution of 6.25 – 12.5 m to sustain resolved turbulence. Therefore, LES of the vSBL soon becomes prohibitive due to overwhelming computational resource requirements.

Modeling the strongly stable regime is further complicated by physical mechanisms such as surface-decoupling (Derbyshire 1999) and intermittency-associated quiescent to

turbulent flow transitions (Jimenez and Cuxart 2005). Beare et al. (2006) pointed out the conundrum of eddy viscosity formulations (corrected empirically through the Richardson number) that struggle to balance numerical stability (favoring long-tail functions) and physical reality (requiring short-tail functions). Furthermore, Zhou and Chow (2011) demonstrated another insufficiency in eddy-viscosity closures. Those models generally do not allow backscatter of turbulent kinetic energy (TKE) from the SFS to the mean flow, which has been shown to be a physical process in the SBL (Carper and Porté-Agel 2004).

A few studies have been performed in the strongly stable regime to model intermittent turbulence. Van de Wiel et al. (2002) simulated an intermittent SBL with a box model, utilizing a stability function that cuts off turbulent mixing beyond a critical Richardson number. Costa et al. (2011) used a single column model coupled to a land-surface model, to show periodic turbulent bursts in the decoupled surface layer. Chung and Matheou (2012) performed DNS of a stratified sheared turbulence in a triply periodic domain, revealing turbulence collapses and formation of intermittent laminar and turbulent layers. Zhou and Chow (2011) performed idealized LES of the SBL across moderate to strong stability conditions with an advanced turbulence closure, which is the dynamic reconstruction model (DRM). They showed that by improving the subfilter-scale (SFS) representation of turbulence, the working range of LES can be extended to stronger stability at lower grid resolution requirements. They also showed good agreement of the DRM results with empirical SBL formulations (Businger et al. 1971; Sorbjan and Grachev 2010).

This work is part of the effort towards moving LES of the ABL out of the idealized box to the physical world with complex terrain. Simulations start off on a meso-scale domain, obtaining realistic initial states and lateral forcings from a reanalysis field, then successively nest down to a micro-scale grid where turbulence resolving LES is performed. Due to the wide span of grid spacing (6400 m to 25 m) used in this nested LES study, crossing regimes of "*Terra Incognita*" is inevitable. *Terra Incognita* is a numerical gray zone where the grid spacing is comparable to the dominant length scale of the flow (Wyngaard 2004). The nighttime *terra incognita* has been conventionally thought to be at the buoyancy length scale O(~10 m), hence has received little attention compared to the daytime counterpart, which is the convective length scale O(~ 1 km). In this study, we show SBL *terra incognita* at a much larger length scale set by gravity waves, and briefly explore related model errors.

4.2 General Description of IOP2 during CASES-99

In the last few decades, a number of field campaigns were, fully or in part, devoted to studying the SBL. Those include the Stable Boundary Layer Experiment in Spain (SABLES) (Cuxart et al. 2000), the Cooperative Atmospheric-Surface Exchange Study – 1999 (CASES-99) (Poulos et al. 2002), and the Meteorological Experiment in Arizona's Meteor Crater (METCRAX) (Whiteman et al. 2008), and the Terrain-Induced Rotor Experiment (T-REX) (Vanda Grubisic et al. 2008). Among them, CASES-99 represents the most extensive field effort on the SBL. It was conducted over the Great Plains of the United States near Leon, Kansas, from October 1-31, 1999. The local terrain is relatively

flat (average slopes are 0.5 degrees), has mostly homogeneous land cover (prairie grass), and lacks obstacles.

This study focuses on the night of Oct. 5-6, during the 2nd intensive observation period (IOP2). It was a clear night with relatively calm conditions at the surface. A low-level jet was observed with peak wind speeds around 10 ms^{-1} about 110 m AGL. A temperature inversion of 8 K over the lowest 70-80 m was established early in the night. Some basic meteorological variables from observations (Van de Wiel et al. 2003) are presented in Table **4-1**. According to the SBL classification by Van de Wiel et al. (2002; 2003), which is based on large-scale pressure gradients and net surface radiation, Oct. 5-6 is an intermittently turbulent night. Compared to a continuously turbulent night, e.g. Oct. 6-7, differences in turbulent quantities are vast. For example, the friction velocity, which is the dominant velocity scale in the surface layer, is nearly 6 times smaller on Oct. 5-6.

Table 4-1 Basic meteorological variables during the night of Oct 5-6 and Oct 6-7. Zi is the depth of the SBL, u* the friction velocity, Qnet the net radiation budget of the surface, and H the sensible heat flux. Values are from Van de Wiel et al. (2003).

Date	Time	U_{10m}	T_{10m}	T_s	Zi	u*	H	Q_{net}	Class
(-)	(LST)	(ms^{-1})	(K)	(K)	(m)	(ms^{-1})	(W m^{-2})	(W m^{-2})	(-)
6 Oct	0000-0600	2.82	285.16	281.41	75	0.075	-6.9	-61.7	Int.
7 Oct	0000-0600	6.40	288.80	286.57	145	0.438	-48.4	-71.2	Turb.

The sporadic nature of turbulence is also apparent from time series of thermocouple temperature measurements at the 60 m main tower in Figure **4-1**. The amplitude of temperature fluctuations was much smaller during IOP2 than the following night. A surface inversion existed on Oct 5-6, represented by an increase in temperature with height. In comparison, the surface layer was well-mixed on Oct 6-7, where temperature measurements at different heights are indistinguishable (Figure **4-1**(b)).

A period with rapid temperature fluctuations between 0530-0600 UTC stands out on in Figure **4-1**(a). The elevated turbulence was triggered by shear-instability waves as seen from lidar data. Figure **4-2** presents a vertical slice of radial velocity measured by the high-resolution Doppler lidar (HRDL) at 0531 UTC (see also the color Fig.1. of NB03). HRDL was located 1.45 km south of the main tower, and was performing shallow vertical scans at an azimuth of 10o pointing towards north. The HRDL scan revealed wavelike structures of wavelength $\lambda \sim 350$ m. More detailed observational analysis is given in NB03.

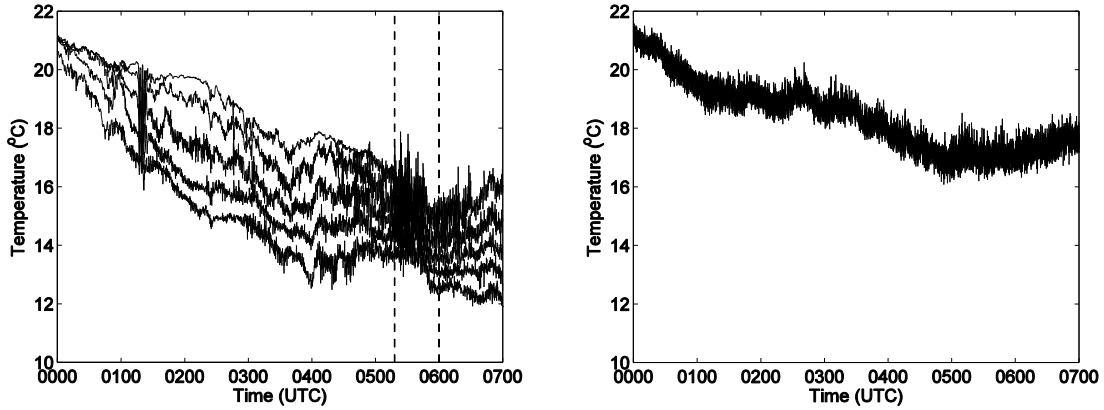

Figure 4-1 Time series of thermocouple temperature on (a) Oct 5-6 (IOP2) and (b) Oct 6-7. Data was measured at 11.3, 20.3, 29.3, 40.1, 50.9m AGL from bottom to top. On Oct. 6-7 the surface layer was well mixed so the lines overlap. Data are resampled at every 10s. The turbulent episode during IOP2 is enclosed by dashed lines.

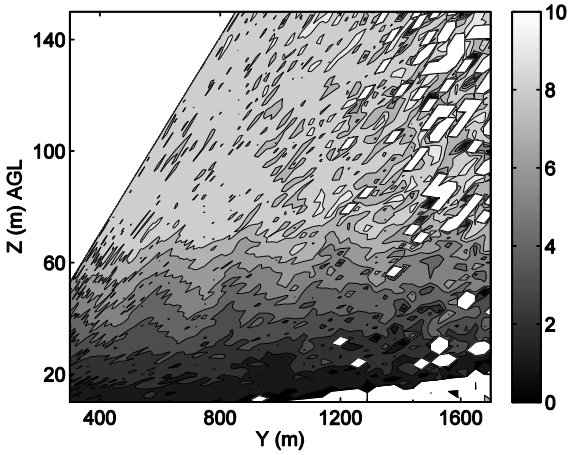

Figure 4-2 Vertical slice scans of radial velocity measured by HRDL (37.6360°N, -96.7339°W) at 0531 UTC. Positive radial velocities indicate flow away from the HRDL, white spots indicate missing data in the HRDL scan.

4.3 Model Configuration and Description

ARPS uses a terrain-following coordinate system on an Arakawa C-grid. Vertical grid stretching is applied to increase grid resolution near the surface. Fourth-order spatial differentiation is used for both momentum and scalar advection. A mode-splitting time integration scheme (Klemp and Wilhelmson 1978) is employed. This technique divides a big integration step (Δt_{big}) into a number of computationally inexpensive small times-steps (Δt_{small}) to update the acoustically active terms, while all other terms are computed once every big time-step.

4.3.1 General Description

ARPS uses a terrain-following coordinate system on an Arakawa C-grid. Vertical grid stretching is applied to increase grid resolution near the surface. Fourth-order spatial differentiation is used for both momentum and scalar advection. A mode-splitting time integration scheme (Klemp and Wilhelmson 1978) is employed. This technique divides a big integration step (Δt_{big}) into a number of computationally inexpensive small times-steps (Δt_{small}) to update the acoustically active terms, while all other terms are computed once every big time-step.

We simulate 10 h of the SBL starting from late afternoon (Oct 5, 2100 UTC/1600 LST) to past mid-night (Oct 6, 0700 UTC/0200 LST). Some important details of the model setup are given in Table 4-2. A total of six LES runs were performed on the finest 25 m grid. Those include three 10 h full runs initialized from the 128 m grid, and three 3 h partial runs restarted at 0400 UTC. Additional model parameters for the LES runs are listed in Table 4-3.

Table 4-2 List of nested simulation parameters.

Nest	Grid size[3] (nx, ny, nz)	Domain (km)	$\Delta x/\Delta y$ (m)	$\Delta z/\Delta z_{min}$ (m)	ΔT_b (s)	Δt_{big} (s)	Δt_{small} (s)	Grid levels below 200m
1	(103,103,63)	640x640x18	6400	300/50	10800	5.0	5.0	5
2	(195,195,103)	123x123x10	640	100/20	1800	1.0	1.0	11
3	(195,195,103)	24.6x24.6x2	128	20/4	900	0.5	0.1	27
4	(363,363,123)	9x9x1.2	25	10/2	180	0.025	0.025	70

Table 4-3 List of simulation parameters on the 25 m grid.

Run name	Lateral grid size (nx=ny)	Initial condition	SGS closure	RSFS Rec-level	T_{start} (UTC)
TKE	363	128 m grid	TKE-1.5	-	10/05-2100
DWL-ADM0	363	128 m grid	DWL	0	10/05-2100
TKE-S	201	128 m grid	TKE-1.5	-	10/05-2100
TKE-ADM1-R	363	TKE (25 m grid)	TKE-1.5	1	10/06-0400
DWL-R	363	TKE (25 m grid)	DWL	-	10/06-0400
DWL-ADM0-R	363	TKE (25 m grid)	DWL	0	10/06-0400

[3] Two ghost points are included in the number of grid points, so the domain size in the x direction, for example, is (nx-3)Δx.

4.3.2 One-way Nested Configuration

ARPS has a one-way grid nesting capability, i.e. the lateral boundary conditions (velocity, potential temperature, moisture, etc.) of a smaller inner-domain can be obtained from a larger outer-domain. The largest domain usually obtains its initial and lateral boundary conditions from reanalysis data. In this study, simulations are initialized with the North American Regional Reanalysis (NARR) on 32 km horizontal grids, and one-way nested down to a very fine grid with 25 m horizontal and 2 m near-surface vertical spacing. The nesting ratio, which is the ratio of horizontal domain sizes of two adjacent nests, is set to 5 to 1 in this study. The domain is centered the main tower location (35.6485^{o}N, 96.7361^{o}W). The innermost grid is nested with an approximately 3 to 1 ratio, and centered at (37.64^{o}N, 96.7361^{o}W), to include an important topographic feature (i.e. the entire width of the valley).

The lateral boundaries are updated at a constant time interval (ΔT_b) set by the user, and are linearly interpolated in between. Michioka and Chow (2008) demonstrated the importance of frequent boundary updates for inner domains. We followed a similar setup to Michioka and Chow (2008), using a small ΔT_b for different nests. For the finest domain, the lateral boundaries are updated every 180s. A lateral boundary relaxation zone of the Davies (1983) type is used to control numerical wave reflections. On the bottom boundary, high-resolution 1/3 arc-second (~10m) topography from the USGS National Elevation Dataset and land cover at 30m resolution from the National Land Cover Database 2006 are used to represent the complex terrain from the 640 m grid onwards. Terrain contours are plotted in Figure 4-3. A Rayleigh damping layer is set for roughly one third of the domain height from the top.

4.3.3 Turbulence Model

Following the recommendation of Xue et al. (1996), the boundary layer parameterization of Sun and Chang (1986) is used for the meso-scale grids at 6400 m spacing. The 1.5-order turbulent kinetic energy-based closure (TKE-1.5) of Moeng (1984) is used on all computational grids. In addition, the dynamic Wong and Lilly model (DWL) (Wong and Lilly 1994) and the dynamic reconstruction model (DRM) (Chow et al. 2005) are used on the 25 m LES grid to investigate model sensitivity to the turbulence closure.

The explicit filtering and reconstruction LES methodology is applied on the 25 m grid level. As previous studies have shown (Chow et al. 2005; Chow and Street 2009; Zhou and Chow 2011), explicit filtering and reconstruction greatly improves the SFS representation of turbulence on both flat and complex terrain. The reconstruction procedure is based on explicit filtering of the Navier-Stokes equations:

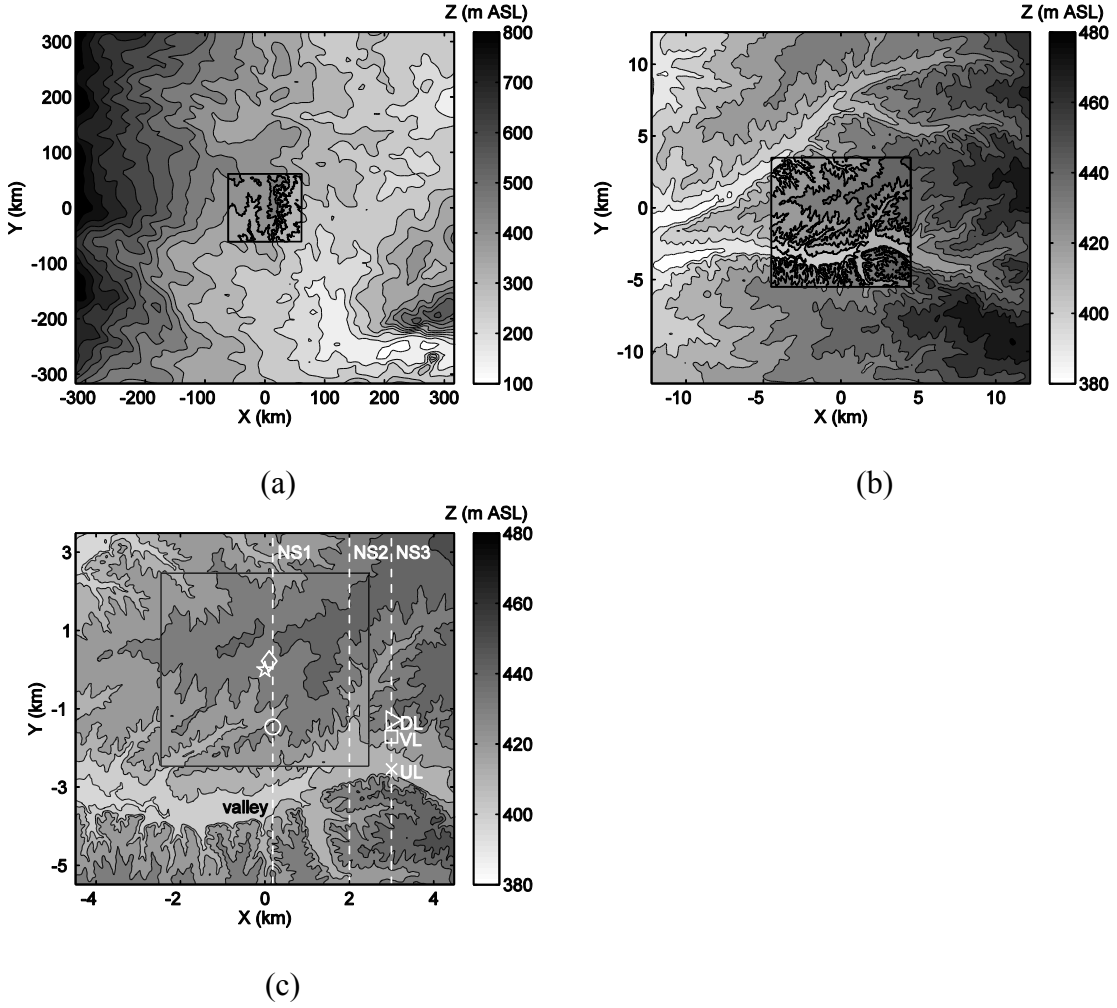

Figure 4-3 Elevation contours for (a) the 6400 m grid with the 640 m grid shown within, (b) the 128 m grid with the 25 m grid shown within, (c) the two 25 m grids, with the smaller domain marked by the solid lines within the larger one. Location of the tower is marked by a star, radiosonde by a diamond, lidar by a circle. Dashed line represents three north-south slices locations (NS1, NS2 and NS3). Three point locations along NS3 are marked by a cross for the upwind location, a square for the valley location, and a triangle for the downwind location. Contour intervals are 50 m for (a) and 10m for (b) and (c).

$$\frac{\partial \overline{\tilde{\rho}}\,\overline{\tilde{u}}_i}{\partial t} + \frac{\partial \overline{\tilde{\rho}}\,\overline{\tilde{u}}_i\,\overline{\tilde{u}}_j}{\partial x_j} = -\frac{\partial \overline{\tilde{p}}}{\partial x_i} - \overline{\tilde{\rho}}\,g\delta_{i3} + \overline{\tilde{\rho}}\epsilon_{imn}f_n\overline{\tilde{u}}_m - \frac{\partial \overline{\tilde{\rho}}\,\tilde{\tau}_{ij}}{\partial x_j}$$

$$\frac{\partial \overline{\tilde{\theta}}}{\partial t} + \frac{\partial \overline{\tilde{\rho}}\,\overline{\tilde{u}}_i\overline{\tilde{\theta}}}{\partial x_i} = -\frac{\partial \overline{\tilde{\rho}}\,\tilde{\chi}_i}{\partial x_i}$$

$$\frac{\partial \overline{\tilde{\rho}}}{\partial t} + \frac{\partial \overline{\tilde{\rho}}\,\overline{\tilde{u}}_i}{\partial x_i} = 0$$

where the explicit filter is denoted by a bar, and the implicit discretization operator by a tilde. $\overline{\tilde{u}_i}$ are the velocity components, $\overline{\tilde{p}}$ the pressure, $\overline{\tilde{\rho}}$ the density, f the Coriolis parameter, and $\overline{\tilde{\theta}}$ the potential temperature. We assume all filtering is with a Favre-type density weighted filter (details in Chow 2004). The moisture transport equation is similar to the potential temperature equation, and not presented here.

Traditionally, the discretization procedure is treated as an implicit filter based on the finite difference/volume methods. Implicit filtering can lead to truncation and aliasing errors in the nonlinear terms (Lund 1997). Explicit filtering can minimize the influence of truncation errors and has been shown to be beneficial in LES (Lund 1997; Gullbrand 2001; Carati et al. 2001; Winckelmans et al. 2001; Gullbrand and Chow 2003). In this study, a top-hat filter of width twice the grid spacing is applied. Due to the explicit filtering procedure, turbulent momentum and heat fluxes can be decomposed into resolvable subfilter-scale (RSFS) and SGS stresses:

$$\tau_{ij} = \overline{\tilde{u}_i \tilde{u}_j} - \overline{\tilde{u}}_i\,\overline{\tilde{u}}_j = \underbrace{\overline{\tilde{u}_i \tilde{u}_j} - \overline{\tilde{u}_i}\,\overline{\tilde{u}_j}}_{\tau_{SGS}} + \underbrace{\overline{\tilde{u}_i}\,\overline{\tilde{u}_j} - \overline{\tilde{u}}_i\,\overline{\tilde{u}}_j}_{\tau_{RSFS}}$$

$$\chi_i = \overline{\tilde{u}_i \tilde{\theta}} - \overline{\tilde{u}}_i\;\overline{\tilde{\theta}} = \underbrace{\overline{\tilde{u}_i \tilde{\theta}} - \overline{\tilde{u}_i}\,\overline{\tilde{\theta}}}_{\chi_{SGS}} + \underbrace{\overline{\tilde{u}_i}\,\overline{\tilde{\theta}} - \overline{\tilde{u}}_i\;\overline{\tilde{\theta}}}_{\chi_{RSFS}}$$

The SGS stresses are of scales finer than the grid resolution and must be modeled. The RSFS stresses depend on the resolved and explicitly filtered fields, and can be restored based on knowledge of the explicit filter. Reconstruction is performed through the approximate deconvolution method (ADM) of van Cittert (1931) and Stolz et al. (2001):

$$\tilde{u}_i = \overline{\tilde{u}}_i + (I - G) \star \overline{\tilde{u}}_i + (I - G) \star [(I - G) \star \overline{\tilde{u}}_i] + \cdots$$

where I is the identity operator, G the explicit filter, and $\star$ the convolution operator. The number of terms on the right hand side is referred to as levels of reconstruction. A truncated series of the above equation is used to approximate $\tilde{u}_i$. For example, with one level reconstruction (abbreviated as ADM0) $\tilde{u}_i \approx \tilde{u}_i^* = \overline{\tilde{u}}_i + (I - G) \star \overline{\tilde{u}}_i$, and $\tilde{u}_i^*$ is used in the RSFS terms. The RSFS model can be combined with most eddy viscosity closures, e.g. TKE-ADM, to improve model performance under the explicit filtering framework. When used with a dynamic SGS closure, e.g. DWL-ADM, the overall SFS representation is called the dynamic reconstruction model (DRM).

The RSFS-SGS model framework can be viewed as a mixed model (Bardina et al 1983; Zang et al. 1993). The RSFS component is the so-called scale-similarity term represented by reconstruction, and the SGS component is represented with an eddy-viscosity model. The original scale-similarity model of Bardina et al. (1983) assumed that the smallest resolved scales have a similar structure to the subfilter scales. The reconstruction model seeks a more accurate representation of the resolved scales by inverting the explicit filter operation. With higher levels of reconstruction, model details of high frequency motions approaching the filter cutoff are restored, thus improving the representation of the SFS stresses. In addition, the RSFS formulation term allows backscatter of energy from SFS to resolved scales. This is especially important for the transition from quiescent to turbulent flows in the SBL (Zhou and Chow 2011).

4.4 Model Evaluation

In this section, model results are validated with field measurements. Sensitivity to three key model parameters, grid resolution, turbulence closure, and nest domain, are evaluated. In the process, we describe some key flow features during IOP2.

4.4.1 Sensitivity to Grid Resolution

Figure 4-4 presents the vertical profiles of modeled wind speed, direction, potential temperature, and specific humidity at different grid resolutions. A log-scale y-axis is used to stretch the surface layer. Model results are in general agreement with radiosonde measurements. Significant improvements in the lowest few hundred meters are achieved starting with the 2nd nest level at 640 m horizontal resolution. The vertical profiles on the 128 m grid are similar to those on the 640 m grid. The 25 m grid results (DRM-ADM0) show improvements in the surface layer, mostly below 50 m AGL. For example, at 0259 UTC, near surface wind speed is reduced by nearly 2 ms^{-1} from the 128 m to the 25 m grid, better matching the observed values. The improvement is significant because the associated increase in vertical wind-shear, due to reduced surface winds, provides stronger mechanical mixing to sustain weak SBL turbulence.

Potential temperature θ is under-predicted by ~1 K below the daytime inversion layer (~700 m AGL) at 0000 UTC. Specific humidity q is slightly over-predicted. This error is due to initial and lateral boundary conditions from NARR. It is likely caused by errors in partitioning of sensible and latent heat fluxes. The under/over-estimation persists in the residual layer (RL) above the SBL throughout the simulation until ~0500 UTC. In the boundary layer, modeled θ is up to 2 K warmer below 50 m AGL. Steeneveld et al. (2008) reported similar model over-prediction of θ during strongly cooled nights during CASES-99. They proposed an alternative land-surface scheme to overcome such error by introducing a vegetation layer. In this study, we used ARPS' default 2-layer soil model (Noilhan and Planton 1989), and did not extensively explore model sensitivity to land-surface schemes. However, this error does not seem to affect the dynamics of the flow during the turbulence bursting event around 0600 UTC. By 0500 UTC, the model has caught up with the observed near-surface temperature (see bottom panel in Figure 4-4).

A low-level jet (LLJ) develops at ~110 m AGL around 0100 UTC. While the jet nose reaches 10 ms^{-1} at 0259 UTC according to radiosonde records, it is under-predicted by 2 ms^{-1} in the simulations. The maximum speed of the jet is determined by geostrophic pressure gradients. The under-prediction is again likely attributed errors in the NARR data. Wind directions veer (turn clockwise) with height, as a result of the Coriolis force. The angle between the geostrophic wind above the SBL and the surface wind is around 40^{o} at 0259 UTC. This value is expected for a strongly stable ABL (Van Ulden and Holtslag 1985). The turning is well-captured by the 25 m simulations.

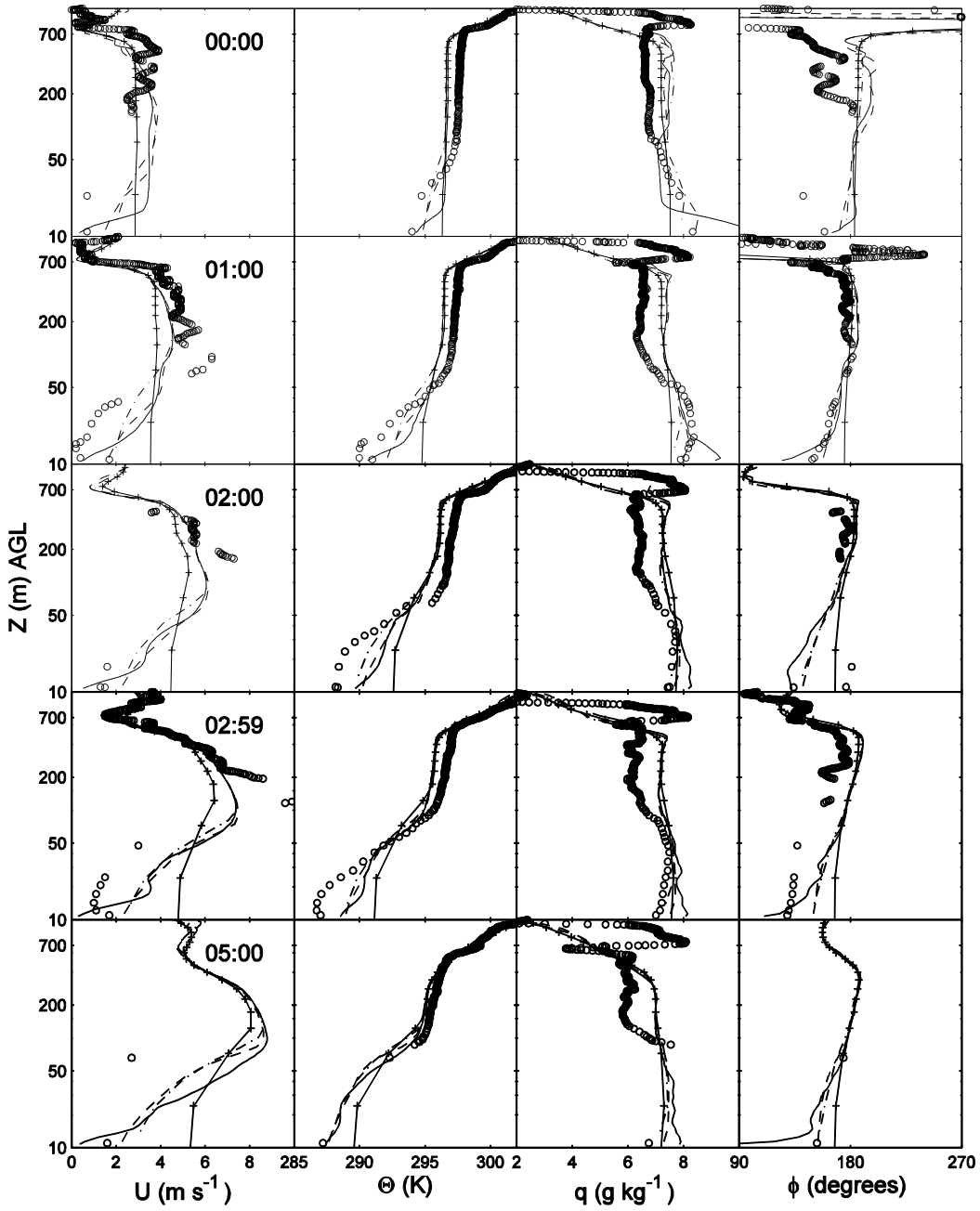

Figure 4-4 Radiosonde observations (circles) compared with 6400 m (solid line with plus signs), 640 m (dash-dotted line), 128 m (dashed line), and 25 m (DRM-ADM0, solid line) grid simulations at the Leon GLASS High Resolution Sounding site (37.6510^{o}N, 96.7350^{o}W), for wind speed, potential temperature, specific humidity and wind direction. Sounding launch times are given on the left panel.

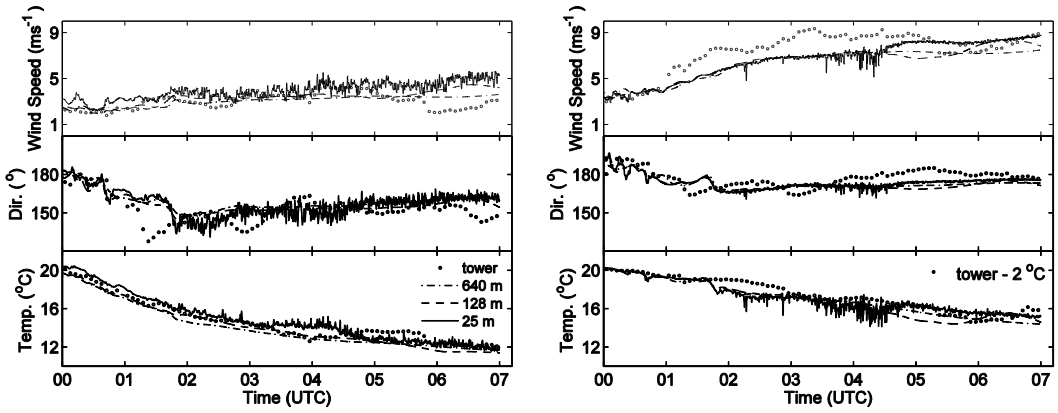

(a) (b)

Figure 4-5 Main tower observations (circles) compared with 640 m (dash-dotted line), 128 m (dashed line), and 25 m (DRM-ADM0, solid line) grid simulations at (a) 10m AGL and (b) 55m AGL, for wind speed, direction and temperature. Observed temperature at 55m is subtracted by 2^{o}C for comparison. Measurements are sampled at every 5min, model data at every 2s.

Time series of modeled wind speed, direction and temperature are compared with the main tower observations, at tower top (55 m) and near the surface (10 m) in Figure 4-5. With all model data recorded every 2 s, only the 25 m DRM-ADM0 run shows fluctuations in the profiles. Good agreement with the surface flow is achieved on all three inner grids (Figure 4-5(a)). At the tower top, wind speed is under-predicted up to ~3 ms^{-1} from 0100 onwards, until 0500 UTC when the 25 m grid wind accelerates to the observed value ~8 ms^{-1}. Model temperature at 55 m is consistently colder than observations. This is in contrast to the comparison with the nearby radiosonde observation where the model temperature is warmer. The temperature deficit does not seem to affect the model prediction of the dynamics of the flow, as shown in Section 0. Better agreement is reached when observed temperature is offset by 2 ^{o}C in Figure 4-5(b).

4.4.2 Sensitivity to Turbulence Closures

The SBL flow transitions into a turbulent period after 0500 UTC as shown in Figure 1-1. A time-height contour plot of thermocouple temperatures at the main tower is presented in Figure 4-6(a). LES with the TKE-1.5 closure (Figure 4-6(b)) reproduces the mean profiles of temperature, but fails to generate any turbulent fluctuations. To study model sensitivity to turbulence closures, three additional runs (TKE-ADM1 -R, DWL-R, and DWL-ADM0-R) on the 25 m grid were performed. These runs were initialized (restarted) from the TKE-1.5 run at 0400 and integrated to 0700 UTC to save computational time, hence the suffix "-R". The purposes of these three runs are to find out whether the model can transition from a laminar to a turbulent state by improving the turbulence model alone. The DWL-R run (Figure 4-6(c)) reveals strong temperature perturbations that

resemble tower measurements. With the addition of a zero-level reconstruction term, the DWL-ADM0-R run (Figure 4-6(d)) further improves the DWL results, and produces even stronger turbulent fluctuations. In comparison, the TKE-ADM1-R run does not show much improvement over the TKE results, hence it is not shown here. Due to computational resource limits, higher levels of reconstruction were not tested.

The normalized temperature variance spectra from the models are compared with thermocouple measurements in Figure 4-7. Spectra were computed using Matlab's pwelch function (Welch 1967) during 0515-0550 UTC when turbulent fluctuations were significant. The thermocouple spectrum has two peaks at low frequencies. The second peak at ~0.017 Hz corresponds to the dominant shear-instability wave frequency (see also Fig. 5 in NB03). The DWL-ADM0-R spectrum has a single sharp peak in-between the observed peaks, while the DWL-R shows a local peak with a smaller magnitude compared to measurements. Comparison of the DWL-R and DWL-ADM0-R reveals their difference in the partitioning of turbulent energy. The spectrum transitions from a broad flat shape (DWL-R) to a narrow sharp one (DWL-ADM0-R), suggesting that more high frequency turbulent motions are excited with the addition of the reconstruction model.

The above sensitivity study suggests that the DWL-ADM0 closure not only enables flow transition from quiescent to turbulent state, but also produces good results matching observations. Therefore, we repeated the entire 10-hour simulation on the 25 m grid with the DWL-ADM0 closure. The time-height contour of temperature (Figure 4-6(e)) reveals intense fluctuations similar to that of the DWL-ADM0-R run. The temperature spectrum in Figure 4-7 matches observations better as well, showing two peaks at lower frequencies with fairly good magnitude agreement.

Finally, all model spectra in Figure 4-7 fall to zero at around 0.05 Hz, while the thermocouple spectrum decreases gradually towards the Nyquist cutoff at 0.25 Hz (half its resampling rate applied here for comparison purposes). The missing high frequency fluctuations are likely due to the effects of computational mixing, which is applied to damp out numerical noise. However, computational mixing also removes small-scale motions which are part of the resolved turbulent field in high-resolution LES (Michioka and Chow 2008). Belusic and Guttler (2010) showed that by minimizing computational mixing, the meso-scale model spectrum was raised to the observed magnitude, reproducing meandering motions during CASES-99. On the 25 m grid, fourth-order computational mixing is applied in the horizontal and vertical direction with a coefficient of 0.01. A smaller value of 0.005 results in numerical noise (i.e. $2\Delta x$ waves) in the flow field.

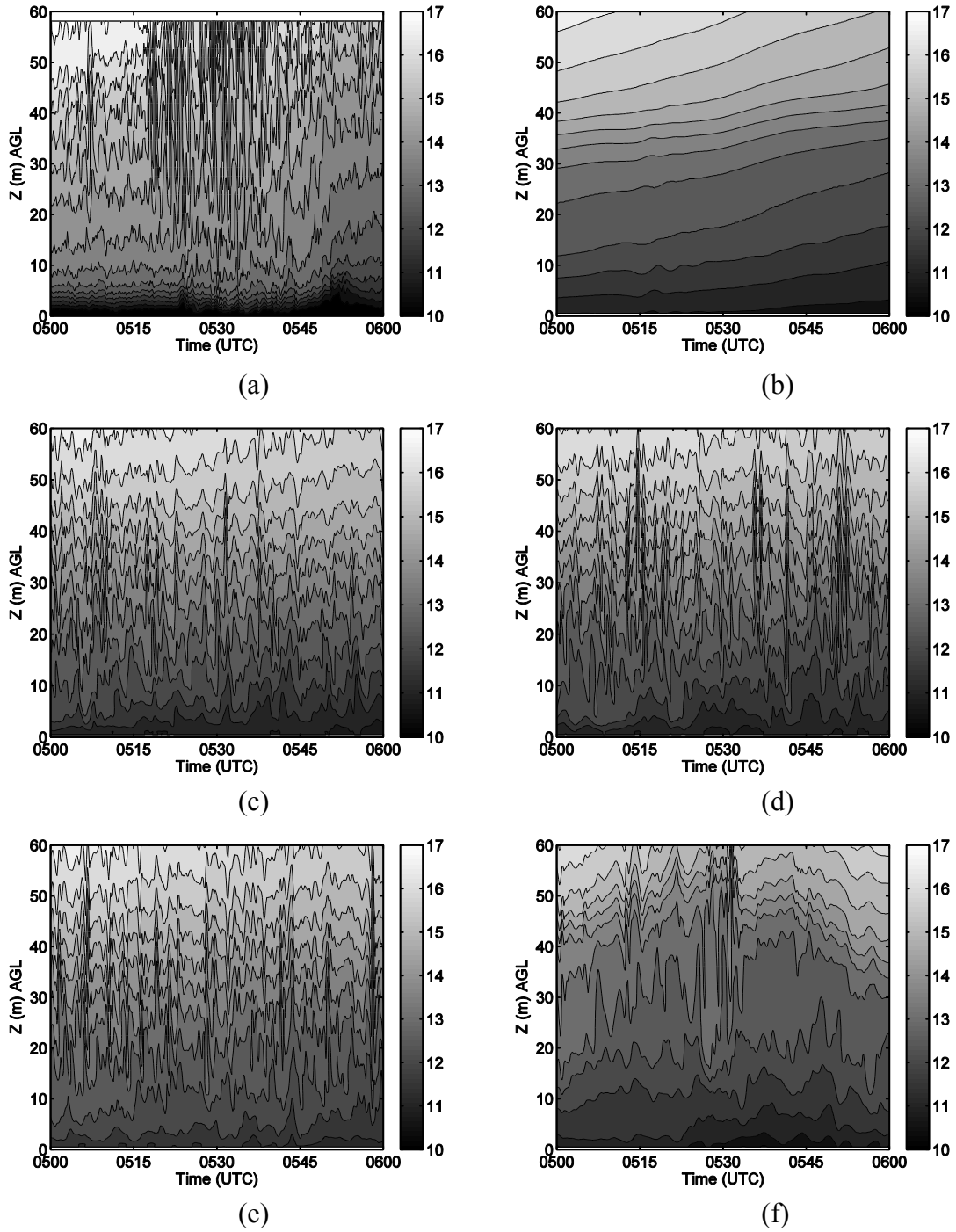

Figure 4-6 Time-height contours of temperature (^{o}C) from (a) thermocouple measurements at the main tower, and LES results on the 25 m grid from (b) the TKE run, (c) the DWL-R run, (d) the DWL-ADM0-R run, (e) the DWL-ADM0 run and (f) the TKE-S run. Contour levels are separated by 0.5 ^{o}C. Data are sampled at every 10 s.

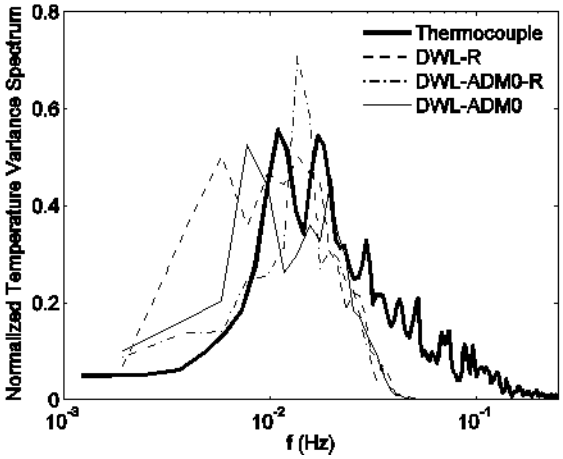

Figure 4-7 Normalized temperature variance spectrum during 0515 to 0550 UTC. Thick solid line represents thermocouple measurements, thin solid line represents the DWL-ADM0, dashed line represents the DWL-R, and dash-dotted line represents the DWL-ADM0-R. Spectra are averaged with data between 30 and 40 m AGL, and normalized by their respective temperature variance. Data are recorded (LES) and resampled (thermocouple) at 0.5 Hz.

4.4.3 Sensitivity to Nest Domain

Model sensitivity to the placement of the nested domain is explored on the 25 m grid. The general rules of thumb for placing lateral boundaries in nested simulations (Zhong and Chow 2012) are 1) to extend as far away from the region of interest as possible (i.e. large domains), so that flows coming from the coarse outer grid Δ_c have sufficient time/space to develop turbulent motion ($2\Delta_c \geq \kappa \geq 2\Delta_f$) corresponding to the finer inner grid Δ_f; 2) to avoid drastic changes in terrain, such that the lateral boundaries are located over smooth terrain whenever possible (Warner et al. 1997). While the first rule is usually limited by the available computational resources, the second rule depends largely on the judgment of the modeler and the particular topography at the site. Over the CASES-99 site, the terrain is relatively simple and flat (Figure 4-3). It was not initially expected that the results would be sensitive to the placement of the nest domain.

Two domain sizes were tested on the 25 m grid with the TKE-1.5 closure. The smaller domain (TKE-S) has 201 grid points in both x and y directions, which is set by following a 5 to 1 nesting ratio from the 128 m grid. The larger domain (TKE) has 363 grid points (Figure 4-3(c)). With identical model configurations, the smaller domain TKE-S and TKE runs produce a laminar flow state for most of the night, but the TKE-S domain then transitions into a somewhat turbulent flow from 0500-0600 UTC (Figure 4-6(f)), while the larger TKE run fails to do so (Figure 4-6(b)). The decreased model performance with increasing domain size is surprising. However, it is found that a shallow valley (Figure 4-3(c)) south of the main tower is an important topographic feature that strongly affected the flow. We attempt to address this counter-intuitive result after exploring the role of the valley in the following section.

4.5 Turbulent bursting event

In this section, model results from the 25 m domain (DRM-ADM0) are used to reconstruct a 3D history of the formation, evolution, and breaking of the observed turbulent bursting event.

4.5.1 Source Location

A north-south vertical slice of θ at 0531 UTC along line NS1 (Figure 3c) is presented in Figure 4-8(a). In the absence of diabatic effects, isentropes of θ can be viewed as instantaneous streamlines, which the flow tends to follow (Cramer 1972). Wave-like motions are present in the region of the HRDL scan (enclosed between dashed lines in the figure), both in the simulations and in the observations (see Figure 4-2). The waves are centered at ~40 m AGL with respect to the tower site, and have horizontal wavelength λ~350 m, agreeing with HRDL observations (see Figure 4-2 and section 4.c.3 in NB03). A vertical slice of θ at about 2 km east of the HRDL (line NS2) reveals similar wave patterns, with a slightly longer wavelength in Figure 4-8(b). The most structured waves are found along line NS2 at a later time (0551 UTC), as seen in Figure 4-8(c), which shows four evenly spaced wave peaks with λ~375 m, and an amplitude of nearly 100 m.

All vertical slices indicate that the waves extend beyond the HRDL scanning range on both ends. This is most clearly seen in Figure 4-8(c) where a train of waves originates from the north end of the valley (around Y = -1.5 km). Moving downwind (north) of the valley, waves grow and steepen, reaching a maximum amplitude past Y = 0 km, and finally break into a turbulent wake. The source of the modeled shear-instability waves is more easily located by inspecting the flow from aloft. Figure 4-9(a) plots the vertical velocity component w on a horizontal plane intersecting the tower top. Intense oscillations are seen north of the valley, especially in the boxed region. Zooming in on Figure 4-9(b), pairs of up and downward going w represent wave crests and troughs propagating towards the north. A qualitative overall picture of the flow field is presented as an iso-surface plot for θ at 290.5K in Figure 4-10. The iso-surface dips over the upwind side of the valley, indicating descending motion into the valley. On the downwind side, the iso-surface rises and exhibits coherent wave structures. In summary, model results show that during IOP2, waves originated from the valley. As they sharpen and propagate downwind, they are captured by the main tower and HRDL.

Having located the source of the waves, we examine the valley cross-section along line NS3 to investigate the time-space history leading up to the breaking waves. NS3 is chosen not only because the most intense wave motions are observed around this particular valley section, but more importantly for its relative topographic simplicity, because it does not intercept any major valley tributaries or gullies (Figure 4-3(c)). We investigate a similar small-scale event around 0200 UTC along NS3, mostly for its relative “cleanness”. In section 5.5, we show that the observed turbulent bursting event around 0530 UTC is of the same nature, and that the SBL goes through several cycles of evolving and breaking shear-instability waves governed by the same mechanism. In the following analysis, we also make use of three locations across line NS3 to represent the upwind, the valley and the downwind flow (UL, VL, and DL in Figure 4-3(c)). Note that

the valley location, where the strongest along-valley flow occurs, is slightly north of the valley bottom. This downwind shift is caused by the descending synoptic flow on the upwind side.

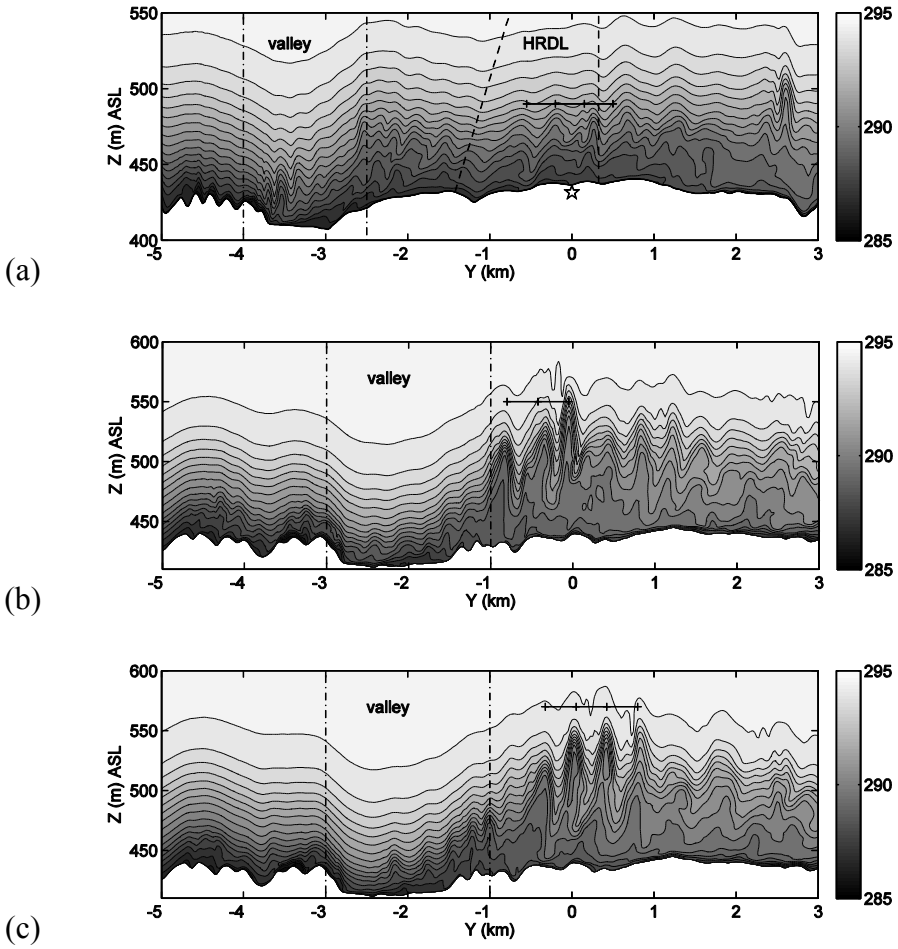

Figure 4-8 Vertical cross sections of potential temperature on the 25 m grid along (a) line NS1 and (b) line NS2 at 0531 UTC, (c) line NS2 at 0551 UTC. Locations of NS1, 2 are presented in Figure 4-3(c). The HRDL scanning range is enclosed by dashed lines in (a). Approximate valley widths are enclosed by dash-dotted lines. Solid horizontal lines separated by plus signs mark 350m for each interval in (a) and 375m in (b) and (c). Contour levels are separated by 0.5 K.

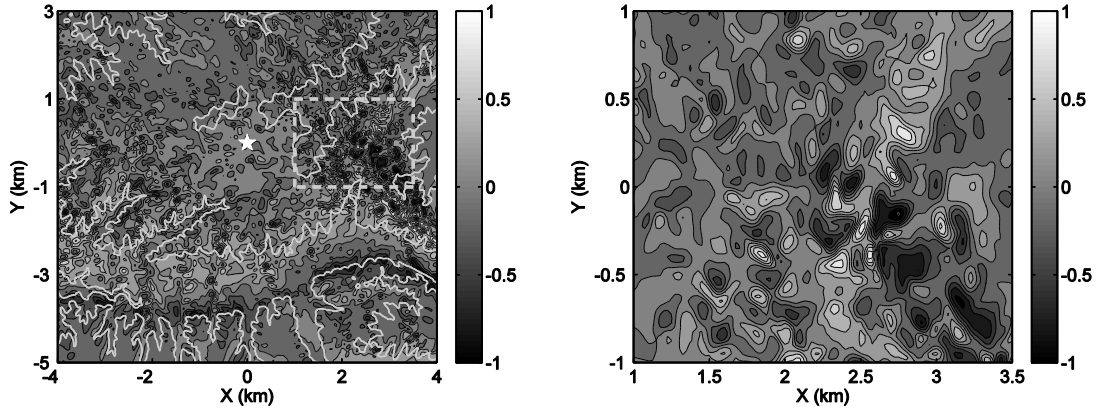

(a) (b)

Figure 4-9 Horizontal cross sections of vertical velocity (w ms^{-1}) contours on the 25 m grid at 0531 UTC at 500m ASL (~55m AGL at the tower site) for (a) the entire horizontal domain with white solid lines representing the terrain, and (b) the partial domain marked by dashed lines on (a). Contours are separated by 0.2 ms^{-1}.

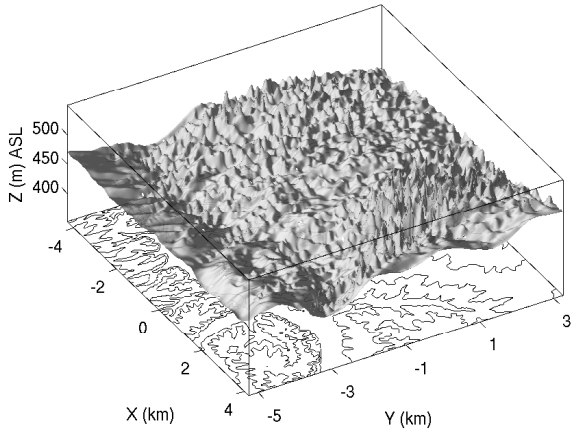

Figure 4-10 Iso-surface height for potential temperature of 290.5K at 0551 UTC.

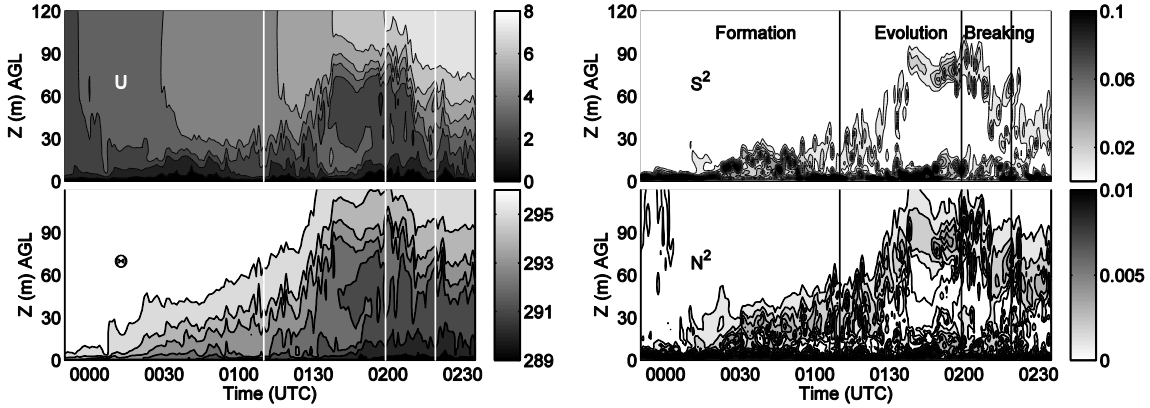

(a) (b)

Figure 4-11 Time-height contours of (a) wind speed U (ms^{-1}, top) and potential temperature θ (K, bottom), and (b) shear S^2 (s^{-2}, top) and buoyancy N^2 (s^{-2}, bottom) at the VA location in Figure 4-3(c). Contour levels are separated by 1 ms^{-1} (U), 1 K (θ), 0.01 s^{-2} (S^2) and 0.001 s^{-2} (N^2). Data are sampled at every minute.

Time-height contours of wind speed U and potential temperature θ are presented in Figure 4-11(a). Starting from the evening (0000/1700 UTC/LST), the SBL evolves in a classic fashion: θ decreases from the surface extending upwards, while U increases away from the surface as the LLJ starts to form. However, past 0110 UTC, U drops between 30-80 m AGL, forming a vertical layer where the wind speed is nearly constant. In the same layer, near isentropic θ is observed. The anomaly is more clearly reflected in the time-height contours of the square of vertical shear (S^2) and buoyancy (N^2) in Figure 4-11(b), where:

$$S^2 = \left(\frac{\partial u}{\partial z}\right)^2 + \left(\frac{\partial v}{\partial z}\right)^2, \qquad N^2 = \frac{g}{\theta}\frac{\partial \theta}{\partial z}$$

A shear/buoyancy layer grows from the surface, reaching ~80 m AGL. Between this elevated layer and the surface layer, minimal shear and buoyancy exist. The elevated layer decreases rapidly past 0200 UTC. This is due to a turbulent mixing event triggered by shear-instability waves, which will be shown in section 5.4. Based on the discussion above, we divide the history of this particular mixing event at 0200 UTC into three time periods: formation, evolution and breaking.

4.5.2 Phase-I-Formation

The history begins with the establishment of a shallow valley drainage flow during the evening transition. As shown in Figure 4-12(a), surface winds are mostly aligned in the north-south direction at sunset. This is the direction of the synoptic wind above the SBL. Shortly after sunset, a shallow drainage flow develops in the valley. By 0150 UTC, the

valley drainage flow is fully established (Figure 4-12(b)). In the particular section around line NS3, the wind direction is around 115^{o}, aligned with local along-valley axis.

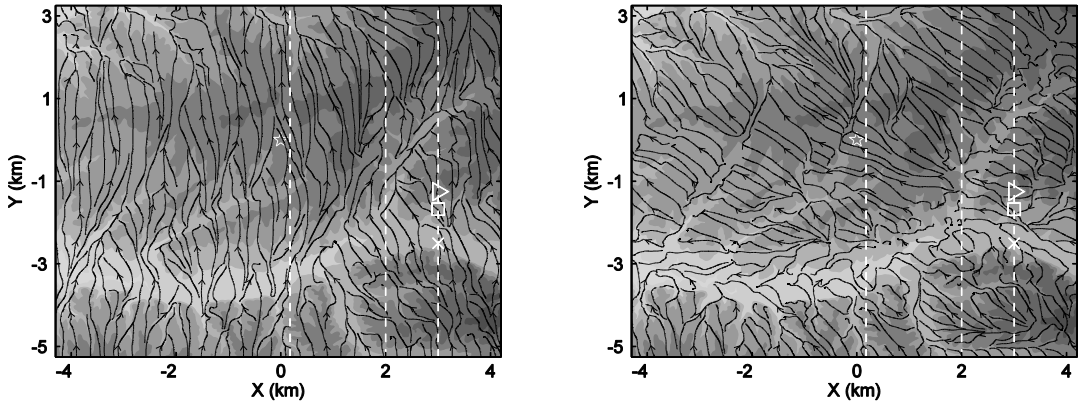

(a) (b)

Figure 4-12 Streamlines of surface wind at (a) 0000 UTC and (b) 0150 UTC. Wind vectors are averaged over 5 minutes around the selected time.

Valley drainage flows were frequently observed at the CASES-99 site (Mahrt et al. 2001). They originated from the Flint Hills, shown as the elevated ground on the east side of the 128 m domain (Figure 4-3(b)). In Figure 4-13, time-series at four selected elevations at location VL reveal two vertical layers based on the direction of the flow. The surface (1.5 m AGL) wind shifts from the synoptic (180^{o}) to the down-valley (115^{o}) direction at around 0120 UTC, and remains so except for the short period during the turbulent burst at 0200 UTC. The drainage flow advects cold-air into the valley such that valley surface temperature drops nearly 3 K from 0000 to 0100 UTC. Mahrt et al. (2001) refers to this drainage flow associated cooling as "the early evening very stable period".

Vertical profiles for the first three hours during evening transition are presented in Figure 4-14. The depth of the drainage flow at 0100 UTC is estimated to be about 7 m deep based on the wind direction range of 115 ± 15^{o}. In the drainage flow layer, rapid cooling results in strong surface inversion. In comparison, cooling is more uniform away from the surface. By 0100 UTC, the overall SBL is about 16 m deep, capped by a self-developed overlying inversion that is characteristic to the SBL.

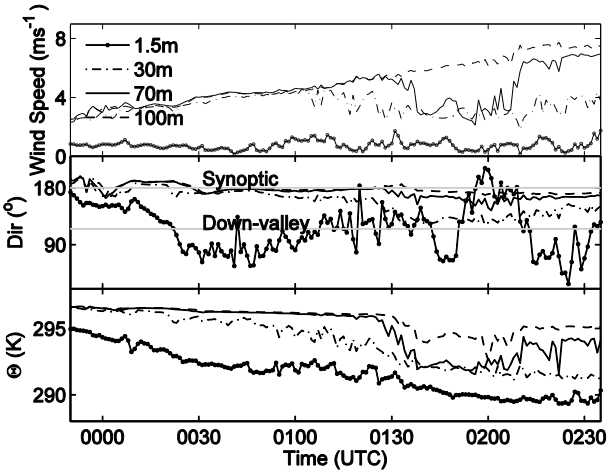

Figure 4-13 Time-series of wind speed (top), wind direction (middle), and potential temperature (bottom), at 1.5m (solid line with circles), 30m (dot-dashed line), 70m (solid line) and 100m (dashed line) AGL at the VL location in Figure 4-3(c).

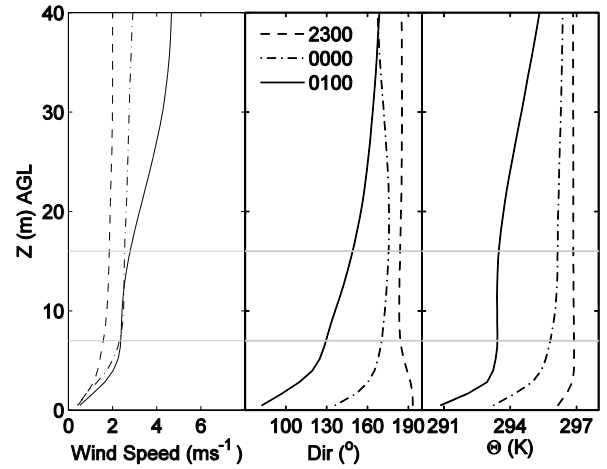

Figure 4-14 Vertical profiles of wind speed (left), wind direction (middle), and potential temperature (right) at 2300 UTC (dashed lines), 0000 UTC (dash-dotted lines) and 0100 UTC (solid lines) at the VL location in Figure 4-3(c). Data are averaged over 5 minutes around the selected time.

4.5.3 Phase-II-Evolution

By the end of Phase-I, a very stable surface layer is established in valley. It can be viewed as a shallow cold-air pool that occupies the valley bottom. As the valley drainage flow continues, the cold-air pool deepens. Soon it is further supplemented by the down-slope flows on both sides of the valley sidewalls. Figure **4-15** presents time series of the surface wind direction and temperature at the UL, VL and DL locations (see Figure 4-3(c)). Past 0130 UTC, down-slope flows at both the UL and DL locations carry colder

air into the valley. Note that unlike the UL side, the down-slope flow on the DL side is nearly 180^o from the synoptic wind.

According to Baines (1997), the dimensionless parameter Nh/U (or inverse Froude number) largely determines the state of stratified flow across valleys. A critical value $|Nh/U|_c$ exists such that:

$$\frac{Nh}{U} < \left|\frac{Nh}{U}\right|_c \qquad sweeping\ flow$$

$$\frac{Nh}{U} > \left|\frac{Nh}{U}\right|_c \qquad stagnant\ valley\ fluid$$

where h is the valley depth, N and U are buoyancy and velocity scales. For hydrostatic flow over a Witch of Agnesi valley, the critical value is 0.85 for uniform U and N (Miles and Huppert 1969). Although $|Nh/U|_c$ is unknown for the CASES-99 valley, given the shallowness of the valley (h~ 20 m deep and L~1 km wide), we expect fluid within the valley to be completely swept out by the cross flow. The strong stratification (high N) associated with the existing cold-air pool, however, seem to shelter the valley fluid, allowing anti-synoptic down-valley flows to form on the downwind side. The combined result is a growing cold-air pool inside the valley.

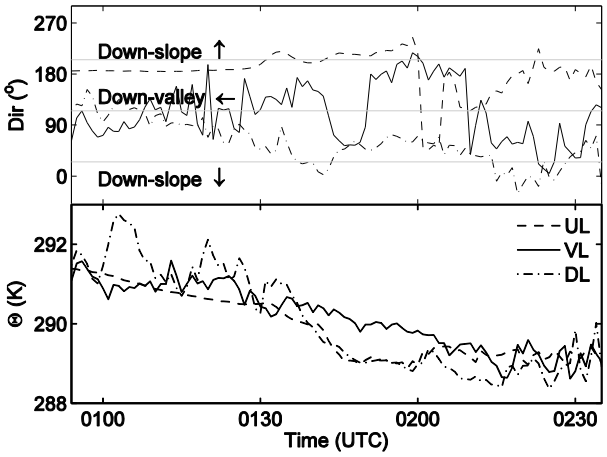

Figure 4-15 Time-series of surface (1.5m AGL) wind direction (top) and potential temperature (bottom), at the UL (dashed lines), VL (solid lines), and DL (dash dotted lines) locations in Figure 4-3(c).

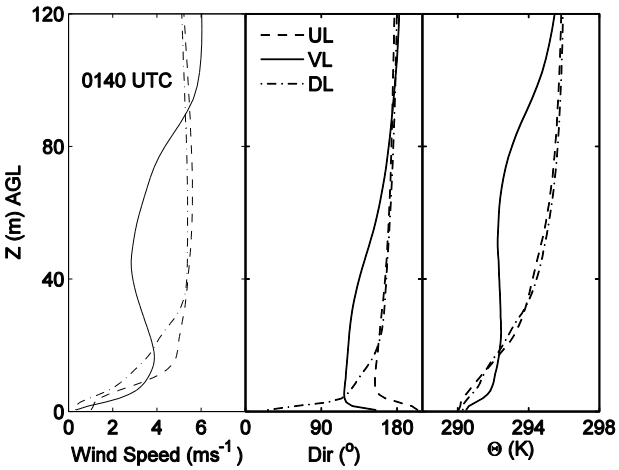

Figure 4-16 Vertical profiles of wind speed (left), wind direction (middle), and potential temperature (right) at the UL (dashed lines), VL (solid lines) and DL (dash-dotted lines) locations in Figure 4-3(c) at 0140 UTC. Data are averaged over 5 minutes around the selected time.

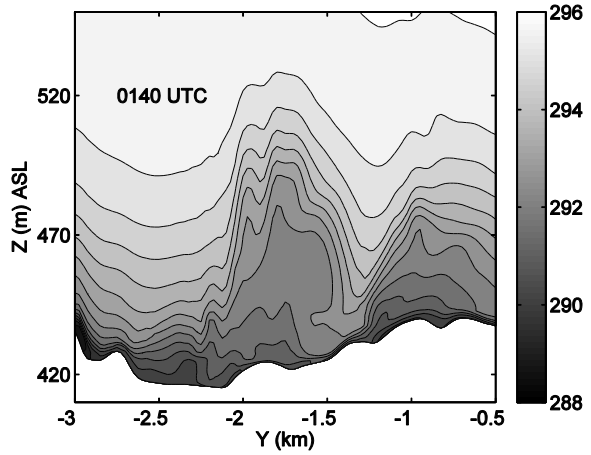

Figure 4-17 Vertical cross section of potential temperature over the valley along line NS3 at 0140 UTC. Contour levels are separated by 0.5 K.

A standing gravity wave emerges downwind of the valley at 0100 UTC. Such waves are expected when the buoyancy timescale $2\pi/N$ is smaller than the advection timescale L/U across the valley. This criterion can be expressed as a Froude number based on the valley width L (Vosper and Brown 2008): $F_r = 2\pi U/NL \leq 1$, where N and U are from the upwind flow. Figure 4-16 shows the vertical profiles of U and θ at the three locations at 0140 UTC, when a mature wave is observed (see Figure 4-17). Taking the upwind U (5.4 ms^{-1}) at 40 m AGL as reference, where the profile is nearly uniform, and computing a bulk buoyancy frequency between 0~40 m (N ≈ 0.06 s^{-1}), we obtain $F_r = 0.57 < 1$.

Similar standing waves are also observed above and downwind of a shallow valley of similar dimension in Vosper and Brown (2008).

The standing lee wave is somewhat non-classic, because it is injected with cold-air from the surface. As the cold down-valley and down-slope flows converge toward the downwind side of the valley, the comparatively warmer air in the valley bottom is forced to rise. In other words, the valley is continuously collecting cold surface flows and shifting relative warmer air upwards. By 0140 UTC, the standing wave evolves into a cold-air bubble, extending to nearly 70 m AGL, as shown in Figure 4-17. The relatively warmer upwind SBL flow (see also Figure 4-16) is forced to flow over the bubble, and recovers downwind. The bubble essentially acts as a barrier that prevents *horizontal* transport of momentum from upwind.

Moreover, the cold-air bubble is capped by a strong inversion, developed mostly by compressing θ isotherms as it grows from below. The capping inversion suppresses turbulent mixing, which minimizes *vertical* transport of momentum from the fast synoptic flow above. Therefore, flow inside the bubble slows down compared to the upwind and downwind locations, as shown in in Figure 4-17. This effect is most clearly seen in vertical profiles at the VL location in Figure 4-18. Three horizontal lines mark the height of the capping inversion at three times during the evolution phase. It is remarkable that these lines also correspond to crossings in the velocity profiles, indicating slowing down of the flow once inside the inversion layer. From 0100 to 0125 UTC, the bubble grows from 16 m to 50 m. Meanwhile, a decrease in wind speed is observed below 50 m, when flow accelerates above. Likewise, as the bubble grows from 50 m to 76 m during 0125-0150 UTC, wind speed decreases/increases below/above 76 m. The same effect is also reflected in Figure 4-13, as wind speed sequentially decreases at higher elevations in time.

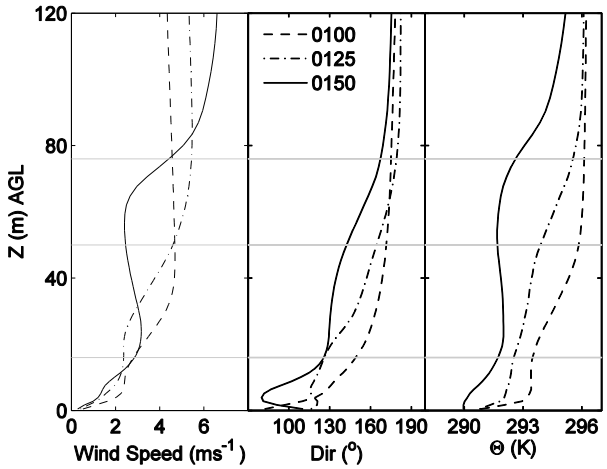

Figure 4-18 Vertical profiles of wind speed (left), wind direction (middle), and potential temperature (right) at 0100 UTC (dashed lines), 0125 UTC (dash-dotted lines) and 0150 UTC (solid lines) at the VL location in Figure 4-3(c). Data are averaged over 5 minutes around the selected time.

4.5.4 Phase-III-Breaking-Shear-instability wave

The capping inversion heights in Figure 4-18 also correspond to inflection points in the velocity profiles. This is a result of reduced momentum over the depth of the bubble away from the surface. As the wind aloft continues to accelerate under the geostrophic pressure gradient forcing, (see 100 m wind speeds in Figure 4-13), the increasingly inflected velocity profile eventually overcomes the stabilizing effect of buoyancy, and breaks into shear-instability waves. Figure 4-19 presents three snapshots of θ contours during the turbulent bursting event. At 0158 UTC, the standing wave sharpens on the downwind side, represented by the near vertical isentropes around Y = -1.5 km. In the next minute, waves with $\lambda \sim$ 275m break from the lee side of the bubble, and are advected downwind.

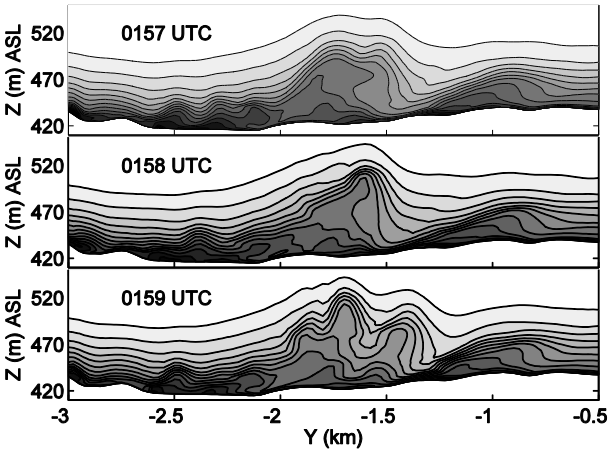

Figure 4-19 Vertical cross sections of potential temperature over the valley along line NS3 at 0157 UTC (top), 0158 UTC (middle) and 0159 UTC (bottom). Colorbar is the same as Figure 4-17. Contour levels are separated by 0.5 K.

The initial linear instability from the inflection points is a Kelvin-Helmholtz wave (Drazin and Reid 2004). The wavelength λ is proportional to the spanwise vorticity thickness $\delta_w \equiv \Delta U/|dU/dz|_{max}$, where ΔU is the difference between two free-stream velocities (Rogers and Moser 1992). δ_w is computed at 0150 UTC before the waves break. As shown in Figure 4-18, ΔU across the inflection point is estimated to be 5 ms^{-1}, between 60 m and 120 m where the wind speeds are fairly constant with height. The maximum elevated shear $|dU/dz|_{max}$ is ~0.17 s^{-1}. Therefore δ_w, representative of the depth of the mixing layer, is approximately 30 m. The shear-instability wavelength λ is about 9 times larger than δ_w. This value is slightly larger than what linear-stability predicts $\lambda \approx 7.8\delta_w$ (Michalke 1965), and much larger than DNS results $5.0\delta_w > \lambda > 3.5\delta_w$ (Rogers and Moser 1994). While inflection point induced shear instability is confirmed by the simulations, whether the observed waves are Kelvin-Helmholtz in nature are still questionable (Banta 2012, personal communication). This is because

subsequent overturning of the KH billows downwind the valley is hardly observed (see lidar scan in Figure 4-2 and LES results in Figure 4-8).

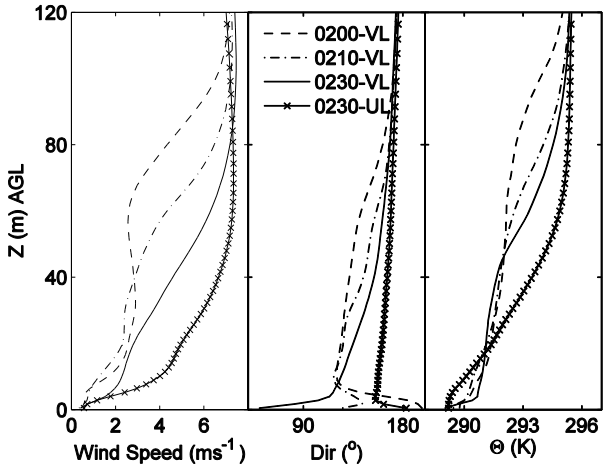

Figure 4-20 Vertical profiles of wind speed (left), wind direction (middle), and potential temperature (right) at 0200 UTC (dashed lines), 0210 UTC (dash-dotted lines), 0230 UTC (solid lines) at the VL location, and at 0230 UTC (solid line with crosses) at the UL location in Figure 4-3(c). Data are averaged over 5 minutes around the selected time.

When the standing wave sharpens and breaks on the downwind side, the cold air within is advected downwind. The absence of the cold-air allows horizontal advection of warmer and faster upwind flow. The result is an increase in U and θ towards the upwind profiles, as shown in Figure 4-20. However, the cold-air bubble is not completely swept out. The vertical extent of the "replacement" stops at ~40 m AGL. Below, the flow stays more or less intact. The shear-instability event also affects the surface flow. Surface winds at the valley location transition briefly into the synoptic direction in Figure 4-13, and then back to the down-valley direction by 0230. Figure 4-20 shows the vertical extent of the direction shift to be ~ 8 m. This does not imply that the bursting event is felt at the surface. Rather, it was caused by the synoptic wind pushing the weaker cold-air bubble further downwind.

4.5.5 Conceptual schematic

A conceptual schematic is presented in Figure 4-21 to highlight the processes leading to shear-instability waves from the shallow valley. During evening transition, a valley drainage flow develops. It brings cold air into the valley, building up a shallow cold-air pool. In Phase-II, a standing wave forms on the downwind side of the valley based on the stratification, wind speed and valley dimensions, i.e. a valley Froude number. In addition to the valley drainage flow, down-slope winds develop at both valley sidewalls. The growing cold-air bubble inhibits horizontal and vertical momentum/heat transfer. In Phase-III, the synoptic wind strengthens. Shear-instability due to the velocity profile

inflection at the top of the cold-air bubble leads to wave breaking. Cold air is advected downwind, and replaced by warmer air from upwind.

The process is cyclic in nature. After Phase-III, the down-slope and down-valley flows are restored, and the cold-air bubble evolves again. Figure 4-22 presents an extension to Figure 4-11 for the entire simulation. Three cycles are identified, mostly easily by tracking the elevated shear/inversion layer. The rising and strengthening of the elevated shear layer is a signature of growing cold-air bubble, which is also associated with decrease of wind speed from top-down, and temperature from bottom-up. Wave-breaking events are followed by falling and weakening of the elevated shear layer, and an increase in U and θ.

As the synoptic flow strengthens, the standing wave/cold-air bubble is pushed further to the downwind side of the valley. It is expected that as Nh/U decreases, the dense fluid should be swept out of the valley. At shown in Figure 4-8, the cold-air bubble is located on the downwind edge of the valley. This result in a most energetic bursting event observed at the tower. However, it is not reflected in Figure 4-22 because the valley location is no longer inside the cold-air bubble.

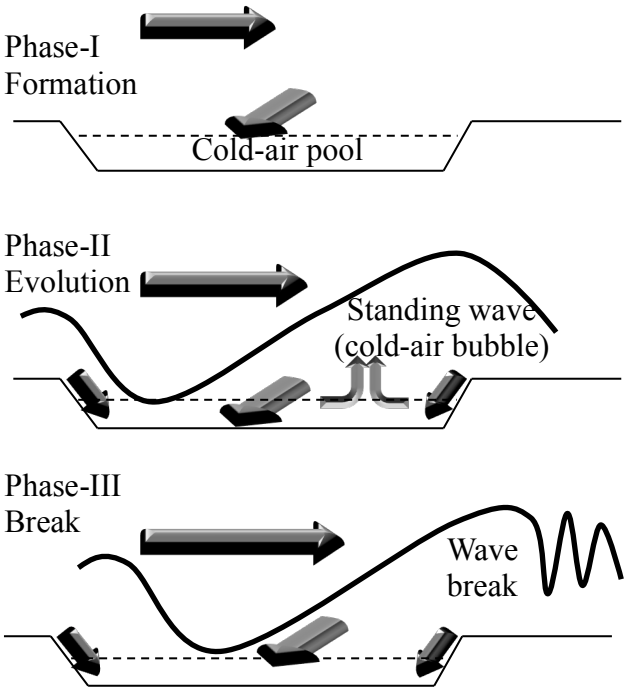

Figure 4-21 Illustration of the shear-instability wave processes.

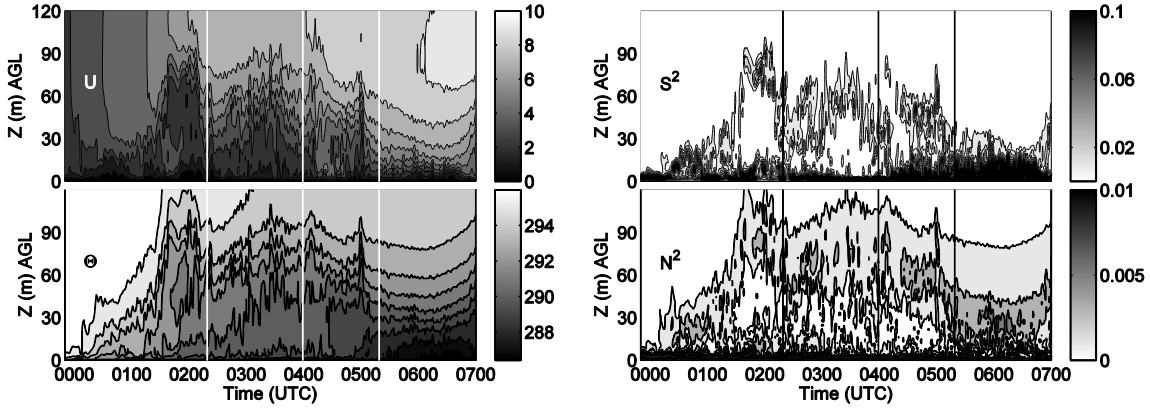

(a) (b)

Figure 4-22 Time-height contours of (a) wind speed U (ms^{-1}, top) and potential temperature θ (K, bottom), and (b) shear S^2 (s^{-2}, top) and buoyancy N^2 (s^{-2}, bottom). Contour levels are separated by 1 ms^{-1} (U), 1 K (θ), 0.01 s^{-2} (S^2) and 0.002 s^{-2} (N^2). Data are sampled at every minute.

4.5.6 Terra Incognita

In this section, we raise an important modeling issue for the SBL, namely the *terra incognita*. The term was proposed by Wyngaard (2004), referring to the situation where the grid resolution Δ is comparable to the dominant length scale l of the flow field. Taking convection for example, the size of the largest eddy in the daytime convective boundary layer (CBL) spans roughly the boundary depth, l~O(1 km). When running in meso-scale mode with Δ~O(10 km), convection cells are entirely subgrid scale (SGS) motions. This enables statistical treatments of the turbulent mixing processes in the CBL, i.e. the use of boundary layer parameterization schemes. On the other hand, in LES mode with Δ~O(100 m) or less, convective motions are explicitly resolved for the most part. The LES turbulence closure takes care of the remaining SGS motions. However, when Δ and l are on the same order, a parameterization is no longer appropriate since the grid box is not large enough to contain a sufficient number of convection cells for statistical averaging. Meanwhile, l is too poorly resolved by Δ to be simulated with LES. Some techniques have been proposed for modeling in this gray zone, such as scale-aware parameterizations, and quasi-3d multi-scale techniques (Arakawa et al. 2011), yet much remains to be developed and tested.

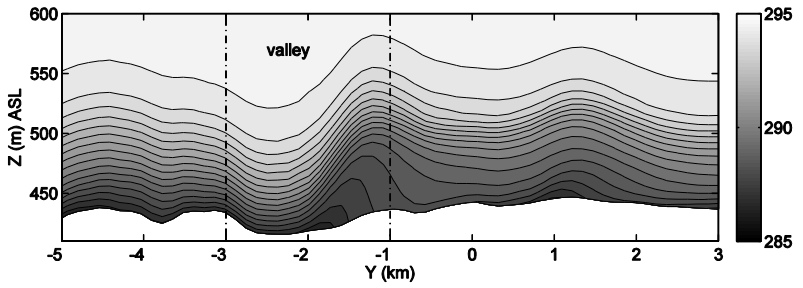

Figure 4-23 Vertical cross section of potential temperature on the 128 m grid along line NS2 at 0531 UTC. The domain is cropped on both sides to resemble the 25 m grid. Contour levels are separated by 0.5 K.

While the *terra incognita* in the CBL is well recognized, the SBL counterpart has received little attention. This is because conventionally the dominant SBL length scale has been considered to be the buoyancy scale (e.g. the Ozmidov scale), which is ~O(10 m), and far beyond current high resolution NWP (Beare 2011). However, if gravity waves are considered, the SBL *terra incognita* is already a pressing issue for practical applications. In the current study, the breaking shear-instability waves have wavelength λ~350 m, which are barely resolved on the 128 m grid. As a result, the standing wave persists throughout the night, as shown in Figure 4-23, compared to the 25 m grid results in Figure 4-8(b) where the standing wave is eroded from the top through wave breaking due to shear-instability. This resulted in a colder, more stable, and less mixed boundary layer downwind the valley. Thus if *terra incognita* is unavoidable due to computational resource constraints, better parameterization must be sought to represent SGS gravity wave breaking events under appropriate circumstances.

4.6 Summary and Conclusion

High-resolution nested LES is performed to simulate an intermittently turbulent night (IOP2) during the CASES-99 field campaign. Simulations are run over moderately complex terrain with realistic initial and lateral boundary conditions. The LES results are validated against surface and air-borne observations. While the outer domains (640 m and 128 m) capture the observed mean profiles, turbulent motions are only resolved on the 25 m LES grid. Furthermore, LES with the TKE-1.5 closure predicts a false laminar flow. Switching to a more sophisticated turbulence closure, the dynamic reconstruction model, improves the model results and reproduces the observed turbulent bursting event. This demonstrates the usefulness of the DRM closure in sustaining SBL turbulence, while relaxing grid-resolution requirements (Zhou and Chow 2011). The improved representation of turbulence is achieved by adding resolved subfilter scale (RSFS) stresses to the subgrid stress terms. It is shown that the RSFS terms excite higher frequency motions in the stratified flow, helping to sustain resolved turbulence. In this study, a zero-level reconstruction term improves the dynamic Wong and Lilly closure at minimal additional computational cost.

The high-resolution 3D flow field is then used to investigate the observed shear-instability wave event. The simulation reveals that wave-breaking is initiated from a standing wave formed across a shallow valley upwind of the main tower. The standing wave was preceded by the formation of a valley cold-air pool due to down-valley drainage flows. This evolved into a significant cold-air bubble fed by down-valley, down-slope flows, and was eroded by inflection point induced shear-instability waves. The cyclic process of formation and erosion were repeated during the night. This study answers the unresolved issue regarding the origin of shear-instability waves raised in NB03, and demonstrates the usefulness of LES to supplement field campaigns. Furthermore, it illustrates another mechanism for intermittent turbulence, which is through breaking gravity waves. Another lesson learned from the above intermittency mechanism is that when conducting nested SBL simulations over complex terrain, the modeler should be extra careful about grid placement even in seemingly flat topography. Under stratified conditions, even a shallow valley could have a significant impact on the SBL flow.

In this study, the smaller LES domain is able to predict a semi-turbulent flow, essentially because the south boundary intersects the valley (Figure 4-3(c)). The standing-wave developed from the 128 m grid is fed in as a boundary condition to the small LES domain. Because the 128 m grid is not able to predict wave breaking, the cold-air bubble is larger and stronger than it should be. The strength of cold-air bubble far exceeds the shear-instability criterion, such that the TKE-1.5 closure on the small domain is able to predict the breaking event. In comparison, the standing wave is simulated locally on the large LES domain. The TKE-1.5 closure failed to predict wave breaking primarily due to its relatively dissipative nature.

Finally, it is shown that besides the buoyancy length scale ~O(10 m), the *terra incognita* for the SBL should include gravity waves ~O(100 m). In particular, it is shown that wave breaking is absent when the resulting shear-instability waves have a wavelength comparable to the grid spacing. Suitable parameterizations should be developed to predict breaking gravity waves and represent the effects of induced turbulent mixing.

Chapter 5 Nighttime Large-eddy Simulation of Turbulent Events in a Steep Valley

Abstract

This numerical study investigates the nighttime flow dynamics in Owens Valley, California during the Terrain-Induced Rotor Experiment. Nested high-resolution large-eddy simulation (LES) is performed to resolve stable atmospheric boundary layer flows within the valley. Simulations are first performed on a 2400 m grid driven with meso-scale reanalysis data, and subsequently nested down to a fine LES grid with 50 m horizontal and 5 m near-surface vertical spacing. On the selected night, the valley atmosphere experienced weak synoptic forcings, and was largely dominated by buoyancy driven down-slope and down-valley flows. Tower observations at the valley floor recorded strong continuous temperature decreases from sunset except for a brief period when cooling was interrupted by a warming episode. This transient warming event is modeled with good magnitude and temporal precision with LES. Analysis of the LES flow field confirms that the observed warming is a result of an intermittent turbulent event triggered by a slope to valley flow transition, as previously suggested by researchers based on tower observations. On the same night, a northerly cold-air flow from the Great Basin is channeled through a pass on the eastern valley sidewall. The gravity current plunges down into the stable valley atmosphere, overshooting the altitude of its neutral buoyancy, and generating a large-scale oscillatory motion. The resulting cross-valley flow creates strong vertical shear against the down-valley flow in the lower layers of the atmosphere. A portion of the cross-valley flow was captured by a scanning lidar. The nested LES is in good agreement with the lidar-recorded radial velocity. Furthermore, LES is able to resolve Kelvin-Helmholtz waves and ejection and sweep events at the two-layer interface, leading to vertical turbulent mixing from the top-down.

5.1 Introduction

The classical description of the nighttime atmospheric boundary layer (Nieuwstadt 1984) is described in a horizontally homogeneous environment over flat terrain, under quasi-steady state conditions. Turbulence is generated at the surface and transported upward. Turbulent fluxes decrease in magnitude from the surface to the top of the stable boundary layer (SBL). Within the SBL, the production of turbulence by mean shear dominates over the destruction by buoyancy, such that turbulence is temporally steady and continuous. The continuously turbulent SBL usually occurs under conditions of strong winds and/or large cloud cover which leads to reduced net radiative surface cooling (Van de Wiel et al. 2003). Furthermore, the traditional SBL also assumes horizontal homogeneity. As a result, past SBL related field campaigns have favored flat locations with uniform land cover, such as Cabauw in the Netherlands (Caughey 1982), the Beaufort Sea (Kosovic and Curry 2000), and the Great Plains in the Unites States (Poulos et al. 2002).

On clear nights with weak winds, the SBL cools rapidly. Turbulent motions are strongly damped by buoyancy stratification and intermittent. When the surface heat flux

exceeds a certain threshold set by the geostrophic wind speed, the SBL decays into a quiescent state (Derbyshire 1990), where turbulence is suppressed over prolonged periods greater than the time scale of the dominant eddies (Nakamura and Mahrt 2005). During these times, energetic mixing events known as turbulent bursts can occur intermittently over relatively short periods, and are usually responsible for the majority of the upward/downward transport of heat/momentum (Coulter and Doran 2002). Besides short, intense turbulent fluctuations, another frequent signature of bursting is warming below the elevation of such events (e.g. Whiteman et al. 2009, hereafter W09). This is because intense vertical mixing tends to bring down warm (in terms of potential temperature) air from aloft, leading to a transient nighttime warming signal. This should be differentiated from propagating gravity currents, when warming associated with wave troughs (downward-curving potential temperature isentropes) vanishes immediately after the wave passes. The latter usually occur on a much shorter time scale ~O(1 min).

Intermittent turbulence has been observed during field experiments since the last decade, yet its origin is not well understood. A few known mechanisms include passing density currents (J. L. Sun et al. 2002), breaking shear-instability waves (Newsom and Banta 2003), solitary waves and downward propagating gravity waves (J. L. Sun et al. 2004), turbulence and mean shear interactions (Nakamura and Mahrt 2005), and slope and valley flow transitions (W09). Note that except the last reference, all mechanisms were derived from the Cooperative Atmospheric-Surface Exchange Study -1999 (CASES-99) over nearly flat terrain. In other words, most of the known intermittency mechanisms are not terrain-induced, and quite generic

The most well-understood mechanism for intermittency is turbulence and mean-shear interactions, verified with wind tunnel measurements (Ohya et al. 2008). It is usually generated aloft due to elevated shear around the low-level jet (LLJ), and transported downward (Banta 2008). The structure of the SBL in this case is considered “upside-down” in contrast to the traditional picture (Mahrt and Vickers 2002). Since this mechanism is independent of the terrain, however, it can still fit into the classical SBL description (Nieuwstadt 1984) by modifying the turbulence closure. One such example is the short-tail Richardson number correction applied to the turbulent eddy viscosity formulation (Van de Wiel, Ronda, et al. 2002).

In reality, SBL flows are usually affected by the complex land-surface. Large-scale topographic features such as mountains and valleys have pronounced effects in stratified flows (Baines 1997). Heterogeneous land cover introduces additional variability into the SBL flow (Derbyshire 1995). Even over relatively flat terrain, drainage flows could still be generated or modulated by very shallow slopes (Mahrt et al. 2001). Although the complexity of terrain-induced flows could potentially lead to sources of intermittency, few have been reported. Zhou and Chow (2013) showed the formation of a standing wave over a shallow valley, and subsequent turbulent events due to gravity wave breaking. The shortage of knowledge on terrain-induced intermittency is partly due to the lack of field observations of the SBL over complex terrain. It is also likely that heterogeneity in the land surface tends to enhance turbulent mixing (Derbyshire 1995b), leading to less strongly stratified and less intermittently turbulent conditions.

In this paper, we move the SBL from the idealized setting to a site with highly complex terrain, focusing on terrain-induced turbulent events in a slope-valley system.

We investigate one of the intermittently turbulent nights described in W09 over a steep valley. With a numerical modeling approach, we reproduce the observed nighttime transient warming episode at the valley floor. The model also uncovers a new terrain-induced mechanism responsible for upside-down turbulent mixing. The elevated source of turbulence is an intruding cold-air drainage flow down a steep slope into a stratified valley atmosphere.

The numerical approach used in this study is large-eddy simulations (LES). LES is based on the definition of a spatial filter that separates the large resolved scales from the subfilter-scale (SFS) motions. The SFS stresses are represented by a turbulence model. The majority of the past LES studies of the SBL have been devoted to flat, periodic terrain, under weakly to moderately stable conditions (Saiki et al. 2000; Kosovic and Curry 2000; Basu and Porte-Agel 2006). This is mostly because stratification limits the length scale of turbulence, such that fine grid resolution, hence more computational resources, must be used to sustain resolved turbulence (Beare et al. 2006).

To conduct LES of realistic SBL flow over complex terrain, a grid nesting approach is adopted. Grid nesting takes information from the coarse grid and passes it to the fine grid as lateral boundary conditions. This procedure can be repeated over several nests until the desired grid resolution, which resolves the motion of interest, is reached (Zhong and Chow 2012). Grid nesting is frequently used in investigating fine flow features, such as katabatic winds on weak slopes (Zhong and Whiteman 2008) and effects of soil moisture and topographic shading on valley flows (Chow et al. 2006). Nested high resolution LES is an emerging numerical tool to study turbulent boundary layer flows over complex terrain. So far only few such studies have been conducted and many numerical issues still remain unsolved (Michioka and Chow 2008; Zhou and Chow 2013). In this paper, we show the feasibility and usefulness of nested LES in studying complex flows in a steep valley, with a simple nesting procedure.

5.2 Description of Site and Instrumentation

The field site of this study is Owens Valley in California, where the 2006 Terrain-Induced Rotor Experiment (T-REX) was conducted. Owens Valley is about 150 km long, 15 to 30 km wide and oriented approximately north to south (see Figure **5-1**(a)). The Sierra-Nevada mountain range west of the valley is at an elevation of ~4000 m above sea level (ASL). To the east of the valley are the Inyo and White Mountain chains at ~3000 m ASL. The average elevation change between the Sierra-Nevada crest and the valley floor is nearly 3000 m. While the west valley sidewall has a relatively gentle slope, the east side is quite steep. The valley has a semiarid climate with low, sparse vegetation. Some evergreen trees are dispersed at the upper elevations of both valley sidewalls.

A comprehensive description of the field instrumentation can be found in Grubisic et al. (2008). As presented in Figure **5-1**(b), this study only uses observation data from the National Center for Atmospheric Research (NCAR) integrated surface flux facility (ISFF) towers and the German Aerospace Center (DLR) Doppler lidar. The 34 m ISFF central tower had high rate sonic anemometers and temperature sensors installed at multiple elevations. The DLR lidar performed Range Height Indicator (RHI) scans in the cross-

valley direction (80^o azimuthal angle to the right and 260^o to the left), and recorded radial velocities.

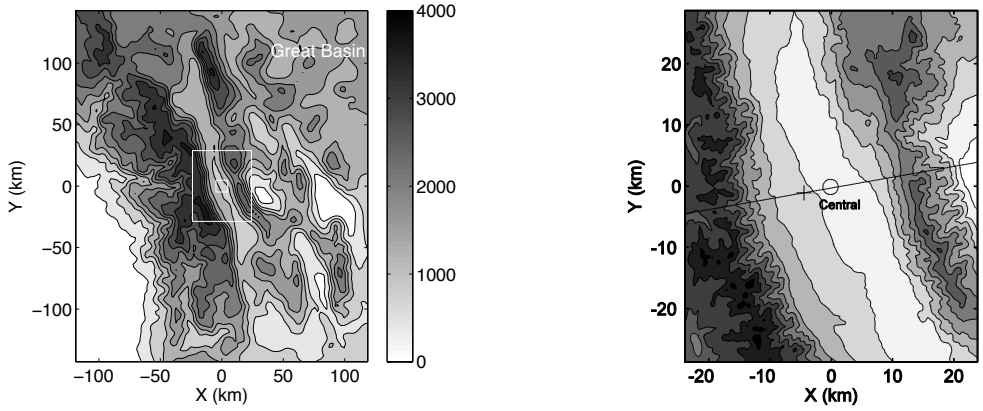

(a) (b)

Figure 5-1 Elevation contours for (a) the 2400 m grid with the 240 m and 50 m grid shown within, (b) the 240 m grid. Contour intervals are at 400m. Location of the NCAR ISFF central tower is marked by a circle. The DLR lidar is marked by a cross. Its cross-valley scan range (RHI80) is marked by the black solid line.

5.3 Model Description and Configuration

The Advanced Regional Prediction System (ARPS) is used for the simulations. ARPS was developed at the Center for Analysis and Prediction of Storms at the University of Oklahoma (Xue et al. 2000; Xue et al. 2001). It is a non-hydrostatic meso-scale and small-scale finite-difference numerical weather prediction model which runs in parallel using the message passing interface (MPI). ARPS uses a generalized terrain-following coordinate on an Arakawa C-grid. A mode-splitting time integration scheme is employed (Klemp and Wilhelmson 1978). This technique divides a big integration step (Δt_{big}) into a number of computationally inexpensive small times-steps (Δt_{small}) and updates the acoustically active terms, while all other terms are computed once every big time-step.

The length of the simulations is 8 hours starting from late afternoon (1600 LST/0000 UTC) to midnight (2400 LST/0800 UTC) on April 17th, 2006. The model domains are centered at the ISFF central tower (36.80152^{o}N, 118.16002^{o}W). Three one-way nested domains (Figure **5-1** (a)) are used to zoom into the region of interest in both horizontal and vertical directions. The ratio of horizontal domain area between successive nests is 5 to 1. Simulations are first performed on a 2400 m horizontally-spaced grid that covers the entire valley and the mountain ranges on both sides. Realistic initial and lateral boundary conditions are obtained from North American Mesoscale (NAM) reanalysis dataset. Results from the 2400 m grid are used to drive lateral boundaries of the 240 m grid, which are fed into the 50 m grid. The lateral boundaries are updated at a constant time interval (ΔT_b) set by the user, and are linearly interpolated in-between. Following the recommendation from the sensitivity study in Michioka and Chow (2008), frequent

updates are used. For the 50 m grid, lateral boundaries are updated every 180 s. Vertical grid stretching is applied to better resolve the surface layer. On the finest grid, the vertical resolution is 20 m with 5 m near surface spacing. Land surface was represented with high resolution terrain (10 m) and land cover (30 m) from the U.S. Geological Survey. A Rayleigh damping layer was set for roughly the top 1/3 of the domain. Some key model parameters are given in Table 5-1.

Table 5-1 List of nested model parameters

Nest	Grid size[4] (nx, ny, nz)	Domain (km)	$\Delta x/\Delta y$ (m)	$\Delta z/\Delta z_{min}$ (m)	ΔT_b (s)	Δt_{big} (s)	Δt_{small} (s)
1	(103, 123, 63)	240 x 288 x 18	2400	300/ 50	21600	1.5	1.5
2	(203, 243, 103)	48 x 57.6 x 12	240	120/50	900	0.5	0.1
3	(195, 195, 195)	9.6 x 9.6 x 3.84	50	20/5	180	0.2	0.05

On the 2400 m grid, ARPS is run in meso-scale mode with boundary layer parameterizations (Sun and Chang 1986). On the inner (240 m and 50 m) grids, large-eddy simulations (LES) is performed to resolve turbulent flows in the atmospheric boundary layer (ABL). The LES governing equations for the resolved fields are the momentum, continuity and scalar transport equations:

$$\frac{\partial \overline{\rho}\,\overline{u}_i}{\partial t} + \frac{\partial \overline{\rho}\,\overline{u}_i\,\overline{u}_j}{\partial x_j} = -\frac{\partial \overline{p}}{\partial x_i} - \overline{\rho}\,g\delta_{i3} + \overline{\rho}\epsilon_{imn}f_n\overline{u}_m - \frac{\partial \overline{\rho}\,\tau_{ij}}{\partial x_j}$$

$$\frac{\partial \overline{\rho}}{\partial t} + \frac{\partial \overline{\rho}\,\overline{u}_i}{\partial x_i} = 0$$

$$\frac{\partial \overline{c}}{\partial t} + \frac{\partial \overline{\rho}\,\overline{u}_i\overline{c}}{\partial x_i} = -\frac{\partial \overline{\rho}\,\chi_i}{\partial x_i} + S$$

where the spatial filter is denoted by an overbar. $\overline{u}_i$ are the velocity components, $\overline{p}$ the pressure, $\overline{\rho}$ the density, f the Coriolis parameter, $\overline{c}$ a scalar (e.g. temperature, moisture), and S a generic source/sink term. The filter can be considered a density-weighted Favre filter, and is applied implicitly in the code. The turbulent stresses τ_{ij} and scalar fluxes χ_{ij} are represented by the 1.5-order turbulent kinetic energy-based closure (TKE-1.5) of Moeng (1984). An additional prognostic equation for TKE is solved to determine turbulent eddy viscosity K_m and diffusivity K_h. More details on the turbulence model are given in Xue et al. (2000).

[4] Two ghost points are included in the number of grid points, so the domain size in the x direction, for example, is (nx-3)Δx.

5.4 Results and Discussion

5.4.1 Transient Warming

Figure 5-2 presents observed and modeled times-series of 30 m (AGL) temperature, wind speed and direction at the ISFF central tower. The observed temperature drops rapidly past 1900 LST at a rate of nearly 3 $^{o}Ch^{-1}$. A transient warming event takes place around 2040 LST and the temperature starts to increase. Over 1 ^{o}C of warming is achieved during the following half-hour period. The cause of this nighttime warming, as explained in W09, is a transition from slope to valley flows. Briefly, in the classic valley flow theory of Defant (1949), which does not consider synoptic influences, nighttime valley winds start with down-slope flows from valley sidewalls after sunset, and end with down-valley flows (from valley to the plain) which continue until morning. Down-slope winds are initiated through horizontal thermal gradients due to cooling of the slope surfaces (Fleagle 1950). After sufficient cooling of the valley, down-valley winds start to develop and gradually take over down-slope winds.

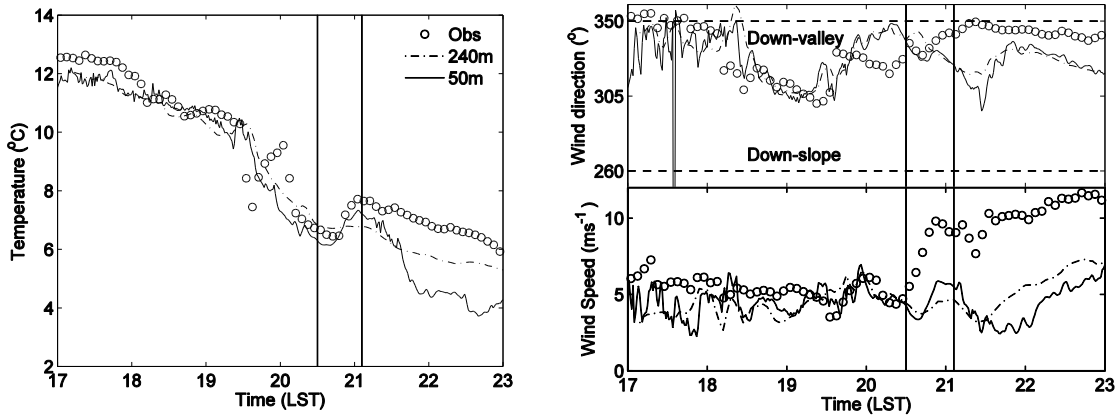

(a) (b)

Figure 5-2 Time-series of (a) temperature, (b) wind direction and speed at 30 m AGL at the central tower. Observation data is represented by circles; model results from the 240 m grid by dash-dotted lines, 50 m grid by solid lines.

In Figure 5-2(b), winds start from the down-valley direction after sunset. This is due to the residual daytime winds which were channeled along the valley by the northwesterly synoptic winds. Due to this background down-valley wind, the flow exhibits a combined down-slope-valley direction (~300^{o}) at the initiation of the down-slope winds. Shortly past 2000 LST, faster down-valley winds begins to dominate. The increased wind speed leads to stronger turbulent mixing that brings down potentially warmer-air from aloft, hence the observed warming signal. Simulations confirm this mechanism deduced from single-point tower measurements. Surface streamlines in Figure 5-3 are plotted at times of peak down-slope (1909 LST) and down-valley flows (2109 LST) corresponding to the central tower recordings. They show the transition from down-slope to down-valley winds over the entire valley.

In Figure 5-2(a), good agreement of modeled and observed temperature is achieved from 1700 to 2000 LST. The following warming event is captured by the 50 m LES with good magnitude and temporal precision. In comparison, the temperature predicted on the 240 m grid is relatively constant during the event, and does not increase. Similarly, both wind speed and direction before the warming episode are well-modeled, as shown in Figure 5-2(b). The transition to down-valley flows and the associated increase in wind speed are predicted on the 50 m LES grid, however to a reduced magnitude. The capability of LES to model the observed nighttime warming should not only be attributed to the increased grid resolution, but also to the lateral boundary conditions obtained from the 240 m grid, which provides satisfactory temperature and wind tendencies.

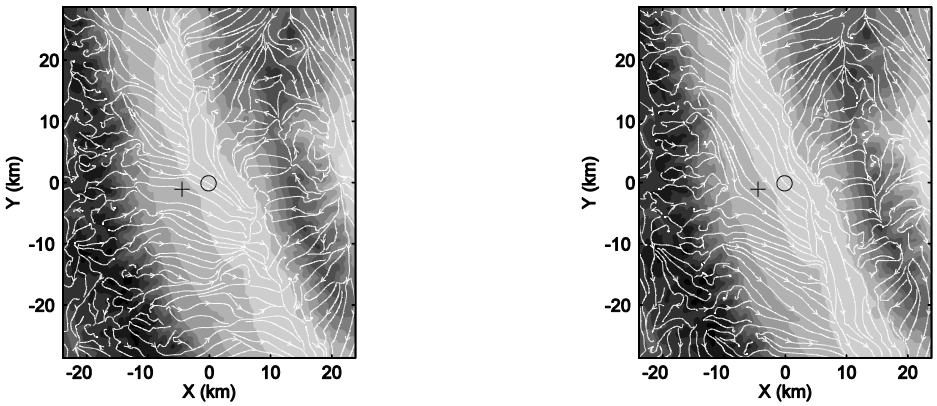

(a) (b)

Figure 5-3 Instantaneous streamlines of surface wind at (a) 1909 LST and (b) 2109 LST from the 240m grid.

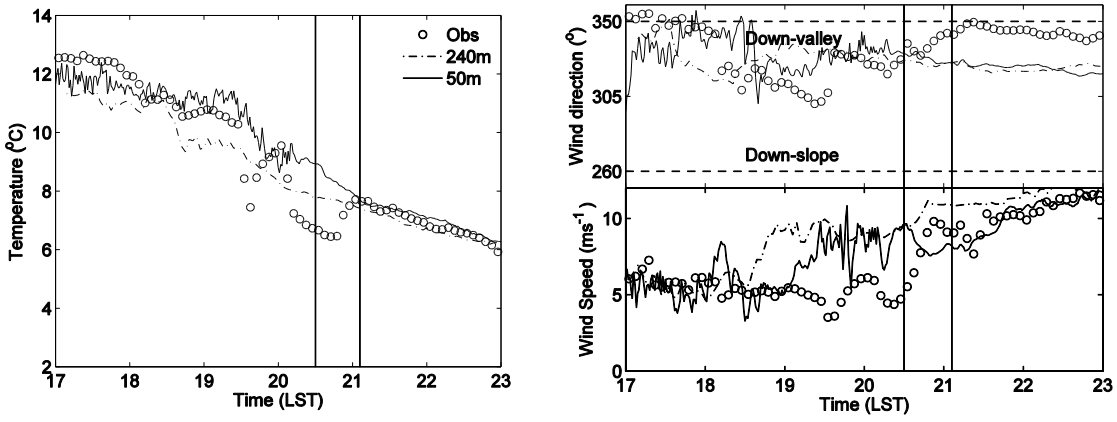

(a) (b)

Figure 5-4 As for Figure 5-2, but for a reduced surface roughness.

Model performance is less satisfactory past 2130 LST. On the LES grid, temperature is under-predicted by ~2 ^{o}C, wind speed by ~5 ms^{-1}, and direction by ~20^{o}. In an attempt to improve model results, a reduced surface roughness length of 1 cm used in the T-REX study by Doyle and Durran (2007) is adopted. In Figure **5-4**, modeled temperature and wind speeds improve significantly in the last 2 hours of the simulation on the LES grid, however, the warming event is no longer predicted. This sensitivity test reveals an important precursor to the observed warming event, which is a strongly stratified surface layer established by the westerly slope-flows. In Figure **5-4**(b), wind direction time-series show that the modeled down-slope winds do not reach the central tower after 1900 LST. At the same time, the associated rapid cooling is also absent (Figure **5-4**(a)). Without the strong cooling from the cold drainage flows, the valley surface layer is less stratified and continuously turbulent throughout. Therefore, the modeled temperature/wind speed decreases/increases smoothly and continuously.

5.4.2 Cold-Air Intrusion

Local sunset on Apr 17th was before 1700 LST. Soon after, the DRL lidar scan reveals an interesting three-layer flow structure in the cross-valley direction. The top panel of Figure 5-5(a) presents the RHI lidar scan in the 80^{o}-260^{o} azimuthal directions at 1716 LST. The axes are adjusted such that the lidar is located at the origin. Since radial velocities towards and away from the lidar were recorded, changes in the sign of velocities horizontally-across the origin indicate flow in one coherent direction. Within the lidar scan plane, a westerly flow component is present in the bottom ~1.5 km and above ~2.5 km from the valley floor. An easterly flow component about 1 km in depth is found in-between. The three-layer flow structure is captured both on the 240 m grid, presented in the bottom panel of Figure 5-5(a), and the 50 m grid (Figure 5-5(b)) which reveals richer details of the flow.

As shown in the previous subsection, westerly flow in the bottom layer is a result of the down-slope flow from the western sidewall. The drainage flow extends east of the lidar and the central tower, to nearly the bottom of the eastern sidewall (see Figure 5-3(a)). The jet-like structure of the drainage flow can be seen on the bottom panel of Figure 5-5(a). The westerly flow in the top layer is a component of the synoptic flow, which is in the northwest direction ~300^{o}. This synoptic flow is responsible for the daytime down-valley flow, because of the channeling effect of the valley (W09). The source of the easterly flow is unclear due to the limited horizontal scan range of the lidar. Ground-based towers are not useful since the flow is present in the mid-altitudes far beyond their reach. Radiosondes could capture this flow, but was unfortunately not launched at that night. 3D simulations, on the other hand, had the advantage of complete spatial and temporal coverage. Once validated against observations, we can use the model results to investigate the source of the flow.

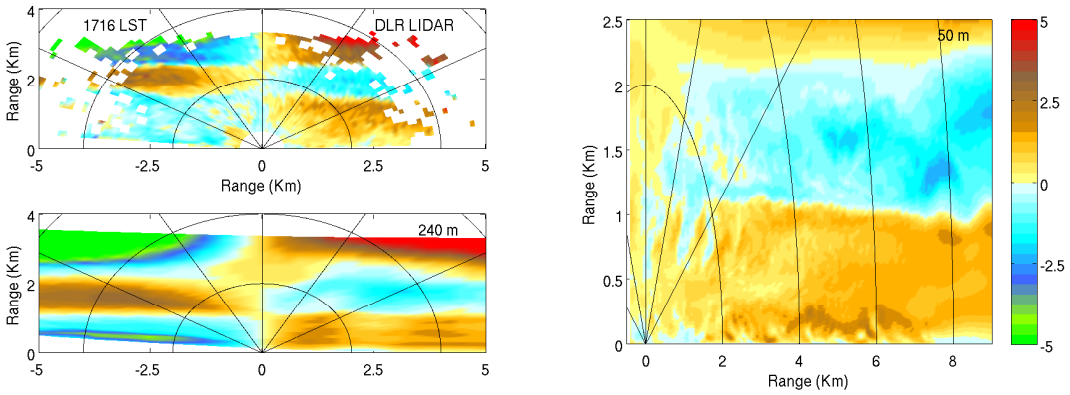

(a) (b)

Figure 5-5 Radial velocity contours in the cross valley direction at 1716 LST from (a) the DRL lidar RHI scan (top panel) and the 240 m grid (bottom panel), (b) the 50 m grid. Lidar is located at the origin. Cold/warm colors indicate flow towards/away from the lidar.

In Figure 5-5, the flow is roughly homogeneous in the horizontal direction. Therefore, to quantitatively assess model results against lidar observations, horizontal averaging is performed along the cross-valley direction to obtain a vertical profile of the wind speed V_H in the horizontal direction on the scanning plane, which is 10^o from the east-west direction. For the lidar data, V_H is obtained by taking the horizontal component of the radial velocity vectors. Significant errors in V_H are expected in the zone directly above the lidar, due to the large angles between the horizontal and the radial direction. Therefore data within 45^o from the vertical axis is not used in averaging. For the model data, V_H is computed by projecting horizontal wind vectors onto the scanning plane.

Figure 5-6 presents both V_H and its standard deviation σ_{V_H} along the horizontal direction computed from data presented in Figure 5-5. The easterly flow spans from 1.5 to 2.4 km AGL, with a maximum speed of ~2 ms^{-1}. The westerly drainage flow zone is roughly 1.5 km deep and less than 1 ms^{-1} fast. The 240 m grid results over-predict wind speeds in both flow zones. In comparison, better agreement in terms of wind speeds are achieved on the 50 m grid. However, both models produce a ~400 m deeper/shallower easterly/westerly flow zone than what the observation shows. σ_{V_H} can be considered a measure of turbulence intensity given the approximate horizontal homogeneity of the flow. Both the lidar and the 50 m LES data showed σ_{V_H} decreasing slightly with height.

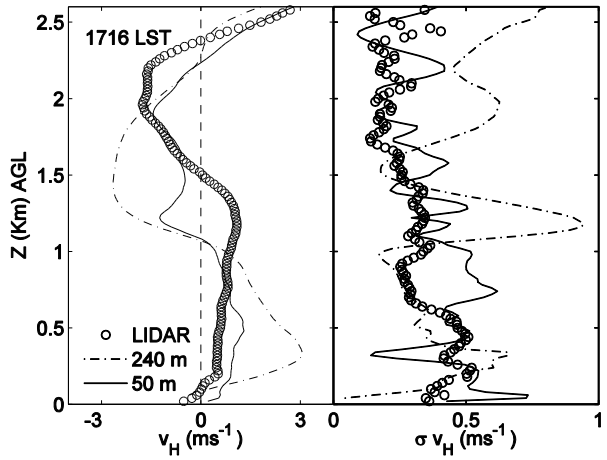

Figure 5-6 Vertical profiles of horizontally averaged velocity (left panel) and standard deviation at 1716 LST. Lidar data is represented by circles, model data from the 240 m grid by dash-dotted lines, the 50 m grid by solid lines.

The 50 m LES shows spikes in σ_{V_H} at the intersections of easterly flow to the synoptic-westerly above at ~ 2.3 km and the down-slope westerly below at ~ 1.1 km AGL. The 240 m results show similar local maxima at the intersections, however with a much larger magnitude. This model over-prediction is a result of the large-scale wave motion on the 240 m grid. As we show in the following subsections, turbulent processes including shear-instabilities waves, ejection and sweep events occur in the flow transition zones. These processes have comparable length scales to the 240 m grid spacing, and hence not well resolved. The subgrid representation of these processes is less sufficient in breaking down the large-scale waves, leading to an over-prediction of σ_{V_H} on the 240 m grid. Overall, Figure 5-6 shows that elevated sources of turbulence, indicated by peaks in σ_{V_H}, are present at the flow transition zones.

5.4.2.1 Slope Region

The source of the cross-valley winds is a synoptic-scale northerly flow from the Great Basin northeast of the Owens valley (see Figure **5-1**(a)). This is shown on the horizontal plane at 2.5 km ASL (~1.5 km AGL) on Figure 5-7(a) from the 2400 m grid. The northerly flow is channeled through the topographic "gap" between the White and the Inyo Mountains at Y ~ 40 km and within the Inyo Mountains at Y ~ 5 km. The 240 m grid on Figure 5-7(b) shows the clockwise-turning of the synoptic flow into the valley. The cross-valley flow is energetic and nearly reaches the western sidewall. The down-valley flow is disrupted between -10 to 10 km in the Y direction.

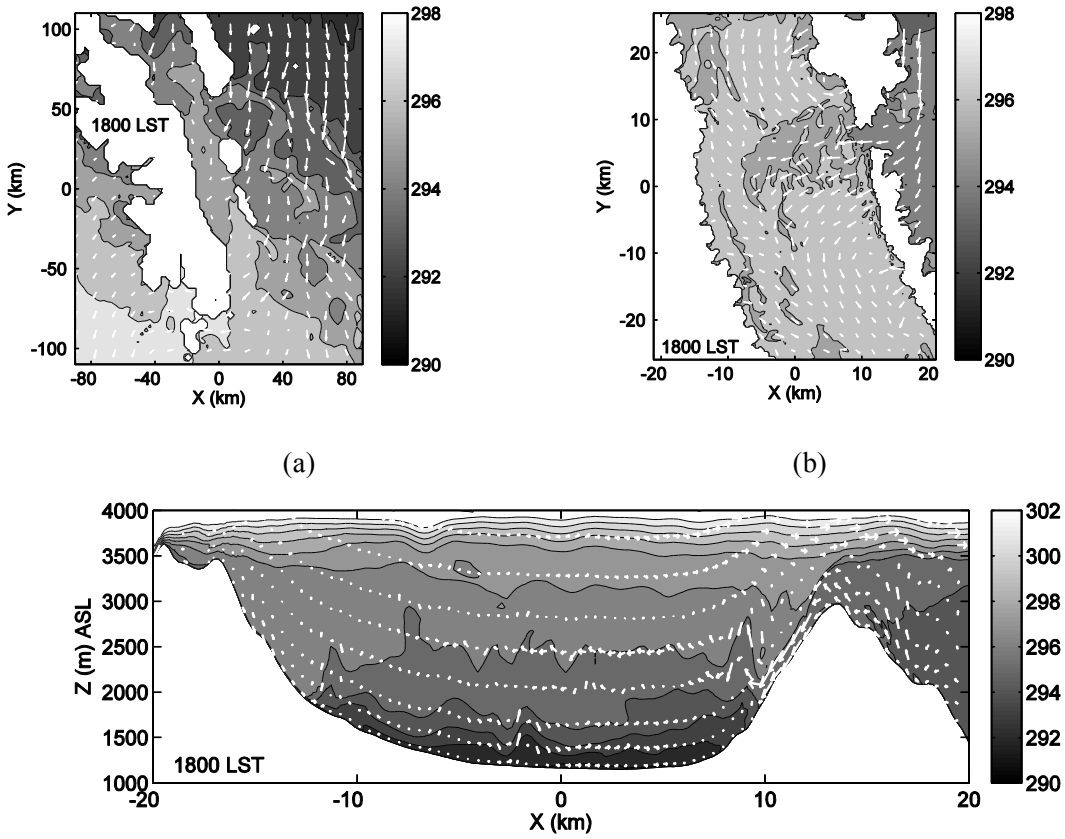

Figure 5-7 Contours of potential temperature $\boldsymbol{\theta}$ in the horizontal plane at 2.5 km ASL (~1.5 km AGL) on the (a) 2400 m and (b) 240 m grid, in the vertical xz plane on the (c) 240 m grid at 1800 LST. Contour intervals are 1 K. White spaces in (a) and (b) indicate mountains higher than 2.5 km ASL.

The potential temperature contours in Figure 5-7(a, b) show that the inflow from the Great Basin is colder than the valley air at the same elevation. Upon entrance into the valley, the cold-air sinks along the sidewall as a down-slope current, plunging to an altitude of neutral density as shown in Figure 5-7(c). Moreover, the excess momentum gained during the katabatic descent leads to the cold-air current overshooting its equilibrium altitude, leaving the vicinity of the down-slope flow, and returning to it in a large-scale cross-valley oscillatory flow. Such a process associated with down-slope dense fluid intrusion into a stratified environment is termed "springback" motion by Baines (2005) and "stratified flow response" by Mayr and Armi (2010). Many natural phenomena are attributed to this process such as powder snow avalanches, dense overflows in the ocean, and cold river flow into lakes (Baines 2001, and references therein). A 3D description of the cold-air intrusion is presented in Figure 5-8 in the form of an iso-surface height for θ at 295 K. The density driven flow resembles a waterfall, with a deeper flow through the topographic gap on the eastern sidewall. Ripples form at the end of the down-slope flow and are advected down valley. Similar flows are also

observed at Owens valley on the evening of March 29th during EOP-2 of the T-REX campaign (Daniels 2010).

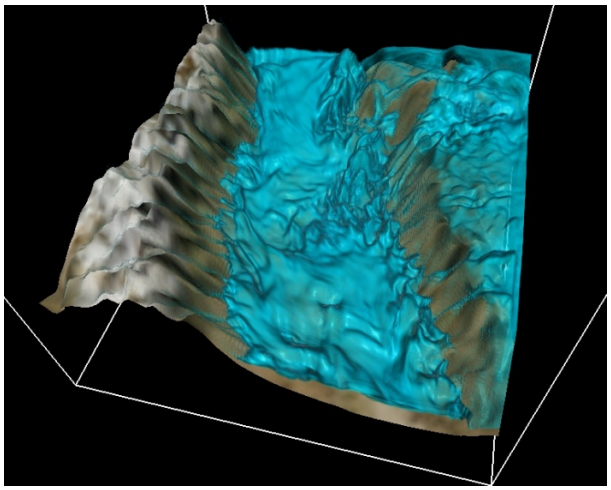

Figure 5-8 Iso-surface height for potential temperature of 295 K at 1800 LST.

Cold-air induced down-slope flows are different from classic drainage-flows. The latter are initiated by a horizontal thermal gradient between the cooled slope surface and the adjacent air (Fleagle 1950). The classic Boussinesq slope flow formulation is usually described in a rotated slope coordinate (n, s) (Haiden 2003).

$$\frac{du_s}{dt} = -\frac{1}{\rho_o}\frac{\partial p}{\partial s} + g\frac{\theta}{\theta_o}sin\alpha$$

$$\frac{dw_n}{dt} = -\frac{1}{\rho_o}\frac{\partial p}{\partial n} + g\frac{\theta}{\theta_o}cos\alpha$$

where u_s and w_n are the along-slope and slope-normal velocities, α the slope angle, p and θ the pressure and thermal perturbations, ρ_o and θ_o the reference density and potential temperature. Since the depth of the drainage flow is usually shallow compared to the down-slope length scale, quasi-hydrostatic equilibrium $\frac{1}{\rho_o}\frac{\partial p}{\partial n} = g\frac{\theta}{\theta_o}cos\alpha$ is often assumed such that flow is parallel and attached to the slope surface (Mahrt 1982). However, the balance is upset during a cold-air intrusion. The temperature deficit associated with the cold air $\theta_{cold-air}$ is larger in magnitude than that of the radiatively cooled slope air θ_{slope}. Therefore, the stronger along-slope acceleration $g\frac{\theta_{cold-air}}{\theta_o}sin\alpha$ causes the flow to accelerate beyond its equilibrium elevation, and lift off from the slope due to the then positive forcing term $g\frac{\theta}{\theta_o}cos\alpha$ in the slope-normal direction.

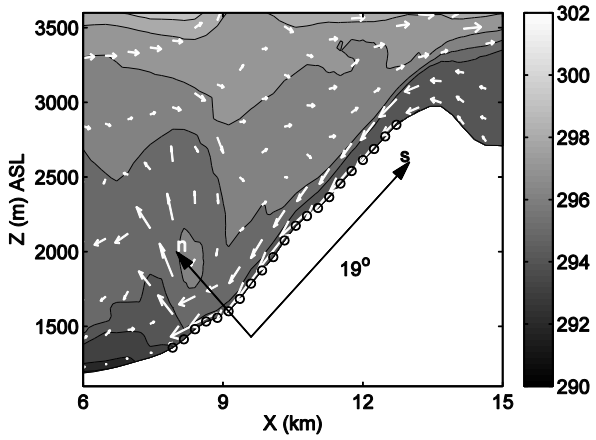

Figure 5-9 Potential temperature contours in the vertical xz plane at 1830 LST on the eastern sidewall. The vertical component *n* of the slope coordinates (*s, n*) is off direction due to different x-y scaling, and plotted only for illustration purposes. Circles mark the locations used in Figure 5-10. Contour intervals are 1 K.

To investigate the characteristics of the density current, we first look at a snapshot of the flow at 1830 LST in Figure 5-9, when the down-slope flow descends deep into the valley. The flow is deep and approximately horizontal on the top of the slope, and quickly plunges, turning into a thin, fast current. It reaches its neutral buoyant elevation at around X ~ 9 km, and spreads out over a deep layer into the valley atmosphere. A linear fit calculates a slope angle of 19^o between X = 9 ~ 13 km. The wind vectors are then rotated into the slope coordinates, and are presented in Figure 5-10. For ease of comparison, the x-axis uses the original X coordinate rather than the slope coordinate s. The density current is in the slope-parallel direction, as indicated by the near-zero values of w_n in Figure 5-10(a). Large positive w_n and corresponding decreases in u_s are observed past 8.88 km to the west, indicating the springback motion.

The depth of the flow h is estimated at the height of the minimum absolute value of u_s. After an initial decrease from the slope top following the plunge, h increases steadily down the slope from 250 m at 11.8 km to 330 m at 9.84 km. The growth rate of the cold-air flow $\left|{dh}/{ds}\right| \approx 0.04$, or $2.1\times10^{-3}\alpha$ normalized by the slope angle. This is larger than, yet in order of magnitude agreement with, the values of $1.1\times10^{-3}\alpha$ obtained from the laboratory studies of Ellison and Turner (1959). The growth of the cold-air flow is primarily due to turbulent entrainment from above the plume (Turner 1986). Baines (2005) furthered showed that entrainment processes are more likely to occur over steep slopes > 20^o. The effect of entrainment of surrounding fluids is a net inflow of mass indicated by the increased depth and speed of the down-slope flow in Figure 5-10(b). Furthermore, since the valley air at the same elevation is potentially warmer than the cold-air plume, downward turbulent mixing leads to warming within the plume. Note that the difference in θ reverses sign above 170 m and approaches 1 K. This is an artifact of the background stratification and elevation difference between the two slope locations.

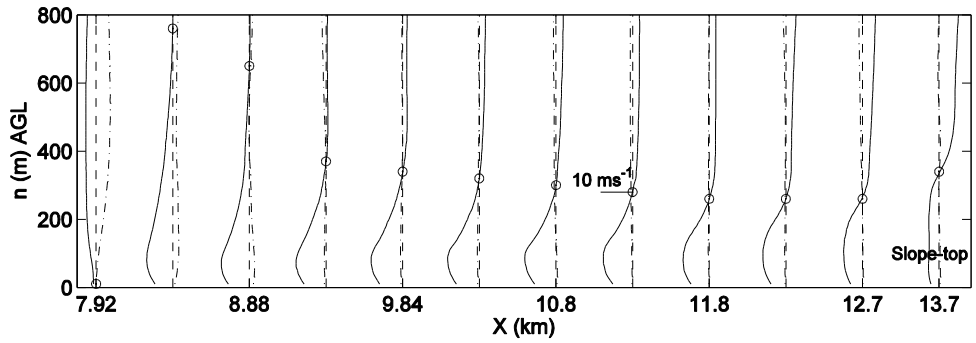

(a)

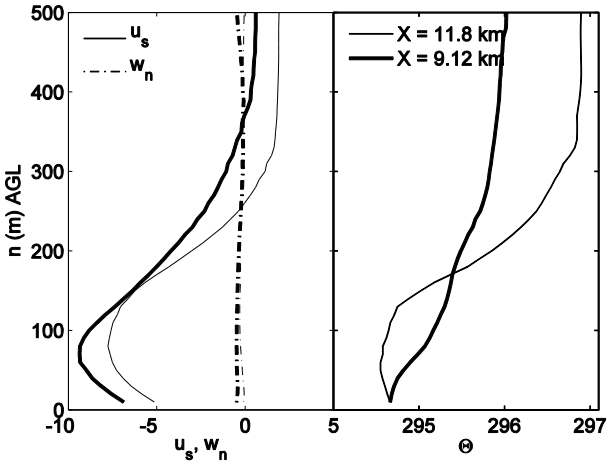

(b)

Figure 5-10 Vertical profiles of (a) wind speed in the slope coordinate and (b) wind and potential temperature at the up-slope (X = 12.7 km) and down-slope (X = 9.12 km) locations at 1830 LST. Solid and dash-dotted lines represent wind components (u_s, w_n) along and perpendicular to the slope. Circles represent the height of the minimum u_s.

The entrainment process is resolved on the 240 m grid as shown by the downward pointing wind vectors above the plume in Figure 5-9. To quantify its extent, the entrainment coefficient E is computed from a mass balance.

$$\frac{dQ}{ds} = EU_s = E\frac{Q}{h}$$

where $Q = \int_0^h u_s dn$ is the 2D volumetric flow rate, U_s is the depth averaged wind speed of the plume. Based on the original laboratory work of Ellison and Turner (1959), and modifications by Turner (1986), the following empirical relationship evaluates E based on the gradient Richardson number Ri.

$$E = \begin{cases} 0.08 & Ri < 0 \\ \dfrac{0.08 - 0.1Ri}{1 + 5Ri} & 0 < Ri < 0.8 \\ 0 & Ri > 0.8 \end{cases}$$

where $Ri = N^2/S^2$ is the ratio of the buoyancy frequency (N) over vertical shear (S) squared. Negative/positive Ri indicates unstable/stable conditions. Turbulence in stratified flows can be further categorized into the continuous regime Ri<0.25, the intermittent regime 0.25<Ri<1, and the quiescent regime Ri>1 (Stull 1988). Since entrainment is fundamentally a turbulent mixing process between the environmental fluid above and the plume below, its negative correlation with Ri is expected. In the above formulation, as stratification increases, turbulent mixing is suppressed, hence E decreases. Above a certain threshold, turbulence is nearly damped out such that turbulent entrainment no longer occurs.

Figure 5-11 presents Q as function of the down-slope distance. A linear fit using data east of 9.84 km estimates $|dQ/ds|$ to be around 220 $m^2s^{-1}km^{-1}$. Variations in $U_s = 5.35 \pm 0.33$ ms^{-1} are small, since both Q and h increased down-slope. An along-slope-averaged $\overline{U_s}$ is used to compute E. Unlike the laboratory setting, the background stratification is not uniform along the slopes of Owens Valley. Therefore, we estimate Ri in a bulk measure from the surface to the elevation n_{max} of the maximum along-slope winds u_s

$$Ri_b = \frac{\frac{g}{\overline{\theta}}[\theta(n_{max}) - \theta_1]n_{max}}{[u_s(n_{max}) - u_{s,1}]^2} cos\alpha$$

where Ri_b is a bulk Richardson number, subscript 1 stands for the elevation of first grid point above the wall, $cos\alpha$ is a converting factor from slope to standard coordinates. Figure 5-12 is obtained by repeating the same procedure from 1730 to 1900 LST during the cold-air intrusion. A considerable spread (0.045 – 0.09) exists in model data within the unstable regime (Ri < 0) early on during the evening transition. Data seems to cluster around E = 0.06 rather than 0.08. The agreement in the stable regime is fairly good, although most model data are obtained under moderately stratified conditions Ri < 0.5.

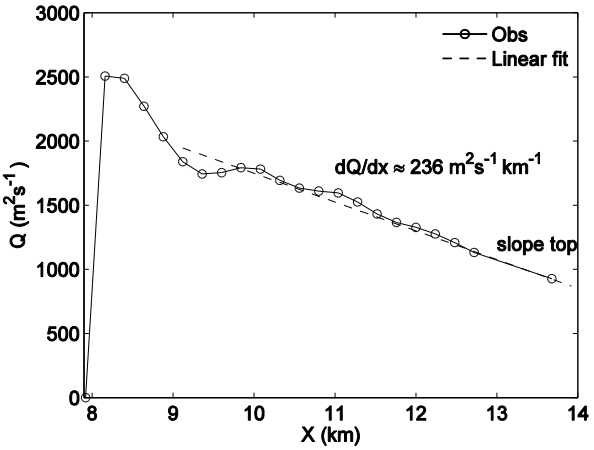

Figure 5-11 Volumetric flow rates along the slope at 1830 LST. Dashed line represents a linear fit.

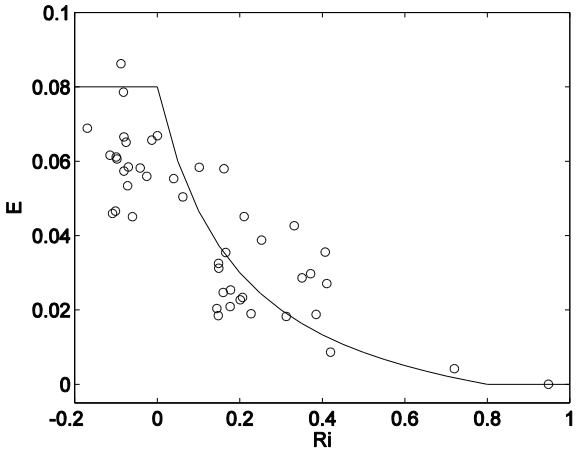

Figure 5-12 Entrainment coefficient E as function of Richardson number R_i. The solid line is the empirical function of Turner (1986). Data were sampled at every 3-minute between 1730 to 1900 LST.

5.4.2.2 Valley Region

Lidar scans in Figure 5-5 reveals the induced cross-valley flow due to cold-air intrusion on the eastern sidewall. This elevated cross-valley current has a significant impact on turbulent mixing in the valley boundary layer during evening transition. Figure 5-13 shows three consecutive xz slices of θ contours on the 50 m LES grid. The presence of a large-scale wave with a peak at X ~ 0.58 km and trough at X ~-1.7 km is indicated by the elevation and depression of the θ isentropes. The wave is at the interface of the easterly cross-valley flow above and westerly drainage flow below (see also Figure 5-5(b) and Figure 5-6). Its amplitude is roughly 200 m and it is propagating from east to west. The

horizontal extent of the wave is visualized by contours of θ and w in Figure 5-14 at the layer interface. Its peak and trough are indicated by zero w, which is 90° out of phase with θ. A phase speed of -4.0 ms^{-1} is measured by tracking the maximum w through consecutive frames.

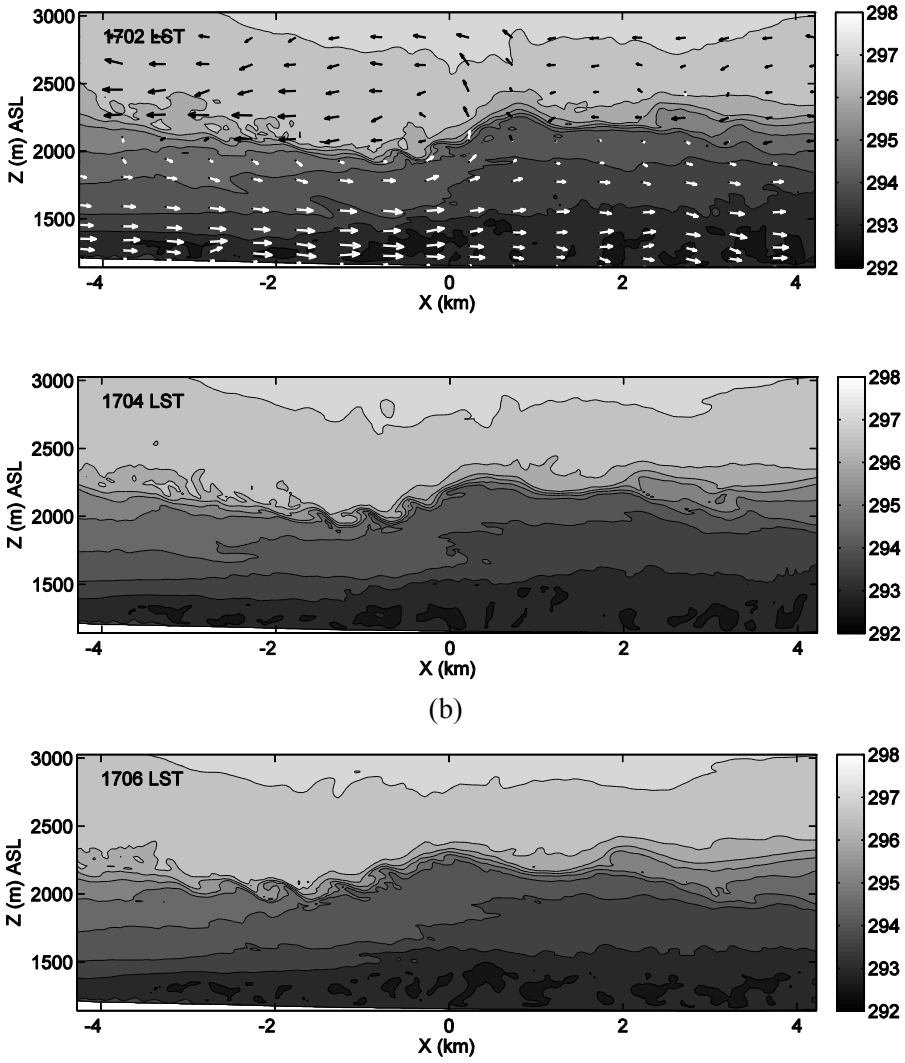

(a)

(b)

(b)

(c)

Figure 5-13 Potential temperature contours in the vertical xz plane at (a) 1702 LST, (b) 1704 LST, and (c) at 1706 LST. Contour intervals are 0.5 K. (*u, w*) velocity components are plotted in (a).

Figure 5-13 shows overturning billows of the Kelvin-Helmholtz (KH) type at the trough ahead of the large-gravity wave. The KH waves have a much smaller wave length λ_{KH}~500 m and are prorogating at 125° to the northwest in Figure 5-14(a). The formation of the KH waves is through a shear-instability mechanism at the two-layer interface. Figure **5-15** presents vertical profiles of key meteorological variables at the domain origin at 1700 LST right before the breaking of KH waves. The two-layer structure is indicated

by opposing u velocities at ~2000 m ASL, separating the cross-valley flow (80°) above and down-valley flow (350°) below. In comparison, the north-south velocity component v varies only slightly from 4 ms^{-1} to 2 ms^{-1} over a depth of 1500 m.

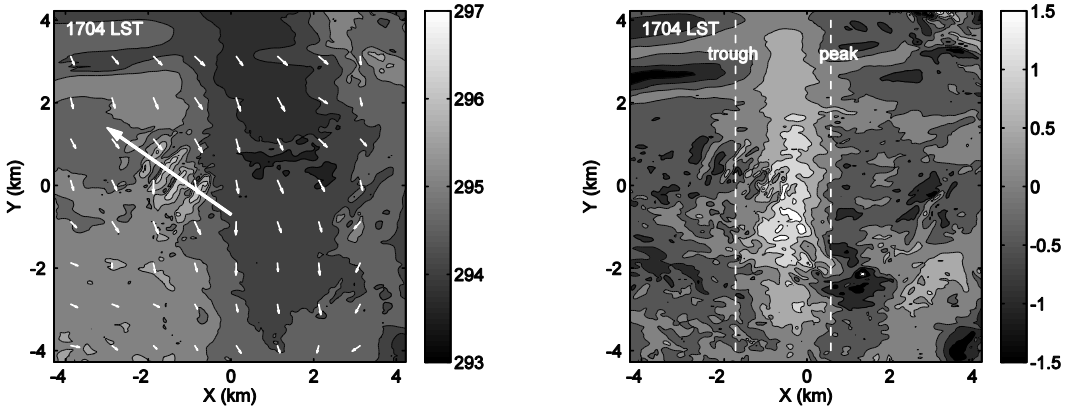

(a) (b)

Figure 5-14 Contours of (a) potential temperature θ and (b) vertical velocity w in the horizontal plane at 2 km ASL (~1 km AGL) at 1704 LST on the 50 m grid. Contour intervals are 0.5 K for θ, and 0.5 ms^{-1} for w. (u, v) velocity components are plotted in (a). Dashed lines in (b) mark the approximate location of zero w for the large-scale cross-valley flow.

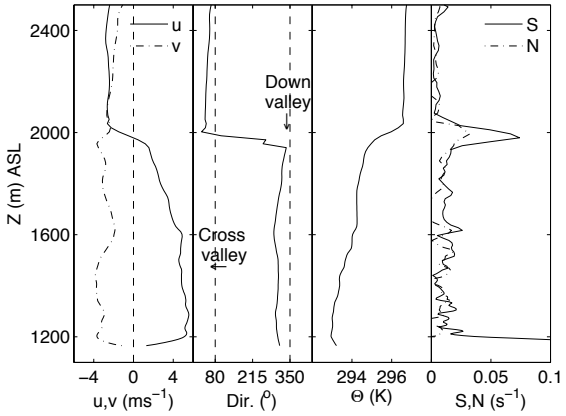

Figure 5-15 Vertical profiles of winds speed, direction, potential temperature, shear and buoyancy frequency at 1700 LST at the central tower location on the 50 m grid. Dash line in the wind speed plot indicates zero velocity. Two dashed lines in the wind direction plot indicate the easterly cross-valley direction (80°), the down-valley direction (350°). Data are averaged over 5 minutes.

The two-layer flows introduce an elevated peak in shear in addition to the surface maximum. The vorticity thickness δ_ω, representative of the depth of the mixing layer, is approximately 100 m based on the vertical extent of the shear layer. The KH wavelength λ_{KH} is about 5 times larger than δ_ω. This value is within the range $5.0\delta_\omega > \lambda_{KH} > 3.5\delta_\omega$ of direct numerical simulation (DNS) results (Rogers and Moser 1994). Finally, to explain the direction of the KH waves, the flow is projected onto a vertical plane of maximum shear, aligned in the 125°-305° wind directions, represented by the solid white line in Figure **5-14**(a). This converts the 3D KH shear-instability into a 2D phenomenon with 180° opposing flows. Therefore, KH billows form in the direction of the projection plane. Meanwhile, the KH billows are advected in the direction perpendicular to the projection plane.

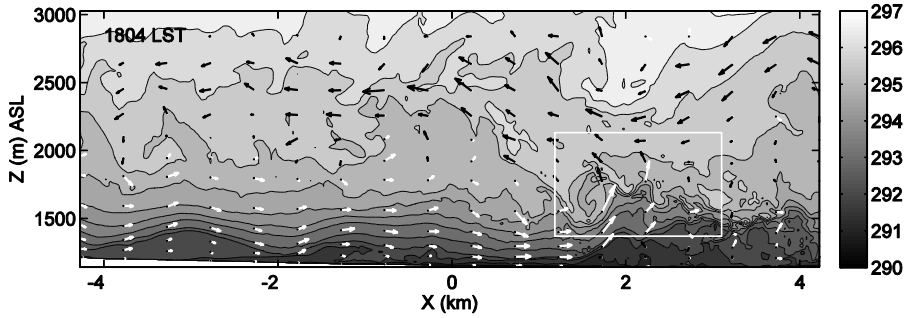

(a)

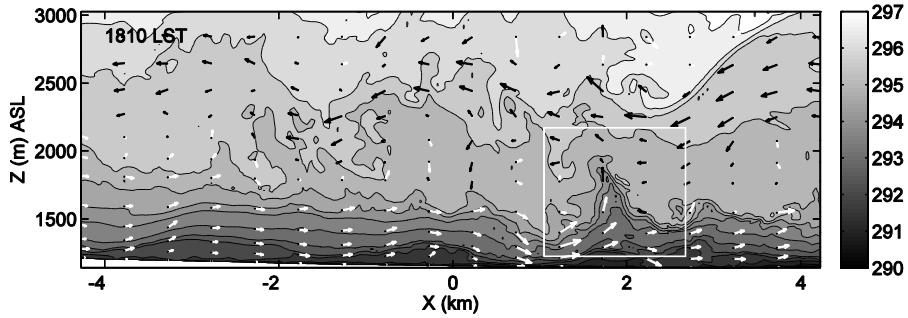

(b)

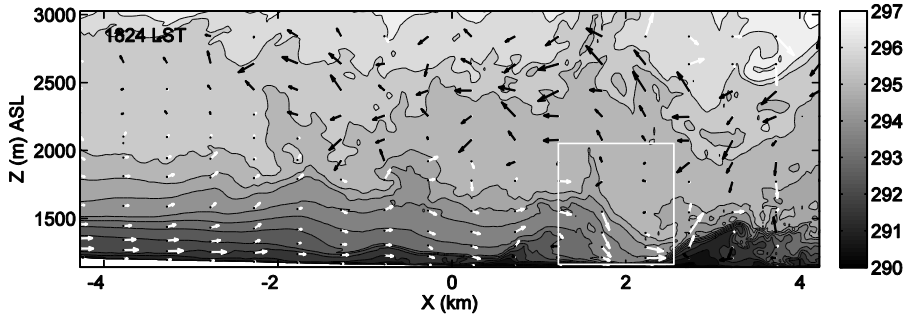

(c)

Figure 5-16 Potential temperature contours in the vertical xz plane at (a) 1804 LST, (b) 1810 LST, and (c) at 1824 LST. Contour intervals are 0.5 K. An overturning billow is highlighted in (a), an ejection event in (b), and a sweep event in (c).

More energetic cross-valley-flow-induced mixing events occur later, particularly on the eastward side of the valley. Past 1800 LST, the cold-air intrusion penetrates deeper into the valley, along with the cross-valley springback motion. The shear-instability process continues, resulting in the formation of KH billows, whose subsequent destruction lead to further turbulent mixing from the top-down. For example, three wave periods are present in the highlighted region in Figure 5-16(a), directly under a large-scale wave trough at 2500 m ASL. The wave amplitudes increase from east to west. Besides KH waves, sporadic upward-ejections in Figure 5-16(b) and downward-sweep events in Figure 5-16(c) are also resolved on the LES grid.

Through large-scale coherent KH, ejection and sweep events, along with the continuous subgrid scale (SGS) mixing processes, the elevated shear layer acts as a source of elevated turbulence during the evening transition in the valley. Figure 5-17 presents time-series of vertical velocity *w* and turbulent kinetic energy (TKE) within the valley boundary layer. While the former represents resolved turbulence, the latter is a measure of the SGS mixing. Significant amount of elevated turbulence is simulated at 2000 m ASL from 1730 LST and extending up and down to a thicker layer between 1500 to 3000 m ASL past 1830 LST.

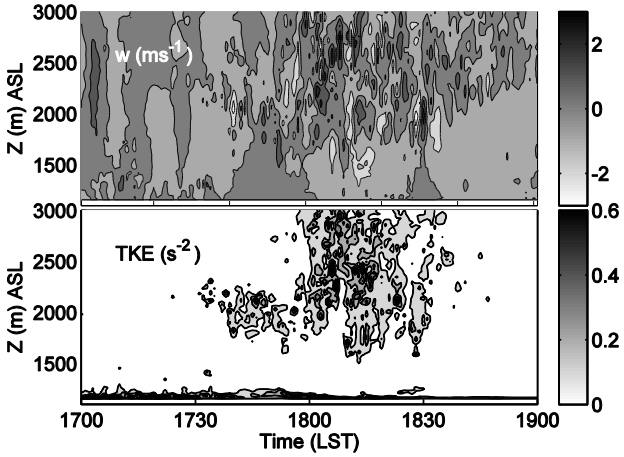

Figure 5-17 Time height contours of vertical velocity (top) and turbulent kinetic energy (bottom). Contour intervals are 1 ms^{-1}, and 0.1 s^{-2}. Data is sampled every minute.

5.5 Summary and Conclusion

High-resolution LES was performed to simulate the nighttime SBL in Owens Valley, California during the T-REX field campaign. This study validates the terrain-induced intermittency mechanism based on slope-valley flow transitions, and uncovers a novel top-down turbulent mixing mechanism due to valley cold-air intrusions. Numerically, this study demonstrates the feasibility and usefulness of nested LES of the SBL flows over complex terrain. Simulations were driven by realistic initial and boundary conditions, and nested sequentially from the NAM reanalysis field to a 50 m resolution micro-scale domain where turbulence was largely resolved. Model results were validated with tower

measurements, and lidar scans. Good agreement was achieved without modeling tuning, especially on the LES grid.

The transient nighttime warming event documented in W09 was reproduced with LES to good magnitude and temporal precision. In comparison, the coarser 240 m grid failed to capture the warming event. This suggested the importance of grid resolution in simulating intermittent turbulence in the SBL over complex terrain (Zhou and Chow 2011). The 3D simulation confirmed the warming mechanism proposed in W09, which was inferred from tower measurements. Surface warming was a result of the transition from cold western-slope drainage flow to the warmer down-valley flow about four hours after sunset. A decrease of surface roughness improved model predictions past the warming event. However, the resulting down-valley flow dominated over the slope flow early in the evening such that the warming event was absent. The sensitivity study showed that rapid cooling associated with the drainage flow at the onset of evening transition was an important precursor to the surface warming event.

On the eastern slope, a synoptic scale cold-air flow from the Great Basin to the northeast of Owens Valley was advected into the valley through topographic "gaps" along sidewall. The cold-air intrusion resembled the laboratory study of dense flows on slopes of intermediate steepness into a stratified environment (Baines 2005). Our simulations of the highly turbulent atmospheric flow showed good qualitative agreement with the laboratory-scale salt-water current. Upon entrance into the valley, the dense cold-air plume plunged down the steep (~19^o) eastern slope, overshot the altitude corresponding to its neutral buoyancy, took off from the slope due to its excess momentum, and eventually returned to its equilibrium elevation inside the valley. The cold-air plume entrained potentially warmer valley air aloft, leading to a linear increase of volumetric flow rate down the slope. The empirical formulation of Turner (1986) from laboratory studies was used to relate turbulent entrainment to the Richardson number, which represented the state of turbulence in the SBL. A good empirical fit was found for $0 < Ri < 0.5$. A relatively wide spread in the entrainment coefficient E was found for near-neutral conditions during early evening transition. LES data suggested a smaller value of 0.06 compared to the original value of 0.08. In the future, idealized LES of cold-air plumes on uniform slopes should be performed to better characterize turbulent entrainment processes in the slope SBL.

Finally, the impact of the cold-air induced cross-valley current on turbulent mixing in the valley atmosphere was investigated with the 50 m LES. Directional shear between the elevated easterly cross-valley flow and the westerly drainage flow was a source of shear-instability, and led to the development of KH billows along the two-layer interface. Besides breaking KH waves, energetic ejection and sweep events were present around the shear layer, further enhancing turbulent mixing from top-down. This elevated source of turbulence led to a non-classic top-down transfer of TKE, and contributed to a deeper valley SBL.

Chapter 6 Summary and Recommendations

6.1 Summary

This dissertation adopts large-eddy simulation (LES), a numerical approach, to model the nighttime stable boundary layer (SBL). Unlike many previous numerical studies which fall into the weakly and moderately stable regime, typical of overcast, windy nights, this dissertation focuses on the strongly stable conditions which happen during clear, calm nights. Efforts are devoted towards simulating intermittent turbulent bursting events under these strongly stable conditions, and investigating their underlying mechanisms. Another distinguishing feature of the simulations presented in this dissertation is that two of cases are performed over complex terrain, driven by realistic boundary forcings from meso-scale model reanalysis. The nested LES results are directly comparable with field observations, and in many ways complement observations with virtually complete spatial and temporal coverage. The combined nested LES and field approach can be beneficial in investigating ABL flows.

Three cases studies of the SBL are presented. Using an idealized setup, the SBL under a range of stability regimes from moderate to intermittent is modeled with LES in Chapter 2. Among them, the strongly stable ABL is modeled for the first time in the LES literature. Mean profiles of wind and potential temperature, turbulent fluxes and variances are quantified and validated with field observations. Intermittent turbulence develops at the elevated shear region under the low-level jet. The responsible mechanism is shown to be through mean shear and turbulence interactions.

Chapter 4 and 5 present two cases of nested LES over real complex terrain. Chapter 4 investigates an observed turbulent bursting event due to shear-instability waves over a relatively flat site in Kansas. Nested LES reproduces the observed event with good temporal and magnitude accuracy. LES pinpoints the origin of the waves in an upwind valley which is out of range for the field instrumentation. The intermittency mechanism is found to be through gravity wave braking over a stagnant cold-air bubble across and down the shallow valley. The complexity of the terrain is dramatically increased in the case presented in Chapter 5. Nested LES is performed over the Owens Valley in California to investigate a transient nighttime warming event observed at the valley floor. LES validates the mechanism inferred from single point tower observations, which is the transition from down-slope to down-valley flows. Simulations also uncover a three-layer valley flow structure observed through a Doppler lidar. While the top and bottom westerly flows are due to the synoptic and down-slope influences, the middle layer easterly flow originates from a cold-air stream down the eastern slope. The induced elevated mixing through shear-instability in the valley atmosphere is investigated.

In terms of numerical methodology, this dissertation explores in great detail the role of turbulent closures for SBL simulations. Compared with the convective and neutral counterparts, the SBL is much more challenging to model, since turbulent motions are further suppressed by buoyancy stratification. Therefore, an optimal turbulent model for the SBL, especially under strongly stable conditions, is expected to perform well under all atmospheric stability classes. The proposed closure is the dynamic reconstruction model (DRM) under an explicit filtering and reconstruction framework. In Chapter 2, the

DRM is shown to sustain resolved turbulence with less stringent resolution requirements than conventional closures, even under strong atmospheric stability. This is achieved by proper representation of subfilter-scale backscatter of turbulent kinetic energy (TKE).

Chapters 4 and 5 demonstrate the feasibility and benefits of nested simulations down to the turbulence resolving LES scale. In Chapter 4, the role of turbulence closures is shown to be crucial in allowing turbulent motions resolvable on the fine LES grid to develop. The advantages of DRM over conventional closures are demonstrated through its ability to predict shear-instability wave breaking, while the latter failed to do so. The nested LES setup is tested in a highly complex terrain case over the Owens Valley in Chapter 5. Good model results again supported the feasibility and benefits of nested LES. One important issue encountered in the nested simulations is the model gray zone known as the *terra incognita*. *Terra incognita* for the SBL is shown to be at the gravity wave length scale ~O(100 m – 1000 m), instead of the conventional accepted buoyancy length scale ~O(10 m). We suggest avoiding grid spacing in the *terra incognita* range if possible. Otherwise, better parameterization must be sought to represent such SGS processes in the gray zone.

In the past decades, ABL flows have been modeled at the regional-scale with limited area models (LAM), in which turbulent processes are highly parameterized. Numerical advances in LES and increases in computational power are finally allowing for turbulence-resolving ABL flows. The potential applications of LES of the ABL in engineering fields are vast. Chapter 3 and Appendix 1 present two such applications in environmental engineering. In Chapter 3, high resolution LES of the strongly stable boundary layer is used to improve wind farm siting and operations. Appendix 1 applies the nested LES configuration to model short term methane plume over a landfill and achieves good results.

Finally, it is worth mentioning that many tools and models developed for or compatible with LES are readily available. Coupled with those tools, LES will become an increasingly powerful tool in representing the complex atmospheric processes in the broader setting of the biosphere and hydrosphere. For example, by implementing a canopy drag model (Shaw and Schumann 1992), the representation of the forest canopy is much improved in the Sandtown study in Appendix 1. Coupling a ground water model developed by the hydrology community to an atmospheric LES code, better representation of surface processes are achieved (Daniels 2010). In the engineering field, rapid integration of engineering models will also make LES an extremely useful tool for utilizing ABL flows. For example, in wind energy applications, adding a rotary disk model into an atmospheric LES code, ABL flows over wind farms could be accurately simulated (Calaf et al. 2010). Overall, the time has come for LES to move out of the ideal box into the real world, and contribute to the development of many areas in atmospheric science and engineering.

6.2 Recommendations

In a perfect LES, the SFS portion of turbulent processes is small compared to the resolved part, and it is equally well represented by any LES closures (Pope 2004). This scenario happens only at very high resolutions where large turbulent eddies are

sufficiently well resolved. In the SBL, the dominant length scale away from the surface is limited by buoyancy, and is independent of the distance from the bottom boundary. Therefore, the perfect resolution for LES of the SBL must be much smaller than the buoyancy length scale, which is likely less than 1 m. Before computational power becomes available for such high-resolution studies, particular attention should be given to the SFS representation of turbulence, i.e. the LES closure model. In this study, we show the advantages of the DRM over conventional closures in sustaining resolved turbulence at relatively coarse resolutions. The DRM is essentially mixed model consisting of a dynamic eddy-viscosity and a scale-similarity component. If not using the DRM, it is strongly recommended that LES of SBL use a mixed model that has scale-similarity component to represent the backscatter process of turbulent kinetic energy into the mean flow.

To the author, the most valuable information this dissertation has to offer to the atmospheric community is the three-step empirical nesting procedure proposed in Chapter 1. Even when regional or global LES becomes feasible in the future, grid nesting will still be the preferred approach to study ABL flows due to the great savings in computational resources. Therefore, any *systematic* improvement on the grid nesting methodology will have a great impact. Until now, grid nesting is still empirical, and depends highly on the individual modeler. Legacy rules such as the 3 to 1 nesting ratio, and good sense judgment such as avoiding sharp changes in terrain at the domain edge have not been quantitatively examined and tested (Warner et al. 1997). Furthermore, lots of issues associated with grid nesting are still unclear, and many more are expected to surface. Although a systematic and quantitative nesting framework is desirable, finding it through one single study is not feasible. Instead, it could be eventually achieved through many nested simulations studies, where old rules are tested, problems exposed, and new alternative rules proposed.

This dissertation is part of the "learning by doing" effort to improve the grid nesting framework. For example, the conventional 3 to 1 nesting ratio is challenged here. Higher nesting ratios are more advantageous computationally if model results on the finest nest are comparable to the one with a lower nesting ratio. In this dissertation, grid nesting following a 5 to 1 ratio works well, and is no worse than the 3 to 1 ratio, on both relatively flat terrain (the Kansas site) and highly complex terrain (Owens Valley). Higher nesting ratios are not tested, but it would be interesting and worthwhile to find the limits of the nesting ratios in relation to terrain complexity. The work in Chapter 4 at the Kansas site also exposes model sensitivity to both the size and location of the domain over relatively flat terrain. A systematic nesting procedure should take inputs from an analysis of the terrain to determine the dominant length scales(De Wekker 2002). This dissertation also proposes skipping the *terra incognita* zone in nested studies as an empirical solution to avoid the model gray zone. A better solution is to come up with a creative way of modeling in the *terra incognita* properly. However, this might be related to the particular process involved. Modeling convection and breaking gravity waves might require different approaches.

In terms of making nested LES worthwhile, i.e. making turbulent motions resolvable on the LES grid develop under the nested setup, two additional approaches have been tested besides improving the turbulence closure. The first approach is to replace explicit

computational mixing with an implicit filter of the Raymond and Garder (1991) type. Computational mixing acts like a viscous damping term, targeting to eliminate numerical noises of wavelength twice the grid spacing. The magnitude of high frequency motions is damped exponentially more strongly (e^{-k^2t}, where k is the wavenumber) than low frequency ones. Explicit filtering damps motions at all wavenumbers, more so on the high wavenumber end of the spectrum. This could be disadvantageous for nested simulations where high frequency motions are trying to develop before the flow exits the inner domain. The implicit filer is much shaper spectrally such that the magnitude of high frequency motions is better preserved, although at a higher computational cost.

The other approach is to restore high frequency motions in the outer grid as much as possible within the grid cutoff limit. This is done by spatially reconstructing the flow field on the outer grid, bases on *a priori* knowledge of the SFS filter. Naturally, this approach must be used in concurrence with explicit filtering where the SFS filter is well defined. Both procedures were tested briefly in the CASES-99 simulations at the initial phase for a very stable night (boundary layer depth ~ 50 m), and not pursued further. Although no significant improvements were observed for that night, both approaches might be useful in other nested studies and worth testing out.

The inconsistency in empirical formulations of the horizontally homogenous and temporally quasi-steady-state SBL over flat terrain is another area of interest. In the surface layer (bottom ~10% of the boundary layer), the Businger et al. (1971) profiles for turbulent fluxes are generally accepted and used as surface boundary conditions. In the middle and top layer, turbulence flux profiles are thought to follow the z-less scaling of Nieuwstadt (1984). However, these two formulations are not compatible because the Monin-Obukhov (MO) similarity (Businger) profile is linear while the Nieuwstadt profile scales with $1-(z/h)^{3/2}$, where h is boundary layer depth. This might seem as trivial but the wide use of the Businger profile as the bottom boundary condition in atmospheric models makes any improvements worthwhile.

Along the same line of MO surface similarity, the friction velocity u* is proportional to the surface wind speed U times a stability dependent drag coefficient, and surface heatflux $w\theta_s$ is proportional to u*. This results in a dilemma in specifying the surface flux boundary condition for predicting morning or evening transition slope flows with a single column model. For example, at sunset the slope flow transitions from the up-slope to the down-slope direction. At a point in time, the surface wind U is zero, hence u* and $w\theta_s$. Since surface heat flux is zero, cooling is stopped for the first grid point of above the wall. The down-slope flow, which is driven by temperature gradients, stops developing. As U remains zero, so are u* and $w\theta_s$. The latter causes cooling to stop at surface. A coupled land-surface model might be solution, but needs to be investigated.

References

Andre, Jc, G. Demoor, P. Lacarrere, G. Therry, and R. Duvachat. 1978. "Modeling 24-Hour Evolution of Mean and Turbulent Structures of Planetary Boundary-Layer." *Journal of the Atmospheric Sciences* 35 (10): 1861–1883.

Arakawa, A., J. -H Jung, and C. -M Wu. 2011. "Toward unification of the multiscale modeling of the atmosphere." *Atmospheric Chemistry and Physics* 11 (8): 3731–3742.

Archer, C. L., and M. Z. Jacobson. 2004. "Spatial and temporal distributions of US winds and wind power at 80 m derived from measurements (vol 108, pg 4289, 2003)." *Journal of Geophysical Research-Atmospheres* 109 (D20) (October 29). doi:10.1029/2004JD005099.

Baines, P. G. 1997. *Topographic Effects in Stratified Flows*. Cambridge University Press.

———. 2001. "Mixing in Flows down Gentle Slopes into Stratified Environments." *Journal of Fluid Mechanics* 443 (-1): 237–270.

———. 2005. "Mixing Regimes for the Flow of Dense Fluid down Slopes into Stratified Environments." *Journal of Fluid Mechanics* 538: 245–267.

Baklanov, A. A, B. Grisogono, R. Bornstein, L. Mahrt, S. S. Zilitinkevich, P. Taylor, S. E. Larsen, Mathias W Rotach, and H. J. S Fernando. 2011. "The Nature, Theory, and Modeling of Atmospheric Planetary Boundary Layers." *Bulletin of the American Meteorological Society* 92 (2) (February): 123–128.

Banta, R. M. 2008. "Stable-boundary-layer regimes from the perspective of the low-level jet." *Acta Geophysica* 56 (1) (March): 58–87. doi:10.2478/s11600-007-0049-8.

———., L. Mahrt, D. Vickers, J. Sun, B. B Balsley, Y. L. Pichugina, and E. L. Williams. 2007. "The very stable boundary layer on nights with weak low-level jets." *Journal of the Atmospheric Sciences* 64 (9) (September): 3068–3090.

———., Y. L. Pichugina, and W. A. Brewer. 2006. "Turbulent velocity-variance profiles in the stable boundary layer generated by a nocturnal low-level jet." *Journal of the Atmospheric Sciences* 63 (11) (November): 2700–2719.

Bardina, J, J. H. Ferziger, and W Reynolds. 1983. *Improved Turbulence Models Based on Large Eddy Simulation of Homgeneous, Imcompressible, Turbulent Flows.* Tech. Rep. Stanford University.

Basu, S., and F. Porte-Agel. 2006. "Large-eddy simulation of stably stratified atmospheric boundary layer turbulence: A scale-dependent dynamic modeling approach." *Journal of the Atmospheric Sciences* 63 (8) (August): 2074–2091.

———., J. F. Vinuesa, and A. Swift. 2008. "Dynamic LES modeling of a diurnal cycle." *Journal of Applied Meteorology and Climatology* 47 (4) (April): 1156–1174.

———., A. A. M. Holtslag, B. J. H Van De Wiel, A. F. Moene, and G. J. Steeneveld. 2008. "An inconvenient 'truth' about using sensible heat flux as a surface boundary condition in models under stably stratified regimes." *Acta Geophysica* 56 (1) (March): 88–99.

———., and Fernando Porté-Agel. 2005. "Large-Eddy Simulation of Stably Stratified Atmospheric Boundary Layer Turbulence: A Scale-Dependent Dynamic Modeling Approach." *Journal of the Atmospheric Sciences* 63 (8) (August): 2074-2091.

Beare, R. J. 2011. “Modelling Convective Boundary Layers in the Terra-incognita.” In *ECMWF/GABLS Workshop on Diurnal Cycles and the Stable Atmospheric Boundary Layer*.

———., M. Macvean, A. Holtslag, J. Cuxart, I. Esau, J. C. Golaz, M. Jimenez, et al. 2006. “An Intercomparison of Large-Eddy Simulations of the Stable Boundary Layer.” *Boundary-Layer Meteorology* 118 (2): 247–272.

Bechmann, A., and N. N. Sorensen. 2011. “Hybrid RANS/LES applied to complex terrain.” *Wind Energy* 14 (2) (March): 225–237. doi:10.1002/we.414.

Belusic, D., and I. Guttler. 2010. “Can mesoscale models reproduce meandering motions?” *Quarterly Journal of the Royal Meteorological Society* 136 (648) (April): 553–565.

Blumen, W., R. M. Banta, S. P. Burns, D. C. Fritts, R. Newsom, G. S. Poulos, and J. L. Sun. 2001. “Turbulence statistics of a Kelvin-Helmholtz billow event observed in the night-time boundary layer during the Cooperative Atmosphere-Surface Exchange Study field program.” *Dynamics of Atmospheres and Oceans* 34 (2-4) (October): 189–204. doi:10.1016/S0377-0265(01)00067-7.

Brasseur, J. G, and T. Wei. 2010. “Designing large-eddy simulation of the turbulent boundary layer to capture law-of-the-wall scaling.” *Physics of Fluids* 22 (2) (February).

Brown, A. R., J. M. Hobson, and N. Wood. 2001. “Large-eddy simulation of neutral turbulent flow over rough sinusoidal ridges.” *Boundary-Layer Meteorology* 98 (3) (March): 411–441. doi:10.1023/A:1018703209408.

Businger, J. A., J. C. Wyngaard, Y. Izumi, and E. F. Bradley. 1971. “Flux-Profile Relationships in Atmospheric Surface Layer.” *Journal of the Atmospheric Sciences* 28 (2): 181–&.

Byunghyun H., P. T. Imhoff, C. Rella, B. Zhou, F. K. Chow, 2012. "Short-Term Analysis of Airborne and Ground Measurements for Quantifying Methane Emissions from Landfills". Submitted to Environmental Science & Technology.

Calaf, M., C. Meneveau, and J. Meyers. 2010. “Large eddy simulation study of fully developed wind-turbine array boundary layers.” *Physics of Fluids* 22 (1) (January).

Carati, D., G. S. Winckelmans, and H. Jeanmart. 2001. “On the modelling of the subgrid-scale and filtered-scale stress tensors in large-eddy simulation.” *Journal of Fluid Mechanics* 441 (August 25): 119–138.

Carper, M. A., and F. Porte-Agel. 2004. “The role of coherent structures in subfilter-scale dissipation of turbulence measured in the atmospheric surface layer.” *Journal of Turbulence* 5 (November 15).

Caughey, S. J. 1982. “Observed Characteristics of the Atmospheric Boundary Layer.” *Atmospheric Turbulence and Air Pollution Modelling* -1: 107.

Cederwall, R. T. 2001. “Large-eddy Simulation of the Evolving Boundary Layer over Flat Terrain.” Ph.D. Dissertation, Stanford University.

Chandrasekhar, S. 1961. *Hydrodynamic and Hydromagnetic Stability*. Oxford University Press, USA.

Chemel, C., C. Staquet, and Y. Largeron. 2009. “Generation of internal gravity waves by a katabatic wind in an idealized alpine valley.” *Meteorology and Atmospheric Physics* 103 (1-4) (March): 187–194.

Chow, F. K. 2004. “Subfilter-scale Turbulence Modeling for Large-eddy Simulation of the Atmospheric Boundary Layer over Complex Terrain”. Stanford University, Environmental Fluid Mechanics and Hydrology, Department of Civil and Environmental Engineering.

———., and R. L. Street. 2009. “Evaluation of Turbulence Closure Models for Large-Eddy Simulation over Complex Terrain: Flow over Askervein Hill.” *Journal of Applied Meteorology and Climatology* 48 (5) (May): 1050–1065.

———., R. L. Street, M. Xue, and J. H. Ferziger. 2005. “Explicit filtering and reconstruction turbulence modeling for large-eddy simulation of neutral boundary layer flow.” *Journal of the Atmospheric Sciences* 62 (7) (July): 2058–2077.

———., A. P. Weigel, R. L. Street, M. W. Rotach, and M. Xue. 2006. “High-resolution large-eddy simulations of flow in a steep Alpine valley. Part I: Methodology, verification, and sensitivity experiments.” *Journal of Applied Meteorology and Climatology* 45 (1) (January): 63–86.

Chung, D., and G. Matheou. 2012. “Direct numerical simulation of stationary homogeneous stratified sheared turbulence.” *Journal of Fluid Mechanics* 696 (April 10): 434–467.

van Cittert, P. 1931. “Der Spaltbreite Auf Die Intensitasverteilung in Spektrallinien Ii.” *Z. Phys.* 69: 298–308.

Clarke, R. H., A. J. Dyer, R. R. Brook, D. G. Reid, and A. J. Troup. 1971. *The Wangara Experiment: Boundary Layer Data*. Tech. Paper. CSIRO Div. of Meteorol. Phys.

Coleman, G. N., J. H. Ferziger, and P. R. Spalart. 1992. “Direct Simulation of the Stably Stratified Turbulent Ekman Layer.” *Journal of Fluid Mechanics* 244 (November): 677–712.

Conangla, L., and J. Cuxart. 2006. “On the turbulence in the upper part of the low-level jet: An experimental and numerical study.” *Boundary-Layer Meteorology* 118 (2) (February): 379–400.

Costa, Felipe D., Otavio C. Acevedo, Jose C. M. Mombach, and Gervasio A. Degrazia. 2011. “A Simplified Model for Intermittent Turbulence in the Nocturnal Boundary Layer.” *Journal of the Atmospheric Sciences* 68 (8) (August): 1714–1729.

Coulter, R. L., and J. C. Doran. 2002. “Spatial and temporal occurrences of intermittent turbulence during CASES-99.” *Boundary-Layer Meteorology* 105 (2) (November): 329–349.

Cramer, O. P. 1972. “Potential temperature analysis for mountainous terrain.” *Journal of Applied Meteorology* 11 (1) (February): 44–5050.

Cuxart, J., P. Bougeault, and J. L. Redelsperger. 2000. “A turbulence scheme allowing for mesoscale and large-eddy simulations.” *Quarterly Journal of the Royal Meteorological Society* 126 (562) (January): 1–30.

Cuxart, J., and M. A. Jimenez. 2007. “Mixing processes in a nocturnal low-level jet: An LES study.” *Journal of the Atmospheric Sciences* 64 (5) (May): 1666–1679.

Daniels, M.H. 2010. “Soil Moisture in Complex Terrain: Quantifying Effects on Atmospheric Boundary Layer Flow and Providing Improved Surface Boundary Conditions for Mesoscale Model”. Ph.D. Dissertation, University of California, Berkeley.

Davies, Hc. 1983. “Limitations of Some Common Lateral Boundary Schemes Used in Regional Nwp Models.” *Monthly Weather Review* 111 (5): 1002–1012.

Deardorff, J. W. 1980. “Stratocumulus-Capped Mixed Layers Derived from a 3-Dimensional Model.” *Boundary-Layer Meteorology* 18 (4): 495–527.

———. 1974a. “Three-dimensional numerical study of the height and mean structure of a heated planetary boundary layer.” *Boundary-Layer Meteorology* 7 (1) (August): 81–106.

———. 1974b. “Three-dimensional numerical study of turbulence in an entraining mixed layer.” *Boundary-Layer Meteorology* 7 (2) (October): 199–226226.

Defant, F. 1949. “A Theory of Slope Winds, Along with Remarks on the Theory of Mountain Winds and Valley Winds” (1A): 421–450.

Deleersnijder, E., J. M. Campin, and E. J. M. Delhez. 2001. “The concept of age in marine modelling I. Theory and preliminary model results.” *Journal of Marine Systems* 28 (3-4) (April): 229–267.

Derbyshire, S. H. 1990. “Nieuwstadt’s Stable Boundary Layer Revisited.” *Quarterly Journal of the Royal Meteorological Society* 116 (491): 127–158.

———. 1995a. “Stable Boundary-Layers - Observations, Models and Variability .1. Modeling and Measurements.” *Boundary-Layer Meteorology* 74 (1-2) (April): 19–54.

———. 1995b. “Stable Boundary-Layers - Observations, Models and Variability .2. Data-Analysis and Averaging Effects.” *Boundary-Layer Meteorology* 75 (1-2) (July): 1–24.

———. 1999. “Boundary-layer decoupling over cold surfaces as a physical boundary-instability.” *Boundary-Layer Meteorology* 90 (2) (February): 297–325.

Doyle, J. D., and Dale R. Durran. 2007. “Rotor and Subrotor Dynamics in the Lee of Three-Dimensional Terrain.” *Journal of the Atmospheric Sciences* 64 (12) (December): 4202–4221.

Drazin, P. G., and W. H. Reid. 2004. *Hydrodynamic Stability*. Cambridge University Press.

Ellison, T. H., and J. S. Turner. 1959. “Turbulent Entrainment in Stratified Flows.” *Journal of Fluid Mechanics* 6 (03): 423–448.

Fleagle, R. G. 1950. “A Theory of Air Drainage.” *Journal of Meteorology* 7 (3): 227–232.

Garratt, J. R. 1992. *The Atmospheric Boundary Layer*. Cambridge University Press.

Germano, M., U. Piomelli, P. Moin, and W. H. Cabot. 1991. “A Dynamic Subgrid-scale Eddy Viscosity Model.” *Physics of Fluids A: Fluid Dynamics* 3 (7) (July 1): 1760–1765.

Gerz, T., U. Schumann, and Se Elghobashi. 1989. “Direct Numerical-Simulation of Stratified Homogeneous Turbulent Shear Flows.” *Journal of Fluid Mechanics* 200 (March): 563–594.

Grachev, A. A., E. L. Andreas, C. W. Fairall, P. S. Guest, and P. Ola G. Persson. 2007. “On the turbulent Prandtl number in the stable atmospheric boundary layer.” *Boundary-Layer Meteorology* 125 (2) (November): 329–341.

Grisogono, B., and L. Enger. 2010. “The Angle of Near-surface Wind-turning in Weakly Stable Boundary Layers.”.

Grubisic, V., J. D. Doyle, J. Kuettner, S. Mobbs, R. B. Smith, C. D. Whiteman, R. Dirks, et al. 2008. “THE TERRAIN-INDUCED ROTOR EXPERIMENT A Field

Campaign Overview Including Observational Highlights." *Bulletin of the American Meteorological Society* 89 (10) (October): 1513–+.

Gullbrand, J. 2001. *Explicit Filtering and Subgrid-scale Models in Turbulent Channel Flow.* Annual Research Briefs. Center for Turbulence Research, NASA Ames–Stanford University.

———., and F. K. Chow. 2003. "The effect of numerical errors and turbulence models in large-eddy simulations of channel flow, with and without explicit filtering." *Journal of Fluid Mechanics* 495 (November 25): 323–341.

Haiden, T. 2003. "On the Pressure Field in the Slope Wind Layer." *Journal of the Atmospheric Sciences* 60 (13) (July): 1632–1635.

Hogstrom, U. 1996. "Review of some basic characteristics of the atmospheric surface layer." *Boundary-Layer Meteorology* 78 (3-4) (March): 215–246.

IEC. 2005. "Wind Turbubine Generator System Part 1: Safety Requirements. International Electrotechnical Commission". Geneva, Switzerland.

Jimenez, M. A., and J. Cuxart. 2005. "Large-Eddy simulations of the stable boundary layer using the standard Kolmogorov theory: Range of applicability." *Boundary-Layer Meteorology* 115 (2) (May): 241–261.

Kelley, N. D., B. J. Jonkman, and G. N. Scott. 2006. *The Great Plains Turbulence Environment: Its Origins, Impact and Simulation.* Tech. Rep. Golden, CO: National Renewable Energy Laboratory.

———., R. M. Osgood, J. T. Bialasiewicz, and A. Jakubowski. 2000. "Using Wavelet Analysis to Assess Turbulence/Rotor Interactions." *Wind Energy* 3 (3): 121–134.

Kirkpatrick, M. P., A. S. Ackerman, D. E. Stevens, and N. N. Mansour. 2006. "On the application of the dynamic Smagorinsky model to large-eddy simulations of the cloud-topped atmospheric boundary layer." *Journal of the Atmospheric Sciences* 63 (2) (February): 526–546.

Klemp, J. B., and R. B. Wilhelmson. 1978. "The Simulation of Three-Dimensional Convective Storm Dynamics." *Journal of the Atmospheric Sciences* 35 (6) (June): 1070–1096.

Kosovic, B., and J. A. Curry. 2000. "A large eddy simulation study of a quasi-steady, stably stratified atmospheric boundary layer." *Journal of the Atmospheric Sciences* 57 (8) (April 15): 1052–1068.

Kumar, V., G. Svensson, A. A. M. Holtslag, C. Meneveau, and M. B. Parlange. 2010. "Impact of Surface Flux Formulations and Geostrophic Forcing on Large-Eddy Simulations of Diurnal Atmospheric Boundary Layer Flow." *Journal of Applied Meteorology and Climatology* 49 (7) (July): 1496–1516.

Lalic, B., and D. T. Mihailovic. 2004. "An empirical relation describing leaf-area density inside the forest for environmental modeling." *Journal of Applied Meteorology* 43 (4) (April): 641–645.

Lilly, D. K. 1992. "A Proposed Modification of the Germano-Subgrid-Scale Closure Method." *Physics of Fluids a-Fluid Dynamics* 4 (3) (March): 633–635.

Ludwig, F. L., F. K. Chow, and R. L. Street. 2009. "Effect of Turbulence Models and Spatial Resolution on Resolved Velocity Structure and Momentum Fluxes in Large-Eddy Simulations of Neutral Boundary Layer Flow." *Journal of Applied Meteorology and Climatology* 48 (6) (June): 1161–1180.

Lund, T. S. 1997. *On the Use of Discrete Filters for Large Eddy Simulation.* Annual Research Briefs. Center for Turbulence Research, NASA Ames–Stanford University.

Lundquist, K. A., F. K. Chow, and J. K. Lundquist. 2010. "An Immersed Boundary Method for the Weather Research and Forecasting Model." *Monthly Weather Review* 138 (3) (March): 796–817.

Mahrt, L. 1982. "Momentum Balance of Gravity Flows." *Journal of the Atmospheric Sciences* 39 (12): 2701–2711.

———. 1998. "Stratified Atmospheric Boundary Layers and Breakdown of Models." *Theoretical and Computational Fluid Dynamics* 11 (3): 263–279.

———. 1999. "Stratified atmospheric boundary layers." *Boundary-Layer Meteorology* 90 (3) (March): 375–396.

———., and D. Vickers. 2002. "Contrasting Vertical Structures of Nocturnal Boundary Layers." *Boundary-Layer Meteorology* 105 (2): 351–363.

———., D. Vickers, R. Nakamura, M. R. Soler, J. Sun, S. P. Burns, and D. H. Lenschow. 2001. "Shallow Drainage Flows." *Boundary-Layer Meteorology* 101 (2): 243–260.

Malhi, Y. S. 1995. "The Significance of the Dual Solutions for Heat Fluxes Measured by the Temperature-Fluctuation Method in Stable Conditions." *Boundary-Layer Meteorology* 74 (4) (June): 389–396.

Mason, P. J., and S. H. Derbyshire. 1990. "Large-Eddy Simulation of the Stably-Stratified Atmospheric Boundary-Layer." *Boundary-Layer Meteorology* 53 (1-2) (October): 117–162.

Mason, P. J., and D. J. Thomson. 1992. "Stochastic Backscatter in Large-Eddy Simulations of Boundary-Layers." *Journal of Fluid Mechanics* 242 (September): 51–78.

Mayr, G. J., and L. Armi. 2010. "The Influence of Downstream Diurnal Heating on the Descent of Flow Across the Sierras." *Journal of Applied Meteorology and Climatology* 49 (9) (September): 1906–1912.

McNider, R. T. 1982. "A Note on Velocity Fluctuations in Drainage Flows." *Journal of the Atmospheric Sciences* 39 (7) (July): 1658–1660.

Meneveau, C., T. S. Lund, and W. H. Cabot. 1996. "A Lagrangian dynamic subgrid-scale model of turbulence." *Journal of Fluid Mechanics* 319 (July 25): 353–385.

Michalke, A. 1965. "On Spatially Growing Disturbances in an Inviscid Shear Layer." *Journal of Fluid Mechanics* 23 (03): 521–544.

Michioka, T., and F. K. Chow. 2008. "High-Resolution Large-Eddy Simulations of Scalar Transport in Atmospheric Boundary Layer Flow over Complex Terrain." *Journal of Applied Meteorology and Climatology* 47 (12) (December): 3150–

Miles, J. W. 1961. "On the Stability of Heterogeneous Shear Flows." *Journal of Fluid Mechanics* 10 (4): 496–508.

———., and H. E. Huppert. 1969. "Lee Waves in a Stratified Flow .4. Perturbation Approximations." *Journal of Fluid Mechanics* 35: 497–&.

Mirocha, J. D., J. K. Lundquist, and B. Kosovic. 2010. "Implementation of a Nonlinear Subfilter Turbulence Stress Model for Large-Eddy Simulation in the Advanced Research WRF Model." *Monthly Weather Review* 138 (11) (November): 4212–4228.

Moeng, C. H. 1984. “A Large-Eddy-Simulation Model for the Study of Planetary Boundary-Layer Turbulence.” *Journal of the Atmospheric Sciences* 41 (13): 2052–2062.

Nakamura, R., and L. Mahrt. 2005. “A study of intermittent turbulence with cases-99 tower measurements.” *Boundary-Layer Meteorology* 114 (2) (February): 367–387.

Newsom, R. K., and R. M. Banta. 2003. “Shear-flow instability in the stable nocturnal boundary layer as observed by Doppler lidar during CASES-99.” *Journal of the Atmospheric Sciences* 60 (1) (January): 16–33.

Nieuwstadt, F. T. M. 1984. “The Turbulent Structure of the Stable, Nocturnal Boundary Layer.” *Journal of the Atmospheric Sciences* 41 (14) (July): 2202–2216.

Noilhan, J., and S. Planton. 1989. “A Simple Parameterization of Land Surface Processes for Meteorological Models.” *Monthly Weather Review* 117 (3) (March): 536–549.

Ohya, Y., R. Nakamura, and T. Uchida. 2008. “Intermittent bursting of turbulence in a stable boundary layer with low-level jet.” *Boundary-Layer Meteorology* 126 (3) (March): 349–363.

Paiva, L. M. S., G. C. R. Bodstein, and W. F. Menezes. 2009. “Numerical simulation of atmospheric boundary layer flow over isolated and vegetated hills using RAMS.” *Journal of Wind Engineering and Industrial Aerodynamics* 97 (9-10) (November): 439–454.

Palma, J. M. L. M., F. A. Castro, L. F. Ribeiro, A. H. Rodrigues, and A. P. Pinto. 2008. “Linear and nonlinear models in wind resource assessment and wind turbine micro-siting in complex terrain.” *Journal of Wind Engineering and Industrial Aerodynamics* 96 (12) (December): 2308–2326.

Perry, A. E., S. Henbest, and M. S. Chong. 1986. “A Theoretical and Experimental-Study of Wall Turbulence.” *Journal of Fluid Mechanics* 165 (April): 163–199.

Pleim, J. E., and A. Xiu. 1995. “Development and Testing of a Surface Flux and Planetary Boundary-Layer Model for Application in Mesoscale Models.” *Journal of Applied Meteorology* 34 (1) (January): 16–32. doi:10.1175/1520-0450-34.1.16.

Pope, S. B. 2004. “Ten questions concerning the large-eddy simulation of turbulent flows.” *New Journal of Physics* 6 (March 16). doi:10.1088/1367-2630/6/1/035.

Porté-Agel, F., M. B. Parlange, C. Meneveau, W. E. Eichinger, and M. Pahlow. 2000. “Subgrid-scale dissipation in the atmospheric surface layer: Effects of stability and filter dimension.” *Journal of Hydrometeorology* 1 (1) (February): 75–87.

———., Y. Wu, and L. Charmorro. 2010. “Large-eddy Simulation of Wind-turbine Wakes: Evaluation of Turbine Parameterizations.”

Poulos, G. S., W. Blumen, D. C. Fritts, J. K. Lundquist, J. Sun, S. P. Burns, C. Nappo, et al. 2002. “CASES-99: A comprehensive investigation of the stable nocturnal boundary layer.” *Bulletin of the American Meteorological Society* 83 (4) (April): 555–581.

Raymond, W. H., and A. Garder. 1991. “A Review of Recursive and Implicit Filters.” *Monthly Weather Review* 119 (2) (February): 477–495.

Rogers, M. M., and R. D. Moser. 1992. “The Three-dimensional Evolution of a Plane Mixing Layer: The Kelvin–Helmholtz Rollup.” *Journal of Fluid Mechanics* 243: 183–226.

———. 1994. “Direct Simulation of a Self-similar Turbulent Mixing Layer.” *Physics of Fluids* 6 (2) (February 1): 903–923.

Saiki, E. M., C. H. Moeng, and P. P. Sullivan. 2000. “Large-Eddy Simulation Of The Stably Stratified Planetary Boundary Layer.” *Boundary-Layer Meteorology* 95 (1): 1–30.

Schumann, U., and T. Gerz. 1995. “Turbulent Mixing in Stably Stratified Shear Flows.” *Journal of Applied Meteorology* 34 (1) (January): 33–48.

Shaw, R. H., and U. Schumann. 1992. “Large-Eddy Simulation of Turbulent-Flow Above and Within a Forest.” *Boundary-Layer Meteorology* 61 (1-2) (October): 47–64.

Shih, L. H., J. R. Koseff, J. H. Ferziger, and C. R. Rehmann. 2000. “Scaling and parameterization of stratified homogeneous turbulent shear flow.” *Journal of Fluid Mechanics* 412 (June 10): 1–20.

Sisterson, D. L., and P. Frenzen. 1978. “Nocturnal Boundary-Layer Wind Maxima and Problem of Wind Power Assessment.” *Environmental Science & Technology* 12 (2): 218–221.

Smith, K., G. Randall, N.D. Kelley, and B. Smith. 2002. “Evaluation of Wind Shear Patterns at Midwest Wind Energy Facilities.” In *Proceedings American Wind Energy Association (AWEA) Windpower 2002 Conference*.

Sorbjan, Z. 2006. “Local structure of turbulence in stably stratified boundary layers.” *Journal of the Atmospheric Sciences* 63 (5) (May): 1526–1537.

———. 2010. “Gradient-based scales and similarity laws in the stable boundary layer.” *Quarterly Journal of the Royal Meteorological Society* 136 (650) (July): 1243–1254.

———., and A. A. Grachev. 2010. “An Evaluation of the Flux-Gradient Relationship in the Stable Boundary Layer.” *Boundary-Layer Meteorology* 135 (3) (June): 385–405.

Sreenivasan, K. R., and R. A. Antonia. 1997. “The phenomenology of small-scale turbulence.” *Annual Review of Fluid Mechanics* 29: 435–472. doi:10.1146/annurev.fluid.29.1.435.

Steeneveld, G. J, T. Mauritsen, E. I. F de Bruijn, J. Vila-Guerau de Arellano, G. Svensson, and A. a. M Holtslag. 2008. “Evaluation of limited-area models for the representation of the diurnal cycle and contrasting nights in CASES-99.” *Journal of Applied Meteorology and Climatology* 47 (3) (March): 869–887.

Stolz, S., N. A. Adams, and L. Kleiser. 2001. “The approximate deconvolution model for large-eddy simulations of compressible flows and its application to shock-turbulent-boundary-layer interaction.” *Physics of Fluids* 13 (10) (October): 2985–3001.

Storm, B., J. Dudhia, S. Basu, A. Swift, and I. Giammanco. 2009. “Evaluation of the Weather Research and Forecasting Model on Forecasting Low-level Jets: Implications for Wind Energy.” *Wind Energy* 12 (1) (January): 81–90.

Stull, R. B. 1988. *An Introduction to Boundary Layer Meteorology*. Kluwer Academic Publishers.

Sun, J., S. P. Burns, D. H. Lenschow, R. Banta, R. Newsom, R. Coulter, S. Frasier, et al. 2002. “Intermittent turbulence associated with a density current passage in the stable boundary layer.” *Boundary-Layer Meteorology* 105 (2) (November): 199–219.

———., D. H. Lenschow, S. P. Burns, R. M. Banta, R. K. Newsom, R. Coulter, S. Frasier, et al. 2004. “Atmospheric disturbances that generate intermittent

turbulence in nocturnal boundary layers." *Boundary-Layer Meteorology* 110 (2) (February): 255–279.

Sun, W. Y., and C. Z. Chang. 1986. "Diffusion model for a convective layer. I. Numerical simulation of convective boundary layer." *Journal of Climate and Applied Meteorology* 25 (10) (October): 1445–14531453.

Turner, J. S. 1986. "Turbulent Entrainment - the Development of the Entrainment Assumption, and Its Application to Geophysical Flows." *Journal of Fluid Mechanics* 173 (December): 431–471.

Van Ulden, A. P., and A. A. M. Holtslag. 1985. "Estimation of Atmospheric Boundary Layer Parameters for Diffusion Applications." *Journal of Climate and Applied Meteorology* 24 (11) (November): 1196–1207.

Vosper, S. B., and A. R. Brown. 2008. "Numerical Simulations of Sheltering in Valleys: The Formation of Nighttime Cold-Air Pools." *Boundary-Layer Meteorology* 127 (3) (April 5): 429–448.

Warner, T. T., R. A. Peterson, and R. E. Treadon. 1997. "A tutorial on lateral boundary conditions as a basic and potentially serious limitation to regional numerical weather prediction." *Bulletin of the American Meteorological Society* 78 (11) (November): 2599–2617.

De Wekker, S. F. J. 2002. "Structure and Morphology of the Convective Boundary Layer in Mountainous Terrain". The University of British Columbia.

Welch, P. 1967. "The Use of Fast Fourier Transform for the Estimation of Power Spectra: A Method Based on Time Averaging over Short, Modified Periodograms." *IEEE Transactions on Audio and Electroacoustics* 15 (2) (June): 70 – 73.

Whiteman, C. D. 2000. *Mountain Meteorology: Fundamentals and Applications*. 1st ed. Oxford University Press, USA.

———., S. W. Hoch, and G. S. Poulos. 2009. "Evening Temperature Rises on Valley Floors and Slopes: Their Causes and Their Relationship to the Thermally Driven Wind System." *Journal of Applied Meteorology and Climatology* 48 (4) (April): 776–788.

———., A. Muschinski, S. Zhong, D. Fritts, S. W. Hoch, M. Hahnenberger, W. Yao, et al. 2008. "METCRAX 2006 Meteorological Experiments in Arizona's Meteor Crater." *Bulletin of the American Meteorological Society* 89 (11) (November): 1665–1680.

Van de Wiel, B. J. H., A. F. Moene, O. K. Hartogensis, H. a. R. De Bruin, and A. a. M. Holtslag. 2003. "Intermittent turbulence in the stable boundary layer over land. Part III: A classification for observations during CASES-99." *Journal of the Atmospheric Sciences* 60 (20) (October): 2509–2522.

———., A. F. Moene, R. J. Ronda, H. a. R. De Bruin, and A. a. M. Holtslag. 2002. "Intermittent turbulence and oscillations in the stable boundary layer over land. Part II: A system dynamics approach." *Journal of the Atmospheric Sciences* 59 (17) (September): 2567–2581.

———., A. F. Moene, W. H. De Ronde, and H. J. J. Jonker. 2008. "Local similarity in the stable boundary layer and mixing-length approaches: consistency of concepts." *Boundary-Layer Meteorology* 128 (1) (July): 103–116116.

———., R. J. Ronda, A. F. Moene, H. a. R. De Bruin, and A. a. M. Holtslag. 2002. "Intermittent turbulence and oscillations in the stable boundary layer over land. Part I: A bulk model." *Journal of the Atmospheric Sciences* 59 (5): 942–958.

Winckelmans, G. S., A. A. Wray, O. V. Vasilyev, and H. Jeanmart. 2001. "Explicit-filtering large-eddy simulation using the tensor-diffusivity model supplemented by a dynamic Smagorinsky term." *Physics of Fluids* 13 (5) (May): 1385–1403.

Wong, V. C., and D. K. Lilly. 1994. "A Comparison of Two Dynamic Subgrid Closure Methods for Turbulent Thermal Convection." *Physics of Fluids* 6 (2) (February 1): 1016–1023.

Wyngaard, J. C. 2004. "Toward numerical modeling in the "terra incognita''." *Journal of the Atmospheric Sciences* 61 (14) (July): 1816–1826.

———., and O. R. Cote. 1974. "The evolution of a convective planetary boundary layer-A higher-order-closure model study." *Boundary-Layer Meteorology* 7 (3) (November): 289–308308.

Xue, M., K. K. Droegemeier, and V. Wong. 2000. "The Advanced Regional Prediction System (ARPS) - A multi-scale nonhydrostatic atmospheric simulation and prediction model. Part I: Model dynamics and verification." *Meteorology and Atmospheric Physics* 75 (3-4): 161–193.

———., K. K. Droegemeier, V. Wong, A. Shapiro, K. Brewster, F. Carr, D. Weber, Y. Liu, and D. Wang. 2001. "The Advanced Regional Prediction System (ARPS) - A multi-scale nonhydrostatic atmospheric simulation and prediction tool. part II: Model physics and applications." *Meteorology and Atmospheric Physics* 76 (3-4): 143–165.

———., J Zong, and K. K. Droegemeier. 1996. "Parameterization of PBL Turbulence in a Multi-scale Nonhydrostatic Model." In , 363–365. Norfolk, VA.

Yamada, T., and G. Mellor. 1975. "Simulation of Wangara Atmospheric Boundary-Layer Data." *Journal of the Atmospheric Sciences* 32 (12): 2309–2329.

Zang, Y., R. L. Street, and J. R. Koseff. 1993. "A dynamic mixed subgrid-scale model and its application to turbulent recirculating flows." *Physics of Fluids A (Fluid Dynamics)* 5 (12) (December): 3186–31963196.

Zhong, S., and F. K. Chow. 2012. "Mesoscale Numerical Modeling over Complex Terrain: Operational Applications." In *Mountain Meteorology: Bridging the Gap Between Research and Forecasting*. Berlin: Springer.

———., and C. D. Whiteman. 2008. "Downslope Flows on a Low-Angle Slope and Their Interactions with Valley Inversions. Part II: Numerical Modeling." *Journal of Applied Meteorology and Climatology* 47 (7) (July): 2039–2057.

Zhou, B., and F. K. Chow. 2011. "Large-Eddy Simulation of the Stable Boundary Layer with Explicit Filtering and Reconstruction Turbulence Modeling." *Journal of the Atmospheric Sciences* 68 (9) (September): 2142–2155.

Appendix A Short-Term Analysis of Airborne and Ground Measurements for Quantifying Methane Emissions from Landfills

A.1 Overview

Quantifying methane emissions from individual landfills may be necessary to evaluate methane emission control measures. While the tracer dilution method is well-suited for measuring whole-landfill methane emissions, it is difficult to apply because of the cost of making real-time measurements of a tracer gas and methane. To overcome this limitation, a prototype gas analyzer that employs cavity ring-down spectroscopy was used to measure a passive tracer (acetylene) and methane in 2 s with a measurement precision of 0.8 ppb and 0.2 ppb, respectively. Measurements were made at ground level and airborne using a weather balloon in the downwind plume from the Sandtown Landfill in Delaware (US). An atmospheric dispersion model was developed for this site and used to predict plume meandering, vertical tracer gas profiles, and gas travel times from the landfill to the measurement location. Over a 2-hour measurement period, observed methane emissions varied fourfold and were correlated with wind conditions on the landfill surface, if a mean travel time of emitted gases from the landfill to the measurement location was 9 or 10 minutes, which was within 30% of the mean gas travel time predicted from the atmospheric dispersion model. The appendix describes the numerical part of the methane dispersion study (Byunghyun et al. 2012). Together with field measurements, the project demonstrates the value of airborne data and atmospheric dispersion modeling, and suggests that significant short-term variations in whole-landfill methane emissions may be caused by wind variability.

A.2 Numerical Model Configuration and Description

The Advanced Regional Prediction System (ARPS) was used for the simulations. ARPS was developed at the Center for Analysis and Prediction of Storms at the University of Oklahoma. It is a non-hydrostatic meso-scale and small-scale finite-difference numerical weather prediction model which runs in parallel using the message passing interface (MPI). Descriptions of the model can be found in Xue et al. (2000; 2001), with relevant details presented below.

ARPS uses a generalized terrain-following coordinate on an Arakawa C-grid. A mode-splitting time integration scheme is employed. This technique divides a big integration step (Δt_{big}) into a number of computationally inexpensive small times-steps (Δt_{small}) and updates the acoustically active terms, while all other terms are computed once every big time-step. Fourth-order spatial differentiation is used here for both momentum and scalar advection. We simulated 3 hours of daytime atmospheric flow starting from 13:00 to 16:00 local time on March 6th, 2010. Results from the last 2-hour period are used for analysis.

Table A-1 List of nested model parameters. ΔT_b is the lateral boundary update interval for nested simulations.

Nest	Grid size (nx, ny, nz)[5]	Domain (km)	$\Delta x/\Delta y$ (m)	$\Delta z/\Delta z_{min}$ (m)	ΔT_b (s)	Δt_{big} (s)	Δt_{small} (s)
1	(91, 91, 53)	211.2 x 211.2 x 16	2400	320/50	21600	5.0	5.0
2	(275, 275, 103)	40.8 x 40.8 x 5	150	50/10	900	1.0	0.2
3	(163, 163, 163)	4.8 x 4.8 x 3.2	30	20/5	300	0.25	0.025

To resolve the local flow around the landfill (39.0389° N, 75.7259 ° W), we adopt a multi-scale approach. Simulations were first performed on a 200 x 200 km^2 area with 2400 m horizontal resolution which covered the entire Delmarva Peninsula. Realistic initial and lateral boundary conditions were obtained from meteorological analysis data produced by the North American Mesoscale Forecast System. Results from the 2400 m grid were used to drive lateral boundaries of a 150 m grid, which was fed into a 30 m grid. Vertical grid stretching was applied to better resolve the surface layer. On the finest grid, the vertical resolution is 20 m with 5 m spacing near the surface. The land surface was represented with high resolution terrain (10 m) and land cover (30 m) data from the U.S. Geological Survey. Figure A-1 presents the two nest domains, as well as land cover on the finest grid. Model setup parameters are given in Table A-1.

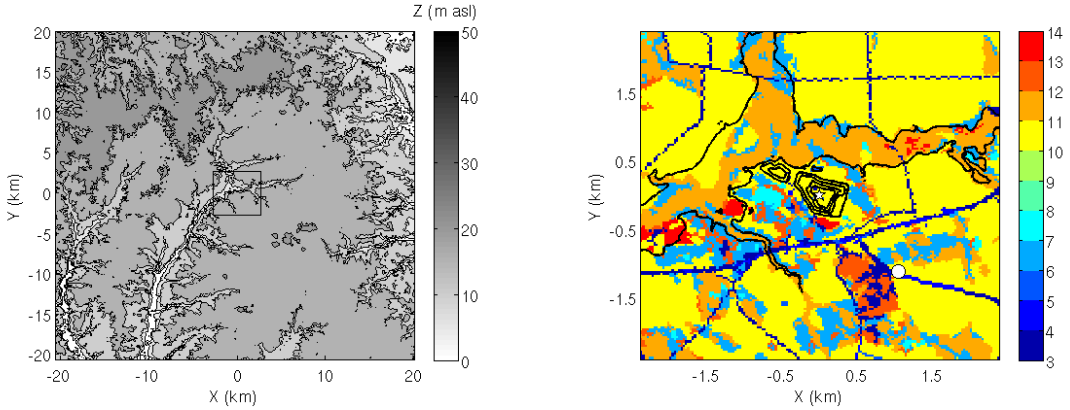

Figure A-1 Elevation contours for the (a) 150 m grid with the 30 m grid shown within, and (b) the 30 m grid. Contour interval is 5 m. The Sandtown Landfill is the elevated hill in the center of (b): the tracer release point is marked with a star, and the stationary downwind measurement location of the tracer and methane is marked with a solid white circle. Land cover is classified by the Olson World Ecosystem Classes. The four major

[5] Two ghost points are included in the number of grid points, so the domain size in the x direction, for example, is (nx-3)Δx.

land cover types at Sandtown are cultivation (yellow), marsh (orange), forest (blue) and dwarf shrub (red).

On the 2400 m grid, ARPS was run in meso-scale mode with boundary layer parameterizations (Sun and Chang 1986) to model the synoptic-scale flows. On the inner (150 m and 30 m) grids, large-eddy simulations (LES) were performed to resolve turbulent flows in the atmospheric boundary layer (ABL). LES is based on the definition of a spatial filter that can be adjusted to resolve necessary flow features. The spatial filter separates the large resolved scales from the subfilter-scale (SFS) motions. The effect of the latter on the resolved scales must be represented by a turbulence model. The LES governing equations for the resolved fields are the momentum, continuity and scalar transport equations:

$$\frac{\partial \overline{\rho}\,\overline{u}_i}{\partial t} + \frac{\partial \overline{\rho}\,\overline{u}_i\,\overline{u}_j}{\partial x_j} = -\frac{\partial \overline{p}}{\partial x_i} - \overline{\rho}\,g\delta_{i3} + \overline{\rho}\epsilon_{imn}f_n\overline{u}_m - \frac{\partial \overline{\rho}\,\tau_{ij}}{\partial x_j}$$

$$\frac{\partial \overline{\rho}}{\partial t} + \frac{\partial \overline{\rho}\,\overline{u}_i}{\partial x_i} = 0$$

$$\frac{\partial \overline{c}}{\partial t} + \frac{\partial \overline{\rho}\,\overline{u}_i\overline{c}}{\partial x_i} = -\frac{\partial \overline{\rho}\,\chi_i}{\partial x_i} + S$$

where the spatial filter is denoted by a bar. $\overline{u}_i$ are the velocity components, $\overline{p}$ the pressure, $\overline{\rho}$ the density, f the Coriolis parameter, $\overline{c}$ a scalar (e.g. temperature, moisture, passive scalar), and S a generic source/sink term. The turbulent stresses τ_{ij} and scalar fluxes χ_i are represented by the 1.5-order turbulent kinetic energy-based closure (TKE-1.5) of Moeng (1984). An additional prognostic equation for TKE is solved to determine turbulent eddy viscosity K_m and diffusivity K_h:

$$\tau_{ij} = \overline{u_i u_j} - \overline{u_i}\,\overline{u_j} = -2K_m\,\overline{S_{ij}}$$

$$\chi_{ij} = \overline{u_i c} - \overline{u_i}\,\overline{c} = -K_h\,\frac{\partial\,\overline{c}}{\partial x_i}$$

where $\overline{S_{ij}} = \frac{1}{2}\left(\frac{\partial \overline{u}_i}{\partial x_j} + \frac{\partial \overline{u}_j}{\partial x_i}\right)$ is the resolved strain rate tensor. More details on the turbulence model are given in Xue et al. (2001).

On the 25m grid, numerical tracers were released at a constant mass flow rate on top of the landfill from 1400 LST onwards. To reproduce the field setup, three tracer sources were located in a line nearly perpendicular to the wind direction, and were each separated by 67 m. A vertical column of model results at the balloon location were recorded every 2 sec, while 3D flow fields were output every minute.

A.2 Model Validation with Observations

Surface wind measurements from the ground weather station on top of Sandtown Landfill were used to validate the model. Figure A-2(a) shows good agreement of modeled 2 m wind speed and direction with observations. Relevant statistics are presented in Section 4.5 of the paper. Times series of tracer concentration at the balloon location are presented

in Figure A-2(b). The tracer concentrations displayed high, sharp peaks aloft, and low, broad peaks at the surface, consistent with field data.

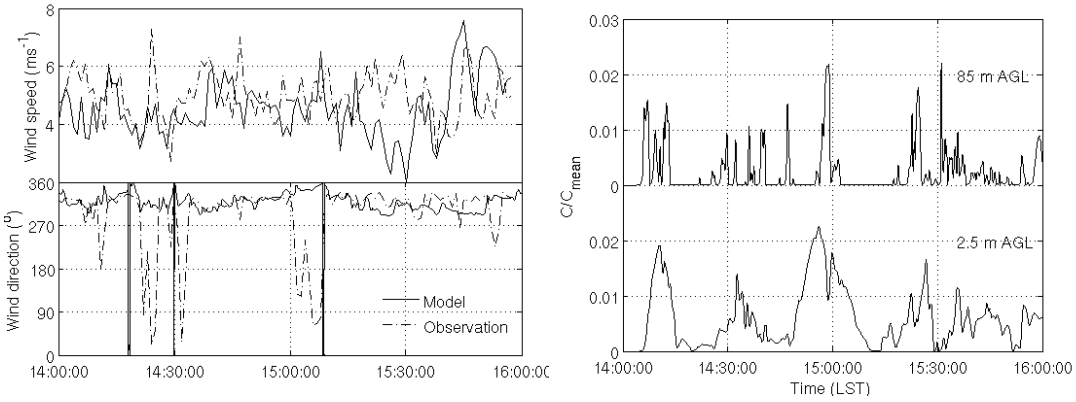

(a) (b)

Figure A-2 Times-series of (a) observed and modeled surface wind speed (above) and direction (below). Solid lines represent model results from the 25m grid, dash-dotted lines represent observations from surface stations. (b) Normalized modeled tracer concentration at the surface and at 85m aloft. C_{mean} is the time-averaged tracer concentration at the release location.

A.3 Travel Time Estimate

The numerical technique of Deleersnijder et al. (2001) was applied to estimate the travel time of the tracer gas. During the simulations, apart from the passive tracer C_p which represented C_2H_2, a decaying tracer C_r was released at the same locations with identical mass flow rates. This tracer underwent a 1st order decay with a preset half-life of $\tau ln2$, i.e. the sink term S in the scalar transport equation was set to be $-c/\tau$. Since both tracers go through the same turbulent advection and diffusion processes, their concentration difference at the measurement location must be due to the "aging" process of the decaying tracer since its initial release. Therefore, the travel time $T(t, \underline{x})$ at time t, location $\underline{x}$, can be estimated as:

$$T(t, \underline{x}) = \tau \ln \frac{C_p(t, \underline{x})}{C_r(t, \underline{x})}$$

Due to the unsteadiness and randomness of turbulent transport processes, T at the measurement location over the 2-hour period is represented by a probability distribution, as shown in Figure A-3. Travel time statistics at different heights at the balloon location are presented as a box plot in Figure A-4. The decrease of T with height is mainly due to increased wind speed aloft.

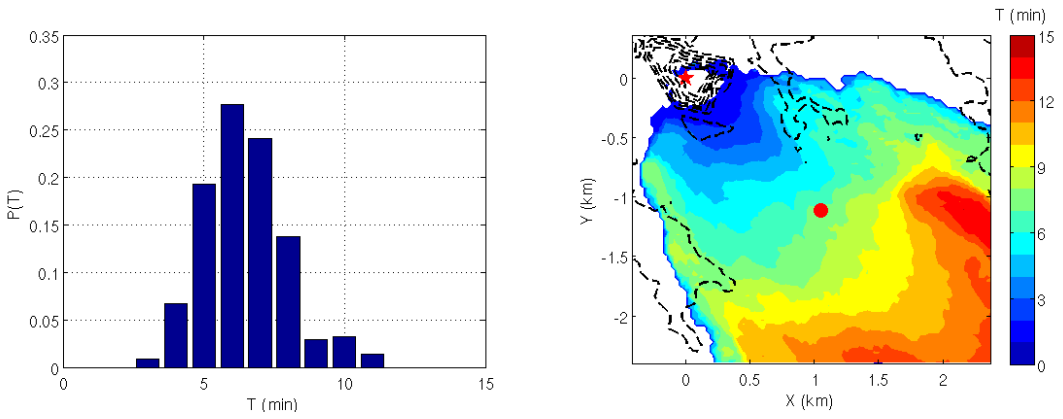

(a) (b)

igure A-3 Histogram of passive tracer travel times from landfill to downwind measurement location at 85 m APG (a), and contour plot of mean travel times at 85 m APG (b). Star indicates location of tracer release on landfill, while circle indicates downwind measurement location.

A.4 Canopy Drag Model

The landfill is surrounded by 25 to 30 m high pine trees that break the wind. On the 25 m LES grid, the pine tree areas were resolved (blue colors in Figure A-1(b)) in the computational domain. Due to the fine vertical grid spacing with near surface grid-stretching, the 30 m trees are represented by 7 grid points in the vertical direction. The traditional representation of tress in meso-scale atmospheric models with an elevated roughness length ($z_o \sim$ 1 m) was too crude and insufficient for the LES domain. Therefore we adopted a canopy model to explicitly resolve the additional drag on the atmospheric flow by the trees.

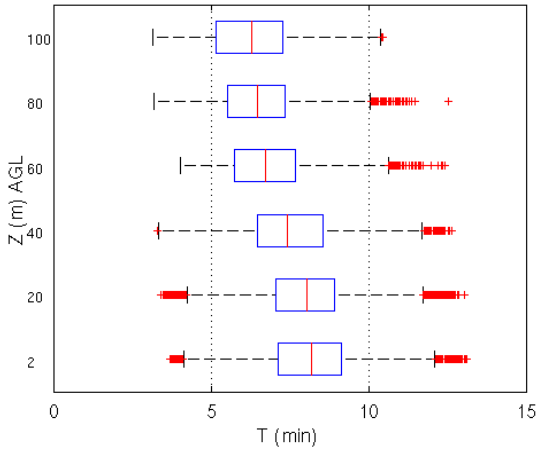

Figure A-4 Box plot of travel time *T* at the different heights at the balloon location. The red line represents the sample median, the left and right edges of the blue box are the 25th

and 75th percentiles, the whiskers are 1.5 times the interquartile range away from the box, and outliers are displayed with a red + sign.

Following Shaw and Schumann (1992), we represented the effects of the tree canopy by adding a drag term F_i in the momentum equation,

$$F_i = -C_d a V \overline{u}_i, \quad i = 1,2$$

where C_d is the drag coefficient set to be 0.15, a is the leaf area density (LAD) as a function of height, V is the wind speed, and $\overline{u}_i$ are the horizontal wind components. Lalic and Mihailovic (2004) presented empirical formulations of a,

$$a(z) = a_m \left(\frac{h - z_m}{h - z}\right)^n \exp\left[n\left(1 - \frac{h - z_m}{h - z}\right)\right], \quad n = \begin{cases} 6 & 0 \le z < z_m \\ 0.5 & z_m < z < h_c \end{cases}$$

where $a(z)$ reaches maximum value a_m at height z_m, n is a shape parameter, and h_c is the height of the canopy. In this study, we followed Lalic and Mihailovic (2004) and set $a_m = 0.37$, $z_m = 0.6h_c$ to represent pine trees. h_c was set to be 30 m, according to observations.

The canopy model had a large impact on the flow. At the balloon site, the upwind pine trees (see Figure A-1(b)) retarded the flow through the canopy, such that the surface wind speed was reduced by more than half compared to simulations where trees were only represented by increased roughness. The increased turbulence within the canopy layer led to more mixing of the tracer, and resulted in low, broad peaks near the surface, as shown in Figure A-2(b). In general, the canopy model acted like a semi-permeable flow obstacle. An internal boundary layer formed downwind of the canopy, so that wind speed reduction was also felt above the canopy height. At the 85 m balloon height, mean wind speed was reduced by ~10%. The overall reduction of wind and the increase in turbulent mixing within and above the canopy layer resulted in a longer tracer travel time that better matched observed values.

Appendix B Grid nesting strategies for convective boundary layer simulations

B.1 Introduction

Day 33 of the Australian Wangara Dataset (Clarke et al. 1971) has been widely used as a test case of numerical simulations of the convective boundary layer (CBL). Those include higher-order closures for Reynolds Averaged Navier-Stokes (RANS) equations (Deardorff 1974a; Deardorff 1974b; Wyngaard and Cote 1974; Yamada and Mellor 1975; Andre et al. 1978), planetary boundary layer (PBL) parameterization schemes (Sun and Chang 1986; Pleim and Xiu 1995), and turbulence models for large-eddy simulations (LES) (Deardorff 1980; Moeng 1984; Basu et al. 2008). Based on the Wangara test case, this study sets out to

1. Investigate model sensitivity to grid-resolution and turbulence representation in a periodic domain setup.
2. Evaluate model performance with different nesting configurations.

B.2 Model Configuration

The model setup for the Wangara test case follows Yamada and Mellor (1975) and (Xue et al., 1996). Simulations are performed from 0900 LST to 1800 LST on Day 33 (Aug 16th, 1967) of the Wangara experiment, located at (34.5^{o}S 133.93^{o}E) in Australia. The bottom surface is flat with a momentum roughness height of 0.01 m. A time-varying surface flux boundary condition is applied uniformly to drive daytime heating:

$$sflx = \sin\left(\frac{\pi}{11\times3600}t + \frac{1.5}{11}\pi\right)$$

$$\overline{w'\theta'}_s = 0.216 sflx\ Kms^{-1}; \quad \overline{w'q'}_s = 2.29\times10^{-5} sflx\ ms^{-1}$$

where t(s) is set to 0 at the initial integration time 0900 LST, $\overline{w'\theta'}_s$ (Kms^{-1}) and $\overline{w'q'}_s$ (ms^{-1}) are the surface heatflux and moisture flux, θ (K) is the potential temperature, and q (kg of H_20 per kg of total air mass) is the specific humidity. Temporally constant geostrophic winds (U_g, V_g) are applied to simulate a synoptic pressure gradient.

$$U_g = \begin{cases} 0.0029z - 5.5 & 0 \le z < 1000 \\ 0.0014z - 4 & 1000 \le z < 2000' \end{cases} \quad V_g = 0$$

The initial profiles are specified according to the atmospheric sounding in Table B-1, and interpolated in between.

A total of 9 simulations are performed with varying grid spacing and turbulence representations. The number of grid points (nx, ny, nz) = (43, 43, 43) is the same for all simulations, except for run M5, where nz = 23. The subgrid scale (SGS) turbulence closure for all simulations is TKE-1.5 (Moeng 1984). The PBL parameterization scheme of Sun and Chang (1986) is applied on some runs. Simulations with the TKE-1.5 closure alone are initialed with "M". Those with TKE-1.5 plus the PBL scheme are initialed with

"S". The isotropic turbulence option applies the same mixing length scale specified by the grid spacing ($\sqrt[3]{\Delta x \Delta y \Delta z}$) in all directions, while the anisotropic option differentiates the horizontal mixing length scale ($\sqrt{\Delta x \Delta y}$) from the vertical one Δz. The anisotropic option is often applied in meso-scale simulations when the grid aspect ratio $\sqrt{\Delta x \Delta y}/\Delta z$ is large (the general threshold being 100). A list of model parameters is given in Table B-2.

Table B-1 Sounding at 0900 LST, Day 33 of the Wangara Experiment. P is the pressure, T the temperature, Q the specific humidity, U, and V the horizontal wind components.

P (mb)	T (K)	Q (g kg^{-1})	U (ms^{-1})	V (ms^{-1})
10	208.16	0	35	0
15	208.16	0	35	0
35	233.16	0.23	30	0
48	258.16	0.23	25	0
62.3	268.16	0.26	15	0
72.3	271.66	0.31	7	0
79.9	272.96	0.6	0.5	1.1
82	274.56	0.7	-0.7	1.72
84	274.86	0.8	-1.19	0.26
86.1	275.16	0.8	-1.45	0.07
88.3	275.46	1.5	-1.93	-0.9
89	275.76	1.8	-2.29	-1.41
90.5	275.66	2	-2.55	-1.16
91.6	276.06	2.2	-2.28	-0.76
92.8	276.66	2.5	-2.45	-0.48
93.9	276.96	2.9	-2.43	-0.35
95.1	277.86	3.2	-2.79	-0.26
96.3	278.96	3.3	-2.49	-0.37
97.4	279.96	3.3	-3.2	-0.47
98.6	280.56	3.7	-3.12	-0.51
99.8	280.66	3.8	-2.79	-0.57
101.1	278.56	3.8	-2.92	-0.38
101.7	278.26	3.7	-2.84	0.03
102.3	278.66	4.2	0	0

Table B-2 List of model parameters.

Run Name	Δx/Δy (m)	Δz (m)	Δt_{big} (s)	Δt_{small} (s)	isotropic	PBL scheme
M1	125	50	4.0	0.2	yes	off
M2	500	50	5.0	0.8	yes	off
M3	1000	50	5.0	1.6	yes	off
M4	6000	50	5.0	5.0	no	off
S1	125	50	4.0	0.2	yes	on
S2	500	50	5.0	0.8	yes	on
S3	1000	50	5.0	1.6	yes	on
S4	6000	50	5.0	5.0	no	on
M5	6000	100	5.0	5.0	no	off
M6	6000	50	1.0	1.0	yes	off
M7	6000	50	1.0	1.0	no[6]	off

B.3 Mean Profiles

The daytime CBL is generally well mixed due to energetic convective motions. Therefore, an isentropic potential temperature θ is expected. Figure B-1 presents horizontally averaged mean profiles of θ at 0900, 1200, 1500 and 1800 LST for model runs M1-4 and S1-4. The observed vertical temperature profiles from Clarke et al. (1971) are presented on the top panel of Figure B-1. Simulated profiles from model runs M1-2 and S1-4 agree well with observations. Model results from M1-3 are quite consistent in terms of the overall profiles, while M4 is clearly overheated near the surface. In M1, a super-adiabatic surface layer, where $d\theta/dz$ is negative, is represented by the first 2 grid points above the wall. In M2-4, surface layers are less sharp, and spread over a deeper distance. The sustained negative temperature gradient is due to a less well mixed CBL. This suggests that vertical turbulent mixing is less efficient as the horizontal grid spacing coarsens.

The overall turbulent heatflux in the model consists of a resolved and a SGS part:

$$\overline{w\theta} = \underbrace{\bar{w}\bar{\theta}}_{Resolved} + \underbrace{w\theta - \bar{w}\bar{\theta}}_{SGS}$$

where overbars represent planar averaging. As the grid resolution coarsens, the amount of resolved convection is decreased. Meanwhile, the SGS contribution is expected to increase. If the increments in the SGS flux fully compensate for the loss in the resolved flux, the total flux $\overline{w\theta}$ remains unchanged. This should be the case when the grid resolution falls in the inertial subrange, and the SGS processes are represented by an LES closure.

In the CBL, the dominant size of the convective eddies is roughly the boundary layer depth Z_i. In the Wangara test case, $Z_i \sim 1500$ m at 1800 LST, as indicated by the height of the capping inversion. At a grid resolution of 6 km (such as in M4), convection is entirely a SGS process. The LES closure (TKE-1.5 in this case) alone is not capable of

[6] In M7, the vertical mixing length is set as $\sqrt{\Delta x \Delta z}$ rather than Δz in the non-isotropic configuration.

compensating for the loss in resolved turbulence. Therefore, heat added to the CBL at the bottom boundary is trapped near the surface until 1500 LST due to insufficient vertical mixing. The accumulated heat is released into the upper CBL between 1500 to 1800 LST in D4.

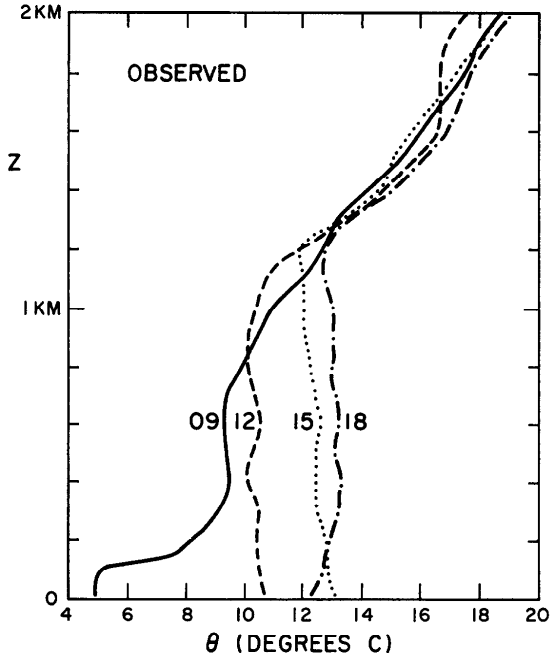

(Observations from Clarke et al. (1971))

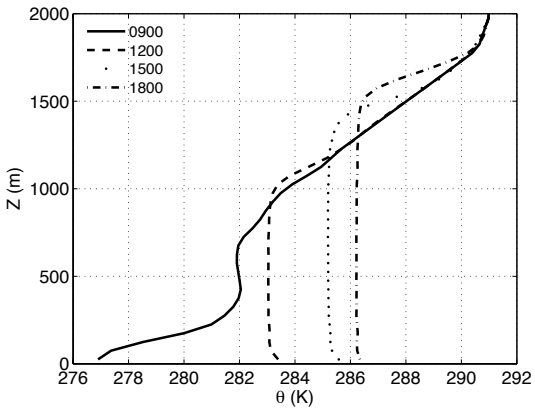

(M1)

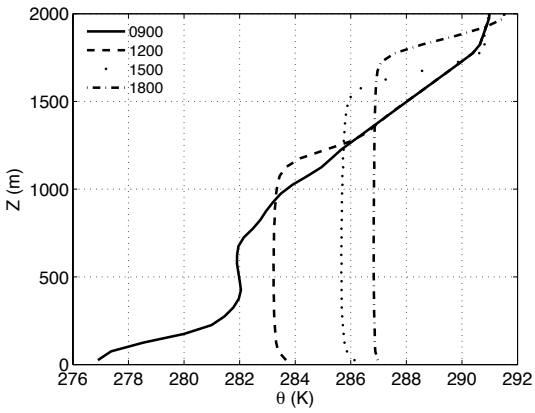

(S1)

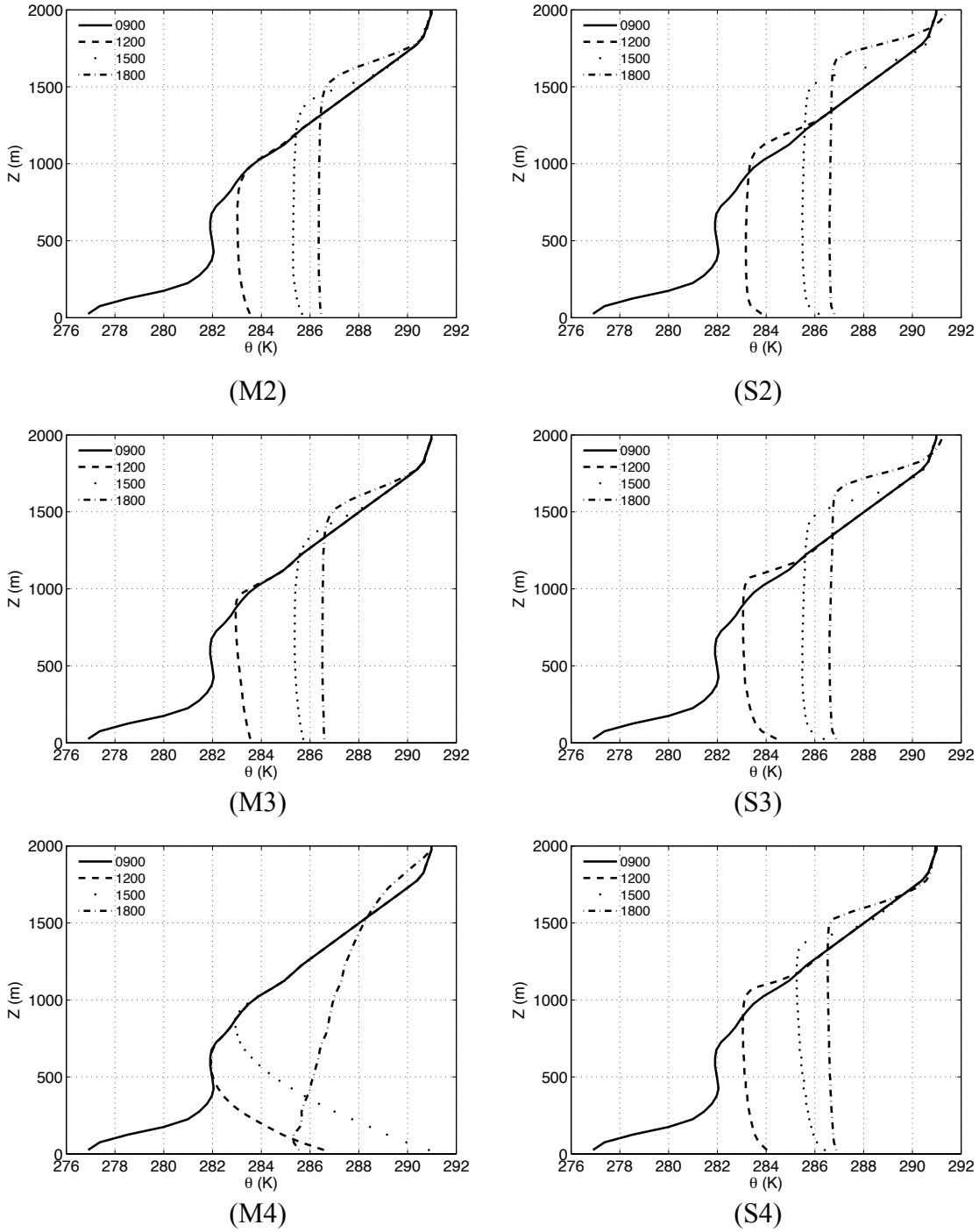

Figure B-1 Vertical profiles of horizontally averaged potential temperature θ. The observed vertical profile plot is adapted from Deardorff (1974a). Run names are given in the labels. Solid line represents <θ> at 0900 LST, dashed line at 1200 LST, dotted line at 1500 LST and dash-dotted line at 1800 LST.

When performing meso-scale simulations (grid spacing ~O(10 km)), planetary boundary layer (PBL) parameterization schemes must be used to represent the correct the SGS mixing process. In this test case, the Sun and Chang (1986) PBL scheme is used to replace the vertical SGS length scale l_v in the TKE-1.5 closure, while the horizontal length scale l_h is kept the same $\sqrt[3]{\Delta x \Delta y \Delta z}$.

$$l_v = 0.25\{1.8Zi[1 - \exp\left(-\frac{4z}{Zi}\right) - 0.0003\exp\left(\frac{8z}{Zi}\right)]\}$$

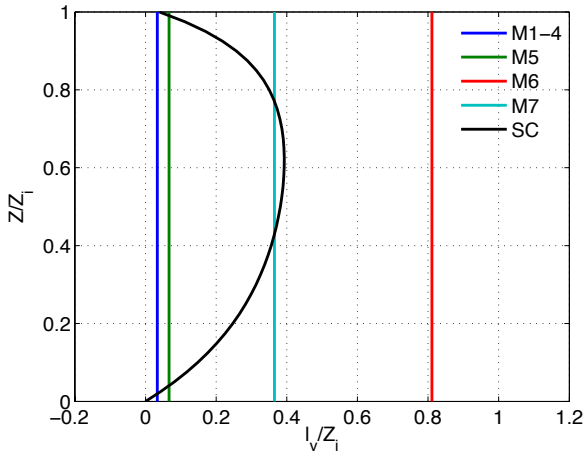

Figure B-2 Vertical profile of the vertical turbulence length scale in M4-M7, and Sun and Chang scale. A boundary layer depth Zi of 1500 m is used.

The parameterization imposes a somewhat parabolic profile bounded by the surface and the capping inversion. It is supposed to represent the "true" turbulent mixing length as a function of height in the CBL. In comparison, the LES representation of l_v is a function of the local grid spacing, therefore constant throughout in the current setup without vertical grid stretching. In the non-isotropic configuration in M4, l_v (50 m) is only 3% of the boundary layer depth Z_i. While the difference is compensated by resolved turbulence at the LES scale, it is limited to the meso-scale grid resolution, leading to an under-mixed CBL. Coarsening the vertical grid spacing in M5 improves the vertical profiles from M4 in Figure B-3.

The above analysis explains why parameterization must be turned on when the grid resolution is coarse compared to the dominant turbulence length scale. Such model switching depends on the *a priori* knowledge of the important length scale L of the atmospheric flow. During daytime, the vertical mixing length scale (L_v) is generally the boundary layer depth. At nighttime, L can be the buoyancy length scale, or the wavelength of gravity waves. Over complex terrain, L is often set by the topography, and hard to determine.

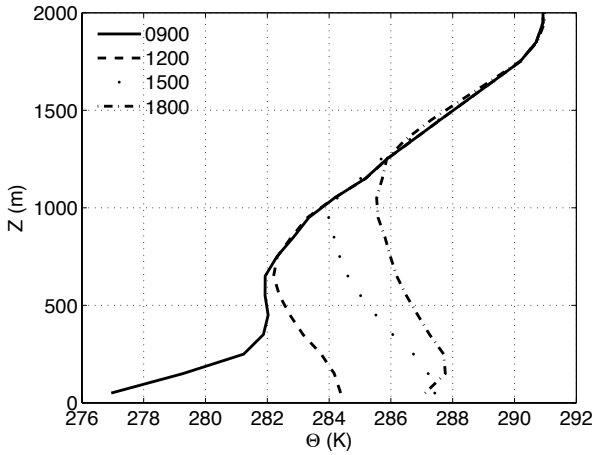

Figure B-3 As for Figure B-1, but for case M5.

Ideally, a single model that works across all scales is preferred. There are two ways to approach such a unified model. One can either modify the meso-scale approach, i.e. PBL parameterizations, to function at the micro-scale, or one can modify the micro-scale approach, i.e. LES turbulence closures, to function at the meso-scale. Some simple attempts are made here in both directions. First, the PBL scheme is applied at the small scales without any modification (cases S1-2). The vertical mean profiles of $\bar{\theta}$ are predicted well for all grid resolutions, as shown in Figure B-1. This is due to the enhanced SGS mixing of the PBL parameterizations when applied at the LES grid, as shown in Figure B-2. The vertical length scale of the PBL scheme is much larger than the LES mixing length set by the local grid spacing. Over mixing does not affect $\bar{\theta}$ because it has zero vertical gradients under well-mixed conditions. In other words, enhanced mixing shortens the timescale (Z_i^2/ν_T) of the boundary layer response to surface heating, but does not affect the mean profiles. However, the resolved motions do lose a considerable amount of variability due to over mixing on the 125 m LES grid, as seen in Figures B-4 and B-6. On the 500 m grid, the differences in turbulent profiles are less significant between M2 and S2, as shown in Figure B-5 and B-7. The LES closure gives more variability in the flow field than the PBL scheme.

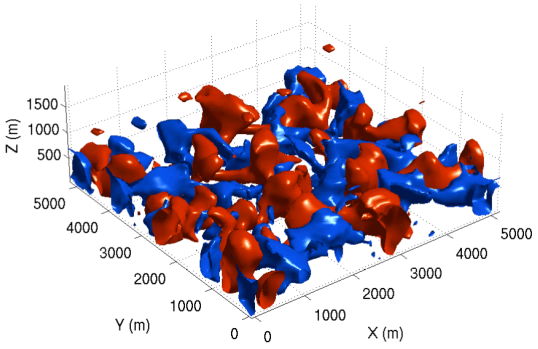

(M1-1200 LST)

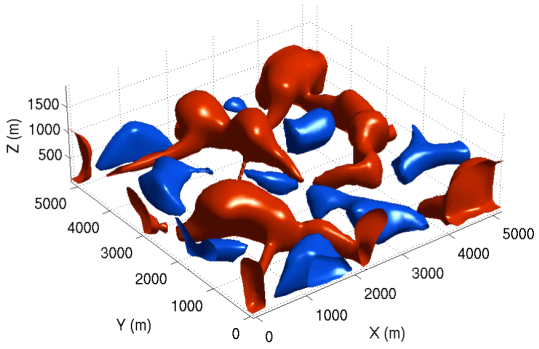

(S1-1200 LST)

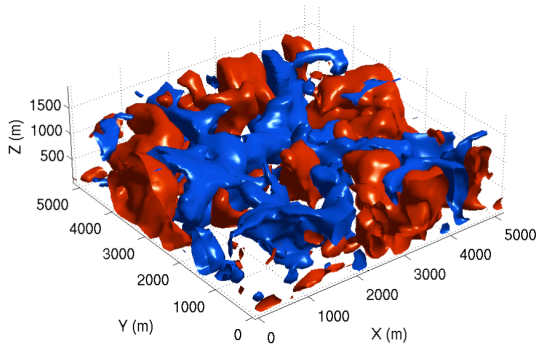

(M1-1500 LST)

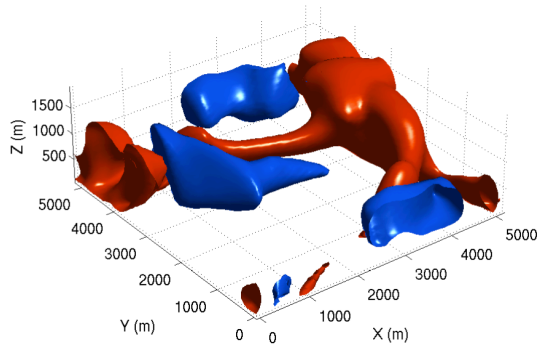

(S1-1500 LST)

Figure B-4 Isosurfaces of vertical velocity w at 1200 LST (upper panel) and 1500 LST (lower panel), for the case M1 (left panel) and S1 (right panel). Red surfaces represent w = 1.0 ms^{-1}, blue surfaces represent w = -1.0 ms^{-1}.

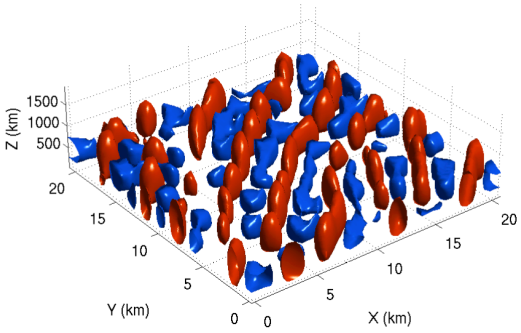

(M2-1200 LST)

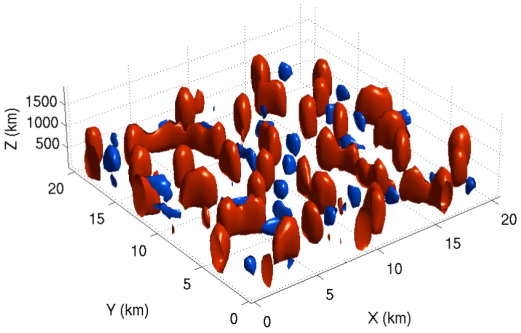

(S2-1200 LST)

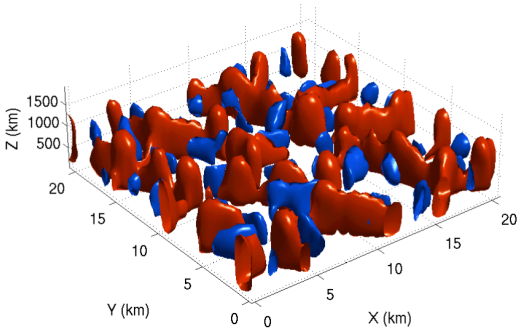

(M2-1500 LST)

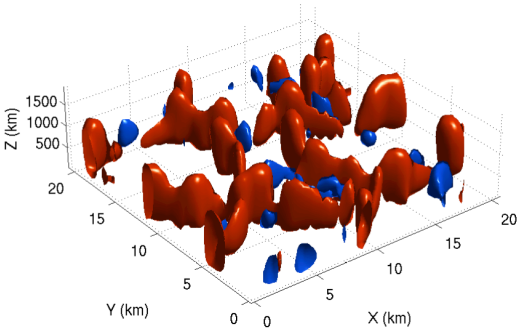

(S2-1500 LST)

Figure B-5 As for Figure B-4, but for case M2 (left panel) and S2 (right panel).

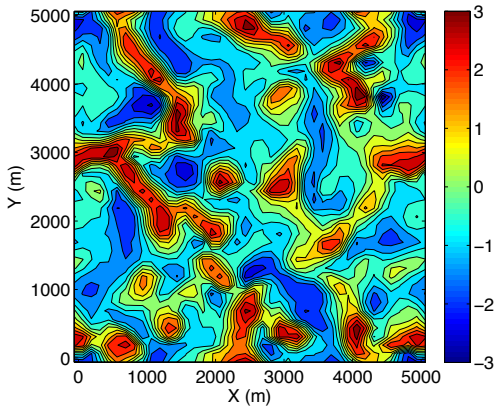

(M1-1200 LST)

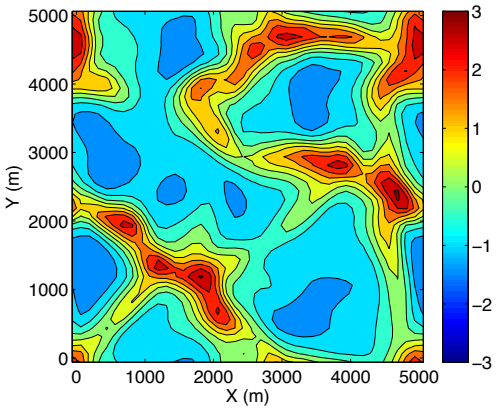

(S1-1200 LST)

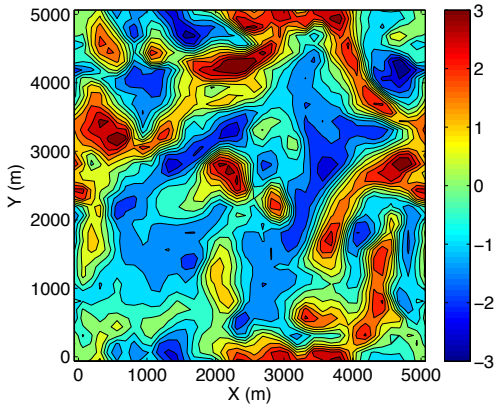

(M1-1500 LST)

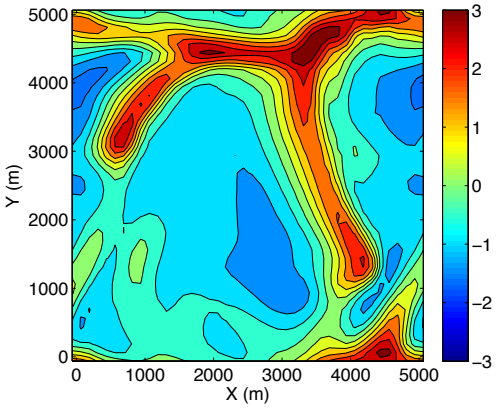

(S1-1500 LST)

Figure B-6 Contours of vertical velocity w at 425 m AGL at 1200 LST (upper panel) and 1500 LST (lower panel), for the case M1 (left panel) and S1 (right panel). Contours are separated by 0.5 ms^{-1}.

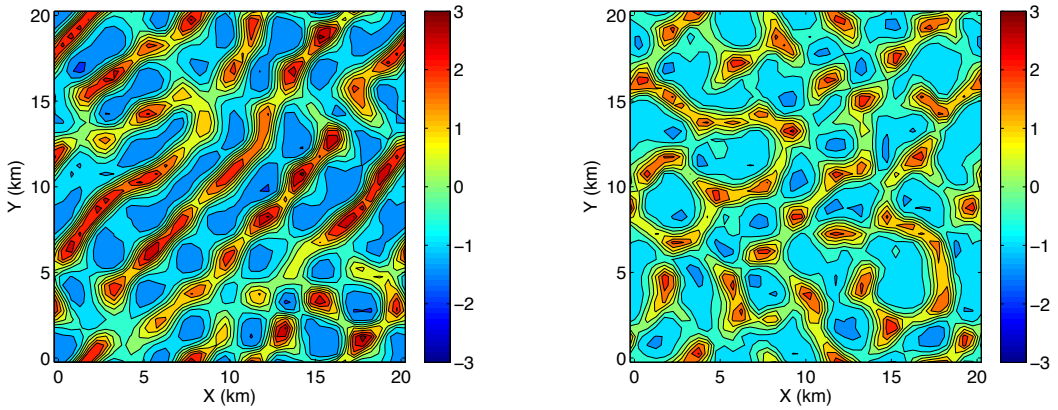

(M2-1200 LST) (S2-1200 LST)

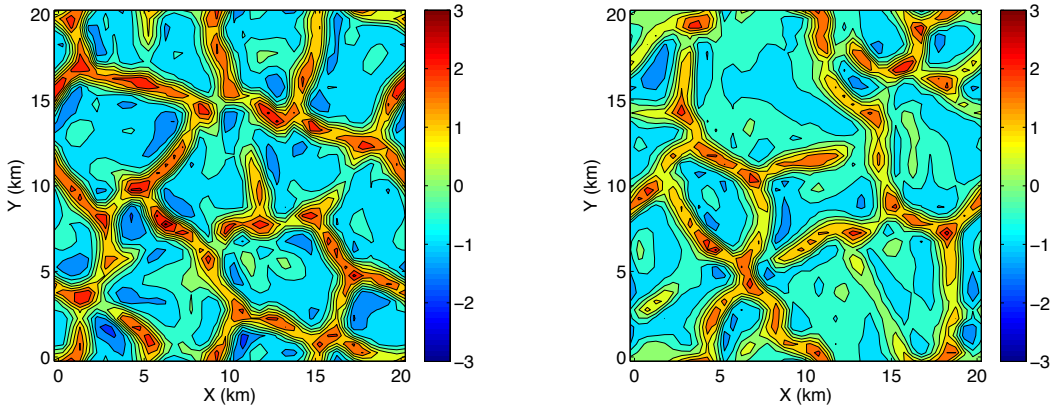

(M2-1500 LST) (S2-1500 LST)

Figure B-7 As for Figure B-6, but for case M2 (left panel) and S2 (right panel).

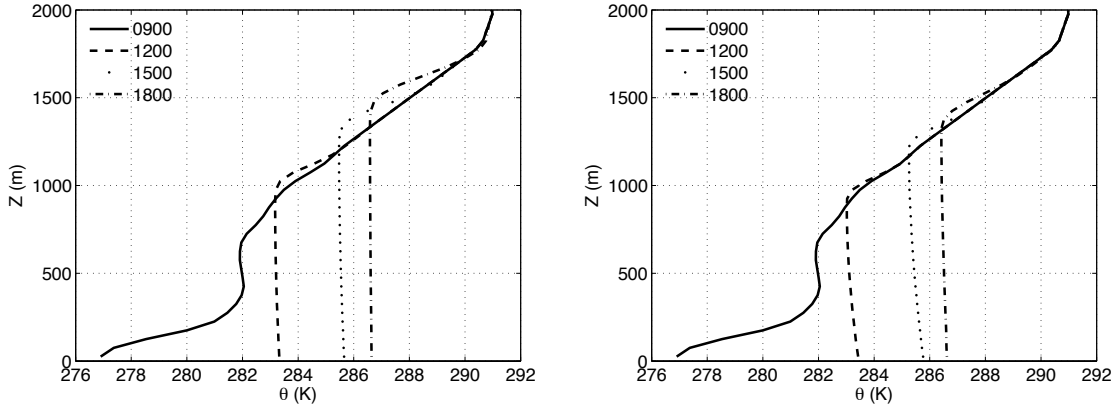

(M6) (M7)

Figure B-8 As for Figure B-1, but for cases M6 and M7.

The LES closure is also applied at the meso-scale with modifications to the vertical turbulent length l_v. In M6, the isotropic option is chosen, such that $l_v = \sqrt[3]{\Delta x \Delta y \Delta z}$ rather than Δz. This is not generally recommended when the grid aspect ratio is large. The general rule of thumb sets the threshold at 100 (in the 6000 m horizontal grid, the aspect ratio is 6000/50 = 120). M7 arbitrarily sets a smaller $l_v = \sqrt{\Delta x \Delta z}$. The predicted $\bar{\theta}$ profiles in Figure B-8 are quite satisfactory with both of these modifications. This illustrates that the vertical mixing length scale from LES must be larger in order to fully represent the SGS convective mixing on a meso-scale grid. This could be arbitrarily accomplished by adjusting the LES length scales.

B.4 Nested Simulations

When performing one-way nested simulations with the Advanced Regional Prediction System (ARPS), horizontal roll vortices are sometimes observed during daytime convective conditions. To explore the nature and formation mechanism for these "convection rolls", the Wangara test case is performed in a one-way nested setup. The outer domain has horizontal/vertical spacing at 3600 m and 50 m, respectively. The simulation is performed under the idealized setting described in section B-1, i.e. periodic lateral boundary conditions, prescribed geostrophic winds and surface heatflux. The inner domain receives lateral boundary updates from the outer domain every 15 min. Two nesting configurations are tested, one with horizontal spacing of 1200 m (N12-P36) and the other 200 m (N2-P36). The numbers of grid points of both inner domains are set such that the size of the inner domain width is 1/3 of the outer domain. The Sun and Chang PBL parameterization scheme is used on the outer domain. The inner domain is run in LES mode with the isotropic option, which sets the turbulent mixing length to be $\sqrt[3]{\Delta x \Delta y \Delta z}$ in both horizontal and vertical directions. More details of the model parameters are given in Table B-3. Periodic runs are initialed with "P", and nested runs with "N", followed by the run name of the outer domain.

Table B-3 List of nested model parameters. ΔT_b is the lateral boundary update interval.

Run Name	Δx/Δy (m)	Δz (m)	(nx, ny, nz)	Δt_{big} (s)	Δt_{small} (s)	ΔT_b (s)	PBL scheme
P36	3600	50	43, 43, 53	5.0	2.5	N.A.	on
N12-P36	1200	50	43, 43, 53	2.0	1.0	900	off
N2-P36	200	50	243, 243, 53	0.5	0.25	900	off
P12	1200	50	43, 43, 53	5.0	2.0	N.A.	off
N2-N12-P36	200	50	83, 83, 53	0.5	0.25	900	off
P2	200	50	83, 83, 53	0.5	0.25	N.A.	off

Figure B-9 presents horizontally averaged vertical profiles of potential temperature, wind speed and direction for the outer domain (P36) and two inner domains (N12-P36 and N2-P36). Good agreement is achieved overall. Figure B-10 presents horizontal contours of w at 200 m AGL. The outer domain (N36) clearly does not resolve any

vertical motions, leaving convection a SGS process. Significant differences are observed between the two nested configurations. While cellular structures are present in the fine nested grid (N2-P36), roll structures along the wind direction are observed from the domain center to the outflow boundary (east side) in the coarse nested grid (N12-P36). Note that on both nested domains, roll structures perpendicular to the winds are present at the inflow boundary. In N2-P36, these vertical rolls only occupy a small fraction of the domain and quickly transition into convective cells.

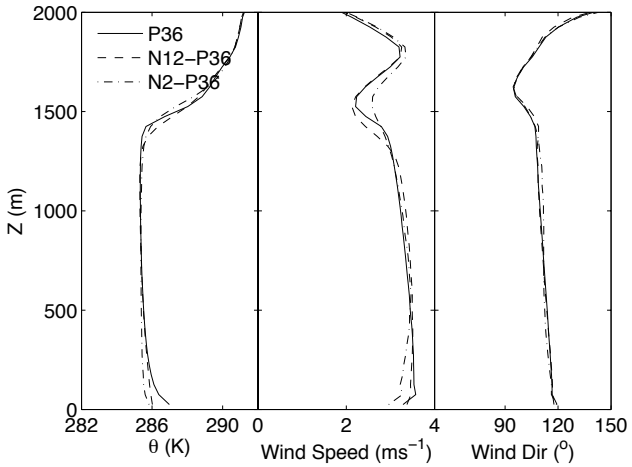

Figure B-9 Vertical profiles of horizontally averaged potential temperature θ, wind speed and wind direction. Solid lines represent P36, dashed lines N12-P36, and dashed dotted lines N2-P36.

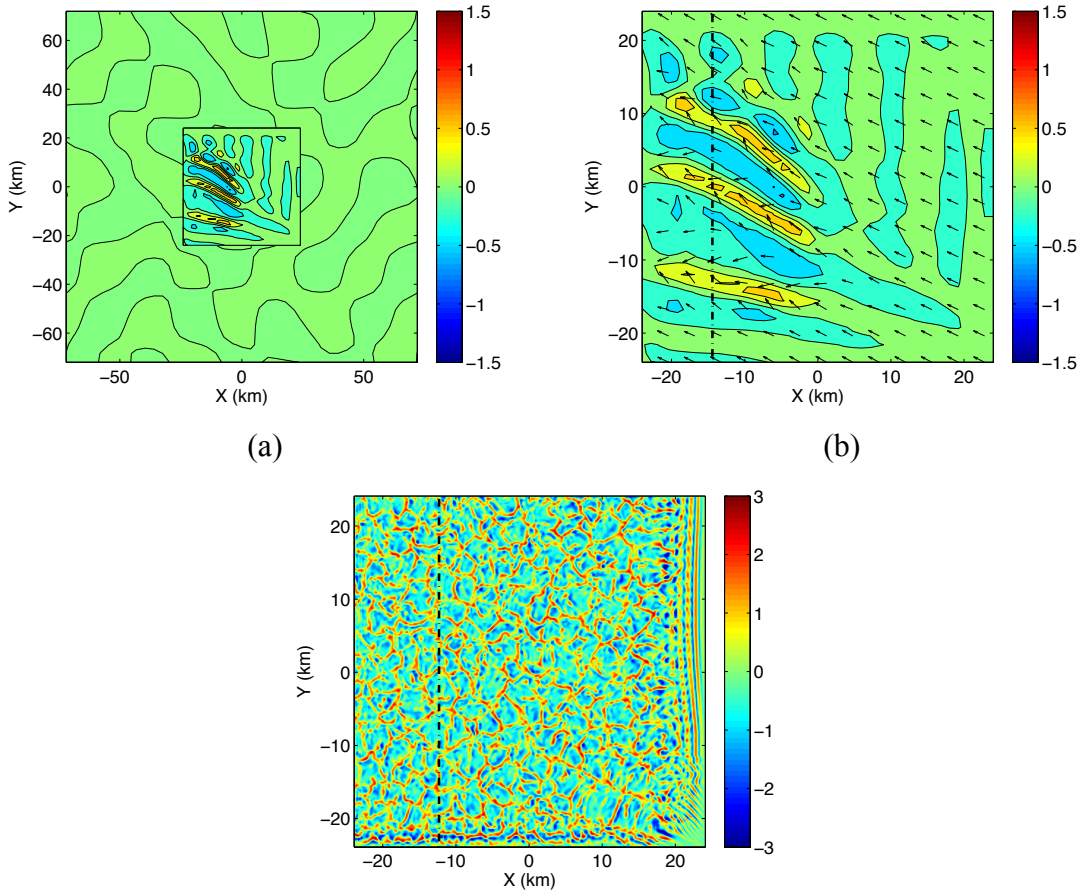

Figure B-10 Contours of vertical velocity component w (ms^{-1}) at 200 m AGL for (a) N12-P36 plotted within P36, (b) N12-P36, and (c) N2-P36. Contours are separated by 0.25 ms^{-1}. Colorbars are set to different scales according to max|w| for clarity.

Figure B-11 presents contours of w on the yz plane, represented by dashed lines in Figure B-10(b) and (c). The vertical extent of both cells and rolls spans the entire CBL. To investigate the effects of nesting, a stand-alone simulation P12 with identical model setup to N12-P36 except with periodic lateral boundary conditions is performed. In Figure B-12(a), cellular structures similar to Figure B-10(c), although of greater sizes, develop in P12. The vertical contours of P12 are similar to those of N12-P36. Vertical motions are more energetic and the boundary layer depth is deeper in P12.

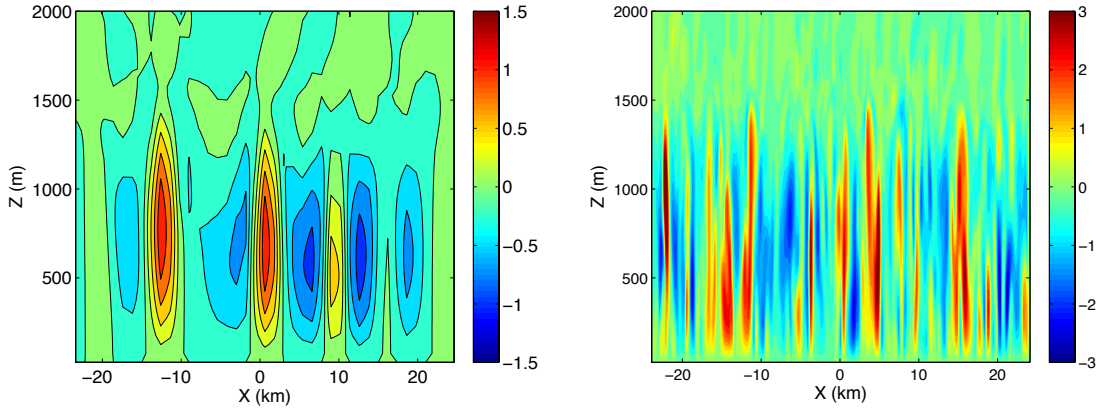

(a) (b)

Figure B-11 Contours of vertical velocity component w (ms^{-1}) on the yz plane marked by dash-dotted lines in Figure B-11 for (a) N12-P36 and (b) N2-P36. Contours are separated by 0.25 ms^{-1}.

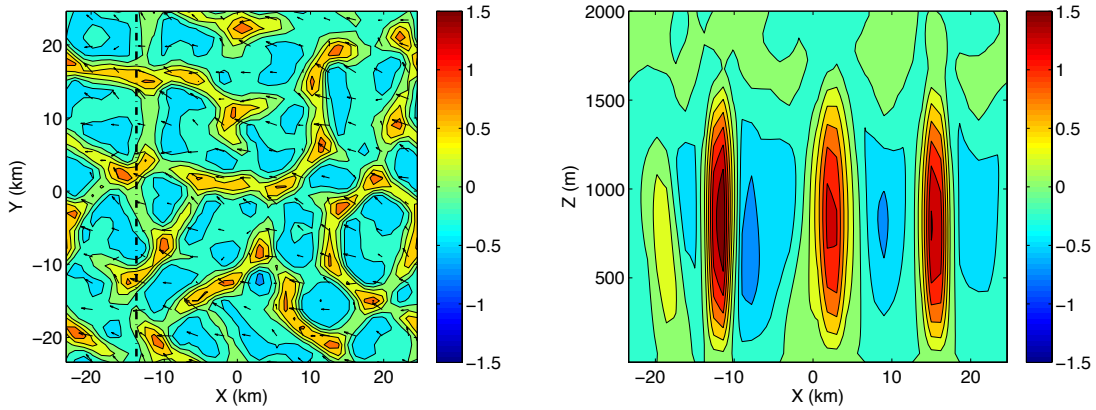

(a) (b)

Figure B-12 Contours of vertical velocity component w (ms^{-1}) on the (a) xy plane and (b) yz plane marked as dash-dotted lines in (a) for P12. Contours are separated by 0.25 ms^{-1}.

Another set of simulations is performed where N12-P36 is further nested to a 200 m grid (N2-N12-P36), following a 3 to 1 nesting ratio in terms of domain width. A stand-alone periodic run P2 is also performed to compare with results from the nested configuration. In Figure B-13 (a), the roll structures developed in N12-P36 (Figure B-10 (b)) do *not* seem to have propagated down to the next grid level. In other cases, for example the Sandtown case in Appendix A, the rolls do propagate down and contaminate the next nest level.

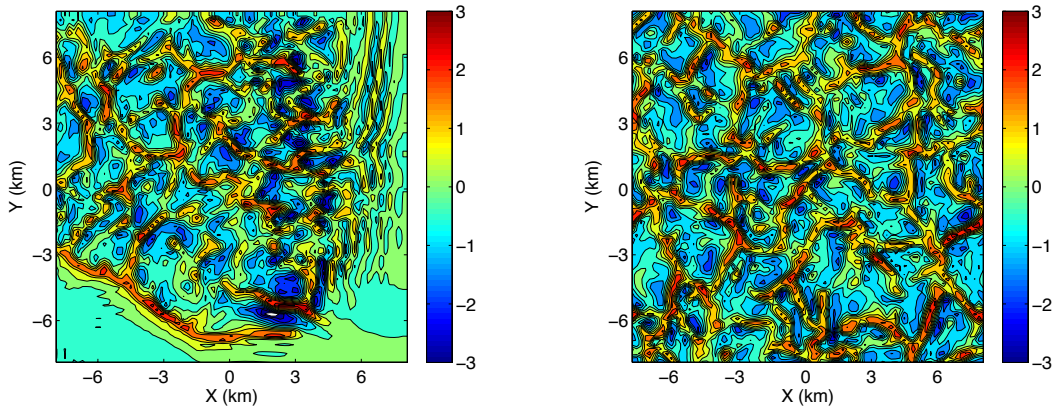

(a) (b)

Figure B-13 As for Figure B-10, but for (a) N2-N12-N36 and (b) P2, Contours are separated by 0.5 ms^{-1}.

Overall, this preliminary study shows that N2-P36 performs better than N2-N12-P36. In other words, a higher nesting ratio with fewer nest-levels might be a better option than a lower nesting ratio with more nest-levels. However, there are many uncertainties in the above statement. First, the effect of terrain is not considered in this test case. Second, it is not clear whether the number of grid points or domain sizes matters for this study. Third, simulations are performed in a one-way nested configuration, where information is only passed down from the outer to the inner domain. The alternative two-way interactive nesting has not been tested and its effects unclear. The most useful conclusion from this study is that N12-P36 is definitely NOT worth running. To generalize, nested simulations of CBL should not be run at grid spacing comparable to the boundary layer depth. The roll structures that develop in N12-P36 could be due to *terra incognita* effects, but this is not certain.

Appendix C Derivation of the critical Richardson number

This is a detailed reproduction of the derivation of the critical Richardson number for stratified flow to transition from quiescent to turbulent states. The argument is originally presented on page 491 of Chandrasekhar (1961). The elegancy of the argument lies in its simplicity. As commented by Drazin and Reid (2004):

"The essential mechanism of instability is the conversion of the available kinetic energy of the relative motion of layers of the basic flow into the kinetic energy of the disturbances, overcoming the potential energy needed to raise or lower fluid under stably stratified conditions."

Consider two vertically adjacent parcels of air A and B in a stratified shear flow. Parcel A is slightly lighter than B, therefore sitting at a higher elevation. Interchanging elevations of the two parcels leads to an overall increase of the potential energy of the system, because the heavier parcel B is moved above the lighter parcel A. To allow for the interchange, the increase in potential energy must be compensated by the decrease of the kinetic energy of the system, so that energy is conserved. The overall system is considered unstable if such interchanges can happen, and stable otherwise.

Table C-1 Wind speeds and elevations of parcels A and B before and after swapping positions.

	Before			After		
Parcel	Elevation	Density	Wind speed	Elevation	Density	Wind speed
A	$z + \Delta z$	ρ	$u + \Delta u$	z	ρ	$u + (1-k)\Delta u$
B	z	$\rho + \Delta\rho$	u	$z + \Delta z$	$\rho + \Delta\rho$	$u + k\Delta u$

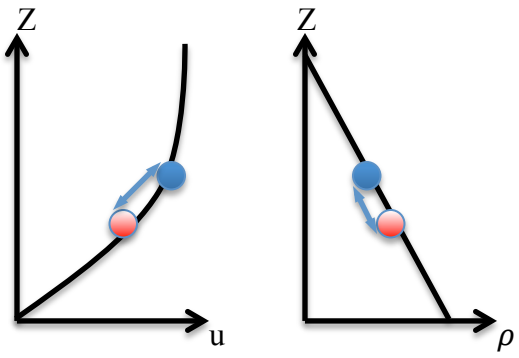

Figure C-1 Schematic of vertical wind speed and density profiles in a stable boundary layer.

The wind speeds and elevations of both parcels are listed in Table C-1, a schematic of vertical profiles of wind speed and density is presented in Figure C-1. Under stable

stratification, $\Delta\rho$ and Δu > 0. The constant k is between 0 and 1. It is applied so that the slow moving parcel B, when ejected upwards to the elevation z + Δz, does not move faster than the surrounding fluid at wind speed u + Δu. Similarly, when the fast moving parcel A is swept downwards to elevation z, it does not move slower than the surrounding fluid. The formulation of wind speeds after the interchange must satisfy momentum conservation.

$$M_{before} = \underbrace{\rho(u+\Delta u)}_{A} + \underbrace{(\rho+\Delta\rho)u}_{B} = 2\rho u + \rho\Delta u + u\Delta\rho$$

$$M_{after} = \underbrace{(\rho+\Delta\rho)[u+(1-k)\Delta u]}_{A} + \underbrace{\rho(u+k\Delta u)}_{B}$$
$$= 2\rho u + \rho\Delta u + u\Delta\rho + (1-k)\Delta\rho\Delta u$$

The second order term $\Delta\rho\Delta u$ is much smaller than the leading first order terms $\rho\Delta u$ and $u\Delta\rho$, therefore ignored in M_{after}. Momentum is conserved so we must have $M_{before} = M_{after}$.

Now we compute the overall increase in potential energy PE of the system:

$$\frac{PE_{before}}{g} = \underbrace{\rho(z+\Delta z)}_{A} + \underbrace{(\rho+\Delta\rho)z}_{B} = 2\rho z + \rho\Delta z + z\Delta\rho$$

$$\frac{PE_{after}}{g} = \underbrace{\rho z}_{A} + \underbrace{(\rho+\Delta\rho)(z+\Delta z)}_{B} = 2\rho z + \rho\Delta z + z\Delta\rho + \Delta\rho\Delta z$$

The overall potential energy increased by:

$$\Delta PE = PE_{after} - PE_{before} = g\Delta\rho\Delta z > 0$$

The kinetic energy of system before and after the swap are:

$$2KE_{before} = \underbrace{\rho(u+\Delta u)^2}_{A} + \underbrace{(\rho+\Delta\rho)u^2}_{B} = 2\rho u^2 + \rho\Delta u^2 + u^2\Delta\rho + 2\rho u\Delta u$$

$$2KE_{after} = \underbrace{\rho[u+(1-k)\Delta u]^2}_{A} + \underbrace{(\rho+\Delta\rho)(u+k\Delta u)^2}_{B}$$
$$= 2\rho u^2 + (2k^2-2k+1)\rho\Delta u^2 + u^2\Delta\rho + 2\rho u\Delta u + k^2\Delta\rho\Delta u^2$$

Again, neglecting the third order term $(1-k)^2\Delta\rho\Delta u^2$ in comparison to the lower order terms, the overall kinetic energy is decreased by:

$$\Delta KE = KE_{after} - KE_{before} = (k^2-k)\rho\Delta u^2 + o(\Delta\rho\Delta u^2) < 0$$

The interchange is only possible when there is enough kinetic energy converted into potential energy, i.e. $|\Delta PE| \le |\Delta KE|$. The maximum decrease of kinetic energy is reached at k = ½, given the parabolic dependence of ΔKE on k. Therefore, the *sufficient* condition for possible interchange is if $\Delta PE \le \max(|\Delta KE|)$. In other words, if $\Delta PE > \max(|\Delta KE|)$, the interchange is definitely not possible.

$$g\Delta\rho\Delta z \le \max(|(k^2-k)\rho\Delta u^2|) = \frac{1}{4}\rho\Delta u^2$$

Dividing by Δz^2, and rearrange gives:

$$\frac{-\frac{g}{\rho}\frac{\Delta\rho}{\Delta z}}{\left(\frac{\Delta u}{\Delta z}\right)^2} \leq \frac{1}{4}$$

The term $-\frac{g}{\rho}\frac{\Delta\rho}{\Delta z} / \left(\frac{\Delta u}{\Delta z}\right)^2$ is the gradient Richardson number R_i. Therefore, the sufficient condition for instability is $R_i < ¼$. ¼ is called the critical R_i above which the flow decays into a quiescent state and below which the flow could stay in a continuously turbulent state.

Appendix D Lagrangian-averaging for the dynamic reconstruction model with explicit filtering and reconstruction

This appendix describes the formulation of the dynamic Wong-Lilly model (Wong and Lilly 1994) with explicit filtering and reconstruction (Chow 2004), the Lagrangian-averaging concept for computing eddy viscosities (Meneveau et al. 1996), and finally the formulation of a Lagrangian-averaged dynamic Wong-Lilly model. Derivations are based on impressible flows, discretized on an isotropic grid of spacing Δ for simplicity.

D.1 Dynamic reconstruction model (DRM) with explicit filtering and reconstruction

Notation:
$\overline{\ }$: explicit filter of width 2Δ
$\widehat{\ }$: explicit filter of width 4Δ
$\widetilde{\ }$: implicit filter due to LES grid and numerical method
$\hat{\Delta}$: coarse grid spacing (assumed equal to 2Δ)
* : reconstructed quantities
^{c} : for coarse quantities
$\langle\rangle$: averaging operator
φ : generic variable

The governing equations for the explicitly filtered momentum and potential temperature transport equations are as follows:

$$\frac{\partial \overline{\tilde{u}}_i}{\partial t} + \frac{\partial \widehat{\overline{\tilde{u}}_i}\,\widehat{\overline{\tilde{u}}_j}}{\partial x_j} = -\frac{1}{\rho}\frac{\partial \overline{\tilde{p}}}{\partial x_i} - \frac{\partial\, \tilde{\tau}_{ij}}{\partial x_j}$$

$$\frac{\partial \overline{\tilde{\theta}}}{\partial t} + \frac{\partial \overline{\tilde{u}}_i \overline{\tilde{\theta}}}{\partial x_i} = -\frac{\partial\, \tilde{\chi}_i}{\partial x_i}$$

where the subfilter scale (SFS) stresses are:

$$\tau_{ij} = \overline{u_i u_j} - \overline{\tilde{u}}_i\,\overline{\tilde{u}}_j = \underbrace{\overline{u_i u_j} - \overline{\tilde{u}_i \tilde{u}_j}}_{\tau_{SGS}} + \underbrace{\overline{\tilde{u}_i \tilde{u}_j} - \overline{\tilde{u}}_i\,\overline{\tilde{u}}_j}_{\tau_{RSFS}}$$

$$\chi_i = \overline{u_i \theta} - \overline{\tilde{u}}_i\,\overline{\tilde{\theta}} = \underbrace{\overline{u_i \theta} - \overline{\tilde{u}_i\,\tilde{\theta}}}_{\chi_{SGS}} + \underbrace{\overline{\tilde{u}_i\,\tilde{\theta}} - \overline{\tilde{u}}_i\,\overline{\tilde{\theta}}}_{\chi_{RSFS}}$$

Applying a coarse filter $\widehat{\ }$ on top of the filtered momentum and potential temperature equations, and discretizing on a coarse grid, represented by $\widetilde{\ }^c$, we obtain:

$$\frac{\partial \widehat{\bar{u}_i^c}}{\partial t} + \frac{\partial \widehat{\widetilde{\bar{u}_i^c \bar{u}_j^c}}^c}{\partial x_j} = -\frac{1}{\rho}\frac{\partial \widehat{\bar{p}^c}}{\partial x_i} - \frac{\partial \widetilde{T_{ij}}^c}{\partial x_j}$$

$$\frac{\partial \widehat{\bar{\theta}^c}}{\partial t} + \frac{\partial \widehat{\widetilde{\bar{u}_i^c \bar{\theta}^c}}^c}{\partial x_i} = -\frac{\partial \bar{X}_i^c}{\partial x_i}$$

where the SFS stresses are:

$$T_{ij} = \widehat{\overline{u_i u_j}} - \widehat{\bar{u}_i^c}\widehat{\bar{u}_j^c} = \underbrace{\widehat{\overline{u_i u_j}} - \widehat{\overline{u_i}^c \overline{u_j}^c}}_{T_{\mathrm{SGS}}} + \underbrace{\widehat{\overline{u_i}^c \overline{u_j}^c} - \widehat{\bar{u}_i^c}\widehat{\bar{u}_j^c}}_{T_{RSFS}}$$

$$X_i = \widehat{\overline{u_i \theta}} - \widehat{\bar{u}_i^c}\widehat{\bar{\theta}^c} = \underbrace{\widehat{\overline{u_i \theta}} - \widehat{\overline{u_i}^c \bar{\theta}^c}}_{\mathrm{X_{SGS}}} + \underbrace{\widehat{\overline{u_i}^c \bar{\theta}^c} - \widehat{\bar{u}_i^c}\widehat{\bar{\theta}^c}}_{\chi_{RSFS}}$$

The implicitly filtered variables $\tilde{u}$ and $\tilde{\theta}$ can be reconstructed from their explicitly filtered counterparts with the iterative method of van Cittert:

$$\tilde{\varphi} = \bar{\tilde{\varphi}} + (I - G) * \bar{\tilde{\varphi}} + (I - G) * [(I - G) \star \bar{\tilde{\varphi}}] + \cdots$$

$$\tilde{\varphi}^c = \widehat{\bar{\tilde{\varphi}}^c} + (I - G^c) * \widehat{\bar{\tilde{\varphi}}^c} + (I - G^c) * \left[(I - G^c) \star \widehat{\bar{\tilde{\varphi}}^c}\right] + \cdots$$

where I is the identity operator, G the explicit filter $\bar{\ }$, G^c the explicit filter $\widehat{\ }$, and $*$ the convolution operator. The number of terms on the right hand side (n+1) is related to the level of reconstruction (n). A truncated series of the above equation is used to approximate $\tilde{u}_i$. For example, with one level reconstruction (abbreviated as ADM1) $\tilde{\varphi}_i \approx \tilde{\varphi}_i^\star = \bar{\tilde{\varphi}}_i + (I - G) * \bar{\tilde{\varphi}}_i$, and $\tilde{\varphi}_i^\star$ is used in the RSFS terms. Using the Wong and Lilly formulation for the SGS part, we obtain:

$$\tau_{ij} - \frac{\delta_{ij}}{3}\tau_{kk} = -2\nu_t\left(\widetilde{\bar{S}_{ij}} - \frac{\delta_{ij}}{3}\widetilde{\bar{S}_{kk}}\right) + \tau_{RSFS}^\star$$

$$\chi_i = -\nu_\theta \frac{\partial \bar{\tilde{\theta}}}{\partial z} + \chi_{RSFS}^\star$$

where:

$$\tau_{RSFS}^\star = \tau_{ij,RSFS}^\star - \frac{\delta_{ij}}{3}\tau_{kk,RSFS}^\star$$

ν_t and ν_θ are the eddy viscosity for momentum and diffusivity for heat based on the fine filter:

$$\nu_t = C_\epsilon\ \Delta^{4/3}, \quad \nu_\theta = \frac{C_\epsilon}{Pr_T}\ \Delta^{4/3}$$

where C_ϵ is the coefficient to be computed and Pr_T is the turbulent Prandtl number.

The coarse-filtered SFS stresses are:

$$T_{ij} - \frac{\delta_{ij}}{3}T_{kk} = -2N_T\left(\widehat{\widetilde{\bar{S}_{ij}}^c} - \frac{\delta_{ij}}{3}\widehat{\widetilde{\bar{S}_{kk}}^c}\right) + \left(T_{ij,RSFS}^* - \frac{\delta_{ij}}{3}T_{kk,RSFS}^*\right)$$

$$X_i = -N_\theta \frac{\partial \widehat{\overline{\tilde{\theta}^c}}}{\partial z} + X_{i,RSFS}$$

where N_t and N_θ are the eddy viscosity for momentum and diffusivity for heat based on the coarse filter:

$$N_t = C_\epsilon \ \hat{\Delta}^{4/3}, \quad N_\theta = \frac{C_\epsilon}{Pr_T} \ \hat{\Delta}^{4/3}$$

The Germano identities are:

$$L_{ij} \overset{\text{def}}{=} T_{ij} - \widehat{\tau_{ij}} = \widehat{\overline{\tilde{u}_i}\overline{\tilde{u}_j}} - \widehat{\overline{\tilde{u}_i}^c}\widehat{\overline{\tilde{u}_j}^c}$$

$$R_i \overset{\text{def}}{=} X_i - \widehat{\chi_i} = \widehat{\overline{\tilde{u}_i}\overline{\tilde{\theta}}} - \widehat{\overline{\tilde{u}_i}^c}\widehat{\overline{\tilde{\theta}}^c}$$

Both L_{ij} and R_i can be evaluated directly based on explicitly filtered variables $\overline{\tilde{u}_i}$ and $\overline{\tilde{\theta}}$, and can also be computed from the turbulence closure:

$$L_{ij} - \frac{\delta_{ij}}{3}L_{kk} = 2C_\epsilon \left(\Delta^{\frac{4}{3}} - \hat{\Delta}^{\frac{4}{3}}\right)\left(\widehat{\overline{\tilde{S}_{ij}}^c} - \frac{\delta_{ij}}{3}\widehat{\overline{\tilde{S}_{kk}}^c}\right) + H_{ij} - \frac{\delta_{ij}}{3}H_{kk}$$

$$R_i = \frac{C_\epsilon}{Pr_T}\left(\Delta^{\frac{4}{3}} - \hat{\Delta}^{\frac{4}{3}}\right)\frac{\partial \widehat{\overline{\tilde{\theta}}^c}}{\partial x_i} + Q_i$$

where

$$H_{ij} = \left(\widehat{\overline{\tilde{u}_i}^{c*}\overline{\tilde{u}_j}^{c*}} - \widehat{\overline{\tilde{u}_i}^{c*}}\,\widehat{\overline{\tilde{u}_j}^{c*}}\right) - \left(\widehat{\overline{\tilde{u}_i}^{*}\overline{\tilde{u}_j}^{*}} - \widehat{\overline{\tilde{u}_i}^{*}}\,\widehat{\overline{\tilde{u}_j}^{*}}\right)$$

$$Q_i = \left(\widehat{\overline{\tilde{u}_i}^{c*}\overline{\tilde{\theta}}^{c*}} - \widehat{\overline{\tilde{u}_i}^{c*}}\,\widehat{\overline{\tilde{\theta}}^{c*}}\right) - \left(\widehat{\overline{\tilde{u}_i}^{*}\overline{\tilde{\theta}}^{*}} - \widehat{\overline{\tilde{u}_i}^{*}}\,\widehat{\overline{\tilde{\theta}}^{*}}\right)$$

A total of 6 independent equations result for the momentum stress tensor L_{ij} and 3 for the scalar stress tensor R_i. Therefore, we use the least squares method (Lilly 1992) to minimize the overall error, and solve for ν_t and ν_θ:

$$2\nu_t = 2C_\epsilon \bar{\Delta}^{\frac{4}{3}} \approx \frac{< [L_{ij} - H_{ij} - \frac{\delta_{ij}}{3}(L_{kk} - H_{kk})](\widehat{\overline{\tilde{S}_{ij}}^c} - \frac{\delta_{ij}}{3}\widehat{\overline{\tilde{S}_{kk}}^c}) >}{\left[1 - \left(\frac{\hat{\Delta}}{\bar{\Delta}}\right)^{\frac{4}{3}}\right] < \left(\widehat{\overline{\tilde{S}_{lm}}^c} - \frac{\delta_{lm}}{3}\widehat{\overline{\tilde{S}_{nn}}^c}\right)^2 >}$$

$$\nu_\theta = \frac{C_\epsilon}{Pr_T}\Delta^{4/3} \approx \frac{< (R_i - Q_i)\frac{\partial \widehat{\overline{\tilde{\theta}}^c}}{\partial x_i} >}{\left[1 - \left(\frac{\hat{\Delta}}{\bar{\Delta}}\right)^{\frac{4}{3}}\right] < \left(\frac{\partial \widehat{\overline{\tilde{\theta}}^c}}{\partial x_i}\right)^2 >}$$

where <> indicates local averaging in space, or planar averaging for horizontally homogeneous flows. Alternatively, Lagrangian averaging seeks a better representation of <> by taking into account the history of the fluid parcel.

D.2 The Lagrangian-averaging method

Formulation of the Lagrangian-averaging method is presented here based on the Dynamic Smagorinsky model following the original derivation in Meneveau et al. 1996. It will be applied to the dynamic reconstruction model in the following section.

Starting from Germano's dynamic Smagorinsky model (Germano et al. 1991):

$$L_{ij} = \widehat{\bar{u}_i \bar{u}_j} - \hat{\bar{u}}_i \hat{\bar{u}}_j$$

$$M_{ij} = 2\Delta^2 (|\bar{S}|\bar{S}_{ij}^{\widehat{}} - 4\widehat{|\bar{S}|\bar{S}_{ij}})$$

$$e_{ij} = L_{ij} - c_s^2 M_{ij}$$

The Smagorinsky constant c_s can be contained by minimizing the error term e_{ij} based on the least squares method:

$$c_s^2 = \frac{< L_{ij} M_{ij} >}{< M_{mn} M_{mn} >}$$

where <> represents some averaging procedure, usually local volume averaging or planar averaging. The Lagrangian-averaging approach is instead performed along particle trajectories. This is advantageous for flow over complex geometries where there lacks a homogeneous direction for volume averaging. First, define $\underline{z}(t)$ to be the location of a fluid parcel at time t. In the Lagrangian framework, the error term is defined locally in space and time:

$$e_{ij}[\underline{z}(t)] = L_{ij}[\underline{z}(t)] - c_s^2[\underline{z}(t)] M_{ij}[\underline{z}(t)]$$

The error is minimized along the parcel trajectory:

$$E[\underline{z}(t)] = \int_{-\infty}^{t} e_{ij}[\underline{z}(t')] e_{ij}[\underline{z}(t')] W(t - t') dt'$$

where W is a weighting function in time, with more emphasis on values near t. $E[\underline{z}(t)]$ is minimized with respect to $c_s^2[\underline{z}(t)]$:

$$\frac{\partial E[\underline{z}(t)]}{\partial c_s^2[\underline{z}(t)]} = \int_{-\infty}^{t} 2 e_{ij}[\underline{z}(t')] \frac{\partial e_{ij}[\underline{z}(t')]}{\partial c_s^2[\underline{z}(t)]} W(t - t') dt'$$

Setting $\partial E[\underline{z}(t)] / \partial c_s^2[\underline{z}(t)]$ to be zero, and substituting the definition of e_{ij}, we obtain:

$$c_s^2[\underline{z}(t)] = \frac{\phi_{LM}[\underline{z}(t)]}{\phi_{MM}[\underline{z}(t)]}$$

where

$$\phi_{LM}[\underline{z}(t)] = \int_{-\infty}^{t} L_{ij}[\underline{z}(t')]M_{ij}[\underline{z}(t')]W(t-t')dt'$$

$$\phi_{MM}[\underline{z}(t)] = \int_{-\infty}^{t} M_{ij}[\underline{z}(t')]M_{ij}[\underline{z}(t')]W(t-t')dt'$$

Meneveau et al. (1996) proposed the following exponential form for $W(t-t')$:

$$W(t-t') = \frac{1}{T}\exp\left(\frac{t'-t}{T}\right)$$

By doing so, $\phi_{LM}[\underline{z}(t)]$ is a solution to the relaxation transport equation:

$$\frac{D\phi_{LM}}{Dt} \stackrel{\text{def}}{=} \frac{\partial \phi_{LM}}{\partial t} + \underline{u}\cdot\nabla\phi_{LM} = \frac{1}{T}(L_{ij}M_{ij} - \phi_{LM})$$

A similar equation can be written for ϕ_{MM} by replacing $L_{ij}M_{ij}$ with $M_{ij}M_{ij}$, We present here a simple proof to shown why an exponential decaying weighing function W is a solution to the above relaxation transport equation. Consider a fluid parcel at time t, spatial location $\underline{x}$, with velocity $\underline{u}$, and $\phi_{LM}(\underline{x},t)$. After some small fraction of time Δt later, the new location of the fluid parcel is $\underline{x}+\underline{u}\Delta t$. The updated $\phi_{LM}(\underline{x}+\underline{u}\Delta t, t+\Delta t)$ is:

$$\begin{aligned}\phi_{LM}(\underline{x}+\underline{u}\Delta t, t+\Delta t) &= \int_{-\infty}^{t+\Delta t} L_{ij}[\underline{z}(t')]M_{ij}[\underline{z}(t')]W(t+\Delta t-t')dt' \\ &= \underbrace{\int_{-\infty}^{t} L_{ij}[\underline{z}(t')]M_{ij}[\underline{z}(t')]W(t+\Delta t-t')dt'}_{PartI} \\ &+ \underbrace{\int_{t}^{t+\Delta t} L_{ij}[\underline{z}(t')]M_{ij}[\underline{z}(t')]W(t+\Delta t-t')dt'}_{PartII}\end{aligned}$$

By construction, the weighting function W has the following property:

$$\begin{aligned}W(t+\Delta t-t') &= \frac{1}{T}\exp\left[\frac{-(t+\Delta t-t')}{T}\right] \\ &= \frac{1}{T}\exp\left[\frac{-(t-t')}{T}\right]\exp\left(-\frac{\Delta t}{T}\right) = W(t-t')\exp\left(-\frac{\Delta t}{T}\right)\end{aligned}$$

So part *I* becomes:

$$PartI = \phi_{LM}(\underline{x}, t)\exp\left(-\frac{\Delta t}{T}\right)$$

When Δt is small, Taylor series expansion of the exponential term gives the following expression:

$$PartI = \phi_{LM}(\underline{x}, t)\left(1 - \frac{\Delta t}{T}\right) + O(\Delta t^2)$$

Integration of part *II* can be approximated to the first order of Δt based on its value at t, multiplied by Δt:

$$PartII = L_{ij}(\underline{x}, t)M_{ij}(\underline{x}, t)\,\frac{1}{T}\exp\left(-\frac{\Delta t}{T}\right)\Delta t$$

Again when Δt is small, $\exp\left(-\frac{\Delta t}{T}\right) = 1 - \frac{\Delta t}{T}$, so the leading order $O(\Delta t)$ term in part *II* is:

$$PartII = L_{ij}(\underline{x}, t)M_{ij}(\underline{x}, t)\,\frac{\Delta t}{T} + O(\Delta t^2)$$

Therefore:

$$\begin{aligned}\phi_{LM}(\underline{x} + \underline{u}\Delta t, t + \Delta t) &= PartI + PartII \\ &= \phi_{LM}(\underline{x}, t)\left(1 - \frac{\Delta t}{T}\right) + L_{ij}(\underline{x}, t)M_{ij}(\underline{x}, t)\frac{\Delta t}{T} + +O(\Delta t^2)\end{aligned}$$

or:

$$\frac{\phi_{LM}(\underline{x} + \underline{u}\Delta t, t + \Delta t) - \phi_{LM}(\underline{x}, t)}{\Delta t} = \frac{1}{T}\left[L_{ij}(\underline{x}, t)M_{ij}(\underline{x}, t) - \phi_{LM}(\underline{x}, t)\right] + O(\Delta t)$$

Taking the limit $\Delta t \to 0$, we obtain the relaxation transport equation:

$$\frac{D\phi_{LM}}{Dt} = \frac{1}{T}(L_{ij}M_{ij} - \phi_{LM})$$

The relaxation time T is chosen to be $1.5\Delta(\phi_{LM}\phi_{MM})^{-1/8}$ in Meneveau et al. (1996). Overall, ϕ is integrated based on the relaxation transport equation, using the following formulation, for example, to march forward in time. For example, $\phi^{n+1}(\underline{x}^{n+1})$ at n+1th time step at location $\underline{x}^{n+1}$ is computed based on its value $\phi^n(\underline{x}^n)$ at the nth time step at location $\underline{x}^n$:

$$\frac{\phi^{n+1}(\underline{x}^{n+1}) - \phi^n(\underline{x}^n)}{\Delta t} = \frac{1}{T^n}\left[L_{ij}^{n+1}M_{ij}^{n+1}(\underline{x}^{n+1}) - \phi^{n+1}(\underline{x}^{n+1})\right]$$

$$\phi^{n+1}(\underline{x}^{n+1}) = \epsilon L_{ij}^{n+1}M_{ij}^{n+1}(\underline{x}^{n+1}) + (1 - \epsilon)\phi^n(\underline{x}^n)$$

where

$$\epsilon = \frac{\Delta t/T^n}{1 + \Delta t/T^n}, \quad T_n = 1.5\Delta\left[\phi_{LM}^n(\underline{x}^n)\phi_{MM}(\underline{x}^n)\right]^{-1/8}$$

The location $\underline{x}^{n+1}$at time step n+1 is evaluated at the grid points, and the previous location $\underline{x}^{n}$ is computed based on the forward Euler scheme.

$$\underline{x}^{n} = \underline{x}^{n+1} - \underline{u}^{n}\Delta t$$

Based on the location $\underline{x}^{n}$, $\phi^{n}(\underline{x}^{n})$ is evaluated using multi-linear interpolation of grid values at time step n. The use of the relaxation transport equation eliminates the need to carry the full spatial-temporal history of the parcel.

D.3 The Lagrangian-averaged dynamic reconstruction model (LDRM) with explicit filtering and reconstruction

The dynamic Wong-Lilly model with explicit filtering and reconstruction formulation derived in section D.1 is represented here:

$$L_{ij} - \frac{\delta_{ij}}{3}L_{kk} = 2C_{\epsilon}\left(\Delta^{\frac{4}{3}} - \hat{\Delta}^{\frac{4}{3}}\right)\left(\widehat{\overline{\widetilde{S}_{ij}}^{c}} - \frac{\delta_{ij}}{3}\widehat{\overline{\widetilde{S}_{kk}}^{c}}\right) + H_{ij} - \frac{\delta_{ij}}{3}H_{kk}$$

$$R_i = \frac{C_{\epsilon}}{Pr_T}\left(\Delta^{\frac{4}{3}} - \hat{\Delta}^{\frac{4}{3}}\right)\frac{\partial\widehat{\overline{\tilde{\theta}}^{c}}}{\partial x_i} + Q_i$$

where

$$H_{ij} = \left(\widehat{\overline{\widetilde{u}_i}^{c*}\overline{\widetilde{u}_j}^{c*}} - \widehat{\overline{\widetilde{u}_i}^{c*}}\,\widehat{\overline{\widetilde{u}_j}^{c*}}\right) - \left(\widehat{\overline{\widetilde{u}_i}^{*}\overline{\widetilde{u}_j}^{*}} - \widehat{\overline{\widetilde{u}_i}^{*}}\,\widehat{\overline{\widetilde{u}_j}^{*}}\right)$$

$$Q_i = \left(\widehat{\overline{\widetilde{u}_i}^{c*}\overline{\tilde{\theta}}^{c*}} - \widehat{\overline{\widetilde{u}_i}^{c*}}\,\widehat{\overline{\tilde{\theta}}^{c*}}\right) - \left(\widehat{\overline{\widetilde{u}_i}^{*}\overline{\tilde{\theta}}^{*}} - \widehat{\overline{\widetilde{u}_i}^{*}}\,\widehat{\overline{\tilde{\theta}}^{*}}\right)$$

$$\nu_t = C_{\epsilon}\ \Delta^{4/3}, \quad \nu_{\theta} = \frac{C_{\epsilon}}{Pr_T}\ \Delta^{4/3}$$

Denote $1 - \left(\frac{\hat{\Delta}}{\Delta}\right)^{\frac{4}{3}}$ as C_{fc}. The error terms are:

$$e_{ij} = \left(L_{ij}^{a} - H_{ij}^{a}\right) - 2\nu_t C_{fc}\widehat{\overline{\widetilde{S}_{ij}}^{c}}^{a}$$

$$g_i = (R_i - Q_i) - \nu_{\theta}C_{fc}\frac{\partial\widehat{\overline{\tilde{\theta}}^{c}}}{\partial x_i}$$

where the superscript *a* denotes the anisotropic part of the tensor. Using Lagrangian averaging, we obtain

$$2\nu_t = \frac{\phi_{LHS}}{\phi_{SS}}, \quad \nu_{\theta} = \frac{\phi_{RQT}}{\phi_{TT}}$$

where

$$\phi_{LHS}[\underline{z}(t)] = \int_{-\infty}^{t} \left(L_{ij}^{a} - H_{ij}^{a}\right) C_{fc} \widehat{\widetilde{S}_{ij}^{c}}^{a} [\underline{z}(t')] W(t-t')dt'$$

$$\phi_{SS}[\underline{z}(t)] = \int_{-\infty}^{t} C_{fc}^{2} \widehat{\widetilde{S}_{ij}^{c}}^{a} \widehat{\widetilde{S}_{ij}^{c}}^{a} [\underline{z}(t')] W(t-t')dt'$$

$$\phi_{RQT}[\underline{z}(t)] = \int_{-\infty}^{t} (R_i - Q_i) C_{fc} \frac{\partial \widehat{\widetilde{\theta}^{c}}}{\partial x_i} [\underline{z}(t')] W(t-t')dt'$$

$$\phi_{TT}[\underline{z}(t)] = \int_{-\infty}^{t} C_{fc}^{2} \frac{\partial \widehat{\widetilde{\theta}^{c}}}{\partial x_i} \frac{\partial \widehat{\widetilde{\theta}^{c}}}{\partial x_i} [\underline{z}(t')] W(t-t')dt'$$

Units for ϕ_{LHS} are [L^2/T^3], and those for ϕ_{SS} are [$1/T^2$]. ϕs can be solved with an relaxation transport equation outlined in section D.2, for example:

$$\frac{D\phi_{LHS}}{Dt} = \frac{1}{T}\left[\left(L_{ij}^{a} - H_{ij}^{a}\right) C_{fc} \widehat{\widetilde{S}_{ij}^{c}}^{a} - \phi_{LHS}\right]$$

Based on dimensional analysis, the relaxation time for the LDRM is:

$$T = C_{LDRM} \left(\frac{\phi_{LHS}\phi_{SS}}{\Delta^2}\right)^{-1/5}$$

T is a decorrelation time scale for the Lagrangian parcel. Since the above expression is derived based on dimensional arguments, C_{LDRM} needs to be determined based on tests on simple flows. Preliminary tests show that C_{LDRM} = 1.0 works well for a moderately stable atmospheric boundary layer over flat terrain.

Appendix E USGS topography and land cover

The first part of this appendix lists the mapping of USGS National Land Cover Dataset (NCLD) classifications to the ARPS vegetation types. The second part describes the Albers equal-area conic projection that maps latitude and longitude (ϕ, λ) to Cartesian Coordinates (x, y). This conversion is used in reading USGS land cover into ARPS. The last section documents procedures to obtain high resolution USGS topography and land cover for use in ARPS.

E.1 Mapping of USGS NCLD to ARPS

Table E-1 Mapping of USGS NCLD to ARPS vegetation type, superscript A indicates Alaska only. The USGS vegetation roughness is obtained from WRF VEGPARM.TBL. Unknown values are marked with "-". The ARPS vegetation roughness is obtained from Chapter 8, page 228 of ARPS documentation for Version 4.0.

		USGS			ARPS	
ID	Type	Z_{0min} (m)	Z_{0max} (m)	ID	Type	Z_0 (m)
11	Open water	0.0001	0.0001	14	Water	0.001
12	Perennial ice or snow	0.001	0.001	9	Ice	0.005
21	Developed, open space	-	-	3	Grassland	0.01
22	Developed, low intensity	-	-	4	Grassland with shrub cover	0.1
23	Developed, medium intensity	-	-	5	Grassland with tree cover	
24	Developed, high intensity	-	-	6	Deciduous forest	0.75
31	Barren land (rock/sand/clay)	0.01	0.01	13	Semidesert	0.04
41	Deciduous forest	0.5	0.5	6	Deciduous forest	0.75
42	Evergreen forest	0.5	0.5	7	Evergreen forest	1
43	Mixed forest	0.2	0.5	6	Deciduous forest	0.75
51	Dwarf scrub[A]	-	-	12	Dwarf shrub	0.06
52	Shrub/scrub	0.01	0.05	13	Dwarf shrub	0.06
71	Grassland/herbaceous	0.1	0.12	3	Grassland	0.01
72	Sedge/herbaceous[A]	-	-	-	-	-
73	Lichens[A]	-	-	-	-	-
74	Moss[A]	-	-	-	-	-
81	Pasture/hay	0.02	0.15	10	Cultivation	0.02
82	Cultivated crops	0.02	0.2	10	Cultivation	0.02
90	Woody wetlands	0.4	0.4	11	Bog or march	0.02

95	Emergent herbaceous wetlands	0.2	0.2	11	Bog or march	0.02

E.2 Albers equal-area conic projection

The subroutines in arpssfclib.f90 inside /src/arpssfc obtain land cover by converting the ARPS grid from latitude-longitude (ϕ, λ) to Cartesian coordinates (x, y). The land cover dataset is given in equally spaced Cartesian coordinates. The ARPS grid is then overlaid on top of the land cover grid, and grid values are determined from the closest land cover data point. A map projection is used to map (ϕ, λ) to (x, y). Different datasets are made with different projection schemes. The ARPS default 1 km resolution land cover requires conversion through a Lambert conformal projection. The USGS 30 m resolution land cover requires an Albers equal-area conic projection. The latter scheme was implemented as part of this work in arpsslib.f90 to allow ARPS to read in USGS land cover. Mapping from (ϕ, λ) to (x, y) with the Albers equal-area conic projection is described as follows:

$$x = \rho sin\theta$$

$$y = \rho_0 - \rho cos\theta$$

where

$$\theta = n(\lambda - \lambda_0)$$

$$\rho = (a\sqrt{C - n\alpha})/n$$

$$\rho_0 = (a\sqrt{C - n\alpha_0})/n$$

and

$$C = m_1^2 + n\alpha_1$$

$$n = (m_1^2 - m_2^2)/(\alpha_1 - \alpha_2)$$

$$m_i = \frac{\cos\phi_i}{\sqrt{1 - e^2\sin^2\phi_i}}, \quad i = 1,2$$

$$\alpha = (1 - e^2)[\frac{sin\phi}{1 - e^2\sin^2\phi} - \frac{1}{2e}\ln(\frac{1 - esin\phi}{1 + esin\phi})]$$

$$\alpha_i = (1 - e^2)\left[\frac{sin\phi_i}{1 - e^2\sin^2\phi_i} - \frac{1}{2e}\ln\left(\frac{1 - esin\phi_i}{1 + esin\phi_i}\right)\right], \quad i = 0,1,2$$

where (ϕ_0, λ_0) are the coordinates of the ARPS domain center (ctrlat, ctrlon), ϕ_1 and ϕ_2 are the latitudes of the 1st and 2nd standard parallel (29.5° and 45.5°) set by USGS NLCD. a is the radius of the earth, which is 6378137 m. e is the eccentricity of the earth, which is 0.0818191911.